



JOHANNES GUTENBERG
UNIVERSITÄT MAINZ



Max-Planck-Institut
für Polymerforschung

Max Planck Institute
for Polymer Research



Visible Light-induced Organic Transformations Using Benzothiadiazole Derivatives as Highly Efficient Photocatalysts

Dissertation

Zur Erlangung des Grades

“Doktor der Naturwissenschaften”

im Promotionsfach Chemie

dem Fachbereich Chemie, Pharmazie und Geowissenschaften

der Johannes Gutenberg-Universität Mainz

Run Li

Geboren in HuBei, China

Mainz, 2017

Dekan:

1. Berichterstatter:

2. Berichterstatter:

Tag der mündlichen Prüfung:

Affidavit

I hereby confirm that I have completed the present dissertation independently and without inadmissible external support. I have not used any sources or tools other than those indicated and have identified literal and analogous quotations.

Furthermore, I confirm that this thesis has not yet been submitted as part of another examination process neither in identical nor in similar form.

Ort, Datum:

Unterschrift:

Einführung

Das Ziel dieser Arbeit ist es, niedermolekulare und makromolekulare organische Halbleiter auf Basis von 2,1,3-benzothiadiazole (BT) als entweder homogene oder heterogene Photokatalysatoren zu entwickeln, die unter Bestrahlung vom sichtbaren Licht aktiviert und für organische Photoredox-Reaktionen eingesetzt werden können.

Das erste Projekt befasst sich mit der Konstruktion von einem niedermolekularen organischen Halbleiter auf Basis von BT- und Phenyl-(PH-)einheiten. Diese Elektronendonator- und Akzeptor-Kombination erlaubt eine effiziente Ladungsseparation und Entstehung des Elektron-Loch-Paars via Lichtaktivierung. Hohe Redoxpotentiale von -1.30 V und +1.64 V vs SCE können erreicht werden. Sowohl die Diels-Alder-Reaktion und die direkte Bromierung von Alkoholen können entweder über reduktive oder oxidative Lösungsprozesse mit hohen Ausbeuten katalysiert werden. Mit Hilfe fortgeschrittener photophysikalischer Messmethoden wie zeitaufgelöste Photolumineszenz- oder transiente Absorptionsspektroskopien können der genaue Elektronentransfer und Wechselwirkung zwischen Komponenten ermittelt werden.

Als nächstes wird der entworfene molekulare organische Halbleiter in ein hoch poröses, dreidimensionales und nicht durchkonjugiertes Polymernetzwerk durch direkte Vernetzung eingebaut. Hohe Oberflächen von über 1000 m²/g können erreicht werden. Die porösen Polymernetzwerke werden dann als heterogene Photokatalysatoren für direkte Bromierung an Aromaten eingesetzt. Eine hohe Stabilität und Wiederverwendbarkeit der porösen Polymere können durch Wiederholungsexperimente demonstriert werden.

Um die Einsatzbarkeit der BT-Ph-Einheiten zu untersuchen, wird ein durchkonjugiertes Polymernetzwerk eingebaut. Das Polymer kann die photokatalytische [2+2]-Cycloaddition unter Bestrahlung von sichtbarem Licht erfolgreich katalysieren. Außerdem können Naturstoffe wie Di-*O*-methylenendiandrin A oder Endiandrin A dadurch effizient hergestellt werden.

Als letztes wird ein weit verbreitetes Problem bei organischen Halbleitern untersucht, nämlich die relativ kurze Lebensdauer der Exzitonen im Nanosekundenbereich. In dem letzten Projekt stellen wir ein neues Konstruktionsprinzip der organischen Halbleiter dar, indem die Donor- und Akzeptoreinheiten senkrecht zueinander stehen und dadurch wenige Überlappungen der *p*-Orbitale zustande kommen. Durch dieses strukturelle Design kann die Lebensdauer der Exzitonen von Nanosekunden auf Mikrosekunden erhöht werden. Außerdem kann beobachtet werden, dass die Elektronen in ihrem ersten angeregten Zustand noch einmal Photonen absorbieren und auf ein energetisch höheres Level übergehen können. Anspruchsvolle Photoredox-Reaktionen wie die Aktivierung von *sp*²- oder *sp*³-Kohlenstoff-Halogenbindungen kann dadurch erfolgreich katalysiert werden.

Abstract

In this work, both small molecular and macromolecular organic semiconductors containing 2,1,3-benzothiadiazole (BT) moiety were designed and synthesized as either homogeneous or heterogeneous visible light-active photocatalysts for redox reactions.

The first project aimed to design a molecular organic semiconductor-based photocatalyst consisting of BT as electron-withdrawing unit and phenyl as electron-donating moiety. The obtained photocatalyst exhibited sufficient photoredox potentials at -1.30 V and +1.64 V vs. SCE. It could efficiently catalyze both cationic Diels-Alder reaction and direct conversion of aliphatic alcohols to bromides via reductive and oxidative quenching processes, respectively. Advanced photophysical studies such as time-resolved photoluminescence and transient absorption spectroscopy revealed the details about photo-induced electron transfer pathway during the catalytic process.

In order to introduce surface properties and obtain heterogeneous organic photocatalytic systems, the donor-acceptor-type molecular organic semiconductor designed before was incorporated into a series of non-conjugated, microporous organic polymers. High surface areas larger than 1000 m²/g were achieved. The porous polymer networks were employed as heterogeneous photocatalysts for visible light-promoted, highly selective bromination reaction of electron-rich aromatic compounds using HBr as economic bromine source and molecular oxygen as clean oxidant. High stability and reusability were demonstrated for the prepared polymer photocatalysts.

To further study the feasibility of the BT-based photocatalytic systems, the BT unit was incorporated into a fully conjugated microporous polymer network. The photocatalytic [2+2] cycloaddition as a useful tool for the synthesis of cyclobutane derivatives, which contribute a large part to natural compounds production, was then investigated. Both unsymmetrical and homo-cycloaddition could be achieved with high conversion and selectivity. In addition, some natural products, such as di-*O*-methylendiandrin A and endiandrin A were also synthesized with excellent catalytic efficiency.

Light-induced charge separation with typical exciton lifetimes in nanosecond range belongs to the characteristic feature of organic semiconductor-based photocatalysts. The exciton recombination prevents possible long charge separation lifetime and thereby inhibits the catalytic efficiency. In the last project in this thesis, this major problem of organic photocatalytic systems has been addressed and a potential solution has been introduced. To scavenge the fast charge recombination, a highly twisted donor-acceptor molecular structure was designed with the molecular orbitals of the donor and acceptor units being perpendicular to each other. The designed twisted photocatalyst exhibited an extremely long fluorescence lifetime of 37 μs. Furthermore, the excited electron on the LUMO level could undergo the second excitation process and was transferred from LUMO to LUMO+X

level. This led an unexpected high reduction potential of the photocatalyst. As model reactions, both sp^2 and sp^3 carbon-halogen bonds could be successfully activated accompanying with the formation of dehalogenated products.

Acknowledgment

While only my name is written on the cover of this dissertation, many people also make contribution to its production. At this special moment, I would like to appreciate those who make this dissertation possible and my PhD study an impressive experience.

Firstly, I would like to express my gratitude to my supervisor, Prof. Katharina Landfester, for her untiring guidance, encouragement and support during my PhD study. I am very lucky to have a high quality supervisor who trusts me and gives me enough freedom to form my own cognitive framework. During the past three years, she has already shown me how to systematically analyze the backgrounds, precisely identify the gaps, efficiently construct the solutions, and carefully design the experiments, which impresses me deeply.

Secondly, I am really grateful to my project leader, Dr. Kai Zhang, for his practical guidance, untiring patience, and unconditional trust. I could always achieve some insightful comments and feedbacks whenever I come across some challenges. Meanwhile, I would like to appreciate that he offers me an opportunity to study in a world-renowned institute.

Thirdly, I would like to thank my group members, Lei Wang, Dr. Zi Jun Wang, Wei Huang, Dr. Beatriz Ma, Dr. Saman Ghasimi, and Dr. Jeehye Byun. Lei offers many practical suggestions about organic synthesis and fruitful discussions about experiment design. In addition, I thank some friends in my department, Dr. Li-ping Lv, Dr. Shuai Jiang, and Wei He. All of them enrich my spare time and help me getting used to German lifestyles. Moreover, I also thank my collaboration partners, Dr. Hao Lu, Dr. Dominik Gehrig, Simon Bretschneider, Dr. Charusheela Ramanan, and Dr. Manfred Wagner. It is worth to mention that I am really grateful to all friends and colleagues in MPI-P (both AK Landfester and other departments) for making my PhD work going smoothly, and providing a friendly working atmosphere.

Fourthly, I desire to express my heart-felt acknowledge to my family, my father, my mother, and my brother for their perpetual love and support.

Lastly, I greatly appreciate the financial support from China Scholarship Council (CSC).

Table of Contents

Einführung.....	i
Abstract.....	ii
Acknowledgment	iv
List of Figures	5
List of Tables.....	12
List of Acronyms.....	13
1 Introduction	16
2 Aim of work	17
3 Theoretical Background	18
3.1 Photocatalysis.....	18
3.1.1 General mechanisms of photocatalysis.....	19
3.2 Photocatalytic organic transformations catalyzed by transition metals.....	20
3.2.1 Inorganic photocatalysts	20
3.2.2 Ruthenium and Iridium polypyridyl complexes	21
3.2.3 Other organometallic photocatalysts	24
3.3 Organic semiconductors as photocatalysts for organic reactions.....	24
3.3.1 Cyanoarenes, benzophenones and quinones	25
3.3.2 Xanthene and pyrylium dyes	26
3.3.3 Acridiniums and quinoliniums.....	29
3.3.4 Visible light-active polymers as heterogeneous photocatalysts.....	31
3.4 Novel photocatalysts based on benzothiadiazole chromophores.....	33
3.4.1 Basic properties of benzothiadiazoles	33
3.4.2 Photocatalytic oxidation reactions with benzothiadiazole photocatalysts	34
3.4.3 Photocatalytic reduction reactions with benzothiadiazole photocatalysts.....	37
4 Characterization Techniques.....	41
4.1 UV-Vis and UV/Vis Diffuse Reflectance Spectroscopy.....	41
4.2 Fluorescence Spectroscopy	41
4.3 Nuclear Magnetic Resonance Spectroscopy (NMR).....	42
4.4 Cyclic Voltammetry (CV)	43

4.5 Electron Paramagnetic Resonance (EPR).....	44
4.6 Gas Chromatography-Mass Spectrometry (GC-MS).....	44
5 Results and Discussion.....	45
5.1 A metal-free, dually redox-active organic photocatalyst for visible light-promoted Diels-Alder reaction and direct conversion of aliphatic alcohols to bromides	45
5.1.1 Motivation	46
5.1.2 Synthesis and characterization of Ph-BT-Ph	47
5.1.3 Photocatalytic redox transformation with Ph-BT-Ph	48
5.1.4 Conclusion and outlook.....	64
5.2 Photocatalytic selective bromination of electron-rich aromatic compounds using microporous organic polymers with visible light.....	65
5.2.1 Motivation	65
5.2.2 Synthesis and characterization of MOPs	66
5.2.3 Photocatalytic capacity test of MOPs for selective bromination on aromatic rings	74
5.2.4 Conclusion and outlook.....	82
5.3 Photocatalytic regio- and stereo-Selective [2+2] cycloaddition of styrene derivatives using a heterogeneous organic photocatalyst.....	83
5.3.1 Motivation	83
5.3.2 Synthesis and characterization of B-BT	84
5.3.3 Photocatalytic [2+2] cycloaddition with the obtained photocatalyst B-BT	88
5.3.4 Conclusion and outlook.....	93
5.4 Design of organic semiconductors with extreme long exciton life time for photocatalytic reduction of aryl and alkyl halides	94
5.4.1 Motivation	94
5.4.2 Synthesis and characterization of photocatalyst BT-DHA	95
5.4.3 Photocatalytic activity test for BT-DHA.....	99
5.4.4 Conclusion and outlook.....	106
6 Experimental Section.....	107
6.1 A metal-free, dually redox-active organic photocatalyst for visible light-promoted Diels-Alder reaction and direct conversion of aliphatic alcohols to bromides	107
6.1.1 Materials	107

6.1.2 Methods and characterizations.....	107
6.1.3 Synthesis of photocatalyst Ph-BT-Ph.....	108
6.1.4 Photocatalytic redox reaction with Ph-BT-Ph.....	109
6.1.5 Photocatalytic oxidation of DMF with organic photocatalysts.....	116
6.1.6 Insights of radical pathway for photocatalytic bromination reaction.....	117
6.1.7 Repeating experiments for photocatalytic Diels-Alder reaction.....	118
6.1.8 NMR spectra.....	119
6.2 Photocatalytic selective bromination of electron-rich aromatic compounds using microporous organic polymers with visible light.....	135
6.2.1 Materials.....	135
6.2.2 Methods and characterization.....	135
6.2.3 Synthesis of photocatalysts MOPs.....	136
6.2.4 Photocatalytic selective bromination of aromatic compounds using the MOPs as heterogeneous photocatalysts.....	137
6.2.5 Investigation of Cl ⁻ and I ⁻ as halide source.....	143
6.2.6 Determination of H ₂ O ₂	144
6.2.7 NMR spectra.....	145
6.3 Photocatalytic regio- and stereo-Selective [2+2] cycloaddition of styrene derivatives using a heterogeneous organic photocatalyst.....	158
6.3.1 Materials.....	158
6.3.2 Methods and characterization.....	158
6.3.3. Synthesis of photocatalyst B-BT.....	159
6.3.4 Photocatalytic [2+2] cycloaddition reaction with B-BT.....	159
6.3.5 NMR spectra.....	167
6.4 Design of twisted structure with thermally activated delayed fluorescence characteristic and its catalytic application for reduction of aryl and alkyl halides via consecutive visible light-induced charge transfer.....	179
6.4.1 Materials.....	179
6.4.2 Methods and characterization.....	179
6.4.3 Preparation of photocatalyst BT-DHA.....	179
6.4.4 Photocatalytic reduction of aryl and alkyl halides.....	182
6.4.5 Deuterium labeling experiment.....	182

6.4.6 NMR spectra	183
7 Overall summary and Outlook	186
8 References.....	188
9 Scientific Contributions	199

List of Figures

Figure 3.1 Schematic illumination of the photoinduced electron transfer processes from the conduction or to the valence band in a typical inorganic semiconductor-based photocatalyst. Sub: reactive substrates, [ox]: oxidants, [red]: reductants.

Figure 3.2 Photocatalytic oxidation of aryl alcohols, aryl amines and alkenes with TiO_2 as photocatalyst.

Figure 3.3 Molecular orbital depiction of $\text{Ru}(\text{bpy})_3^{2+}$ photochemistry (left) and *fac*- $\text{Ir}(\text{ppy})_3$ photochemistry (right).

Figure 3.4 Schematic illuminations of photocatalytic organic transformations with ruthenium and iridium photocatalyst. Black, blue, green balls stand for leaving functional groups, radical keeping groups and radical accepting groups, respectively.

Figure 3.5 Examples of molecular organic semiconductor-based photocatalysts.

Figure 3.6 Photocatalytic intramolecular and intermolecular cyclization and oxidative addition reactions with cyanoarenes photocatalysts.

Figure 3.7 Photocatalytic organic transformations with xanthene dyes as visible light photocatalysts.

Figure 3.8 Jablonski diagram of Mes-Acr⁺.

Figure 3.9 Photo-driven oxidative reactions with acridiniums derivatives as visible light photocatalysts.

Figure 3.10 Detection of singlet oxygen in organic solvent and water based on oxidative addition reactions.

Figure 3.11 (a) Reactive monomers for polymer network construction, and (b) degradation process of ciprofloxacin using poly-BTs/ TiO_2 hybrid materials.

Figure 3.12 (a) Geometry design principle of band position of conjugated microporous poly(benzooxadiazole) network, (b) photocatalytic oxidative coupling of benzylamines, and (c) corresponding reaction mechanism.

Figure 3.13 (a) Photocatalytic cyclization between N-methylanilines and N-substituted maleimides with polymer photocatalyst and (b) corresponding reaction mechanism.

Figure 3.14 Construction of benzothiadiazole-based porous polymers and photocatalytic application for hydrogen evolution.

Figure 3.15 (a) Photocatalytic reduction of aryl bromides with polymer photocatalyst and (b) corresponding reaction pathways.

Figure 3.16 (a) photocatalytic C-C coupling between bromides and aldehydes and (b) C-C coupling between diethyl bromomalonate and heteroaromates. Value in parentheses in (a) indicates the enantioselectivity.

Figure 4.1 (a) A typical curve obtained from cyclic voltammetry measurement (Ferrocene as an example) and (b) energy chart of HOMO and LUMO of sample comparing to the reference electrode.

Figure 5.1 (a) Structure of Ph-BT-Ph; (b) simulated electron density of Ph-BT-Ph on its HOMO and LUMO levels; (c) UV-Vis (black, solid) and fluorescence (red, dash) of Ph-BT-Ph; Cyclic voltammetry of Ph-BT-Ph in the oxidative cycle (d) and reductive cycle (e) and (f) the photoredox potential comparison of Ph-BT-Ph with the other state-of-art organic and metal-based molecular photocatalysts. Values of $[\text{Ru}(\text{bpy})_3]^{2+}$, *fac*- $[\text{Ir}(\text{ppy})_3]$, eosin Y and $\text{Acr}^+\text{-Mes}$ are taken from literature. bpy = 2,2'-bipyridyl; ppy = phenylpyridyl.

Figure 5.2 (a) Monitoring experiment of photocatalytic Diels-Alder reaction and (b) reaction conversion change for light on and off.

Figure 5.3 Proposed reaction mechanism of photocatalytic Diels-Alder reaction using Ph-BT-Ph as visible light-active photocatalyst.

Figure 5.4 EPR spectra for neat DMPO (0.1 M) solution in acetonitrile in dark (black), and mixture of DMPO (0.1 M) and Ph-BT-Ph (1 mg/mL) in dark (red) and under the irradiation of blue LED for 10 min (blue).

Figure 5.5 Scope of the photocatalytic Diels-Alder reaction using Ph-BT-Ph as photocatalyst.

Figure 5.6 Repeating experiment of the photocatalytic Diels-Alder reaction.

Figure 5.7 UV-Vis spectra of Ph-BT-Ph before (black) and after (red) photocatalytic Diels-Alder reaction.

Figure 5.8 Fluorescence intensity of Ph-BT-Ph change after bubbling with N_2 and O_2 for 10 min, respectively. I_0 for emission intensity after degassing with N_2 and I for emission intensity after degassing with O_2 .

Figure 5.9 Fluorescence decay spectra of Ph-BT-Ph under N_2 (black), O_2 (red), and with anethole under N_2 (green) and in air (blue), the concentration of Ph-BT-Ph and anethole in acetonitrile solution were 20 mg/L and 2 mM, respectively. Excitation wavelength at 400 nm.

Figure 5.10 Transient absorption spectra of pure Ph-BT-Ph (20 mg/L) in N₂ (a) and O₂ (b) atmospheres, and (c) mixture of Ph-BT-Ph (20 mg/L) and *trans*-anethole (20 mM) at different time intervals in CH₃CN. (d) Time profiles of the absorbance decay at 675 nm of pure Ph-BT-Ph (20 mg/L, black), with 10 mM *trans*-anethole (red) and 20 mM *trans*-anethole (blue) in CH₃CN. Excitation at 355 nm.

Figure 5.11 Comparison of decay profiles of transient absorption (TA) at 660 - 690 nm and time-resolved photoluminescence (TRPL) at 480 - 520 nm in CH₃CN. Pure Ph-BT-Ph under N₂ (a) and O₂ (b) and mixture of Ph-BT-Ph and *trans*-anethole under N₂ atmosphere (c) and O₂ atmosphere in CH₃CN (d). Concentration for Ph-BT-Ph and *trans*-anethole are 20 mg/L and 2 mM, respectively.

Figure 5.12 (a) GC spectrum of crude product after photocatalytic bromination with deuterium DMF and (b) corresponding MS spectrum for the second peak.

Figure 5.13 (a) GC spectrum of crude product after photocatalytic bromination of α -methylstyrene and corresponding MS spectra for the third (b), the fourth (c) and the fifth peak (d).

Figure 5.14 Proposed reaction mechanism of photocatalytic direct conversion of alkyl alcohols to bromides using Ph-BT-Ph as visible light-active photocatalyst.

Figure 5.15 Scope of the photocatalytic conversion of alkyl alcohols to bromides using Ph-BT-Ph as photocatalyst.

Figure 5.16 UV-Vis spectra of Ph-BT-Ph before (black) and after (red) photocatalytic conversion of aliphatic alcohols to bromides.

Figure 5.17 (a) Fluorescence spectra of Ph-BT-Ph after adding various amounts of CBr₄ quencher and (b) fluorescence intensity change in the presence of CBr₄. I_0 for emission intensity in the absence of quencher and I for emission intensity in the presence of quencher.

Figure 5.18 Fluorescence decay spectra of Ph-BT-Ph (black), mixture of Ph-BT-Ph with CBr₄ (red), with alcohol (green), and with both CBr₄ and alcohol (blue), the concentration of Ph-BT-Ph, CBr₄ and alcohol were 20 mg/L, 8 mM and 4 mM in DMF, respectively. Excitation wavelength at 400 nm.

Figure 5.19 Transient absorption spectra of (a) pure Ph-BT-Ph, (b) with CBr₄ and (c) with alcohol at in DMF at various timescale. (d) Time profiles of absorbance decay at 670 nm of Ph-BT-Ph (black, square), Ph-BT-Ph with CBr₄ (red, circle), Ph-BT-Ph with alcohol (green, up triangle) and Ph-BT-Ph with CBr₄ and alcohol (blue, down triangle). Concentrations of Ph-BT-Ph, CBr₄ and alcohol were 20 mg/L, 8 mM, and 4 mM respectively. Excitation at 355 nm.

Figure 5.20 Comparison of decay profiles of transient absorption (TA) at 660 – 690 nm and time-resolved photoluminescence (TRPL) at 480-520 nm for the bromination reaction. (a) pure Ph-BT-Ph, (b) with CBr₄, (c) with alcohol, and (d) with both CBr₄ and alcohol. Concentrations of Ph-BT-Ph, CBr₄ and alcohol were 20 mg/L, 8 mM, and 4 mM in DMF.

Figure 5.21 SEM images of (a) MOP-0, (b) MOP-1, and TEM images of (c) MOP-0, (d) MOP-1.

Figure 5.22 (a) N₂ sorption and desorption isotherms, and (b) pore size distributions of MOP-0.

Figure 5.23 (a) N₂ sorption and desorption isotherms, and (b) pore size distributions of MOP-0b.

Figure 5.24 (a) N₂ sorption and desorption isotherms, and (b) pore size distributions of MOP-1.

Figure 5.25 (a) N₂ sorption and desorption isotherms, and (b) pore size distributions of MOP-1b.

Figure 5.26 Solid state ¹³C/MAS NMR spectrum with an idealized structure of MOP-0.

Figure 5.27 Solid state ¹³C/MAS NMR spectrum with an idealized structure of MOP-1.

Figure 5.28 (a) FTIR spectra, (b) UV/vis DR spectra, (c) valence band (VB) and conduction band (CB) positions of the MOPs and (d) EPR spectra under light irradiation.

Figure 5.29 Cyclic voltammetry of MOP-0, (a) reduction cycle and (b) oxidation cycle.

Figure 5.30 Cyclic voltammetry of MOP-1, (a) reduction cycle and (b) oxidation cycle.

Figure 5.31 UPS spectra of MOP-0 (a) and MOP-1 (b). The dashed red lines mark the baseline and the tangents of the curve.

Figure 5.32 EPR spectra of MOP-0 taken in dark and under light irradiation.

Figure 5.33 Thermogravimetric analysis of the MOPs.

Figure 5.34 EPR spectra of DMPO-O₂^{•-} (a) and TEMP-¹O₂ adducts (b) using MOP-1 as photocatalyst in dark and under light irradiation.

Figure 5.35 Suggested reaction mechanism of photocatalytic bromination of TMB using the MOPs as photocatalyst. *s* and *t* represent the singlet and triplet states of the excited electrons photogenerated in the MOPs. ISC: intersystem crossing.

Figure 5.36 (a) UV-Vis absorption spectra of pure water and reaction system with or without catalyst after adding DPD and POD for H₂O₂ determination. (b) Standard curve of

H₂O₂ concentration based on its absorption maximum at 551 nm. This method is based on the POD-catalyzed oxidation reaction of DPD by H₂O₂, which gives the radical cation DPD^{•+}. The radical cation can be easily determined by its two typical absorption peaks at ca. 510 and 551 nm.

Figure 5.37 Monitoring experiment of the photocatalytic bromination reaction of TMB.

Figure 5.38 Repeating experiment of the photocatalytic bromination of TMB using MOP-1 as photocatalyst.

Figure 5.39 FTIR spectra of MOP-1 before (black) and after (red) 5 repeating cycles of the photocatalytic bromination of TMB.

Figure 5.40 SEM and TEM images of MOP-1 after 5 repeating cycles of the photocatalytic bromination of TMB.

Figure 5.41 Suggested mechanisms for the formation of benzaldehyde instead of *p*-bromotoluene with toluene being as reactive substrate due to the high oxidation potential of toluene (1.98 V vs. SCE).

Figure 5.42 (a) Chemical structure, (b) SEM and (c) TEM image, (d) FTIR, (e) UV/Vis DR spectra, (f) Kubelka-Munk plot, and (g) HOMO and LUMO band positions of B-BT.

Figure 5.43 Solid-state ¹³C CP-MAS NMR spectrum of B-BT.

Figure 5.44 (a) N₂ sorption and desorption isotherms, and (b) pore size distributions of B-BT.

Figure 5.45 (a) Cyclic voltammetry of B-BT in the reduction cycle and (b) ultraviolet photoelectron spectroscopy (UPS) of B-BT. The dashed red lines mark the baseline and the tangents of the curve.

Figure 5.46 (a) EPR spectra of B-BT taken in dark and after light irradiation for 20 min, and (b) photocurrent responses upon switching the light on and off (blue LED, λ=460 nm).

Figure 5.47 Thermogravimetric analysis of B-BT.

Figure 5.48 (a) EPR spectra of DMPO-O₂^{•-} adducts with B-BT as photocatalyst in dark or under blue light irradiation (λ = 460 nm, 1.2 W/cm²). (b) EPR spectra using PBN as radical trapping agent for the radical intermediate of anethole under light irradiation. Pure PBN (black); PNB with anethole and B-BT under N₂ atmosphere (red); and under O₂ (blue); simulated EPR pattern of the trapped radical (green).

Figure 5.49 Proposed reaction mechanisms for the photocatalytic [2+2] cycloaddition using B-BT via 3 possible routes.

Figure 5.50 (a) Scope of the [2+2] cycloaddition reactions; the value in parentheses indicates the selectivity of unsymmetrical products compared with dimers. (b) Some natural products obtained.

Figure 5.51 Repeating experiment of dimerization (black) and unsymmetrical cycloaddition (red) for 3 cycles.

Figure 5.52 FTIR spectra of B-BT before photocatalysis reaction (black) and after 3 repeating cycles (red).

Figure 5.53 SEM image (a) and TEM image (b) of B-BT after 3 times repeating experiments.

Figure 5.54 (a) General synthesis pathway of photocatalyst BT-DHA between BT-Br and DHA, (b) single crystal structure of the obtained BT-DHA and (c) calculated HOMO and LUMO state.

Figure 5.55 (a) UV-Vis spectra of BT-DHA (black), DHA (red), BT (blue) and mixture of DHA and BT with a molar ratio of 2/1 (magenta), normalized UV-Vis absorption spectra (b) and fluorescence spectra (c) of BT-DHA in different solvents. The solvents used are hexane (black), toluene (red), diethyl ether (blue), THF (magenta), DCM (olive) and DMF (navy). The insert of (b) shows the magnification of absorption between 380 nm and 650 nm. (d) Lippert-Mataga plots with simple line-of-best-fit for BT-DHA. There are two fitted-lines corresponding to all tested solvents (blue) and only polar solvents (red).

Figure 5.56 UV-Vis absorption (solid line) and fluorescence (dash line) spectra of BT-DHA in toluene solution (black), neat BT-DHA film (red), and BT-DHA 10 wt% doped *m*-CP film (blue).

Figure 5.57 Photoluminescence decay of neat BT-DHA film at 291 K.

Figure 5.58 Photoluminescence spectra of 10 wt% BT-DHA/*m*-CP film measure at 77 K. the black and red curve show the fluorescence and phosphorescence spectra, respectively. (b) Photoluminescence decay of doped film at 291 K (black) and 77 K (red).

Figure 5.59 Cyclic voltammetry of BT-DHA for oxidative cycle (a) and reductive cycle (b).

Figure 5.60 Reductive cycle of BT and oxidative cycle of DHA.

Figure 5.61 UV-Vis spectra of BT-DHA (black), DIPEA (red), halogenated acetophenone (blue), mixture of BT-DHA and DIPEA(magenta), BT-DHA and halogenated acetophenone (olive), and BT-DHA, DIPEA and halogenated acetophenone (navy). Halogenated acetophenone indicates 4-iodoacetophenone (a) and 4-bromoacetophenone (b).

Figure 5.62 (a) The emission spectra of the BT-DHA after adding various amounts of DIPEA and (b) emission intensity as a function of DIPEA. I_0 for the emission intensity without DIPEA, and I for the emission intensity in the present of DIPEA.

Figure 5.63 UV-Vis spectra of pure BT-DHA solution and BT-DHA/DIPEA mixture under the irradiation of blue light by given time durations.

Figure 5.64 Cyclic voltammetry spectra of neat BT-DHA in dark (black), under the light irradiation for 1 h (red), mixture of BT-DHA and DIPEA in dark (blue), and under the light irradiation for 1 h (magenta).

Figure 5.65 The proposed reaction mechanism. The value for LUMO+1 was obtained from theory calculation.

Figure 5.66 Scope of photoreduction of aryl and alkyl halides under visible light.

Figure 5.67 Scope of dimerization of benzyl bromides after irradiating under visible light.

Figure 5.68 Synthetic route of imipramine.

List of Tables

Table 3.1 Basic physical and structural properties of TiO₂.

Table 3.2 Photophysical and electrochemical properties of oxathene dyes.

Table 3.3 Photocatalytic organic redox transformations with polymer photocatalysts.

Table 3.4 Photophysical and electrochemical details for some benzothiadiazole compounds.

Table 5.1 Screening and control experiments of the photocatalytic Diels-Alder reaction of *trans*-anethole and isoprene.

Table 5.2 Excited state life time of the measured mixtures.

Table 5.3 Screening and control experiments of the photocatalytic bromination reaction with model substrate.

Table 5.4 Excited state life time of the measured mixtures.

Table 5.5 Porosity data and electrochemical properties of the MOPs.

Table 5.6 Screening and control experiments of the photocatalytic bromination of 1, 2, 4-trimethoxybenzene using the MOPs.

Table 5.7 Scope of the photocatalytic bromination of aromatic compounds using MOP-1 as photocatalyst under visible light.

Table 5.8 Screening and control experiments of the [2+2] cycloaddition using B-BT as photocatalyst.

Table 5.9 Screening and control experiments of the photocatalytic reduction of aryl halides using the model reaction.

List of Acronyms

Atm	atmospheric pressure
ATRA	atom transfer radical addition
AQY	apparent quantum yield
B	magnetic field
BET	Brunauer Emmett Teller
BT	benzothiadiazole
CB	conduction band
Cbz	carboxybenzyl
CMP	conjugated microporous polymer
CP-MAS	cross polarization magic angle spinning
CT	charge transfer state
CV	cyclic voltammetry
DFT	density functional theory
DCM	dichloromethane
DMF	N,N-dimethylformamide
DMSO	dimethyl sulfoxide
DMPO	5,5-dimethyl-1-pyrroline N-oxide
DRS	diffuse reflectance spectra
EDG	electron donating group
E_{opt}	optical band gap
E_{oxi}	oxidative potential
EPR	electron paramagnetic resonance spectroscopy
eq.	equation
E_{red}	reductive potential

EWG	electron withdrawing group
EY	eosin Y
FTIR	Fourier transform infrared
h	Planck constant
HAT	hydrogen atom transfer
HOMO	highest occupied molecular orbital
ISC	intersystem crossing
ICT	intramolecular charge transfer
LE	locally excited state
LED	light emitting diode
LUMO	lowest unoccupied molecular orbital
MLCT	metal to ligand charge transfer
NBS	N-bromosuccinimide
NHC	N-heterocyclic carbene
NIR	near infrared
NMR	nuclear magnetic resonance
PET	photoinduced electron transfer
PL	photoluminescence
PBN	N-tert-butyl- α -phenylnitron
Poly-BTs	polybenzothiadiazoles
RB	rose Bengal
RhB	rhodamine B
r. t.	room temperature
s	singlet state
SCE	saturated calomel electrode

SEM	scanning electron microscopy
SET	single electron transfer
<i>t</i>	triplet state
T	absolute temperature
TADF	thermally activated delayed fluorescence
TEM	transmission electron microscopy
TEMP	2,2,6,6-tetramethylpiperidine
TMPD	N,N,N',N'-tetramethyl-p-phenylenediamine
TGA	thermalgravimetric analysis
THF	tetrahydrofuran
UV	ultraviolet

1 Introduction

Using photocatalysis for the conversion of solar energy into chemical energy has become increasingly appealing during the past decades. It offers a promising solution for the tremendous environmental and health issues caused by the consumption of fossil fuels in traditional industrial processes. The utilization of sunlight for chemical reactions has already been performed in 18th century¹, with a revolutionary concept already introduced by Giacomo Ciamician in 1912². Almost a century after this visionary concept, around 2008, the feasibility of transition metal complexes such as ruthenium polypyridyl as photosensitizer for C-C and C-Br bond activation reactions have been reported³⁻⁵. The utilization of light energy for organic synthesis has thus witnessed an explosive growth ever since.

From the perspective of photocatalysts design, transition metals, especially ruthenium and iridium polypyridyls, have been intensely developed as efficient photocatalysts based on their fully-understood properties, such as visible light absorption, tunable redox potentials, long lived excited state, and efficient single electron transfer-process⁶⁻⁸. Additionally, recent studies also show some common metal-based photocatalysts such as copper⁹, iron¹⁰ and tin¹¹ complexes. However, due to some intrinsic drawbacks for transition metals including toxic, high price, and unstable in aerobic condition, some organic dyes, such as cyanoarenes, xanthenes and acridiniums, have been designed and applied as metal-free alternations¹²⁻¹⁴. Nevertheless, normal organic dyes also suffer some disadvantages of photo-bleaching, limited photoredox capacity, and UV-response in many cases. Therefore, the exploitation and development of new classes of metal-free and stable photocatalysts is highly required.

The aim of this thesis is to design a new class of metal-free and pure organic photocatalytic system. For this purpose, benzothiadiazole, a strong electron-withdrawing unit, is incorporated into various electron donor-acceptor-type photocatalytic systems. Both small molecular and macromolecular systems are designed and applied as either homogeneous or heterogeneous photocatalysts for organic photoredox reactions. Important parameters such as energy band structure, surface property or porosity will be investigated to reveal their influence on the photocatalytic efficiency.

Furthermore, advanced photophysical studies as time-resolved photoluminescence and transient absorption spectroscopy will be conducted to investigate the precise photo-induced electron transfer pathway during the catalytic process.

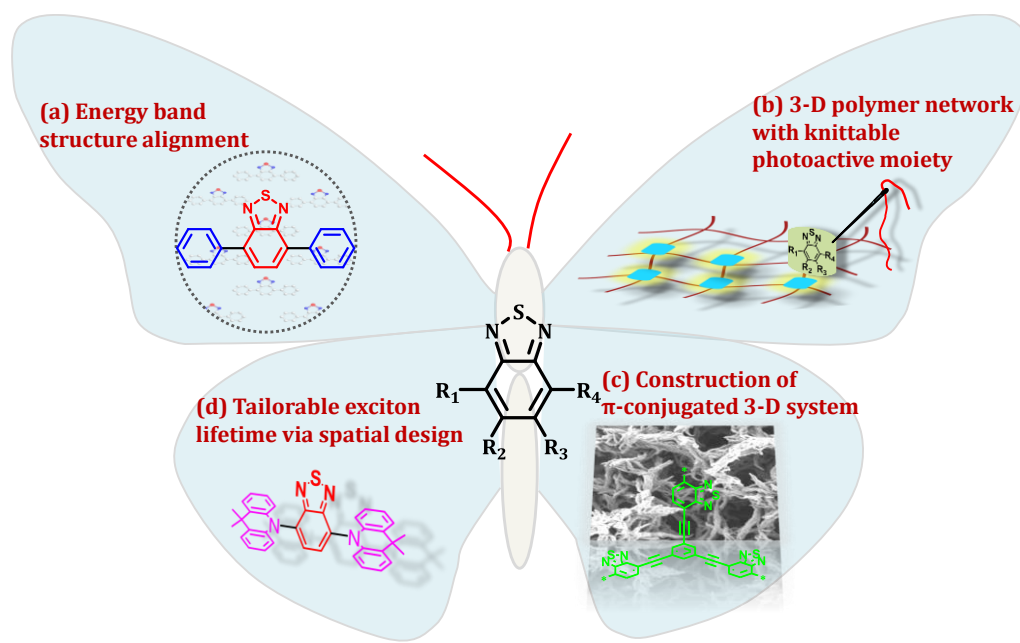
2 Aim of work

The objective of this work was to design benzothiadiazole-based visible light-active photocatalysts as a promising alternative to the traditional transition metal complexes and organic dyes for organic photoredox reactions. Two main design strategies have been applied.

1) Molecular donor-acceptor-type systems as homogeneous photocatalysts. Three main parameters were investigated: (i) energy band structures, i.e. the corresponding photo-reduction and -oxidation potentials; (ii) the lifetime of the excitons, i.e. the photogenerated electron/hole pair after charge separation; (iii) photo-induced charge transfer within the catalytic system. Here, the benzothiadiazole units were either directly coupled with phenyl unit in a simple flat-shaped molecule, or with 9,9-dimethyl-9,10-dihydroacridine in a highly twisted molecule in order to prevent the fast charge recombination and to elongate the exciton lifetime of the photocatalyst.

2) Macromolecular systems with high porosity as heterogeneous photocatalysts. Here, the benzothiadiazole unit was incorporated into either fully conjugated or non-conjugated microporous polymer networks. Important parameters such as porosity, energy band position, and charge separation efficiency were investigated to offer some principles for design of outstanding heterogeneous polymer photocatalysts.

For all photocatalytic systems, the photophysical, photochemical and electrochemical analysis approaches were conducted to reveal the mechanistic insights during the reaction. The individual projects are illustrated in the figure below.



3 Theoretical Background

3.1 Photocatalysis

Photochemistry and photocatalysis using solar energy for the production of valuable chemical and renewable fuel is a promising and future-orientated solution to address the environmental problems caused by the consumption of traditional fossil fuels. In the International Congress of Applied Chemistry in 1912, Giacomo Giamician gave a prophetic lecture entitled “The Photochemistry of the Future”, which is regarded as the first prophecy for the potential of photocatalysis^{2,15}.

“On the arid lands there will spring up industrial colonies without smoke and without smokestacks; forests of glass tubes will extend over the plains and glass buildings will rise everywhere; inside of these will take place the photochemical processes that hitherto have been the guarded secret of the plants, but that will have been mastered by human industry which will know how to make them bear even more abundant fruit than nature, for nature is not in a hurry and mankind is. And if in a distant future the supply of coal becomes completely exhausted, civilization will not be checked by that, for life and civilization will continue as long as the sun shines!”

Beside the production of clean and renewable energy carriers such as hydrogen, methanol or formic acid etc., photo-driven organic transformation reactions offers another useful tool as an alternative to the thermally mediated reactions. Indeed, photochemistry has been established as a crucial synthetic methodology especially in recent decades in the production of fine chemicals, pharmaceuticals and natural products¹⁵⁻¹⁷. Previously, reactive radicals are generated via thermal-control methods as the intermediates towards the desired products. The recent development has demonstrated that various reactive species can also be generated via photochemical approaches. For example, arene radicals^{18,19}, trifluoromethyl radicals^{20,21}, iminium ions^{22,23}, and enone radical anions^{4,24} could be conveniently obtained using photocatalysis. Chemical bonds, thus, can be efficiently constructed based on those intermediates via radical pathways. Furthermore, in cooperation with organocatalysts including redox mediators²⁵, N-heterocyclic carbene (NHC)^{26,27}, enamine catalysts^{3,28} and transition metallic catalysts^{25,27}, photocatalytic systems have been widely applied in a co-called synergetic manner for the chemical bond formations with high conversion and selectivity. However, despite of recent research activities in the field of photocatalysis and the intense development of highly efficient photocatalysts, the application of photocatalysis for industrial use is still rare. Therefore, enhanced efforts ought to be put for the realization of industrial application and even the way of thinking need to be changed to move further towards the prophecy of Giacomo Giamician.

3.1.1 General mechanisms of photocatalysis

The interactions between the excited state photocatalysts and the substrate molecules play an essential role for the feasibility of the photocatalytic reactions. Basically, three types of activation steps are involved into the photocatalytic cycle, i.e. photo-induced electron transfer, atom transfer and energy transfer. Among them, the most reported photochemical synthesis undergoes the photo-induced electron transfer (PET) process. As illuminated in Figure 3.1, in a traditional inorganic semiconductor-based photocatalytic system^{29,30}, the electron is excited from the valence band to the conduction band when one photon is absorbed by the catalyst, resulting in the formation of the photo-induced electron-hole pair. Then on one hand the photo-generated electron migrates to the surface of the catalyst, leading to the reduction of the surrounding substrates. On the other hand, the photo-generated hole can extract one electron from the reactants, causing an oxidative reaction.

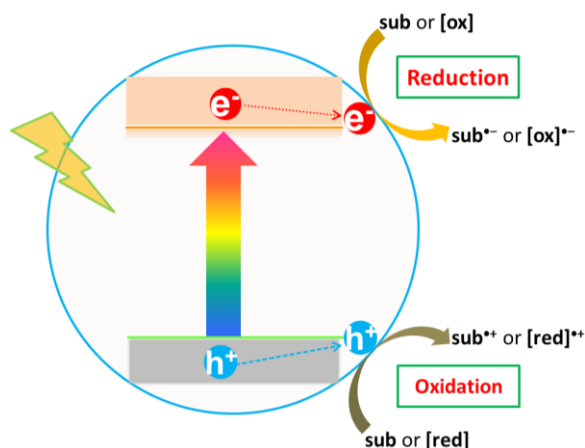


Figure 3.1 Schematic illumination of the photoinduced electron transfer processes from the conduction or to the valence band in a typical inorganic semiconductor-based photocatalyst. Sub: reactive substrates, [ox]: oxidants, [red]: reductants.

Furthermore, photocatalytic reactions may also be completed via photo-induced atom transfer or energy transfer. For example, photoreduction of aryl ketones, such as benzophenone and acetophenone, tends to take place by direct hydrogen atom transfer (HAT)^{31,32}. A similar mechanism can also be found in the radical addition to electron-deficient alkenes catalyzed by decatungstate^{33,34}. Lastly, photocatalytic reactions via energy transfer from the photocatalysts to reactive substrates are also possible if the transfer process is thermodynamically feasible, for example, photocatalytic cycloaddition reactions are apt to undergo via photo-induced energy transfer³⁵⁻³⁷.

In the following subchapters, a compact overview on the photocatalytic organic reactions from the perspective of different classes of photocatalysts will be given.

3.2 Photocatalytic organic transformations catalyzed by transition metals

In the past decades, transition metal-based photocatalysts, including both inorganic metal oxides, metal sulfides and organometallic complexes, have been intensely investigated as state-of-art photocatalytic systems. More recently, transition metal complex-containing photocatalytic systems, especially ruthenium or iridium polypyridyls, have been widely employed due to their outstanding physical and chemical properties. At the same time, other metals complexes, including chromium^{38,39}, copper^{40,41}, zirconium⁴², and cerium⁴³ are reported as photocatalysts for organic transformations. Therefore, this chapter is basically separated into three parts. Inorganic photocatalysts would be described firstly, following by ruthenium and iridium polypyridyls and then other organometallic complexes. For each kind of photocatalyst, the typical characters and corresponding catalytic reactions would be discussed in details.

3.2.1 Inorganic photocatalysts

Inorganic photocatalysts, including both metal oxides such as TiO₂, ZrO₂, SrTiO₃, Nb₂O₅ and ZnO, and metal sulfides such as CdS and ZnS, have shown excellent performances mainly in photocatalytic oxidation of organic compounds, hydrogen evolution and photocatalytic treatment of waste water⁴⁴⁻⁴⁷. Among them, titanium dioxide, especially P25 TiO₂, enjoys the highest popularity probably because of facily available and tailorable. In this chapter, TiO₂ is chosen as the model for this special category because most inorganic photocatalysts share similar structural properties and photocatalytic behaviors.

TiO₂ has typically three different polymorphs, i.e. anatase, rutile and brookite with former two forms frequently be adopted as photocatalysts (basic properties listed in Table 3.1). TiO₂ basically absorbs only UV light while illuminates slight shift depending on its crystallization and morphology. In addition, the charge recombination of electron-hole pairs undergoes rapidly, which may partly suppress the quantum efficiency of TiO₂.

Table 3.1 Basic physical and structural properties of TiO₂.^a

Property	Molecular weight (g/mol)	Light absorption	Mohr`s hardness	Dielectric constant	Crystal structure	Band gap (eV)
Anatase	79.88	< 390	5.5	31	Tetragonal	3.2
Rutile	79.88	< 415	6.5-7.0	114	Tetragonal	3.0

^aValues reproduced from previous report⁴⁸.

Many oxidation reactions have been catalyzed using TiO₂ photocatalyst due to its extremely high oxidation potential (3.1 V vs. NHE)⁴⁹. For example, the photodegradation of organic pollutants and compounds of lignocellulosic biomass could be completed because of its

convenient generation of reactive oxygen species^{46,48,49}. Furthermore, TiO₂ also shows a high efficiency for the photocatalytic oxidation of benzyl alcohols (Figure 3.2, eq. 1)⁵⁰, aryl amines (eq. 2)⁵¹ and olefins (eq. 3)⁵². Since pure TiO₂ absorbs typically UV light, the preparation of visible light-response TiO₂ photocatalysts has aroused much interest in recent decades. Actually, doping titanium with other elements such as nitrogen, fluorine, carbon, sulfur, transition metals (Cr, Co, V and Fe) and noble metals (Ag, Au, Pt and Pd) provide efficient routes to obtain visible light active TiO₂ photocatalysts^{48,53,54}. The doped TiO₂ materials demonstrate a high catalytic capacity for the formation of C-C bond and C-N bond^{45,55-57}.

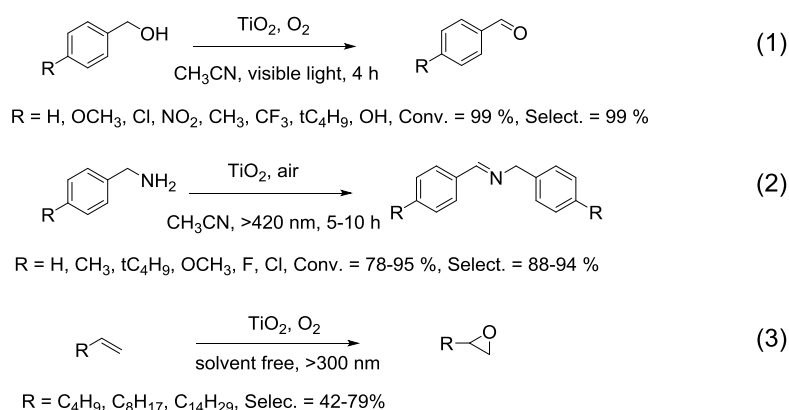


Figure 3.2 Photocatalytic oxidation of aryl alcohols, aryl amines and alkenes with TiO₂ as photocatalyst.

3.2.2 Ruthenium and Iridium polypyridyl complexes

Ruthenium polypyridyl salts, such as Ru(bpy)₃²⁺, may be the most commonly employed visible light photocatalysts for organic photoredox reactions. Since the first report in 1936⁵⁸, Ru(bpy)₃²⁺ has received much attention due to its outstanding photochemical and electrochemical properties in applications for water splitting⁵⁹, CO₂ reduction⁶⁰, and cationic polymerization⁶¹. Under the irradiation of visible light, the electron in metal-centered t_{2g} orbital is excited to ligand-centered π* orbital, which is termed as metal to ligand charge transfer (MLCT), resulting in the generation of a highly reactive species in which the metal could be oxidized to Ru(III) and the ligand could be reduced via single-electron reduction (Figure 3.3)⁶². In addition, the rapid intersystem crossing (ISC) also facilitates the formation of the lower energetic triplet MLCT state from the original singlet MLCT state. Since the triplet MLCT state is a stable, long-living photoexcited state with a life time of ca. 1.1 μs, it could undergo an electron-transfer process from the photocatalyst to the reactive substrate in competing with the deactivation pathway. Another benefit for ruthenium polypyridyl photocatalysts lie in the tailorable redox potentials by altering corresponding ligands. More precisely, increasing the electron density of the metal may

decrease the oxidative capacity of photocatalyst while, conversely, increasing the electron density of ligand could enhance the reductive ability⁶³. Furthermore, the catalysts in excited state normally demonstrate enhanced photoredox properties than ground state due to the participation of additional photo energy, which also benefits to the initiation of chemical reactions.

Parallel to $\text{Ru}(\text{bpy})_3^{2+}$, iridium polypridyl complexes, such as *fac*- $\text{Ir}(\text{ppy})_3$, have also witnessed an impressive growth in recent years. *fac*- $\text{Ir}(\text{ppy})_3$ shares the similar MLCT nature and has a comparable excited state lifetime as that of ruthenium photocatalysts (Figure 3.3)⁸. In addition, iridium photocatalysts, generally have slightly higher reduction potentials, endowing the iridium catalyst with an excellent photo-reduction capacity⁷.

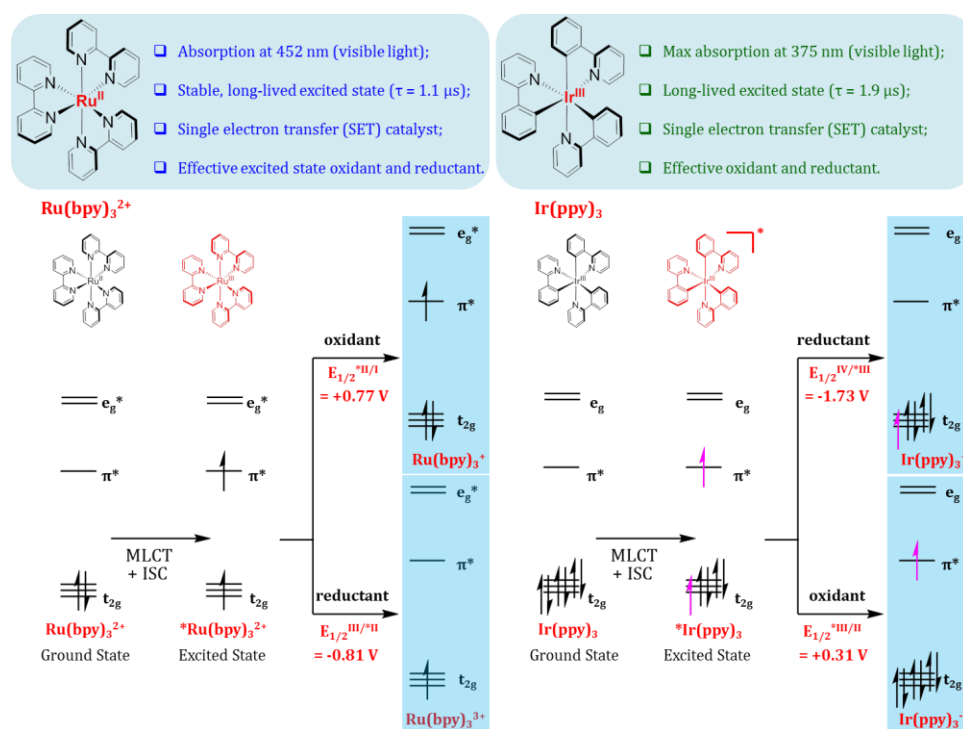


Figure 3.3 Molecular orbital depiction of $\text{Ru}(\text{bpy})_3^{2+}$ photochemistry (left) and *fac*- $\text{Ir}(\text{ppy})_3$ photochemistry (right).

Ruthenium and iridium photocatalysts have contributed to a large part in the current photo-driven organic synthesis. When the catalysts are excited to the excited state, there are two kinds of quenching pathways regarding to the electron transfer or hole transfer between the excited state photocatalysts and reactive substrates. Many organic transformations could be therefore designed based on those electron transfer processes^{7,8,25,62}. For the termed oxidative quenching cycle, the photocatalysts function as reductants by donating an electron to the substrate. Then specific chemical bonds in substrates are activated and disassociated, resulting in the generation of active radicals after those connection bonds are cleaved. Afterwards, active radical intermediates combine

with other neutral substrates to form a new chemical bond (Figure 3.4). There are many function groups which could be employed for the new bond construction based on the oxidative quenching cycle. For instance, halogens, sulfonyl chlorides, diaryliodonium salts and diazonium salt can be facily removed by ruthenium and iridium photocatalysts once the reduction potential are compatible¹⁸. Moreover, the cyano group can be removed by *fac*-Ir(ppy)₃, promoting the construction of C-C bond^{64,65}. Contrastingly, the photocatalysts can also undergo reductive quenching by extracting one electron from the reagents. Numbers of function groups are employed for the design of organic transformations based on reductive quenching pathway. For example, carboxyl^{66,67}, ethynylbenziodoxolones^{68,69}, N-hydroxyphthalimide⁷⁰, and trifluoroborates⁷¹ can be dissociated after releasing an electron, thus generating radicals for new chemical bond formations (Figure 3.4). Additionally, olefins, especially enones, could conveniently be oxidized by the photocatalyst. The generated radicals then could be trapped by other neutral alkenes for producing cyclic compounds. A considerable number of [2+2]^{4,72}, [2+3]⁷³ and [2+4]⁷⁴ cycloaddition reactions have been reported based on this cation radical-directed pathway. Lastly, with selectfluor as fluorine source, monofluorination of organic compounds could also be achieved in photochemical way⁷⁵.

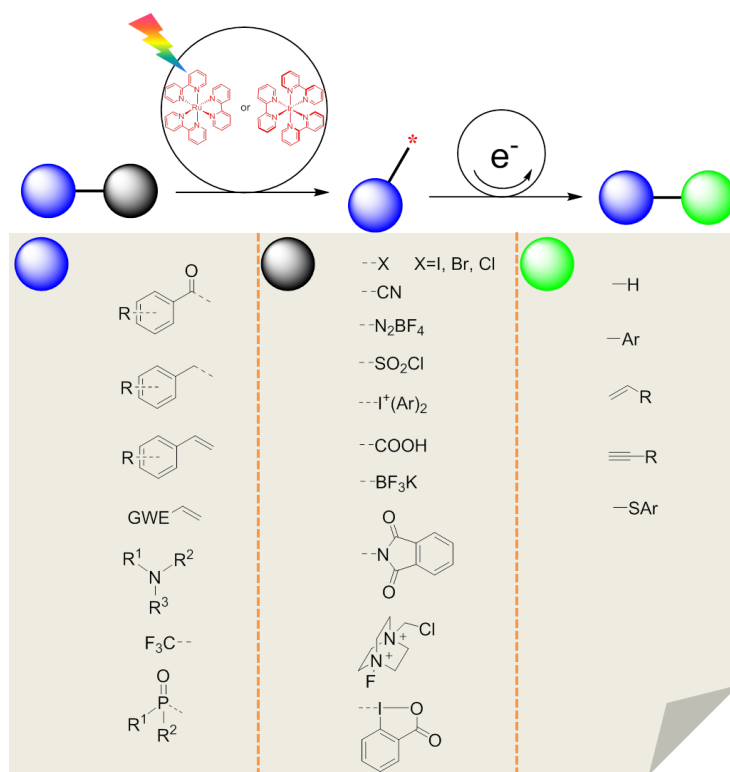


Figure 3.4 Schematic illuminations of photocatalytic organic transformations with ruthenium and iridium photocatalyst. Black, blue, green balls stand for leaving functional groups, radical keeping groups and radical accepting groups, respectively.

3.2.3 Other organometallic photocatalysts

In recent years, common metal-based organometallic photocatalysts have also been reported. For instance, a copper complex, Cu(XantPhos)(neo)BF₄, has been reported for the synthesis of helical polyaromatic carbocycles⁷⁶. Another copper photocatalyst, Cu^I(phenanthroline)₂, shows the utility for atom transfer radical addition (ATRA) reaction⁹. In addition, other organometallic compounds such as chromium has been employed as photocatalyst for [4+2] cycloaddition reaction^{38,39}; zirconium complexes illuminates the catalytic activity for debromination reaction⁴²; cerium could catalyze the aryl coupling reaction by activating the carbon-halogen bond⁴³; and iron promotes the C-C formation with high enantioselectivity⁷⁷.

3.3 Organic semiconductors as photocatalysts for organic reactions

Despite the high efficiency and the wide use of metal complex-based photocatalysts for organic reactions, there are still intrinsic drawbacks associated with those metal systems, which limits their applications⁷⁸. For instance, both metals and corresponding ligands are usually expensive and sensitive to oxygen or moisture. The storage is a huge troublesome. In addition, the toxicity of metals is another unfavorable factor for their broad application in the pharmaceutical industry. Lastly, the mass consumption of metals and the large amount of chemical waste are not favorable for a sustainable industrial process. Therefore, the development of pure organic and metal-free photocatalysts plays a critical role for photocatalytic application. Actually, much development has been achieved in metal-free photo-driven organic synthesis. Up to now, various organic molecules showing semiconducting properties have been reported as photocatalysts, including cyanoarenes, benzophenones, quinones, pyryliums, acridiniums, xanthenes, quinoliniums, thiazines, and perylene diimide (Figure 3.5)^{12,79,80}. According to their photophysical characteristics, a large number of those organic photocatalysts only respond to UV light. Nevertheless, organic dyes, such as xanthenes and acridiniums, demonstrate excellent visible light absorption properties, and have been employed in the current photo-synthetic applications. In this chapter, the organic photocatalysts are basically divided into four parts. Firstly, we describe the UV-sensitive photocatalysts, such as cyanoarenes, benzophenones and quinones. Then, some visible light absorption dyes such as xanthenes and pyryliums are discussed which are followed by organic semiconductors such as acridiniums and quinoliniums. Lastly, various types of polymers will also be demonstrated as part of heterogeneous organic photocatalysts.

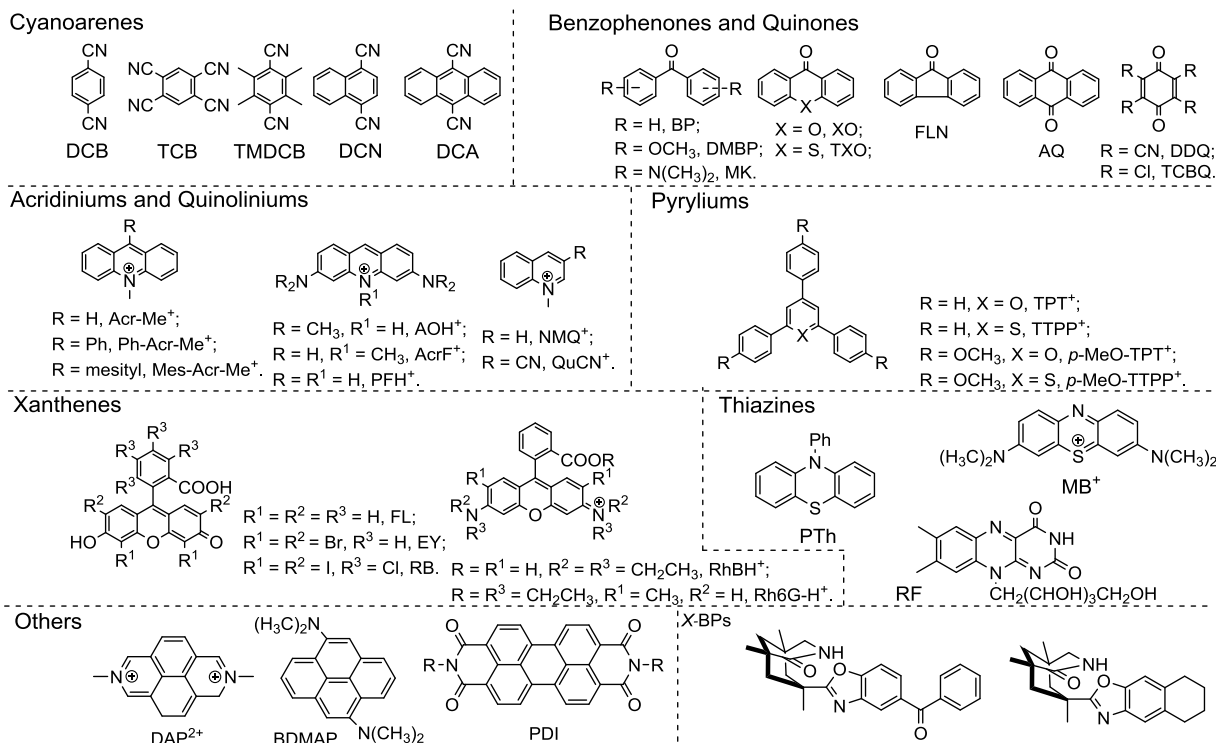


Figure 3.5 Examples of molecular organic semiconductor-based photocatalysts.

3.3.1 Cyanoarenes, benzophenones and quinones

Organic semiconductors, such as cyanoarenes, benzophenones and quinones, respond basically in UV region. Oxidative reactions could be designed due to the strong electron-withdrawing capacity of those photocatalysts. For example, double bonds could be readily oxidized by cyanoarenes photocatalysts, resulting in the generation of cationic radicals, in which annulation-type adducts could be obtained after further electron transfer process (Figure 3.6, eq. 1-3)⁸¹⁻⁸³. Intermolecular [3+2] cycloaddition between α , α -disilylamines and double bonds, including C=C and C=O bonds, could be constructed using 1,4-dicyanonaphthalene (DCN) catalyst under mild conditions (see eq. 4)⁸⁴. Other [3+2] annulation between azirines and triple bonds, imines, and oxiranes could be readily processed with high conversion and selectivity based on similar PET process (see eq. 5-6)^{85,86}. Moreover, with N-methoxyamides as nitrogen source, cross-dehydrogenative benzylic aminations could also be obtained under aerobic conditions (see eq. 7)⁸⁷. Lastly, even though in the minor cases, the reductive part of those semiconductors are also employed for photocatalytic reactions. For example, some enones bearing pendant esters and acrylonitriles could be reduced by dicyanoanthracene (DCA) anion radical to afford the cyclization products in moderate yield (eq. 8)⁸⁸.

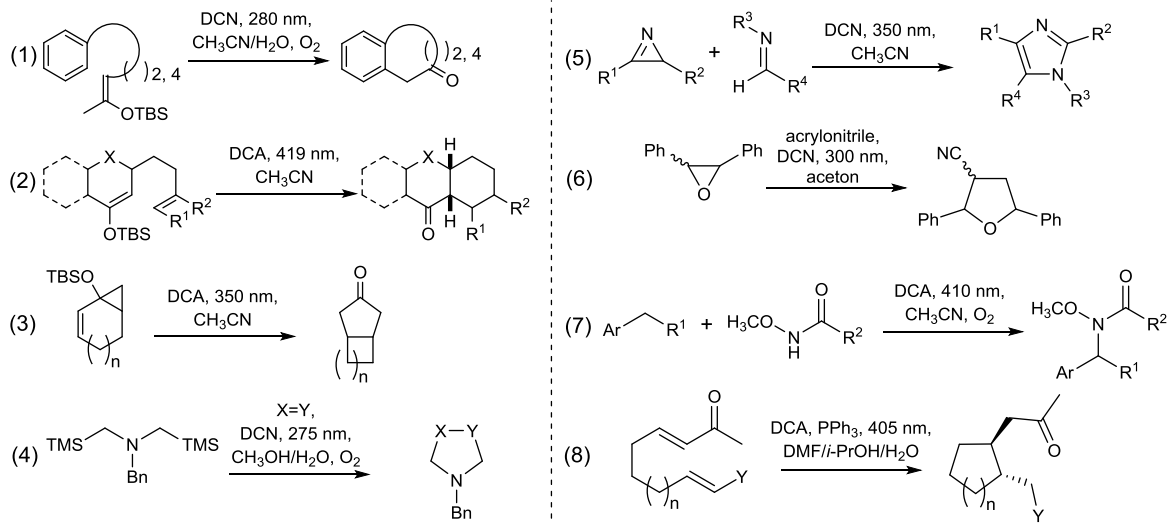


Figure 3.6 Photocatalytic intramolecular and intermolecular cyclization and oxidative addition reactions with cyanoarenes photocatalysts.

Benzophenones and quinones have also been reported as UV-response photocatalysts. However, compared to cyanoarenes, the prototypical reactivity for benzophenones is derived generally by the hydrogen atom transfer (HAT, mentioned in chapter 3.1.1) due to the rapid and high efficient intersystem crossing process resulted from the negligible energy gap between $S_1(n, \pi^*)$ and $T_1(\pi, \pi^*)$. The radical addition between *iso*-propanol and unsaturated carbonyl compounds offers an archetypal example for benzophenones as HAT photocatalyst⁸⁹. Additionally, a chiral PET photocatalyst, χ -BPs, reported by Bach's group, demonstrates an excellent catalytic enantioselective for catalyzing both intramolecular and intermolecular [2+2] cycloaddition reactions⁹⁰⁻⁹².

3.3.2 Xanthene and pyrylium dyes

Xanthene dyes have accounted for a large part of current metal-free photocatalysts for organic transformations due to their cheapness, visible light absorption, and suitable photoredox potentials. The investigation of xanthene dyes has been conducted for more than a century. Typical properties are listed in Table 3.2^{12,93}. Among the xanthene dyes, eosin Y (EY) may enjoy the highest attention. Upon the irradiation of visible light, EY could undergo a rapid ISC process to its stable triplet state with a life time of ca. 24 μs , which is comparable to metal chromophores. The long excited state life time facilitates the electron transfer between EY and the reactive substrates.

Table 3.2 Photophysical and electrochemical properties of oxathene dyes.^a

Dyes	$\lambda_{\text{max}}^{\text{abs}}$ (nm)	τ_f (ns)	Φ_f	Φ_{ISC}	Excited state		Ground state potentials (SCE)		Excited state potentials (SCE)		Excited state potentials (SCE)	
					$E_{0,0}^{S1}$	$E_{0,0}^{T1}$	E_{red}	E_{ox}	E_{red}^{S1}	E_{ox}^{S1}	E_{red}^{T1}	E_{ox}^{T1}
					FLH ₂	437	4.2	0.2	0.03	2.42	1.94	-1.17
EY	520	2.1	0.48	0.32	2.31	1.91	-1.08	+0.76	+1.23	-1.58	+0.83	-1.15
RB	549	0.50	0.09	0.77	2.17	1.8	-0.99	+0.84	+1.18	-1.33	+0.81	-0.96
RhB	550	2.45	0.58	0.12	2.22	1.80	-0.96	+0.91	+1.26	-1.31	+0.84	-0.89
Rh6G	530	4.13	0.90	$\frac{0.00}{2}$	2.32	2.09	-1.14	+1.23	+1.18	-1.09	+0.95	-0.86

^aValue obtained from previous report¹².

Sharing a similar PET mechanism as metals photocatalysts, the excited state EY could also be quenched by surrounding donors or acceptors. In the oxidative bond formation reactions, the initiation step is indeed the electron migration from the donor species to EY. For instance, α -C-H groups in amines can be oxidized into iminiums due to the presence of lone pair on nitrogen. Thus C-C and C-P bond could be easily constructed between tetrahydroisoquinolines and pronucleophiles (Figure 3.7, eq. 1)⁹⁴. Direct bromination on alkyl and benzylic sp³ C-H bonds has been accomplished with CBr₄ as bromine source and morpholino as HAT co-catalyst (eq. 2)⁹⁵. In addition, the oxidative activation of C=S bond in thioamides has been achieved with an EY-based photocatalyst, leading to the formation of 1,2,4-thiadiazoles and acetamides (eq. 3-4)^{96,97}. Conversion of aldoximes and primary amides into nitriles can be completed with EY catalyst, which involves the visible light-induced *in situ* generation of the Vilsmeier-Haack reagent from CBr₄ and DMF, affording the desired conversion to nitriles (eq. 5)⁹⁸. Conversely, in the reductive bond formation reactions, EY acts as a reductant. The electron is transferred from EY to the surrounding acceptor species. Reduction of nitrobenzene into industrially important anilines has been conducted with TEOA as sacrificial reducing agent. The reaction illuminates a high chemoselectivity and tolerates to other reducible groups, such as halogens, carbonyls, and nitriles (eq. 9)⁹⁹. Furthermore, desulfonylation of β -arylketosulfones has been accomplished via photo-electron-induced C-S bond dissociation (eq. 10)¹⁰⁰. Dehalogenative coupling has been reported via C-Br bond activation, leading to the formation of aryl radicals, followed by the coupling reaction with other neutral arenes (eq. 11)¹⁰¹.

It is worth to mention that reductive bond formation via aryl diazonium salts have been well developed recently using EY as photocatalyst (Figure 3.7(c))^{14,102}. Upon the irradiation of visible light, EY is excited to the excited state, giving an electron to the diazonium salt. Then, aryl radicals could be readily obtained after the activation and cleavage of C-N bond. The photo-generated radicals can be trapped by heteroarenes to form an aryl-heteroaryl bond (eq. 14)¹⁰³. In addition, the aryl radical may also be captured by alkynes with benzothiophene or phenanthrene being obtained after radical cyclization (eq. 15-16)^{104,105}.

Lastly, some carbon-heteroatom bonds, such as C-B and C-S could be also constructed successfully with bis(pinacolato)diboron as boron transfer agent and disulfides as sulfur agent, respectively (eq. 17-18)^{106,107}.

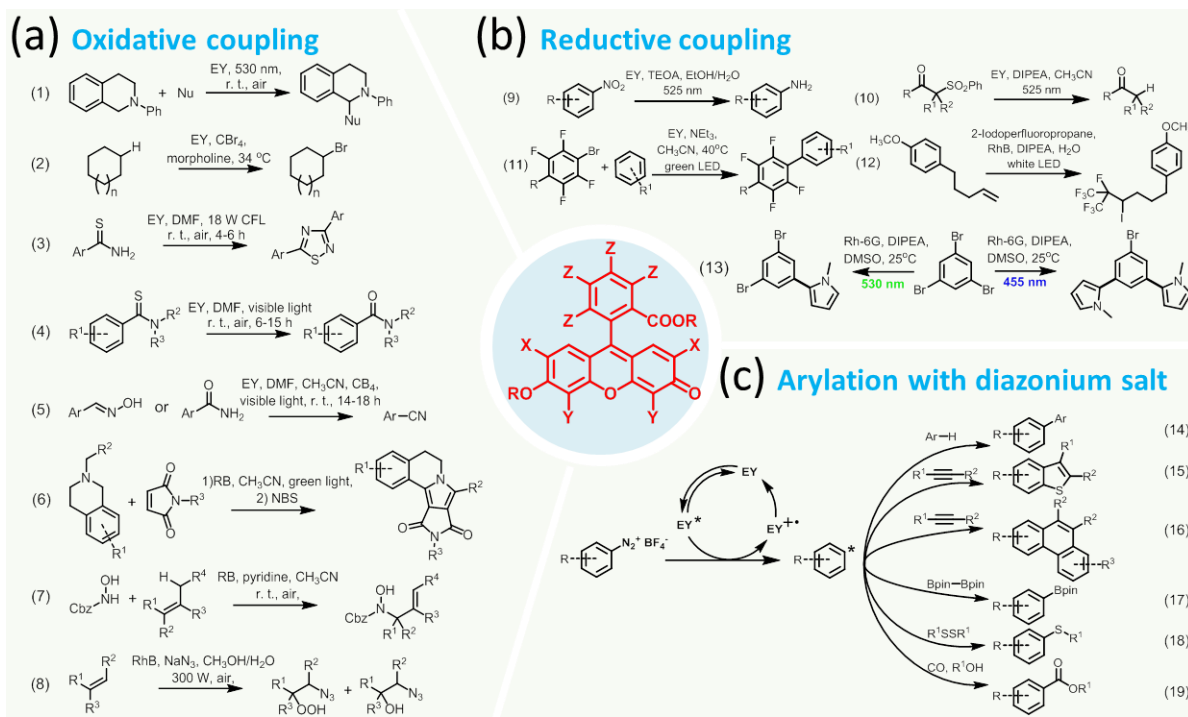


Figure 3.7 Photocatalytic organic transformations with xanthene dyes as visible light photocatalysts.

Apart from EY, other xanthene dyes have also demonstrated catalytic capacity for organic transformations. For example, Rose Bengal (RB) could oxidize tertiary alkylamine to offer iminium cationic radical which is captured by maleinides to form final adducts after dehydrogenation by NBS (eq. 6)¹⁰⁸. Moreover, oxidation of hydroxylamine can be completed by RB which undergoes subsequently dehydrogenation to produce nitroso compounds, giving allyl amines as final products via nitroso-ene reaction (eq. 7)¹⁰⁹. In addition, Rhodamine B (RhB) has also been employed for organic reactions based on photo-redox quenching cycles, such as olefin azidohydroperoxidation and alkene ATRA with perfluoroalkyl iodide (eq. 8 and eq. 12)^{110,111}. Other rhodamine derivative, rhodamine 6G (Rh6G), demonstrates a capacity of photocatalytic activation of carbon-halogen bond. Biaryls and aryl phosphonates are synthesized successively when the photo-generated aromatic radicals are combined by nucleophile pyrroles and trivalent phosphites, respectively^{112,113}. Lastly, since anionic radical of rhodamine, Rh6G⁻ shows an increased reduction potential and different light-response regions compared with neutral Rh6G, chromoselective C-H arylation could be accomplished via consecutive activation of C-Br bond (eq. 13)¹¹⁴.

Triarylpyryliums generally demonstrate a high oxidation potential in both singlet and triplet state while suffer short singlet life time of < 5 ns. While many photocatalysts could generate $^1\text{O}_2$ via energy transfer, pyryliums are thought to be far away from this process because many electron donors could quench excited state pyryliums which is much faster than oxygen¹¹⁵. Therefore, pyryliums could avoid some unfavorable reactions even under the aerobic conditions. Frequently, many cycloaddition reactions including [4+2]¹¹⁶, [2+2]¹¹⁷ and [2+2+2]¹¹⁸ cycloaddition have been effectively accomplished with pyryliums photocatalysts. Moreover, pyryliums could be employed for cationic polymerization of both vinyl ethers and 4-methoxystyrene with a characteristic of living polymerization^{119,120}.

3.3.3 Acridiniums and quinoliniums

Photocatalysis with acridiniums and quinoliniums, especially 9-mesityl-10-methylacridinium (Mes-Acr⁺), has been widely studied by Fukuzumi, and Nicewicz et al. Typical photophysical and electrochemical properties are shown in Figure 3.8. Generally, Mes-Acr⁺ is regarded as powerful oxidants due to extremely high oxidation potential ($E_{\text{oxi}} = 1.88 \text{ V}$)¹²¹. While originally report shows the photo-oxidative activity is attributed to CT state, many following researches illuminate that singlet CT state is not involved in the PET photochemical reactions¹². Actually, Mes-Acr⁺ enjoys a long excited state life time of *ca.* 6 ns and 29 μs for singlet state and triplet state, respectively¹²², thus favoring to the intermolecular charge transfer.

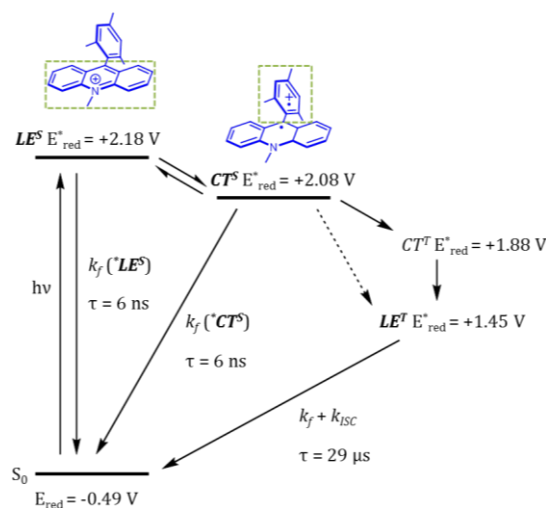


Figure 3.8 Jablonski diagram of Mes-Acr⁺.

Many oxidative reactions have been designed and reported with acridiniums recently. Direct oxidation of cyclic hydrocarbons offering the corresponding ketones and alcohols is accomplished with Mes-Acr⁺ as photocatalyst in the presence of HCl in aerobic conditions (Figure 3.9, eq. 1). The cleavage of C-H bond by Cl• generated by electron transfer plays a

critical role for whole reaction process¹²³. Phenol, an important industrial chemical, initially synthesized from cumene with low yield (5%)¹²⁴, could be prepared with 3-cyano-1-methylquinolinium as photocatalyst via direct benzene oxidation (eq. 2)¹²⁵. Moreover, oxidation of alkenes provides dioxetanes as final products, accompanying with ketones being observed due to the cleavage of dioxetane (eq. 3)¹²⁶. Lastly, oxidation of methyl group and alcohols can be conducted, offering aldehydes and ketones products with various electron-donating and withdrawing groups being tolerable (eq. 4-5)^{127,128}.

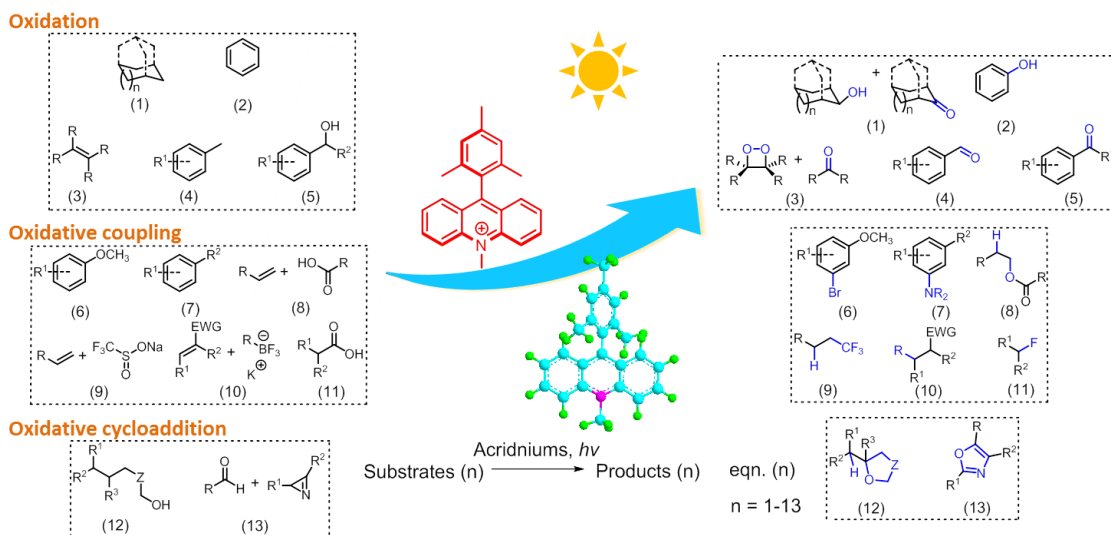


Figure 3.9 Photo-driven oxidative reactions with acridiniums derivatives as visible light photocatalysts.

Except the straight oxygenation, the oxidative addition between cationic radicals, generated by electron transfer, and counterions provides a novel platform for the C-H functionalization of arenes. For example, the oxidative bromination on aromatic compounds could undergo smoothly with HBr as bromine source and oxygen as oxidant (eq. 6)¹²⁹. Furthermore, the intermediacy of aryl cation radical is utilized for C-N coupling, developed by Nicewicz etc., offering a method of site-selective arene C-H amination (eq. 7)¹³⁰. The introduction of TEMPO and O₂ could accelerate the reaction and improve the selectivity. Apart from oxidation of arenes, Mes-Acr⁺ could also oxidize alkenes showing oxidation potentials from 1.3 to 2.9 V vs. SCE which is outside the range of most photocatalysts¹³¹. It is worth to mention that the addition of nucleophiles to olefins cationic radical basically occur at less-substituted position, demonstrating a character of anti-Markovnikov addition. For example, carboxylic ethers are reported via direct anti-Markovnikov addition of carboxylic acids to alkenes with high regioselectivity (eq. 8)¹³². Moreover, other nucleophiles, such as hydroxyl (eq. 12), amine, thioamide, and HCl, add similarly to alkene radicals in anti-Markovnikov fashion¹³¹.

Due to the high oxidation potential, hydro-trifluoromethylation of olefins are accomplished with high regioselectivity via $\bullet\text{CF}_3$ radical, generated by SET from the Langlois reagent to Mes-Acr⁺, the addition to a double bond (eq. 9)¹³³. Generally, organoborates and organic carboxylates are important fragments to offer C-centered radicals which could be applied for C-C bond creation^{66,134}. SET from trifluoroborates or carboxylic acid to Mes-Acr⁺ provides a route for the generation of radicals, after being trapped by electron-deficient alkenes, thus constructing C-C coupling products with high yield (eq. 10)¹³⁵. In addition, the photo-generated radical captured by selectfluor, offers the monofluoroalkanes, aryl monofluoroalkyl ether and fluoroesters which are important compound in pharmaceutical, agrochemical and polymer industries¹³⁶. Lastly, oxidation of 2H-azirines would generate the azaallenyl radicals after ring opening, which are attacked by aldehydes to provide the oxazoles as the final [3+2] cycloadducts (eq. 13)¹³⁷.

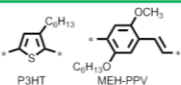
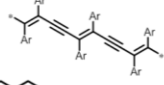
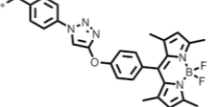
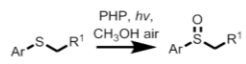
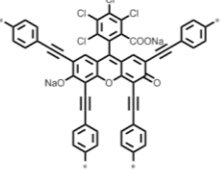
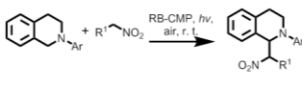
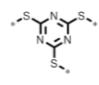
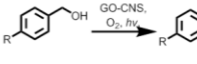
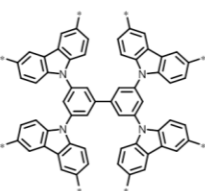
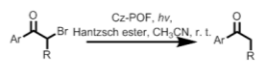
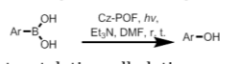
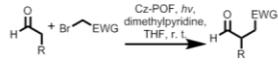
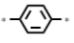
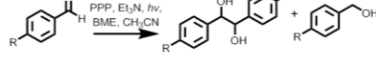
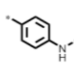
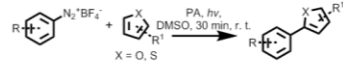
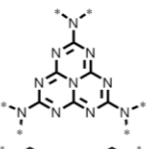
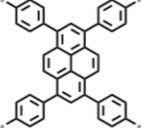
3.3.4 Visible light-active polymers as heterogeneous photocatalysts

Polymer photocatalysts, compared to their small molecular counterparts, enjoy the advantages of being highly stable, easily recoverable and reusable. They can be recycled via simple filtration because of their insoluble nature. Some classical polymer photosensitizers, such as P3HT and MEH-PPV could also degrade organic dyes including Alizarin S, Alizarin G, Orange G, and Remazol brilliant blue, originally being completed by inorganic photocatalyst TiO₂ (Chart 3.1, entry 1). In addition, with soft template, a conjugated polymer with morphology of nanofiber could be obtained, demonstrating an accelerated degradation for both methyl orange and phenol (entry 2)¹³⁸. Except for the conjugated systems, non-conjugated polymers also show photo-catalytic activity for the degradation of organic dyes or phenols^{139,140}.

BODIPY dyes have been regarded as outstanding dyes due to their large absorption coefficients, high fluorescence quantum yields, and good thermal and photochemical stabilities¹⁴¹. The introduction of BODIPY into a polymer matrix via high internal phase emulsion (HIPE) polymerization illuminates a potent oxidative ability, especially the oxidation of thioanisole into sulfoxide (entry 3)¹⁴². Furthermore, the BODIP moiety knitted into conjugated polymer shows an efficient formation of singlet oxygen, which plays an essential role of thioanisole oxidation¹⁴³. In addition, other organic dyes, such as rose bengal incorporated into polymer network displays a photocatalytic activity for Aza-Henry reaction (entry 4)¹⁴⁴. Oxidation of benzyl alcohols by a hybrid photocatalyst consisting of reduced graphene oxide and C₃N₃S₃ offers the corresponding aldehydes with excellent selectivity (entry 5)¹⁴⁵. Oxidation of primary and secondary amine with carbazole-based conjugated polymers provides the imines with moderate to high yields¹⁴⁶. Lastly, three kinds of reactions have been designed and reported based on the quenching pathways of excited state carbazolic organic framework (Cz-POF, entry 6)¹⁴⁷. Hydrogenation of

phenacyl bromides, hydroxylation of aryl-boric acid, and sp^2 - sp^3 α -alkylation have been established with Cz-POF photocatalyst, corresponding to the reductive, oxidative and neutral redox cycle, respectively.

Table 3.3 Photocatalytic organic redox transformations with polymer photocatalysts.

Entry	Polymer name	Synthetic methods	Photoactive moieties	Photocatalytic reactions
1	P3HT and MEH-PPV	Condensation polymerization		Degradation of dyes including AS, AG, OG, and RBBR, and phenol
2	PDPB	Photo-induced polymerization		Degradation of methyl orange and phenol
3	PHPs	High internal phase emulsion (HIPE) polymerization		
4	RB-CMP	Sonagashira-Hagihara coupling		
5	GO-CNS	Condensation polymerization		 (1) Photocatalytic reductive dehalogenation
6	Cz-POF	Oxidative polymerization		 (2) Photocatalytic oxidative hydroxylation
				
				 (3) Photocatalytic α -alkylation
7	PPP	Dehalogenation condensation polymerization		
8	Polyaniline	-		
9	g-C3N4	Thermal polycondensation		Hydrogen evolution
10	CP-CMPs	Suzuki-Miyaura polycondensation		Hydrogen evolution

Various reduction reactions have also been reported with polymer photocatalysts. For instance, the reduction of aldehydes has been completed with PPP polymer photocatalyst, giving ketyl compounds as intermediates and alcohols as final products in the presence of hydrogen atom donor thiol (entry 7)¹⁴⁸. Single electron transfer from polyaniline to

arene diazonium salt is applied for Gomberg-Bachmann reaction, where the photo-generated aryl radicals are captured by heteroarenes (entry 8)¹⁴⁹. An important application for polymer photocatalysts may be the production of hydrogen via H₂O splitting. Since the first report by Wang et al.¹⁵⁰, graphite-carbon nitrides (g-CN) have demonstrated outstanding advantages such as cheapness, high efficiency and visible-light responsibility for H₂ evolution (entry 9)¹⁵¹. Recently, Cooper and coworkers also show numbers of conjugated polymers being utilized as photocatalysts for H₂ evolution (entry 10)^{152,153}. Polymers with either pyrene or fluorine core illuminate a high photo-activity for H₂ generation.

3.4 Novel photocatalysts based on benzothiadiazole chromophores

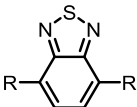
2,1,3-Benzothiadiazole (BT) chromophores have achieved much attentions in recent years, due to their desirable photochemical and photophysical properties. Up to now, applications based on benzothiadiazole unit have been widespread in the photoluminescence-related areas such as solar cell¹⁵⁴, charge transport¹⁵⁵, bioprobe¹⁵⁶ and organic optoelectronic devices¹⁵⁷. So far, the application of BT-containing materials as visible light-active photocatalysts has been reported mainly by our group. In the following subchapter, an overview on the BT-containing organic photocatalysts, in either homogenous or heterogeneous systems, is given.

3.4.1 Basic properties of benzothiadiazoles

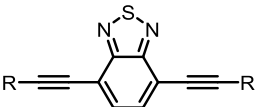
The photophysical and photochemical properties of benzothiadiazole derivatives are listed in Table 3.3. In general, BT and its derivatives have a high reductive potential and electron affinity. The strong electron-withdrawing capacity favors to the possible intramolecular charge transfer and intermolecular hole transport between BT unit and adjacent donor species, which results into an efficient charge separation of BT-containing compounds. Another advantage for BT-containing materials is their high stability, including both high storage and fluorescence stabilization. Furthermore, BT-containing materials have typically large Stokes shifts with broad absorption in the visible light region. The tailorable redox potentials via combination with other electron-donating or withdrawing units, considerable fluorescence quantum yields and relatively long lifetime of the excited state supports BT-containing materials as a promising candidate of pure organic and highly efficient photocatalysts. In the following subchapters, an overview of BT-based photocatalytic systems is given with respect to the type of the redox reactions. Those photocatalytic reactions are divided into two parts according to the reductive and oxidative quenching cycles of the photocatalysts.

Table 3.4 Photophysical and electrochemical details for some benzothiadiazole compounds.^a

Compound	E_{red} (V)	EA (eV)	E_{oxi} (V)	IP (V)	E_{gap}^{el} (eV)	Log ϵ	λ_{abs}^{max} (nm)	λ_{em}^{max} (nm)	Stoke's shift (nm)	Φ_{is}	τ_s (ns)	τ_t (μ s)	E_{gap}^{op} (eV)
1	-1.05	3.55	1.65	6.05	2.70	4.04	402	487	85	0.80	12.2	-	2.73
2	-1.18	3.22	1.44	5.84	2.62	4.08	360	517	157	0.17	4.96	14.4	2.68
3	-1.23	3.17	1.32	5.72	2.55	3.52	362	547	185	0.51	12.70	-	2.54
4	-	-	-	-	-	5.30	368	479	111	0.50	10.40	4.18	2.75
5	-	-	-	-	-	3.86	355	453	98	0.22	6.31	6.04	2.74
6	-1.28	-	-	-	-	3.62	443	495	52	0.71	14.6	-	2.54
7	-1.01	-	-	-	-	4.12	419	503	84	0.58	6.2	-	2.53
8	-1.57	2.83	1.02	5.42	2.59	4.99	403	497	94	0.37	5.53	21.6	2.57
9	-1.68	2.72	1.23	5.63	2.91	3.56	363	434	71	0.36	8.37	6.05	2.99
10	-0.95	3.45	1.47	5.87	2.42	4.40	393	542	149	0.29	6.42	20.01	2.37
11	-1.37	3.03	1.61	6.01	2.98	4.11	407	438	31	0.15	8.18	23.02	2.93
12	-0.68	3.72	1.93	6.33	2.61	4.40	394	469	75	0.86	4.52	29.50	2.60



(1) R = Ph;
(2) R = Naphthyl;
(3) R = *p*-MeO-Ph;
(4) R = *p*-Cl-Ph;
(5) R = *p*-CF₃-Ph;
(6) R = *p*-F-Ph;
(7) R = *p*-CN-Ph



(8) R = Ph;
(9) R = Naphthyl;
(10) R = *p*-MeO-Ph;
(11) R = *p*-N(CH₃)₂Ph;
(12) R = *o*-Py;

^avalues obtained from previous report^{158,159}.

3.4.2 Photocatalytic oxidation reactions with benzothiadiazole photocatalysts

In photocatalytic oxidative reactions, oxygen is frequently involved in the catalytic cycle as an efficient and clean oxidant. Usually, two reactive oxygen species, i.e. $O_2^{\bullet-}$ and 1O_2 , can be generated via either electron transfer or energy transfer, respectively. The addition reaction between α -terpinene and 1O_2 has been frequently applied for the detection of singlet oxygen (Figure 3.10, eq. 1) and 1O_2 also shows a wide application for synthesis of pharmaceutical products¹⁶⁰. The photo activity of poly(benzothiadiazoles) networks (poly-BTs) is the first example of BT-containing photocatalysts reported by Zhang et al., illuminating a high efficiency in the generation of singlet oxygen¹⁶¹. The addition of SiO₂ nanoparticle as template not only increase the surface area of the polymer network but also offer a better accessibility to the photocatalyst, thus improving the catalytic activity. Moreover, the incorporation of the BT unit into the a macroporous polymer could clearly improve the photocatalytic performance for selective oxidation of organic sulfides¹⁶². To achieve the feasibility of photocatalytic reactions in aqueous medium, a hydrophilic BT-containing microporous polymer is prepared via thiol-yne chemistry, providing a completed dispersible polymer in water¹⁶³. The modified poly-BTs demonstrates a high catalytic ability in the formation of singlet oxygen, which could convert the furoic acid into 5-hydroxy-2(5H)-furanone (eq. 2) in aqueous solution. Other polymers incorporating the BT unit have also been reported recently, displaying an enhanced capacity for the generation of singlet oxygen in both organic solvent and aqueous solution (eq. 1 and 3)¹⁶⁴.

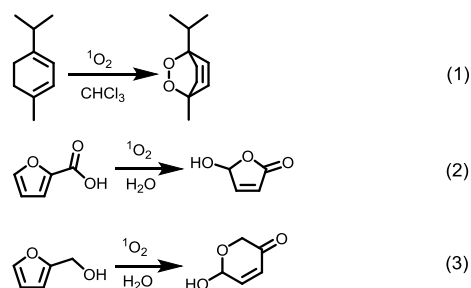


Figure 3.10 Detection of singlet oxygen in organic solvent and water based on oxidative addition reactions.

Photodegradation of organic pollutants is an important application for photocatalysis due to the increasing environmental contamination and destruction issues. Various polymer nanoparticles, with morphologies change from nanospheres, nanorods to nanorings, have been prepared in our group. Different construction units, such as dihexylfluorene, biphenyl and benzothiadiazole are knitted into conjugated polymer matrix (Figure 3.11(a)). Obviously, the structure with benzothiadiazole moieties demonstrates a superior activity in the degradation of rhodamine B (RhB) and *N,N,N',N'*-tetramethyl-*p*-phenylenediamine (TMPD) than that of others¹⁶⁵. Furthermore, other organic pollutants, such as bisphenol A, cimetidine, phenol, ciprofloxacin, and sulfathiazole could also be conveniently removed and degraded from aqueous solution by benzothiadiazole based polyamide¹⁶⁴, poly-BTs/TiO₂¹⁶⁶ and poly-BTs/Bi₂MoO₆¹⁶⁷ hybrid materials photocatalysts, respectively. It seems that both photo-generated hole and O₂^{•-} could be functioned as oxidants for the pollutants degradation (Figure 3.11 (b)).

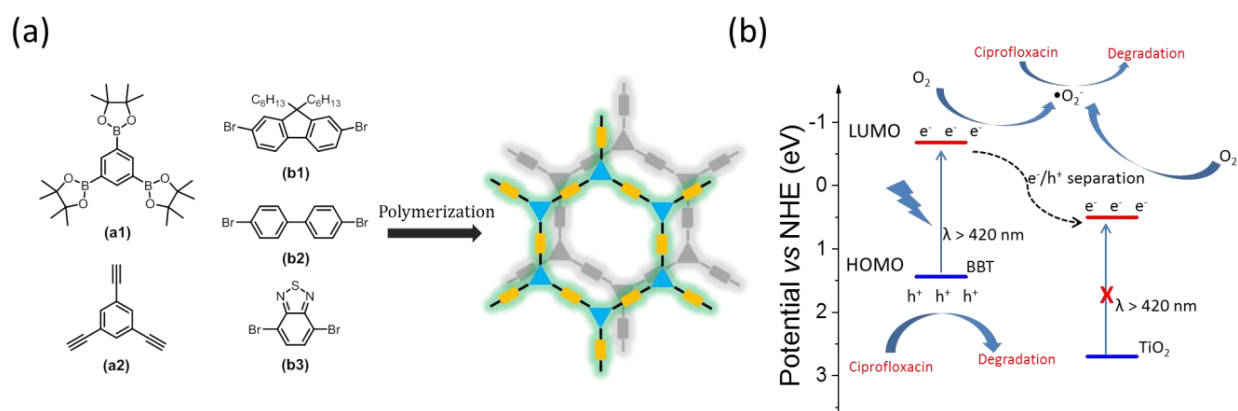


Figure 3.11 (a) Reactive monomers for polymer network construction, and (b) degradation process of ciprofloxacin using poly-BTs/TiO₂ hybrid materials.

Apart from the oxidation of organic pollutants, the oxidative coupling reaction of aromatic amines with oxygen/air as terminal oxidant has been reported for the preparation of imine compounds, which are regarded as useful electrophilic intermediates for organic transformations¹⁶⁸. A series of poly(benzochalcogenadiazole) networks including

benzoxadiazole, benzothiadiazole and benzoselenadiazole are synthesized via facile Sonogashira-coupling, demonstrating a good photocatalytic activity for oxidative coupling of benzylamines¹⁶⁹. The polymer network with benzothiadiazole units shows the highest efficiency. In addition, the band position of the polymer-based photocatalysts could also be tuned via varying the geometry of the 3-dimensional polymer networks (Figure 3.12(a))¹⁷⁰. With the same building unit, the 1,3,5-substituted position of the centered phenyl ring shows better catalytic performers for benzylamines oxidation than that of 1,2,4- and 1,2,4,5-substituted position, resulting from its superior over potentials and enhanced charge mobility due to configuration change. Various aryl amines, bearing either electron-donating groups such as methyl and methoxy or electron-withdrawing groups such as fluoride and chloride are well tolerance for the reaction conditions with moderate conversions (Figure 3.12(b)). The reaction pathway is illustrated in Figure 3.12(c). The benzylamine is oxidized by the photogenerated hole to form cationic radical, combining with reactive oxygen species to become an imine after H₂O₂ elimination. The addition between amine and imine gives the final methanimine after ammonia elimination.

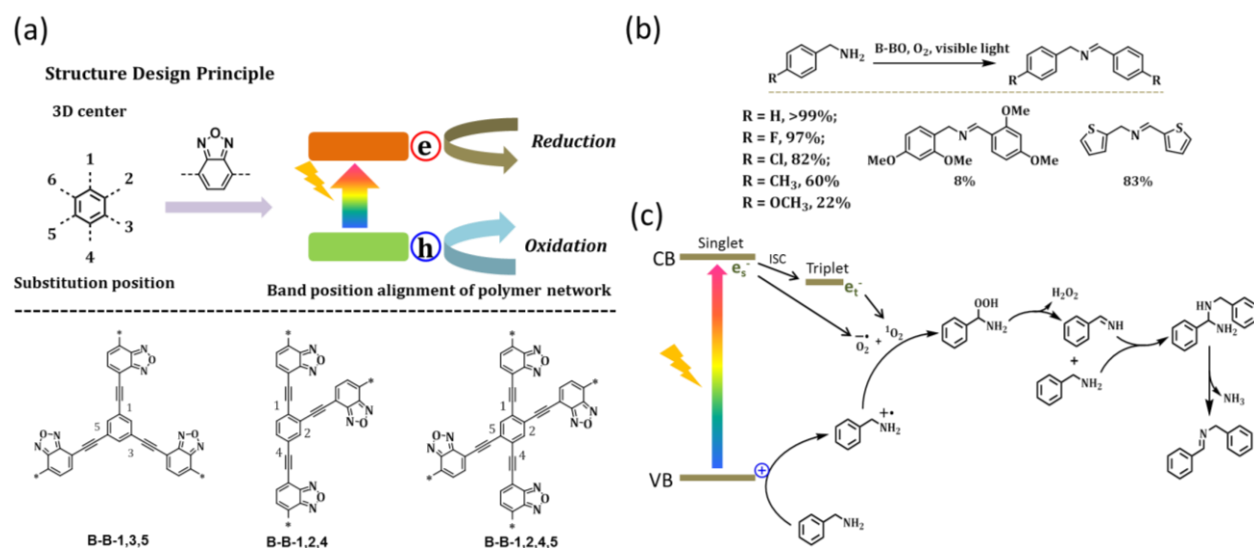


Figure 3.12 (a) Geometry design principle of band position of conjugated microporous poly(benzoxadiazole) network, (b) photocatalytic oxidative coupling of benzylamines, and (c) corresponding reaction mechanism.

Tetrahydroquinolines, an important motif in pharmaceutical industries, could also be obtained with benzobisthiadiazole-based polymer photocatalyst¹⁷¹, with a high conversion comparable to metal catalyst such as CuCl₂¹⁷² and Ru(bpy)₃Cl₂¹⁷³. With 10% benzobisthiadiazole addition into polymer matrix illuminates the highest catalytic performance probably due to suitable visible light absorption and effective oxygen species generation. Various reactive substrates bearing both electron-donating and electron-withdrawing groups are compatible for the cycloaddition reactions (Figure 3.13(a)). The addition between α -amino radical, formed after singlet electron transfer and proton

transfer, and electron deficient alkenes N-benzylmaleimides plays a critical role for the production of final cyclized adducts (Figure 3.13(b)).

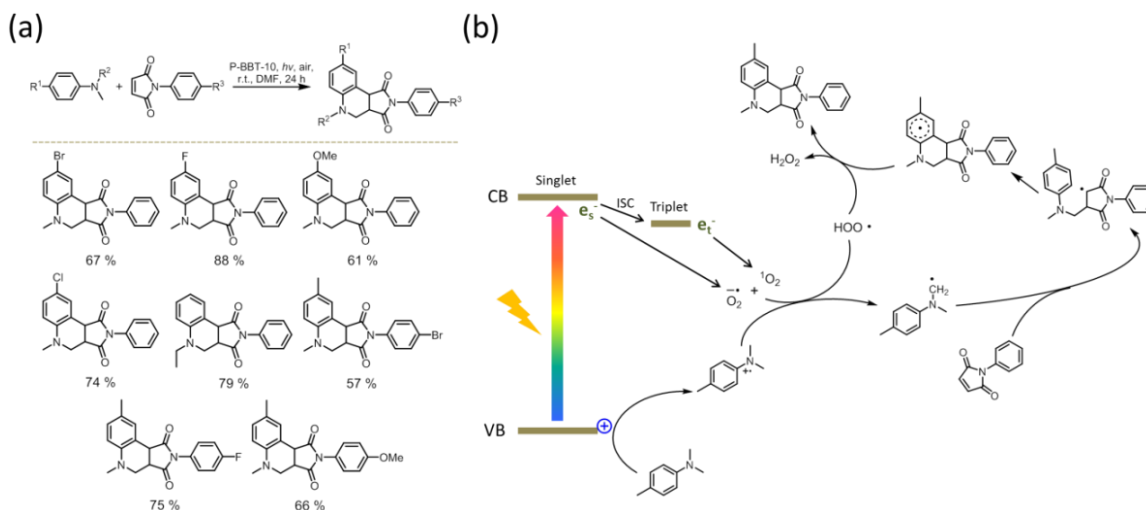


Figure 3.13 (a) Photocatalytic cyclization between N-methylanilines and N-substituted maleimides with polymer photocatalyst and (b) corresponding reaction mechanism.

Organic sulfides function as important intermediates in pharmaceutical and fine chemical industries. Selective oxidation of sulfides into sulfoxides without using additional additives has been achieved with benzothiadiazole based macroporous polymer with excellent selectivity, while traditional thermal method may have the problem of over-oxidation into sulfone¹⁷⁴. In addition, by incorporating porous polymer into a specific photoreactor, sulfoxides could be continuously produced in a flow setup without any catalyst separation procedures. Lastly, it is worth to mention that π -conjugated porous polymer could catalyze the cationic radical polymerization of methyl methacrylate (MMA)¹⁷⁵. The photogenerated hole can oxidize triethylamine into a radical cation which combines with another neutral triethylamine via proton transfer, thus producing a reactive radical and initiating the radical polymerization of MMA.

3.4.3 Photocatalytic reduction reactions with benzothiadiazole photocatalysts

Reductive reactions could also be established using benzothiadiazole-based photocatalysts. Specifically, H₂ evolution with polymer semiconductors in visible light has gained much attention. Different kinds of polymers containing BT moieties varying from linear polymer to conjugated 3D systems, have been synthesized with their photocatalytic activities being investigated (Figure 3.14)¹⁷⁶. The linear polymer containing BT and phenyl units showed the highest H₂ evolution efficiency of ca. 116 $\mu\text{mol h}^{-1}$ with an apparent quantum yield (AQY) of 4.01% at 420 nm, which is comparable to reported pyrene-based polymers¹⁵². In addition, the combination between conjugated poly-BTs and TiO₂ demonstrates a

synergistic effect for enhanced H_2 production up to 20.4 times than the pure polymer probably due to improved e^-/h^+ separation after the formation of BT/TiO₂ heterojunction¹⁶⁶. The increased photocurrents and decreased emission intensity further supports the electron transfer between benzothiadiazole and TiO₂ on the interface of heterojunctions.

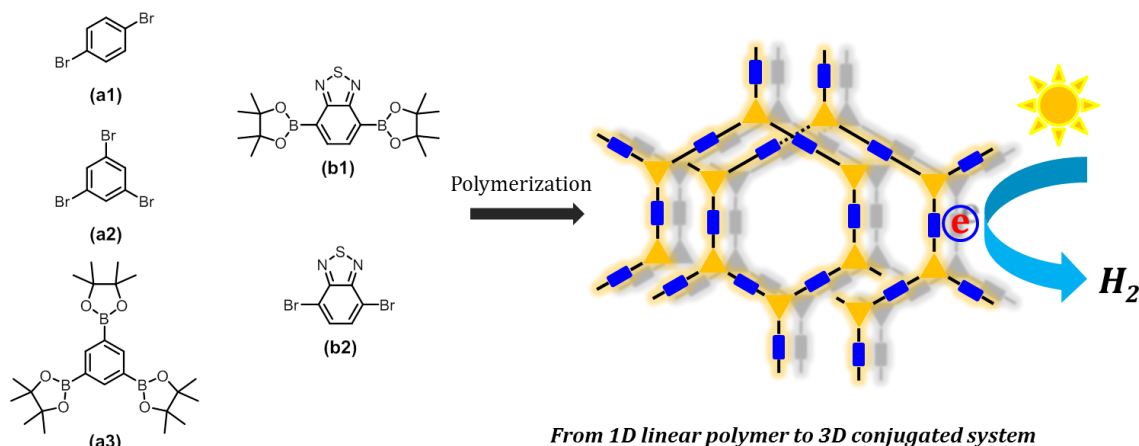


Figure 3.14 Construction of benzothiadiazole-based porous polymers and photocatalytic application for hydrogen evolution.

Cr (VI) is a highly toxic organic contaminant due to its high mobility and solubility in aqueous solution. The removal or reduction of Cr (IV) into the less toxic Cr (III) in water has been widely investigated in the past decades. Photoreduction of Cr (IV) into Cr (III) with polymer catalysts provides a novel approach for waste-water treatment. During the reduction process, Cr (VI) could be directly reduced either by photo-activated electrons or by $O_2^{\bullet-}$, generated by electron transfer from catalyst to oxygen. In a benzothiadiazole/Bi₂MoO₆ hybrid photocatalytic system, directly electron reduction is the major process. In addition, a synergistic enhancement is observed with the introduction of Bi₂MoO₆, due to the formation of Z-scheme heterojunction¹⁶⁷. Furthermore, poly-BTs could be *in situ* growth on the surface of graphitic carbon nitride (g-C₃N₄), providing a hybrid material poly-BTs/g-C₃N₄¹⁷⁷. According to band position design, the hybrid materials show an outstanding catalytic behavior in which photoelectron transfers from poly-BTs to g-C₃N₄. The enhanced photoreductive performance results from the improved visible light absorption and efficient charge separation.

The reduction of *p*-nitrophenol (*p*-NP) into *p*-aminophenol (*p*-AP) is an important chemical transformation due to the use of *p*-AP as important precursor for pharmaceutical productions. A covalent triazine framework containing BT units (CTF-BT) was reported as efficient photocatalyst for the reduction of *p*-NP¹⁷⁸.

The activation of carbon-halogen bonds is a useful step for new C-C bond formations. However, the extremely high dissociation energy of carbon-halogen bond (C-I, 53 kcal mol⁻¹; C-Br, 67 kcal mol⁻¹; C-Cl, 81 kcal mol⁻¹; C-F 109 kcal mol⁻¹) is beyond the activation capacity of most organocatalysts.¹⁷⁹ Recently, photocatalysts work as promising candidate for activating carbon-halogen bond in mild reaction conditions¹⁸⁰⁻¹⁸². While most of them involve the employment of transition metals, porous polymers with benzobisthiadiazole as photoactive moiety also demonstrate catalytic capacity for debromination of haloketones¹⁸³. Various substrates containing electron-donating group such as methyl and methoxy, and electron-withdrawing group such as fluoride, bromide, cyano and nitro are compatible for the reaction with generally high yield in 4 h (Figure 3.15(a)). Under the light irradiation, photo-generated electron can transfer from polymer catalysts to α -bromoketone, thus producing reactive radicals after C-Br bond disassociation and bromide anion leaving. A hydrogenation product is then obtained after HAT process between ketone radical and hantzsch ester (Figure 3.15(b)).

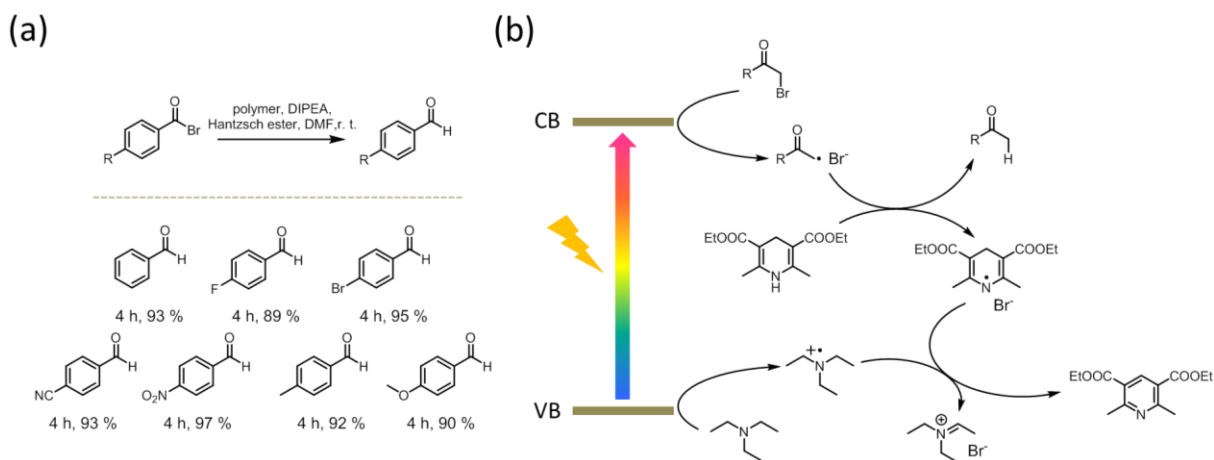


Figure 3.15 (a) Photocatalytic reduction of aryl bromides with polymer photocatalyst and (b) corresponding reaction pathways.

Since photo-reductive dehalogenation reactions normally undergo via a radical pathway, the photogenerated radical could readily combine with nucleophiles such as alkene, alkyne and heteroaromatics and is frequently employed for C-C and carbon-heteroatom bonds construction¹⁸⁴⁻¹⁸⁶. For example, α -alkylation of aldehydes has been completed firstly by MacMillan et al. via an interwoven activation pathway by merging the photocatalyst and chiral organocatalyst³. The obtained products illuminate an excellent enantioselectivity with considerable yield. When replacing the commonly used Ru(bpy)₃²⁺ with a BT-containing polymer photocatalyst, a comparable efficiency is obtained by our group while the polymer catalyst simultaneously enjoys an advantage of convenient separation in the continuous flow setups¹⁸⁷ (Figure 3.16(a)).

As mentioned, heteroarenes such as furan, thiophene, pyrrole, indole and benzofuran, may also act as nucleophiles, which could combine with photo-generated radical, thus giving the arylation products^{103,188}. Under a visible light irradiation, arylation reactions between α -bromomalonate and heteroaromatics, including indole and benzofuran, are carried out with small BT containing molecular semiconductor, 4,7-dithiophene-benzothiadiazole (Th-BT-Th), with high yields (Figure 3.16(b))¹⁸⁹. The reaction seems to undergo via PET process from Th-BT-Th to bromomalonates. The formed malonate radical is then trapped by heteroaryls and become final products after electron transfer and proton transfer.

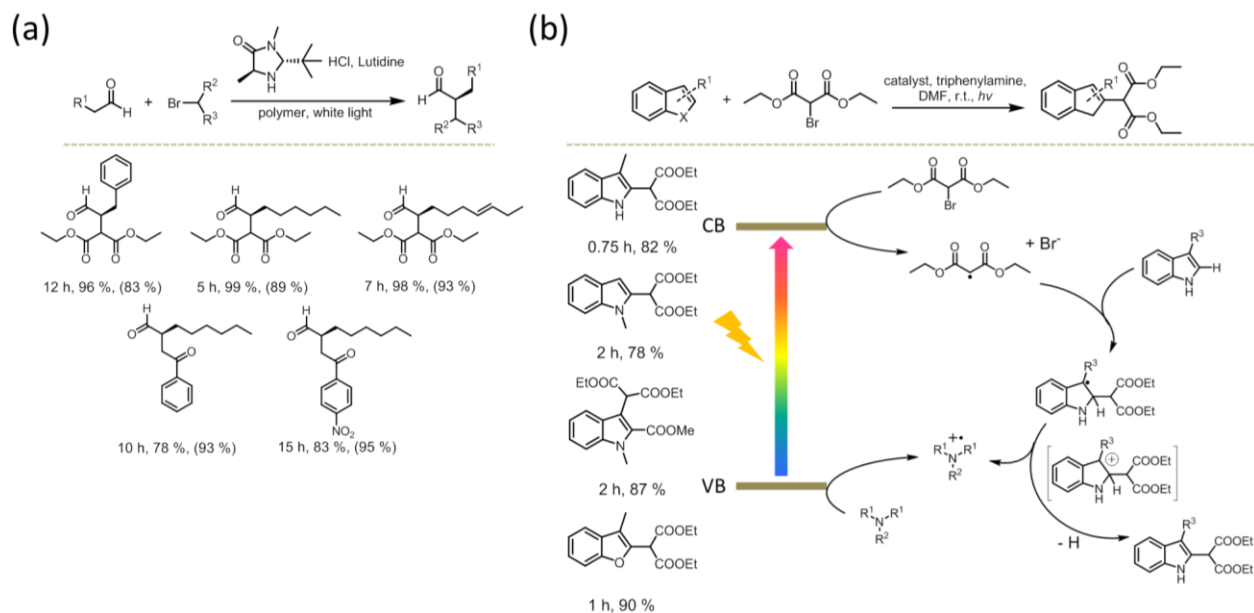


Figure 3.16 (a) photocatalytic C-C coupling between bromides and aldehydes and (b) C-C coupling between diethyl bromomalonate and heteroaromatics. Value in parentheses in (a) indicates the enantioselectivity.

At the point when the dissertation started, there were very limited reports about organic and/or polymer-based, especially benzothiadiazole-based, photocatalysts for visible light-driven organic photoredox reactions. In addition, the photophysical, photochemical and electrochemical analysis on the electron/hole separation and charge transfer during the photocatalytic process was rare. For challenging organic reaction such as the activation of C-H and carbon-halogen bonds had barely been reported using pure organic photocatalysts. Therefore, the thesis will guide the reader a systematic development pathway of benzothiadiazole-containing photocatalytic systems, starting from the structural design on the molecular and spatial levels, via the comprehensive chemical and physical studies of the properties, to their applications in highly challenging organic photoredox reactions.

4 Characterization Techniques

In the following chapter, the characterization techniques applied in this work are described. Experimental details and analysis about each technique are showed in Chapter 6, the experimental section.

4.1 UV-Vis and UV/Vis Diffuse Reflectance Spectroscopy

UV-Vis absorption spectroscopy is a technique, which allows the measurement and analysis of soluble samples in the ultraviolet and visible light region. In principle, the absorption process is basically electron transition from the valence band to the conduction band when the energy of photon is comparable for the transition process. The absorption intensity is a function of wavelength as described by Lambert-Beer law, an empirical law:

$$A = \log \frac{I_0}{I} = \varepsilon \cdot c \cdot d$$

where I_0 and I indicate the incident light intensity before and after passing the measurement cell (generally quartz cuvette); ε , c , d are molar absorption coefficients, concentration of solution and the thickness of measurement cell, respectively.

In addition, since the UV-Vis absorption provides the information of electron transition, the optical band gap could be obtained from the onset absorption in UV-Vis spectra by a function which describes the connection between energy and wavenumber:

$$E = \frac{h \cdot c}{\lambda} = \frac{1239.8(eV \cdot nm)}{\lambda(nm)}$$

UV-Vis Diffuse Reflectance Spectroscopy (DRS) is similar to UV-Vis spectroscopy^{190,191}, which offers a solution for measuring the absorption of insoluble samples. DRS detects the relative change in the amount of reflected light off of sample surface. There are two possible physical light-matter interactions, including specular reflection and diffuse reflection. Most samples produce a combination of those two types of reflections. Furthermore, some influenced factors need to be considered when measuring the reflection spectra of solid samples, such as particle size, packing density and refractive power.

In this work, both UV-Vis and UV-Vis DRS measurements were carried out to offer the absorption and band gap properties of both photocatalysts and reactive substrates.

4.2 Fluorescence Spectroscopy

In contrast to the UV-Vis absorption, which corresponds to the electron transition from the ground state to the excited state, the fluorescence spectroscopy delivers information about the falling back process of the electron from the excited state to the ground state¹⁹². The

intensity of the fluorescence is normally collected by a detector placed at the position perpendicular to the incident light, in order to avoid the reflected incident light.

In this work, the fluorescence spectroscopy measurement was conducted to provide the details about the electron-hole recombination inside the catalyst and the charge migration between the photocatalyst to the substrates.

4.3 Nuclear Magnetic Resonance Spectroscopy (NMR)

The NMR spectroscopy is a popular and efficient tool to analyze and determine the molecular structure, reaction state, dynamics and chemical environment. Before we read the NMR spectra, it is necessary to clarify some physical features and principles that NMR works with. Firstly, a spinning charge could generate a magnetic field with magnetic moment (μ); Secondly, there are two spinning states, $+1/2$ and $-1/2$, in the present of external magnetic field (B) with low energy $+1/2$ state aligning with external field and high energy $-1/2$ state opposing to external field; Thirdly, the energy difference between two spinning states is dependent on the external magnetic field and magnetic moments with a function below:

$$\Delta E = \frac{\mu \cdot B_0}{I}$$

Where μ , B_0 , and I indicate the magnetic moment ($^1\text{H } \mu=2.7927$, $^{13}\text{C } \mu=0.7022$, $^{19}\text{F } \mu=2.6273$, $^{31}\text{P } \mu=1.1305$), external magnetic field and characteristic spin ($I = 1/2$ for ^1H , ^{13}C , ^{19}F , ^{31}P), respectively.

A NMR spectroscope consists of an external magnet, radio frequency (rf) transmitter, receiver and amplifier, and recording and processing unit. When a specific nucleus (proton) is under the irradiation of fixed radio magnet field, with the smooth increase of external magnetic field, hydrogen nuclei would absorb rf energy, resulting the formation of resonance. Since electron around proton could also response to the external magnetic field, generating a secondly field (induced field), shielding the nucleus from applied field, an increased magnetic is needed to achieve the resonance. Therefore, a chemical shift could be obtained when a reference is applied (0 for $(\text{CH}_3)_4\text{Si}$) because protons at different position require different magnetic intensity for resonance. Normally, for a proton with higher electron density, a higher external magnetic field will be needed to compensate the induced field, showing a narrower chemical shift compared with reference. As a consequence, electron-withdrawing groups show a large chemical shift than that of electron-donating groups.

Other details offered by NMR are spin-spin interactions, an interaction between protons bonded on adjacent carbon, resulting in the splitting of signals into two or more resonances. The splitting pattern is independent on the external magnetic field and can be

predicted by n+1 rule. Signal splitting provides some additional information about the position of proton, favoring to the identification of molecular structure.

In this work, NMR measurement was conducted to confirm the chemical structure of the obtained compounds and to monitor reaction conversions and kinetics.

4.4 Cyclic Voltammetry (CV)

Cyclic voltammetry (CV) is an electrochemical technique that widely used to study the redox process of some electroactive species. The basic idea for CV is to use a periodic potential that may alternately oxidize and reduce the material via extracting and injecting electrons, respectively. A typical CV setup consists of three electrodes: a working electrode, a reference electrode and a counter electrode, and electrolyte (normally tetrabutylammonium tetrafluoroborate with concentration of 0.1 M) in organic solvents and aqueous solution. Frequently applied working electrodes are glassy carbon, gold and platinum. Reference electrode and counter electrode are based on aqueous Ag/AgCl or saturated calomel and platinum, respectively.

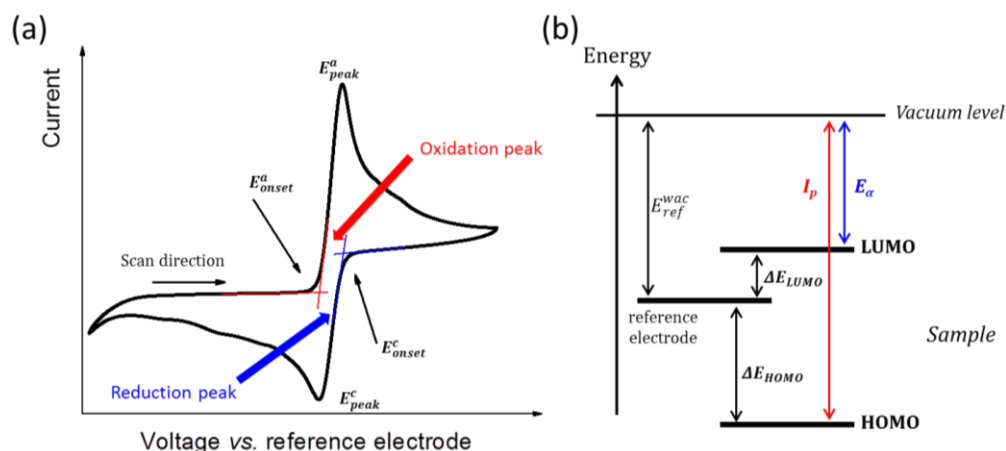


Figure 4.1 (a) A typical curve obtained from cyclic voltammetry measurement (Ferrocene as an example) and (b) energy chart of HOMO and LUMO of sample comparing to the reference electrode.

For a standard CV measurement, an appeared redox peak indicates the electron transfer process between electrode and materials as showed in Figure 4.1(a). There are two pairs of potentials, the anodic and cathodic potentials (E_{peak}^a and E_{peak}^c) and the onset potentials (E_{onset}^a and E_{onset}^c). In addition, it has to mention that the redox peak only offers one energy level, HOMO for example, and the reduction cycle demonstrate electrons coming back from electrode to HOMO of materials. With CV measurement, a HOMO and LUMO energy level could be obtained compared with reference electrode, while with other characterization, an ionization potential (I_p) and electron affinity (E_a) could be achieved with the related function among them showed in below (Figure 4.1(b)):

$$|I_p| = \Delta E_{HOMO} + |E_{ref}^{vac}| \text{ and } |E_a| = \Delta E_{LUMO} + |E_{ref}^{vac}|$$

In this work, CV technique was applied to investigate the HOMO/LUMO level of the photocatalysts and reactive substrates.

4.5 Electron Paramagnetic Resonance (EPR)

The electron paramagnetic resonance (EPR) spectroscopy is a technique widely used to detect and identify the chemical species with unpaired electrons¹⁹³. While similar to NMR, EPR focuses on the electron spin character rather than nuclear spin. When the chemical species bearing the unpaired electrons are under the irradiation of external magnetic field, there are two electron spinning states, with lower energy state parallel to magnetic field and higher energy state antiparallel the magnetic field, which is named Zeeman splitting as illuminated in following functions:

$$E_{+1/2} = 1/2 \cdot g \cdot \mu_B \cdot B$$

$$E_{-1/2} = -1/2 \cdot g \cdot \mu_B \cdot B$$

$$\Delta E = h\nu = g \cdot \mu_B \cdot B$$

Where g , μ_B and B are g -factor, Bohr magneton, and external magnetic field, respectively.

With the increasing of the external magnetic field, the electron resonance takes place when the intensity of external magnetic field is matched to the transition of electron spinning, the energy is absorbed and an emitting electromagnetic energy is detected as EPR signal.

In this work, EPR was employed to detect the photo-generated electrons and some reactive intermediates when some typical trappers were used.

4.6 Gas Chromatography-Mass Spectrometry (GC-MS)

The gas chromatography-mass spectrometry (GC-MS) is an analytical method that consists of gas-chromatography and mass spectrometry that function as compounds separation and compound molecular weight identification, respectively¹⁹⁴. The GC separates different mixtures into pure compounds based on their volatility via flowing an insert gas (mobile phase, helium or nitrogen), which carries the pure compounds to pass through a fixed stationary phased in the column. The purified compounds are transported into mass detector, in which they are bombarded a stream of electrons resulting in the generation of various fragments. The mass charge ratios (M/Z) of different fragments are recorded to confirm and identify the obtained compound.

In this work, GC-MS was applied to analyze compounds inside the reaction mixture to obtain the reaction details.

5 Results and Discussion

In this chapter, various benzothiadiazole-based photocatalysts were designed and synthesized as small molecular and macromolecular photocatalysts. For the homogeneous catalytic systems, first, a simple donor-acceptor type photocatalyst was prepared in the first subchapter as the model benzothiadiazole-based photocatalyst. In addition, a highly twisted structure was synthesized in the subchapter four which illuminated an extended excited state lifetime, endowing the photocatalyst with the capacity of activating carbon-halogen bond via consecutive light-induced electron transfer process. For the heterogeneous catalytic systems, both non-conjugated microporous organic polymers (MOP) and conjugated microporous polymers (CMP) were obtained by knitting the benzothiadiazole moiety into polymer matrix as demonstrated in the subchapters 5.2 and 5.3, respectively. Parallel to the catalysts design, the photocatalytic reaction mechanisms such as electron-transfer pathway and the formation of reactive intermediates were investigated to further enrich the current reaction system and photocatalytic methodologies.

5.1 A metal-free, dually redox-active organic photocatalyst for visible light-promoted Diels-Alder reaction and direct conversion of aliphatic alcohols to bromides

This subchapter is based on the unpublished article “A metal-free, dually redox-active organic photocatalyst for visible light-promoted Diels-Alder reaction and direct conversion of aliphatic alcohols to bromides”. In this chapter, a donor acceptor-type small molecule organic semiconductor based on 2,1,3-benzothiadiazole was designed and used as pure organic, dually redox-active photocatalyst. Two different photoredox reactions, the Diels-Alder reaction and direct conversion of aliphatic alcohols to bromides via either reductive or oxidative quenching process could be catalyzed by the designed photocatalyst, respectively. Advanced photophysical studies were conducted to reveal the photo-induced electron transfer pathway within the catalytic process. This study could pave the way towards metal-free photocatalysis with high efficiency and elucidate the mechanistic insight of this new class of molecular photocatalysts.

5.1.1 Motivation

The employment of visible light-active photocatalysts under sustainable and environmentally benign reaction conditions has attracted much attention among the organic and materials scientists in recent years.¹ In the past decades, enormous effort has been paid to the study about the influence of molecular structure on the redox properties of photocatalysts in order to improve their catalytic performance.¹⁹⁵ Normally, the redox-based transformation reactions undergo either via reductive or oxidative quenching processes of the photocatalyst in its excited state. In the reductive quenching cycle, the excited photocatalyst acts as an oxidant by extracting an electron from the electron-donating substrate. Simply sorted with the respect of photocatalyst, examples of photocatalytic reactions via reductive quenching have been reported such as cyclization reactions,^{196,197} ring opening reaction,¹⁹⁸ radical addition,¹⁹⁹ or cycloaddition reaction,^{72,74,200} Aza-Henry reaction,²⁰¹ or oxidative C-C,^{3,202} C-N,²⁰³ and C-S- bond formations.²⁰⁴ In the oxidative quenching cycle, the excited photocatalyst functions as a reductant by releasing an electron to the electron-accepting substrate. Examples of the electron-initiated photocatalytic reactions have been also widely reported, such as hydrogen evolution,^{205,206} dehalogenation reaction,^{147,182} reductive C-C arylation reactions,¹⁸ trifluoromethylation of alkenes,²⁰⁷ oxidation of alcohols,²⁰⁸ and radical addition reactions.²⁰⁹

Among the well-established redox-active molecular photocatalysts, most reported catalytic systems are transition metal complexes, for example [Ru(bpy)₃]Cl₂^{15,210} and *fac*-[Ir(ppy)₃].^{182,211} Currently, organic semiconductor (OS)-based photocatalysts have emerged as a promising alternative to the traditional metal-containing photocatalysts due to their highly tunable electronical properties. Recent research activities have shown a vast number of small molecular^{12,13,133,202,212-214} or macromolecular^{147,151-153,161,162,176,203,215,216} OS systems as efficient photocatalysts for visible light-promoted photo-redox reactions. Nevertheless, compared to the transition metal complexes, metal-free, stable, visible light and dually redox-active photocatalytic systems based on organic semiconductors have still been underexplored. Indeed, the combination of preferably sufficient dual redox ability, which is caused by the individual energy band positions, with the necessary narrow band gap energy, which ought to be overcome by low energetic photo-generated electrons under visible light irradiation, is highly challenging. More enhanced investigation of this new class of photocatalysts is highly needed.

In this chapter, a donor-acceptor-(D-A)-type molecular organic semiconductor, 4,7-diphenyl-2,1,3-benzothiadiazole as an efficient metal-free and dually redox-active photocatalyst for visible light-promoted chemical transformations was investigated. The organic photocatalyst possessed sufficient photo-redox potentials at +1.64 V and -1.30 V vs. SCE. Diels-Alder reaction and direct bromination reaction of alkyl alcohols could be

catalyzed via reductive and oxidative quenching processes by the photocatalyst in high yields. The photocatalytic efficiency of the organic photocatalyst was comparable to that of the state-of-art metal or non-metal photocatalysts reported. No photobleaching effect of the organic photocatalyst was observed. Furthermore, a detailed photophysical study employing advanced spectroscopic methods such time-resolved photoluminescence decay and transient absorption spectroscopy was conducted to investigate the mechanistic insight of the photo-induced electron transport between the organic photocatalyst and the substrates.

5.1.2 Synthesis and characterization of Ph-BT-Ph

The organic photocatalyst 4,7-diphenyl-2,1,3-benzothiadiazole (Ph-BT-Ph) (Figure 5.1(a)) was synthesized via a simple Suzuki-coupling procedure between 4,7-dibromo-2,1,3-benzothiadiazole and phenylboronic acid, as previously reported.²¹⁷ The synthetic and characterization details are described in chapter 6.1.3. Theoretical calculations using the density functional theory (DFT) at B3LYP/6-31G* level revealed that the electron densities were mainly focused on the electron-donating phenyl and -withdrawing benzothiadiazole moieties on the highest occupied molecular orbital (HOMO) and lowest unoccupied molecular orbital (LUMO) for Ph-BT-Ph, respectively (Figure 5.1(b)). This demonstrated that the D-A-type molecular design of Ph-BT-Ph could enhance the photo-induced electron/hole charge separation and thereby facilitate its dual photoredox activity. The UV/vis absorption spectrum of Ph-BT-Ph showed an absorption range up to ca. 450 nm with a maximum at 387 nm, while the emission area between 400 and 650 nm with the maximum at ca. 505 nm was determined (Figure 5.1(c)). The optical properties of Ph-BT-Ph were similar to that of *fac*-[Ir(ppy)₃], a well-established transition metal photocatalyst.²¹⁸ The cyclic voltammetry (CV) measurement revealed the HOMO and LUMO of Ph-BT-Ph at +1.64 V and -1.30 V vs. SCE (Figure 5.1(d)-(e)), indicating its possibly high redox potentials. A comparison of the photoredox potentials of Ph-BT-Ph with selected state-of-art transition metal complexes such as [Ru(bpy)₃]²⁺, *fac*-[Ir(ppy)₃], or pure organic photocatalysts such as eosin Y,²¹⁹ and 9-mesityl-10-methylacridinium perchlorate (Acr⁺-Mes),¹²² was shown in Figure 5.1(f).

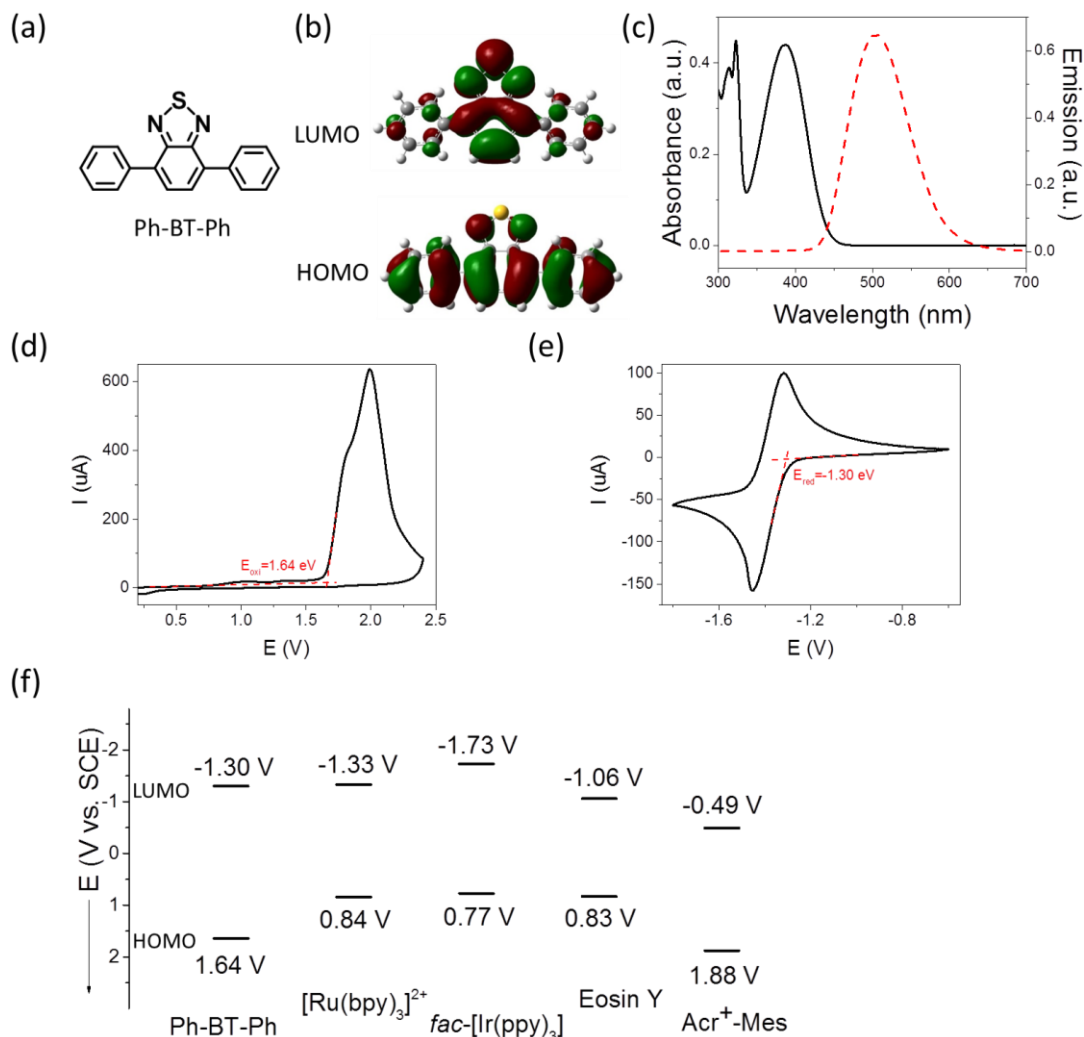


Figure 5.1 (a) Structure of Ph-BT-Ph; (b) simulated electron density of Ph-BT-Ph on its HOMO and LUMO levels; (c) UV-Vis (black, solid) and fluorescence (red, dash) of Ph-BT-Ph; Cyclic voltammetry of Ph-BT-Ph in the oxidative cycle (d) and reductive cycle (e) and (f) the photoredox potential comparison of Ph-BT-Ph with the other state-of-art organic and metal-based molecular photocatalysts. Values of $[Ru(bpy)_3]^{2+}$, $fac-[Ir(ppy)_3]$, eosin Y and Acr^+-Mes are taken from literature.^{121,219} bpy = 2,2'-bipyridyl; ppy = phenylpyridyl.

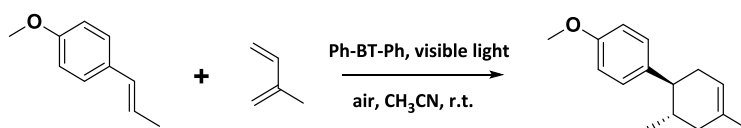
5.1.3 Photocatalytic redox transformation with Ph-BT-Ph

To demonstrate the feasibility of Ph-BT-Ph as a dually redox-active photocatalyst, we chose two different reactions via either reductive or oxidative quenching processes, respectively.

5.1.3.1 Photocatalytic Diels-Alder reaction via reductive quenching

Firstly, the photocatalytic Diels-Alder reaction was investigated to test the oxidizing capacity of Ph-BT-Ph as an example for the reductive quenching mechanism. The screening and control experiments of the model Diels-Alder reaction between *trans*-anethole and isoprene were listed in Table 5.1. Significantly, the Diels-Alder cycloaddition of *trans*-anethole and isoprene was achieved with high selectivity (>99%) in a quantitative manner within 10 min at room temperature in air (entry 1). Control experiments showed that acetonitrile appeared as the best solvent (entries 2 and 3). And no product was determined without light irradiation or the use of Ph-BT-Ph (entries 4 and 5). In the absence of oxygen, the reaction rate decreased dramatically to only 8% conversion after 10 min (entry 6). However, a moderate conversion of 80% could still be obtained after 24 h, which was different to the study of a chromium complex-based catalyst, which showed no reactivity under Ar atmosphere.³⁹ Here, we believed that oxygen should not only function as the electron scavenger to assist the regeneration of the photocatalyst,⁷⁴ but also as the mediator to stabilize the oxidized intermediate of the dienophile, as reported previously.³⁹

Table 5.1 Screening and control experiments of the photocatalytic Diels-Alder reaction of *trans*-anethole and isoprene.^a



Entry	Reaction condition variations	time	Conversion ^b (%)
1	Standard conditions	10 min	> 99
2	CH ₃ NO ₂ as reaction solvent	24 h	90
3	DCM as reaction solvent	24 h	5
4	Reaction without catalyst	24 h	trace
5	Reaction without light	24 h	trace
6	Under nitrogen	10 min	8
		24 h	80
7 ^c	With electron scavenger and under nitrogen	24 h	> 99
8 ^d	With hole scavenger	24 h	trace
9	Eosin Y as catalyst	24 h	trace
10	9-Mesityl-10-methylacridinium as catalyst	10 min	60
11	[Ru(bpy) ₃]Cl ₂ as catalyst	10 min	trace
12	<i>fac</i> -[Ir(ppy) ₃] as catalyst	10 min	trace

^aReaction conditions: [Anethole] = 0.1 M, [Isoprene] = 1 M, acetonitrile 2.4 mL, catalyst 1 mg/ml, blue LED lamp (460 nm, 1.2 W/cm²), room temperature. ^bConversion determined by GC-MS. ^cCuCl₂ as electron scavenger. ^dKI as hole scavenger. ^edimerizations of isoprene as the major product.

By using CuCl₂ as electron scavenger under the nitrogen atmosphere, an increased reaction conversion (>99%) was obtained, indicating that the role of oxygen was most likely as a

stabilizer for the dienophile intermediate (entry 7). Via addition of KI as photo-generated hole scavenger, only traces of the desired product could be determined (entry 8). In direct comparison with other state-of-art organic photocatalysts such as eosin Y (trace, entry 9) and 9-mesityl-10-methylacridinium perchlorate (60%, entry 10), or transition metal complexes such as $[\text{Ru}(\text{bpy})_3]\text{Cl}_2$ (entry 11, trace) or *fac*- $[\text{Ir}(\text{ppy})_3]$ (entry 12, trace), Ph-BT-Ph achieved its superior photocatalytic efficiency. This demonstrated the highly efficient activity of Ph-BT-Ph to catalyze organic reactions via reductive quenching process.

Interestingly, a second kinetic order was found while monitoring the reaction (Figure 5.2(a)). The light on-and-off experiment showed that only trace amount of the product could be determined in dark, indicating that the generated radical cation of *trans*-anethole was only minimally active without light irradiation (Figure 5.2(b)). We proposed a reaction mechanism based on our observations and previous reports.^{39,74} The main reaction pathway was illustrated in Figure 5.3. Under light irradiation, the substrate *trans*-anethole was oxidized by the photo-generated hole of Ph-BT-Ph to its cationic radical intermediate, which reacted with isoprene to form the cyclic intermediate. The cyclic intermediate could be reduced by Ph-BT-Ph formed via reductive quenching, regenerating the photocatalyst back to its ground state and forming the final product to complete the catalytic cycle (pathway a). In addition, the final product can also be obtained either via oxidation of another neutral *trans*-anethole by cyclic intermediate, chain propagation characteristics (pathway c), or oxidation of $\text{O}_2^{\cdot-}$, generated by electron transfer from Ph-BT-Ph to oxygen showed in Figure 5.4 (pathway b).

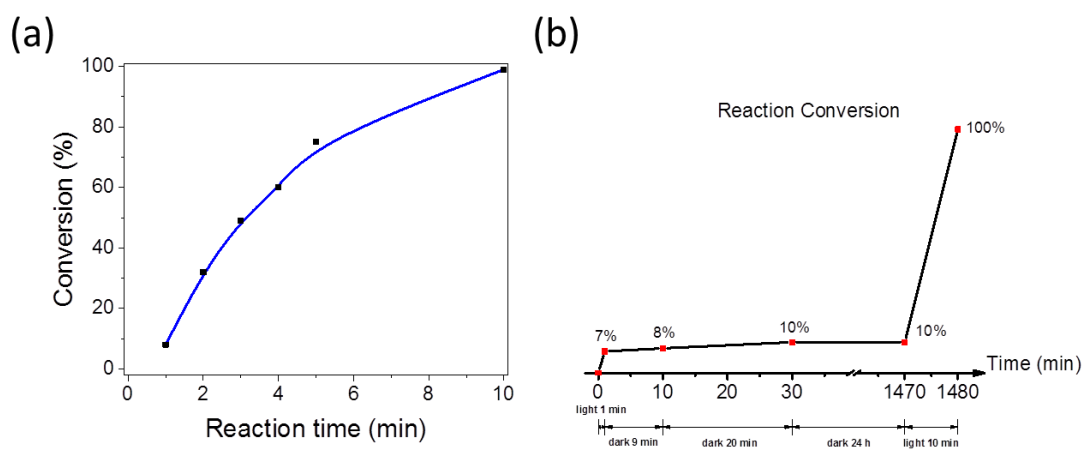


Figure 5.2 (a) Monitoring experiment of photocatalytic Diels-Alder reaction and (b) reaction conversion change for light on and off.

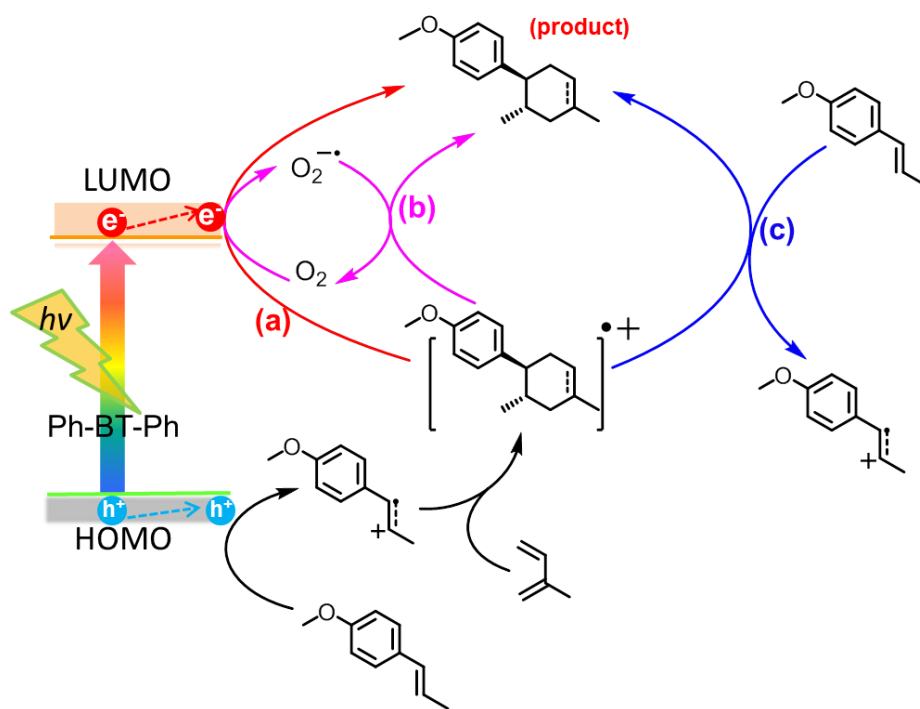


Figure 5.3 Proposed reaction mechanism of photocatalytic Diels-Alder reaction using Ph-BT-Ph as visible light-active photocatalyst.

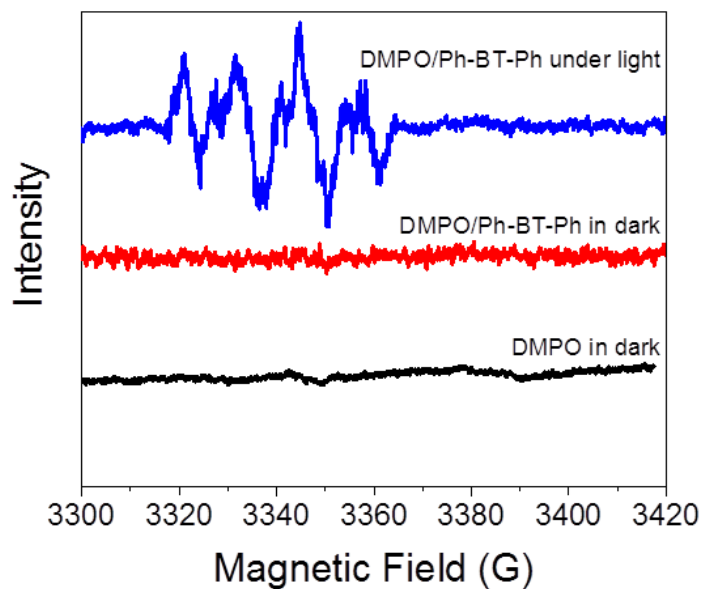


Figure 5.4 EPR spectra for neat DMPO (0.1 M) solution in acetonitrile in dark (black), and mixture of DMPO (0.1 M) and Ph-BT-Ph (1 mg/mL) in dark (red) and under the irradiation of blue LED for 10 min (blue).

A scope of the photocatalytic Diels-Alder reaction employing different dienes and dienophiles was listed in Figure 5.5. High reaction yields from 85% to 96% were obtained, demonstrating the general applicability of Ph-BT-Ph for organic reactions via reductive quenching process. It was worth to mention that molecular photocatalyst Ph-BT-Ph could be repeatedly used for several cycles without dramatically suffering its photocatalytic efficiency (Figure 5.6, for details about repeating experiment in chapter 6.1.7). No photobleaching effect could be found according to the UV/vis absorption spectra of Ph-BT-Ph after the reaction (Figure 5.7). This demonstrated the high stability of Ph-BT-Ph.

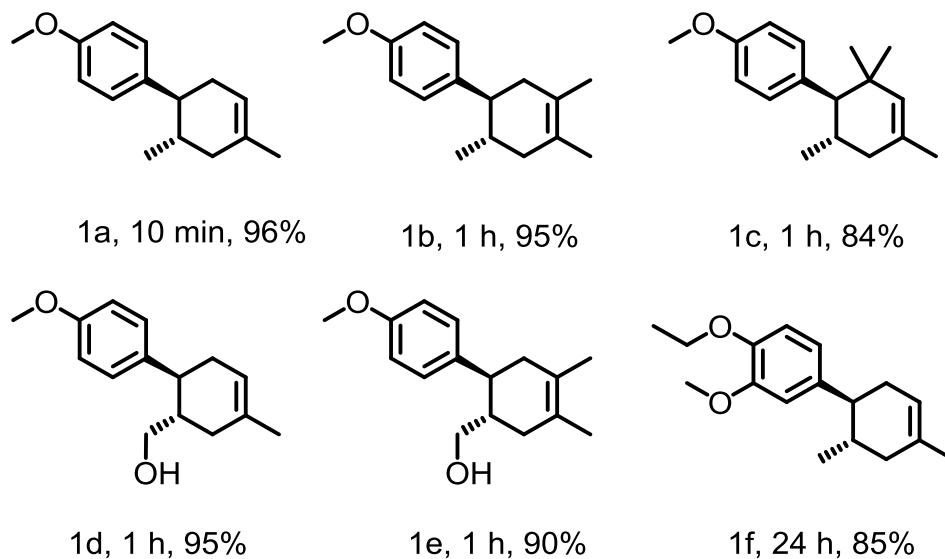


Figure 5.5 Scope of the photocatalytic Diels-Alder reaction using Ph-BT-Ph as photocatalyst.

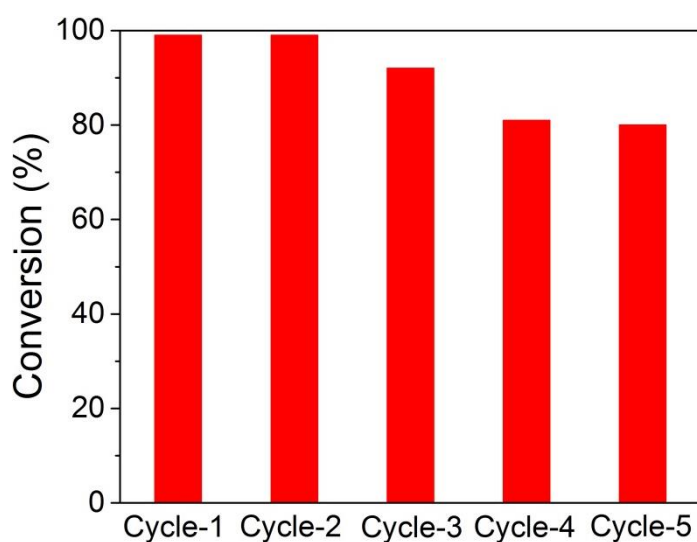


Figure 5.6 Repeating experiment of the photocatalytic Diels-Alder reaction.

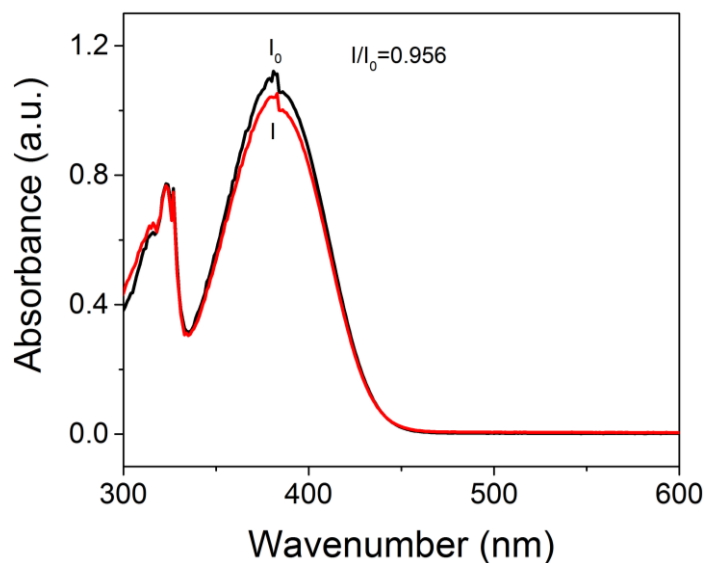


Figure 5.7 UV-Vis spectra of Ph-BT-Ph before (black) and after (red) photocatalytic Diels-Alder reaction.

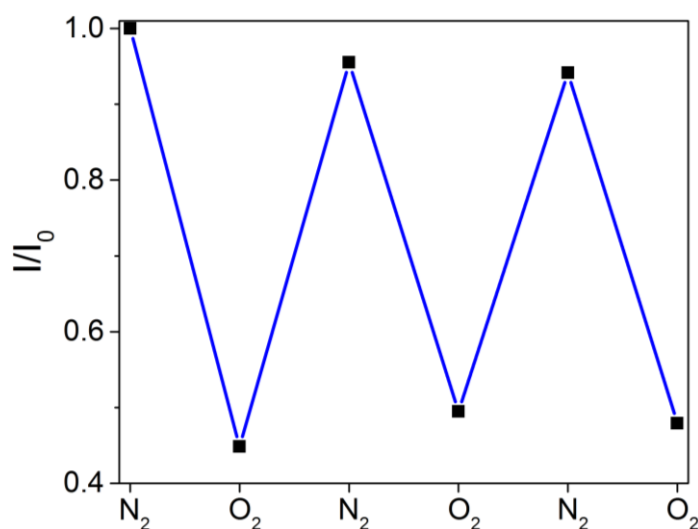


Figure 5.8 Fluorescence intensity of Ph-BT-Ph change after bubbling with N_2 and O_2 for 10 min, respectively. I_0 for emission intensity after degassing with N_2 and I for emission intensity after degassing with O_2 .

The steady-state fluorescence quenching experiments showed that the fluorescence of Ph-BT-Ph could be quenched by adding oxygen, indicating a photo-induced electron transfer between the photocatalyst and oxygen active species (Figure 5.8). To gain a deeper insight and to elucidate the electron transfer between the photocatalyst and substrates during oxidative quenching processes, we then performed advanced photophysical studies such as time-resolved photoluminescence (TRPL) and transient absorption (TA) spectroscopy measurements. As shown in Figure 5.9 and Table 5.2, the fluorescence lifetime of Ph-BT-Ph in CH_3CN was determined to be 12.9 ns, which was comparable to the well-applied organic

photocatalysts, such as Acr⁺-Mes (15 ns)¹²⁹ and eosin Y (6 ns).¹⁰¹ The addition of O₂ could quench the excited state of Ph-BT-Ph to the decreased fluorescence lifetime of 10.7 ns. Similar phenomenon was observed when using *trans*-anethole as quencher, leading to a reduced fluorescence lifetime of 11.5 ns. This indicated a hole filling process by electron transfer between Ph-BT-Ph and *trans*-anethole.²²⁰ By simulating the concrete condition of the Diels-Alder reaction with *trans*-anethole in air, a similar decayed lifetime of Ph-BT-Ph of 11.2 ns was observed. This observation further confirmed the hole initiated process of the photocatalytic cation Diels-Alder reaction.

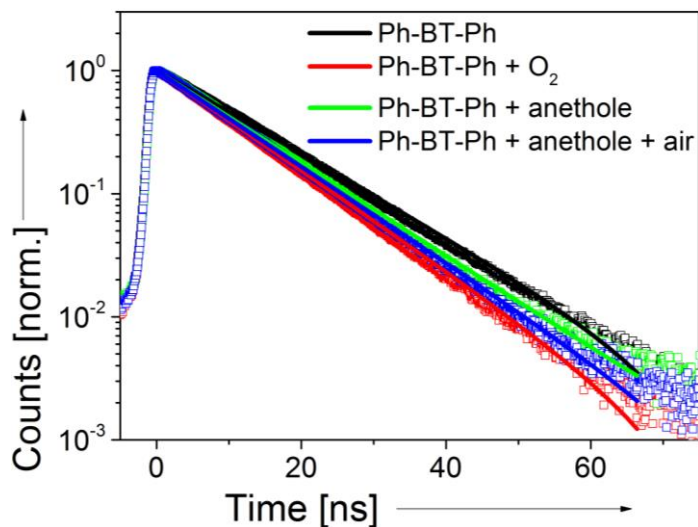


Figure 5.9 Fluorescence decay spectra of Ph-BT-Ph under N₂ (black), O₂ (red), and with anethole under N₂ (green) and in air (blue), the concentration of Ph-BT-Ph and anethole in acetonitrile solution were 20 mg/L and 2 mM, respectively. Excitation wavelength at 400 nm.

Table 5.2 Excited state life time of the measured mixtures.

Entry	Sample name	Fluorescence life time (ns)	Transient state life time (ns)
1	Ph-BT-Ph (CH ₃ CN)	12.9	10.3
2	Ph-BT-Ph + O ₂	10.7	7.5
3	Ph-BT-Ph + anethole	11.5	9.1
4	Ph-BT-Ph + anethole + air	11.2	9.4

Transient absorption spectra were recorded to further investigate the concrete electron transfer process between the photocatalyst Ph-BT-Ph and substrates. As shown in Figure 5.10(a), the signal peaking at 660 nm represented the photo-induced absorption (PIA) of Ph-BT-Ph in its excited state. The lifetime of the singlet excited state of Ph-BT-Ph was determined to be 11.1 ns, which was consistent to that obtained from the TRPL spectroscopy. Interestingly, the addition of O₂ did not affect the PIA of Ph-BT-Ph (Figure 5.10(b)). The possible reason might be that the phosphorescence signal for active oxygen

species such as $^1\text{O}_2$ normally localized on 1270 nm was beyond the detection limit of the transient absorption measurement. In comparison, the PIA curves of Ph-BT-Ph under the addition of *trans*-anethole remained first the similar shape as that of pure Ph-BT-Ph within the initial time from 1 ns to 3.1 ns, and then a new absorption peak at 610 nm appeared after 9.9 ns pulse irradiation (Figure 5.10(c)). This observation indicated that the formation of the radical cation of *trans*-anethole began to occur after 9.9 ns, which was similar as previous report,²²¹ thus supporting the proposed hole initiation mechanism. By increasing the concentration of *trans*-anethole, the absorption intensity of the mixture decayed faster, demonstrating the active electron transfer from the substrate to the photo-generated holes of the photocatalyst (Figure 5.10(d)). To note, the decay profiles of the TA were consistent with the ones of the TRPL (Figure 5.11).

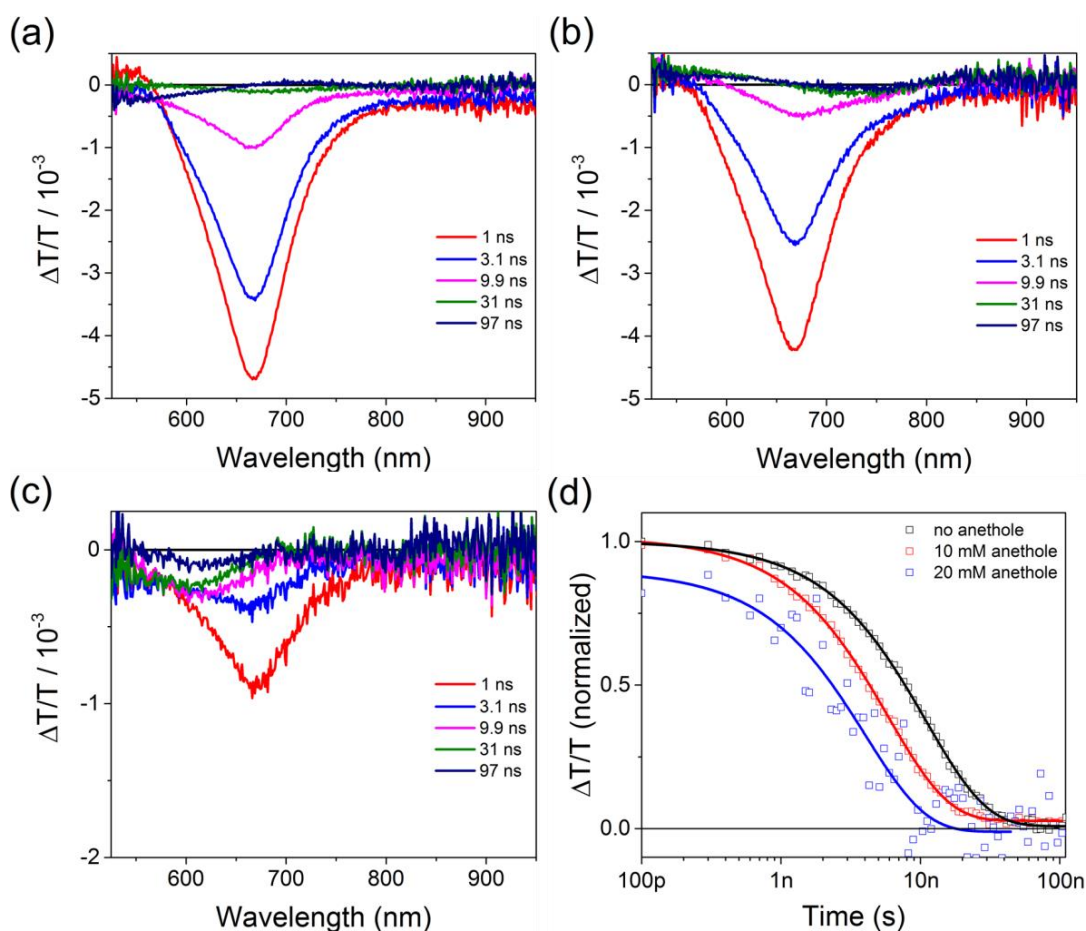


Figure 5.10 Transient absorption spectra of pure Ph-BT-Ph (20 mg/L) in N_2 (a) and O_2 (b) atmospheres, and (c) mixture of Ph-BT-Ph (20 mg/L) and *trans*-anethole (20 mM) at different time intervals in CH_3CN . (d) Time profiles of the absorbance decay at 675 nm of pure Ph-BT-Ph (20 mg/L, black), with 10 mM *trans*-anethole (red) and 20 mM *trans*-anethole (blue) in CH_3CN . Excitation at 355 nm.

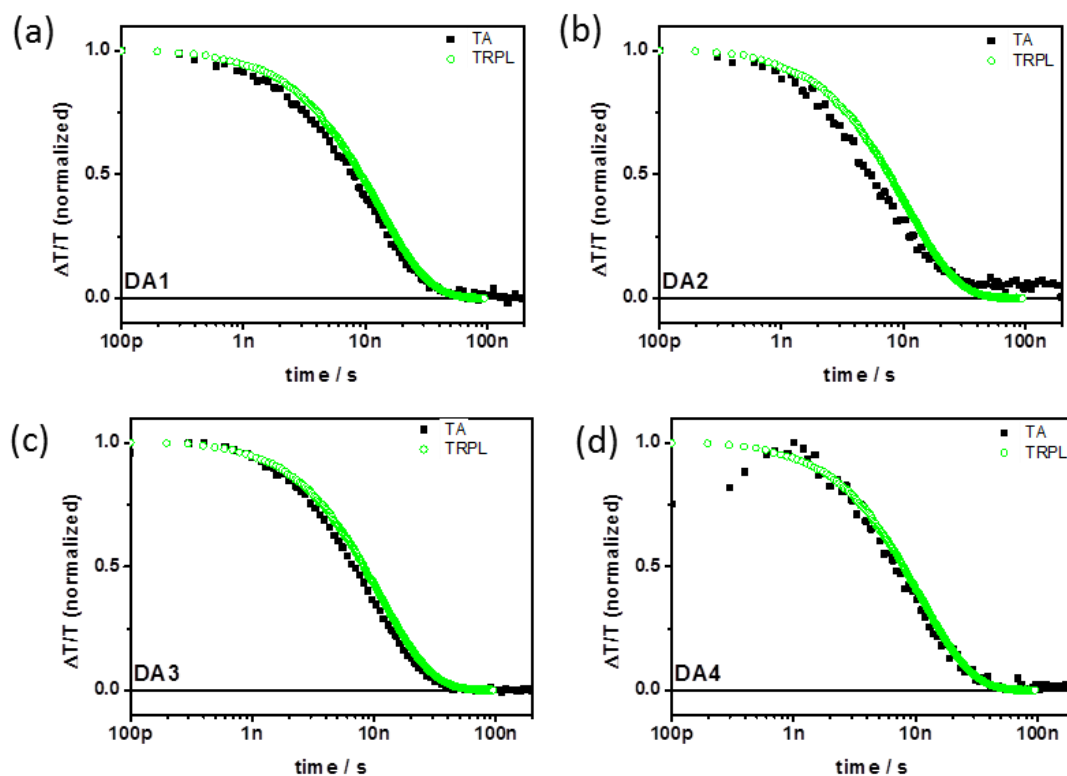


Figure 5.11 Comparison of decay profiles of transient absorption (TA) at 660 – 690 nm and time-resolved photoluminescence (TRPL) at 480-520 nm in CH_3CN . Pure Ph-BT-Ph under N_2 (a) and O_2 (b) and mixture of Ph-BT-Ph and *trans*-anethole under N_2 atmosphere (c) and O_2 atmosphere in CH_3CN (d). Concentration for Ph-BT-Ph and *trans*-anethole are 20 mg/L and 2 mM, respectively.

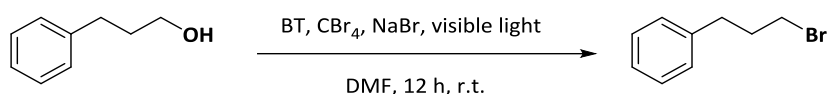
5.1.3.2 Photocatalytic direct conversion of aliphatic alcohols to bromides via oxidative quenching

Brominated compounds play an essential role in organic synthesis such as the formation reaction of carbon-carbon and carbon-heteroatom bonds.²²² For the reactions via oxidative quenching process, we then chose the photocatalytic direct bromination of aliphatic alcohols. The screening and control experiments of the model bromination reaction of 3-phenylpropan-1-ol into (3-bromopropyl)benzene were listed in Table 5.3. The model reaction was carried out with a high conversion of 98% (entry 1), with DMF being the best solvent (entries 2 and 3). Similar to the photocatalytic Diels-Alder reaction, the photocatalytic bromination reaction could not be conducted without either light, or Ph-BT-Ph (entries 4 and 5). Similarly, the photo-generated electron/hole pair of Ph-BT-Ph played a crucial role during the catalytic cycle. Using KI as hole scavenger led to only trace conversion (entry 6). By adding benzoquinone as electron scavenger, a decreased conversion of 29% was obtained (entry 7). To study the origin of the bromine source, we then carried out the model reaction without CBr_4 , 8% conversion was determined (entry

8). Without using NaBr as additive, a decreased conversion of 80% could be obtained (entry 9).

Similar to the Diels-Alder reaction, using eosin Y and 9-mesityl-10-methylacridinium perchlorate as comparison photocatalysts, only trace or no conversion were determined (Table 5.3, entries 10 and 11). Here, an O,N-aminal product was determined with both organic photocatalysts, corresponding the oxidation of DMF followed by nucleophilic addition between alcohol and imine intermediates as illuminated in previous report.²²³ By employing Ru(bpy)₃Cl₂ (entry 12) and *fac*-[Ir(ppy)₃] (entry 13) as photocatalysts, reaction conversions of 96 and 98% were observed. This confirmed the high dual photoredox activity of Ph-BT-Ph as promising photocatalyst.

Table 5.3 Screening and control experiments of the photocatalytic bromination reaction with model substrate.^a



Entry	Reaction condition variations	Conversion ^b (%)
1	Standard conditions	> 98
2	THF as reaction solvent	trace
3	Acetonitrile as reaction solvent	40
4	No catalyst	trace
5	No light	trace
6 ^c	With hole scavenger	trace
7 ^d	with electron scavenger	29
8	No CBr ₄	8
9	No NaBr	80
10	Eosin Y as catalyst	3
11	9-Mesityl-10-methylacridinium as catalyst	trace
12	[Ru(bpy) ₃]Cl ₂ as catalyst	96
13	<i>fac</i> -[Ir(ppy) ₃] as catalyst	98

^aReaction conditions: [Benzenepropanol] = 0.05 M, [CBr₄] = 0.1 M, [NaBr] = 0.1 M, dry DMF 10 mL, [Ph-BT-Ph] = 1 mg/ml (6.5 mol%), blue LED lamp (460 nm, 0.16 W/cm²), room temperature, 12 h. ^bConversion determined by GC-MS. ^cKI as hole scavenger.

^dBenzoquinone as electron scavenger.

To understand the reaction mechanism, we further studied the role of CBr₄. A control experiment conducted in deuterated DMF for 4 h showed that only deuterated formate ester was formed (Figure 5.12, peak 2). This shows that DMF was involved in the bromination reaction. According to previous reports by Léonel²²⁴ and Stephenson²²⁵, there are usually two radical pathways in the formation of the brominated product based on either the formation of a carbene (:CBr₂) or radical (•CBr₃) as the oxidatively quenched intermediates. To precisely study this step, we then conducted an additional experiment

with α -methylstyrene as carbene ($:\text{CBr}_2$) or radical ($\bullet\text{CBr}_3$) trapping agent. As shown in Figure 5.13, both dibromo and tribromo products were determined by GC-MS with a ratio of 1/8.8, demonstrating that both carbene ($:\text{CBr}_2$) and radical ($\bullet\text{CBr}_3$) existed in the reaction mixture. And the radical ($\bullet\text{CBr}_3$) played a major role for the formation of the final product.

Based on the observations, a plausible reaction mechanism was proposed as illustrated in Figure 5.14. In the major pathway, the radical ($\bullet\text{CBr}_3$) was generated via one electron transfer from the LUMO level of Ph-BT-Ph to CBr_4 . The radical was trapped by DMF to form its radical intermediate, which then released an electron and form the iminium intermediate. The iminium intermediate was attacked by the bromide ion to form the Vilsmeier-Haack agent, which reacted with the alcohol to obtain the final product.²²⁶ In the minor reaction pathway, the carbene($:\text{CBr}_2$) could be generated through reducing CBr_4 by the photocatalyst Ph-BT-Ph,²²⁷ followed by similar steps via the Vilsmeier-Haack agent as in the major reaction pathway.

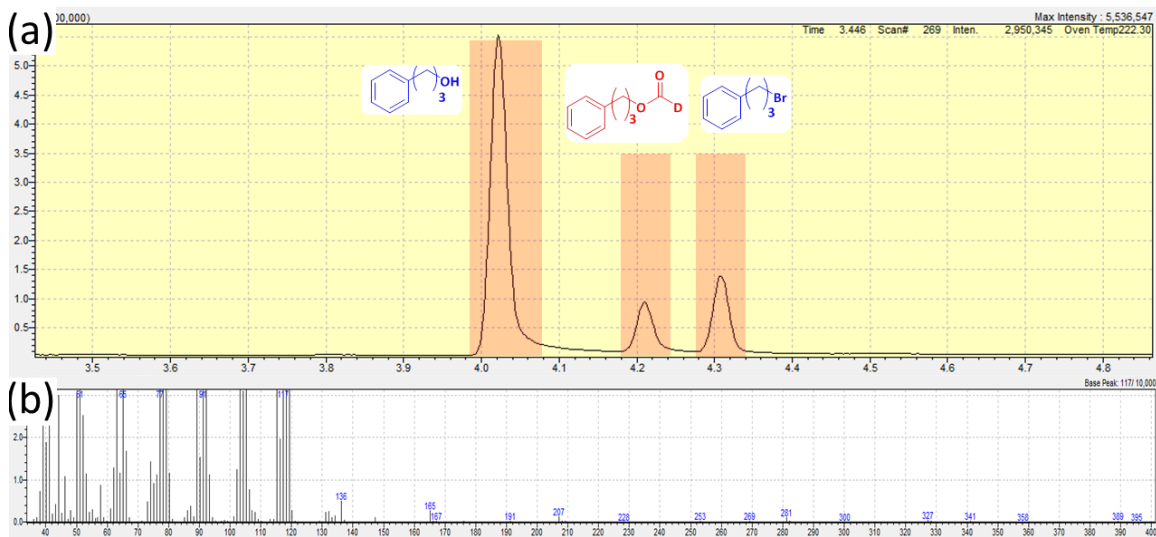


Figure 5.12 (a) GC spectrum of crude product after photocatalytic bromination with deuterium DMF and (b) corresponding MS spectrum for the second peak.

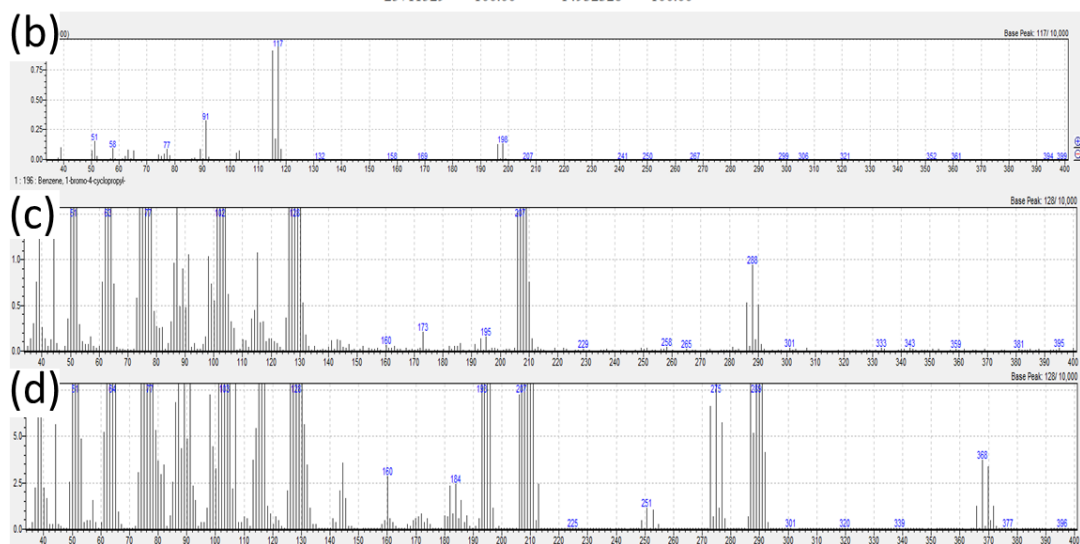
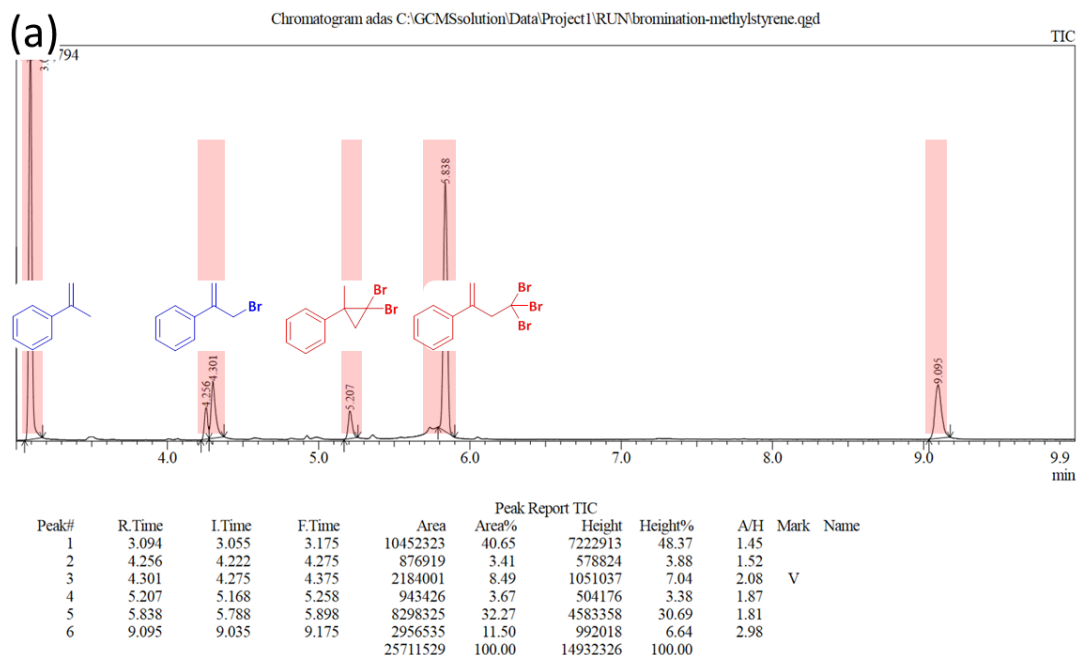


Figure 5.13 (a) GC spectrum of crude product after photocatalytic bromination of α -methyl-styrene and corresponding MS spectra for the third (b), the fourth (c) and the fifth peak (d).

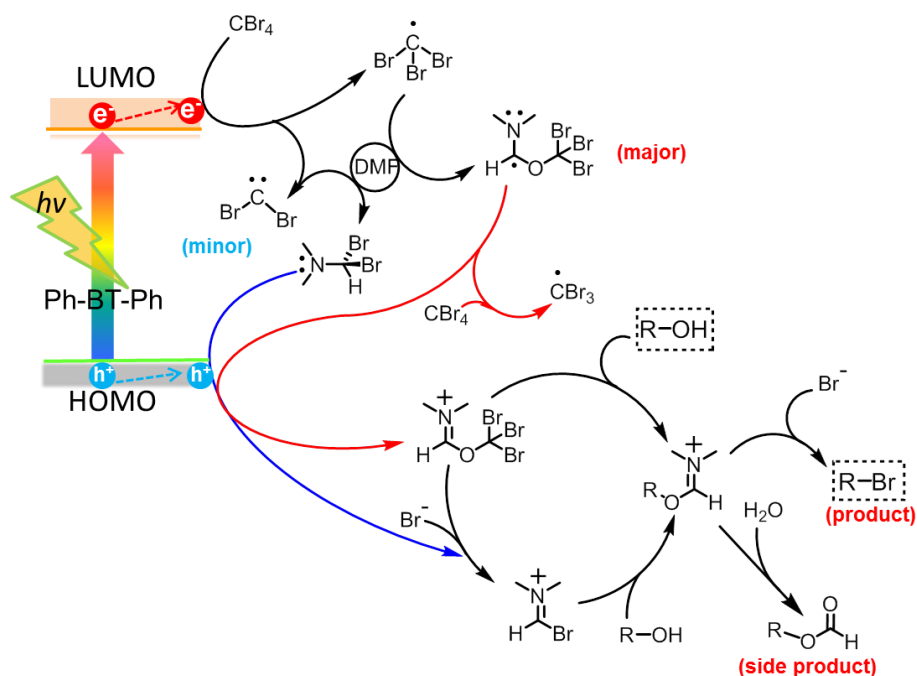


Figure 5.14 Proposed reaction mechanism of photocatalytic direct conversion of alkyl alcohols to bromides using Ph-BT-Ph as visible light-active photocatalyst.

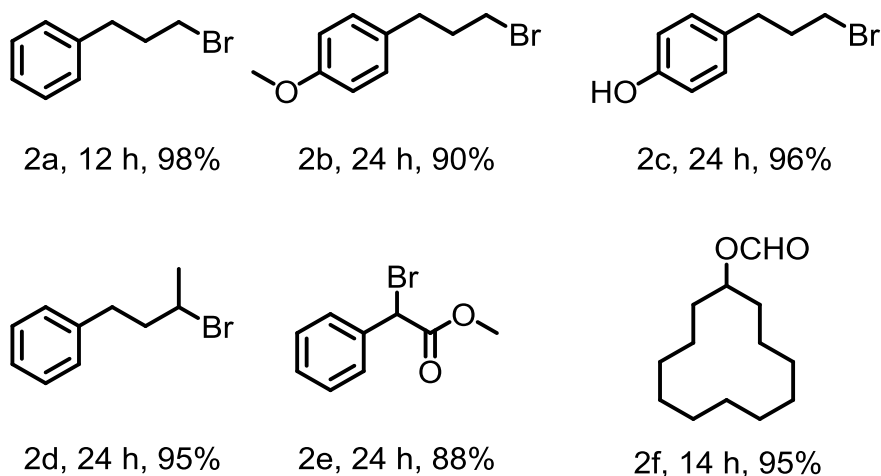


Figure 5.15 Scope of the photocatalytic conversion of alkyl alcohols to bromides using Ph-BT-Ph as photocatalyst.

The scope of various alcohols demonstrated that both primary and secondary alcohols could be transformed into the corresponding bromides using Ph-BT-Ph as photocatalyst (Figure 5.15). And the reactions of the primary alcohols exhibited slightly higher conversion than that of the secondary alcohols. It could be observed that formate ester was the common minor side product for most of the alcohols. Additionally, for the reaction with

cyclododecanol, cyclododecyl formate was determined as the main product with bromide product being trace amount (2f), indicating the potential reactive iminium intermediate generated from the reaction between alcohol and Vilsmeier-Haack reagent, which was similar to a previous report.²²⁵ and finally it also noted to mention that no photobleaching effect was found in the UV-Vis spectra, indicating the excellent stability of Ph-BT-Ph in the oxidative quenching cycle (Figure 5.16).

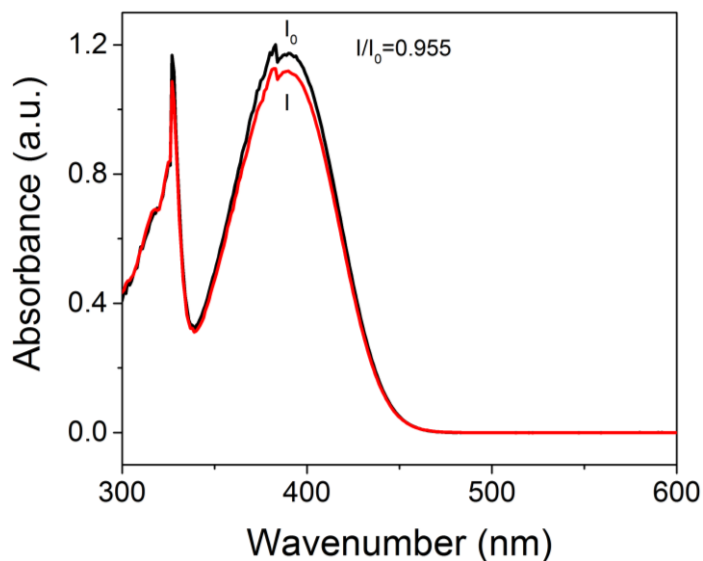


Figure 5.16 UV-Vis spectra of Ph-BT-Ph before (black) and after (red) photocatalytic conversion of aliphatic alcohols to bromides.

The steady-state fluorescence quenching experiments showed that the fluorescence of Ph-BT-Ph could be quenched by adding CBr_4 , indicating a photo-induced electron transfer between the photocatalyst and CBr_4 (Figure 5.17). In addition, the fluorescence lifetime decay of Ph-BT-Ph was observed in a similar manner for the photocatalytic bromination reaction of the alkyl alcohols. As shown in Figure 5.18 and Table 5.4, the fluorescence lifetime of Ph-BT-Ph was determined to be 13.0 ns in DMF, which was then decreased to 9.5 ns determined by adding CBr_4 . This indicated a possible electron migration from the LUMO of Ph-BT-Ph to CBr_4 , which was indeed the initiation step for the bromination reaction, as described in the aforementioned control experiments. In comparison, the fluorescence lifetime of Ph-BT-Ph did not change by adding alcohol (3-phenylpropanol), indicating no interaction between the alcohol and the photocatalyst. By employing the reaction mixture containing CBr_4 , alcohol and Ph-BT-Ph, a similar fluorescence lifetime delay was recorded as only adding CBr_4 , confirming that the reaction between CBr_4 and Ph-BT-Ph was indeed the initial step in the catalytic cycle of the bromination reaction.

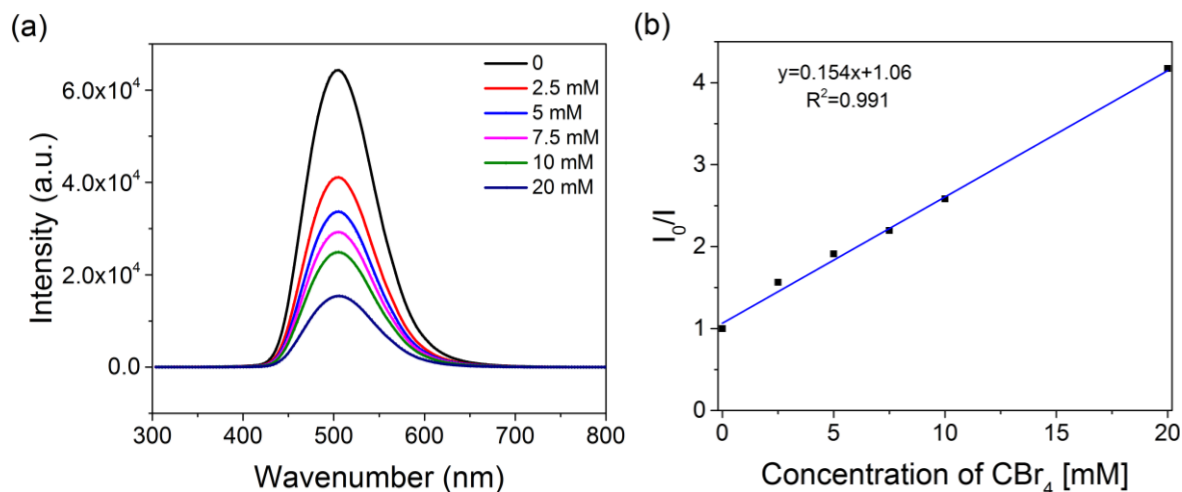


Figure 5.17 (a) Fluorescence spectra of Ph-BT-Ph after adding various amounts of CBr_4 quencher and (b) fluorescence intensity change in the presence of CBr_4 . I_0 for emission intensity in the absence of quencher and I for emission intensity in the presence of quencher.

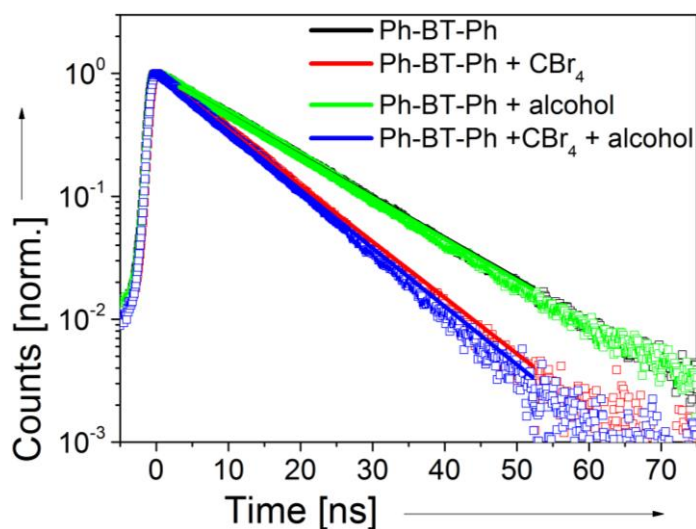


Figure 5.18 Fluorescence decay spectra of Ph-BT-Ph (black), mixture of Ph-BT-Ph with CBr_4 (red), with alcohol (green), and with both CBr_4 and alcohol (blue), the concentration of Ph-BT-Ph, CBr_4 and alcohol were 20 mg/L, 8 mM and 4 mM in DMF, respectively. Excitation wavelength at 400 nm.

Table 5.4 Excited state life time of the measured mixtures.

Entry	Sample name	Fluorescence life time (ns)	Transient state life time (ns)
1	Ph-BT-Ph (DMF)	13.0	13.1
2	Ph-BT-Ph + CBr_4	9.5	7.2
3	Ph-BT-Ph + alcohol	12.9	10.8
4	Ph-BT-Ph + CBr_4 + alcohol	9.2	7.7

Transient absorption spectra were again recorded to investigate the concrete electron transfer process between the photocatalyst Ph-BT-Ph and substrates. A similar phenomenon was also observed in the photocatalytic bromination reaction system as that in Diels-Alder reaction system. The lifetime of the singlet excited state of Ph-BT-Ph was determined to be 13.1 ns in DMF (Figure 5.19(a), and Table 5.4). The addition of CBr₄ did not change the PIA curves of Ph-BT-Ph (Figure 5.19(b)). The reason could be that the signals of the possibly formed intermediates such as the radical ($\bullet\text{CBr}_3$) and carbene ($:\text{CBr}_2$) were located less than 500 nm,²²⁸ which were outside the spectral window. No interaction was found between the excited state of Ph-BT-Ph and 3-phenylpropanol (Figure 5.19(c)), indicating that no electron and hole transfer between the photocatalyst and 3-phenylpropanol occurred during the catalytic cycle. This partially supported our hypothesis that the brominated product should be only obtained via the reaction between the alcohol and reactive intermediate. Although the present of CBr₄ had limited influence on the PIA curve, it obviously still could accelerate the decay profile of the excited singlet state of Ph-BT-Ph from 13.1 ns to 7.7 ns (Figure 5.19(d)), and thereby revealing the electron transfer in the excited state. Furthermore, the same consistence between TA and TRPL was also observed (Figure 5.20).

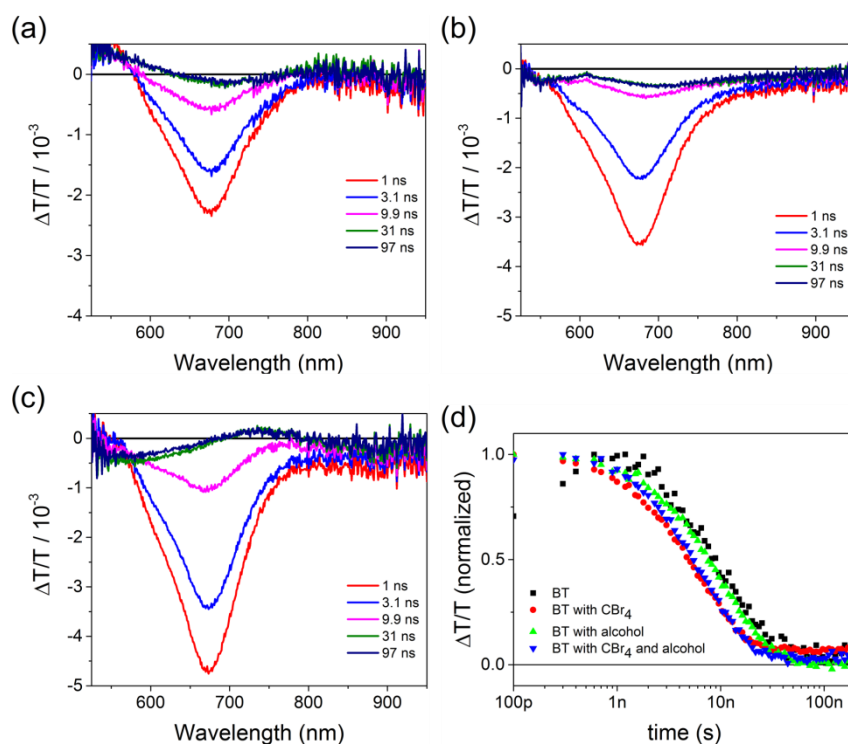


Figure 5.19 Transient absorption spectra of (a) pure Ph-BT-Ph, (b) with CBr₄ and (c) with alcohol at in DMF at various timescale. (d) Time profiles of absorbance decay at 670 nm of Ph-BT-Ph (black, square), Ph-BT-Ph with CBr₄ (red, circle), Ph-BT-Ph with alcohol (green, up triangle) and Ph-BT-Ph with CBr₄ and alcohol (blue, down triangle). Concentrations of Ph-BT-Ph, CBr₄ and alcohol were 20 mg/L, 8 mM, and 4 mM respectively. Excitation at 355 nm.

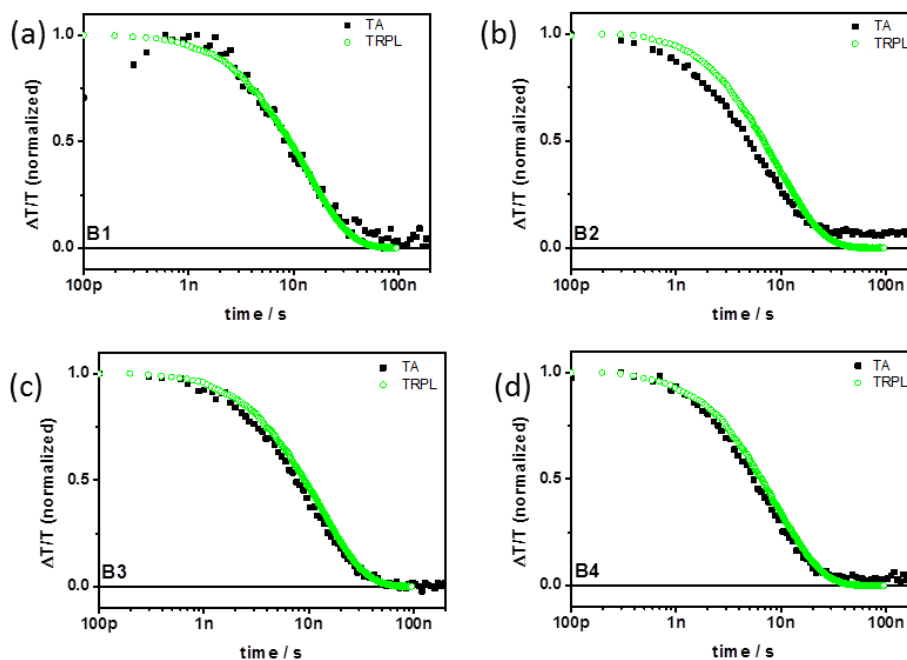


Figure 5.20 Comparison of decay profiles of transient absorption (TA) at 660 – 690 nm and time-resolved photoluminescence (TRPL) at 480-520 nm for the bromination reaction. (a) pure Ph-BT-Ph, (b) with CBr₄, (c) with alcohol, and (d) with both CBr₄ and alcohol. Concentrations of Ph-BT-Ph, CBr₄ and alcohol were 20 mg/L, 8 mM, and 4 mM in DMF.

5.1.4 Conclusion and outlook

As a conclusion for this chapter, a small molecule organic semiconductor, 4,7-diphenyl-2,1,3-benzothiadiazole was presented as an pure organic, dually redox-active and highly efficient photocatalyst for organic transformation reactions. Two different types of photoredox reactions based on reductive and oxidative quenching processes, i.e. the radical cationic Diels-Alder reaction and direct bromination reaction of alkyl alcohols were investigated. The photocatalytic efficiency of 4,7-diphenyl-2,1,3-benzothiadiazole was comparable with the state-of-art organic and transition metal photocatalysts. No photobleaching effect of the organic photocatalyst was observed, demonstrating the excellent stability of the photocatalyst. A deeper mechanistic insight of the photocatalytic process was investigated using advanced photophysical studies. Electron transfer between the photocatalyst and substrates, which involved the electron and hole migration during the catalytic processes, was clearly illuminated and confirmed. With its sufficient photoredox potentials, long photo-generated exciton lifetime and high efficiency, we believed that 4,7-diphenyl-2,1,3-benzothiadiazole can be a promising photocatalyst in a broader range of photoredox reactions.

5.2 Photocatalytic selective bromination of electron-rich aromatic compounds using microporous organic polymers with visible light

This chapter is based on the publication “Photocatalytic selective bromination of electron-rich aromatic compounds using microporous organic polymers with visible light”, **ACS Catalysis**, 2016, 6, 1113-1121. In the previous chapter, we demonstrate the high photocatalytic efficiency of Ph-BT-Ph as homogeneous and molecular photocatalyst. In this chapter, we introduce this photoactive chromophore into the polymer matrix. An insoluble, cross-linked polymer network combining high porosity was thus obtained as heterogeneous photocatalyst. The advantages of the heterogeneous nature of the photocatalyst such as high stability, ease of catalyst separation and recovery, and high reusability could be demonstrated.

5.2.1 Motivation

Brominated organic compounds serve as very important intermediates in organic synthesis due to their versatile applications in the chemical and pharmaceutical industries²²². Aromatic bromides, especially, have been widely employed as key precursors for various carbon-carbon and carbon-heteroatom bond formation reactions, such as Suzuki-Miyaura²²⁹, Sonogashira-²³⁰, Heck-²³¹, Stille-²³², and Buchwald-Hartwig^{233,234} cross-coupling reactions. In the last years, extensive efforts have been made by organic and materials chemists for the development of facile, mild, effective and practical synthetic pathways for aromatic bromides. From the perspective of the bromine source, many bromination reactions involve volatile, corrosive and toxic reaction conditions under the utilization of elemental bromine. Another drawback is that only 50% of the bromine atoms can be used for the reaction with the equivalent amount of hydrogen bromide (HBr) as byproduct. Milder reaction conditions are developed employing N-bromosuccinimide (NBS) as the bromination agent²³⁵⁻²³⁷. However, due to the fact that the synthesis of NBS still requires elemental bromine and its sensitivity to light and heat, the application is limited. HBr, in comparison, offers a high atom economy and can serve as a “green” bromine source, especially when hydrogen peroxide or oxygen was employed as oxidants^{214,238-240}.

Apart from the bromination reagent perspective, another standpoint for the bromination reaction of aromatic compounds is the catalyst design. In the past, noble metal-based catalysts such as indium²⁴¹, gold²³⁷, ruthenium²²⁵, and palladium^{242,243}, and non-noble metal-containing catalysts such as copper²⁴⁴, iron²⁴⁵, and vanadium²⁴⁶ have been used for various bromination reactions. However, there are still some intrinsic drawbacks associated with these metal-based catalysts, for instance, the high cost and toxicity, as well as the limited availability in nature. Another more technologically relevant concept

regarding the catalyst design is the homo- and heterogeneity of the catalytic systems. Compared to homogeneous catalysts, heterogeneous catalysts enjoy the advantage that they can be easily recycled by simple filtration due to their insoluble nature^{47,247}. It is therefore highly desirable to develop pure organic, metal-free and heterogeneous catalysts for the aforementioned bromination reaction of aromatic compounds.

Recently, light, especially visible light has been intensively used as an inexpensive, non-polluting, abundant and clean energy source to drive chemical transformation reactions. Beside the transition metal-based photocatalytic systems²⁴⁸⁻²⁵⁰, a number of non-metal photocatalysts have been developed in the past years^{144,147,150,152,216,251-253}. Among them, highly porous, polymer-based materials containing photoactive organic semiconductors have drawn much attention. Recent research activities have demonstrated their applications in singlet oxygen generation¹⁶¹, high selective oxidation of organic sulfides¹⁷⁴, oxidative C-C¹⁴⁴ and C-N^{170,252} bond formation, oxidative hydroxylation of arylboronic acids¹⁴⁷, reductive dehalogenation reaction¹⁸³, visible light-initiated free radical and cationic polymerization²⁵³, heavy metal reduction²¹⁶, and light-induced hydrogen evolution¹⁵².

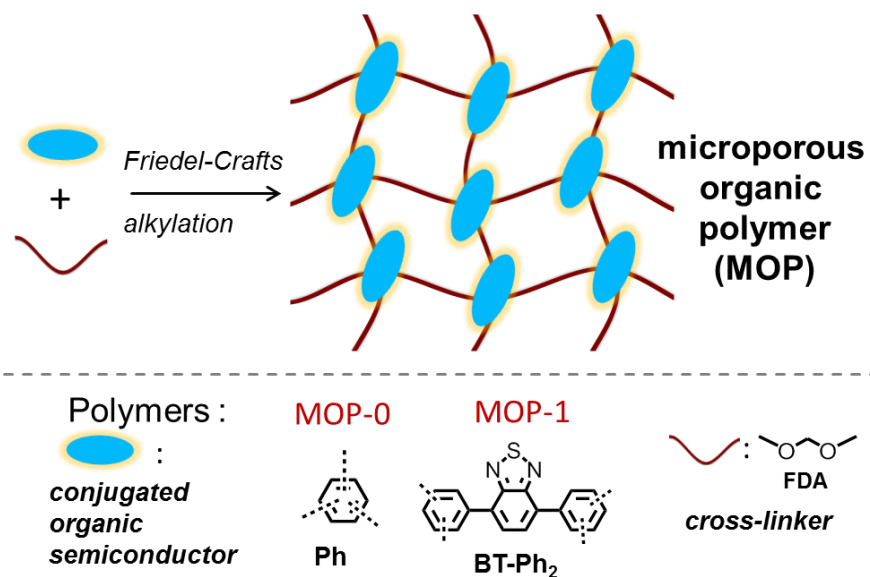
In this chapter, we report a series of microporous organic polymers (MOPs) containing photoactive conjugated organic semiconductor building blocks as heterogeneous photocatalysts for visible light-promoted, highly selective bromination reaction of electron-rich aromatic compounds using HBr as bromine source and molecular oxygen as a clean oxidant. The microporous polymers are prepared via a simple Friedel-Crafts alkylation reaction by simply cross-linking various small molecule organic semiconductors with defined valence and conduction band positions. Furthermore, a detailed study of the photocatalytic reaction mechanism is discussed.

5.2.2 Synthesis and characterization of MOPs

The microporous organic polymer MOP-1 were obtained via FeCl₃ promoted Friedel-Crafts alkylation reaction using formaldehyde dimethyl acetal (FDA) as bridging agent and 4,7-diphenylbenzo[c][1,2,5]thiadiazole (BT-Ph₂) as photoactive units as illustrated in Scheme 5.1. Another known polymer containing only phenyl rings (MOP-0)²⁵⁴ was prepared as a comparison to investigate the structural influence on the photocatalytic activity. To note, a modified synthetic route for MOP-1 was employed. Here, the bridging agent FDA was successively added into the reaction mixture, in order to obtain high porosity of the polymers.

The cross-linked polymers were insoluble in all common organic solvents tested. The SEM and TEM images of the two polymers illustrated different morphological structures at the micrometer scale (Figure 5.21). Specifically, MOP-1 showed a fused larger particle-like

structure than MOP-0. The morphology of MOP-1 was likely driven by the strong π - π stacking interaction between extended π -systems such as the BT-Ph₂ units during the cross-linking process¹⁴⁴.



Scheme 5.1 Illustration of the synthesis and idealized structures of the microporous organic polymers (MOPs).

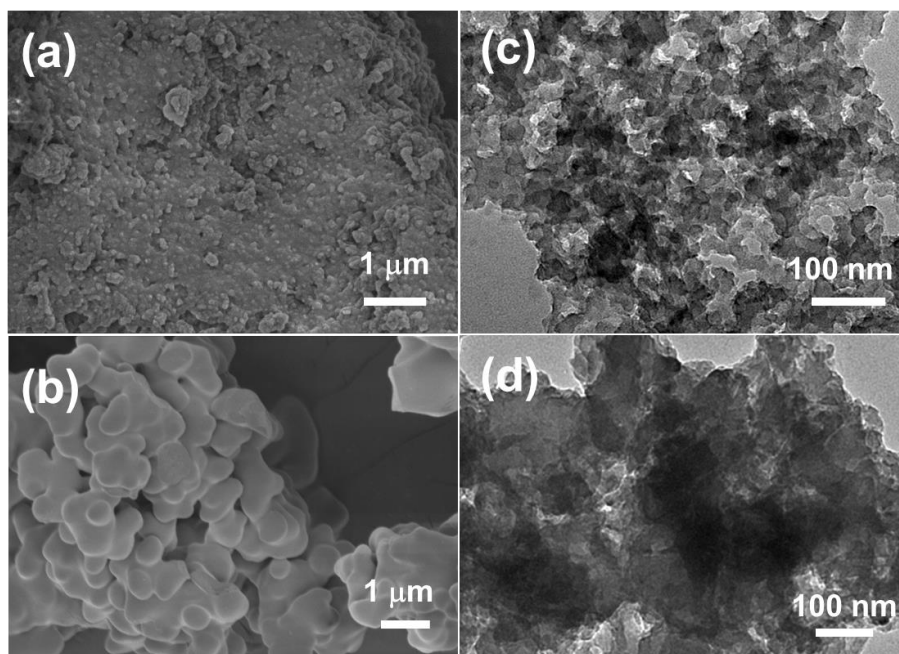


Figure 5.21 SEM images of (a) MOP-0, (b) MOP-1, and TEM images of (c) MOP-0, (d) MOP-1.

The porosity and structural data of the polymers were summarized in Table 5.5. The Brunauer-Emmet-Teller (BET) surface area of the benzene-based polymer (MOP-0b) via the bulk cross-linking method was found to be 1367 m²/g with a pore volume of 1.74 m³/g (Figure 5.23), which was similar to the previous reports²⁵⁴. By using BT-Ph₂ as building block via similar bulk synthesis as for MOP-1, a polymer (MOP-1b) with a significantly lower surface area of 7 m²/g with an average pore diameter of 2.8 nm was obtained. This could be caused by the strong π - π stacking effect between the molecules of BT-Ph₂, which led to planer sheet-like rather than 3-D structure of the polymer. Another reason could be the low reactivity between BT-Ph₂ and FDA due to the electrophilic nature of BT-Ph₂ during the Friedel-Crafts alkylation reaction²⁵⁵. To overcome this, a successive cross-linking pathway was designed to improve the BET surface area of the polymer network. A significant increase of the BET surface area of 80 times was observed. The obtained polymer MOP-1 exhibited a surface area of 586 m²/g with a pore volume of 0.29 m³/g (Table 5.5). For MOP-0b and MOP-1, a similar pore size of ca. 1.5 nm was determined, indicating the microporous nature of all two polymers. By introducing the new successive cross-linking synthesis on the pure benzene-based polymer (MOP-0), a BET surface area of 1120 m²/g with a similar pore diameter of ca. 1.5 nm was determined (Figure 5.22). The pore size distribution of the successively cross-linked polymer MOP-0 appeared narrower than its counterpart (MOP-0b) via bulk synthesis (Figure 5.23), indicating a better formation of micropores in MOP-0. However, a small amount of mesopores were still formed for MOP-0. This could be caused by the high reactivity of the phenyl unit during the cross-linking process, leading to a rather quick and undefined network formation. A better effect on the narrow pore distribution can be found for MOP-1 (Figure 5.24-5.25), which could be caused by the lower reactivity of the monomers BT-Ph₂. ¹³C CP/MAS NMR spectroscopy (Figure 5.26-5.27) showed characteristic signals at about 40 ppm, which can be assigned to the methylene unit between the aromatic building blocks formed after cross-linking reaction. The chemical shifts between 110 and 140 ppm can be assigned to the aromatic carbons of the phenyl units in the polymer backbone. For MOP-1, the signals at about 152 ppm can be assigned to the adjacent carbons to the nitrogen atoms of the benzothiadiazole unit.

Table 5.5 Porosity data and electrochemical properties of the MOPs.

Polymer	S _{BET} (m ² /g)	Pore Diameter (nm)	Pore Volume (m ³ /g)	E _{oxi} (V)	E _{red} (V)	ΔE _{el} (V)
MOP-0	1120	1.5	1.90	1.86	-0.58	2.44
MOP-0b	1367	1.5	1.74	1.36	-0.42	1.78
MOP-1	586	1.5	0.29	1.75	-0.91	2.66
MOP-1b	7	2.8	0.003	1.34	-0.54	1.88

E_{oxi} = oxidation onset potential; E_{red} = reduction onset potential; ΔE_{el} = band gap determined via cyclic voltammetry.

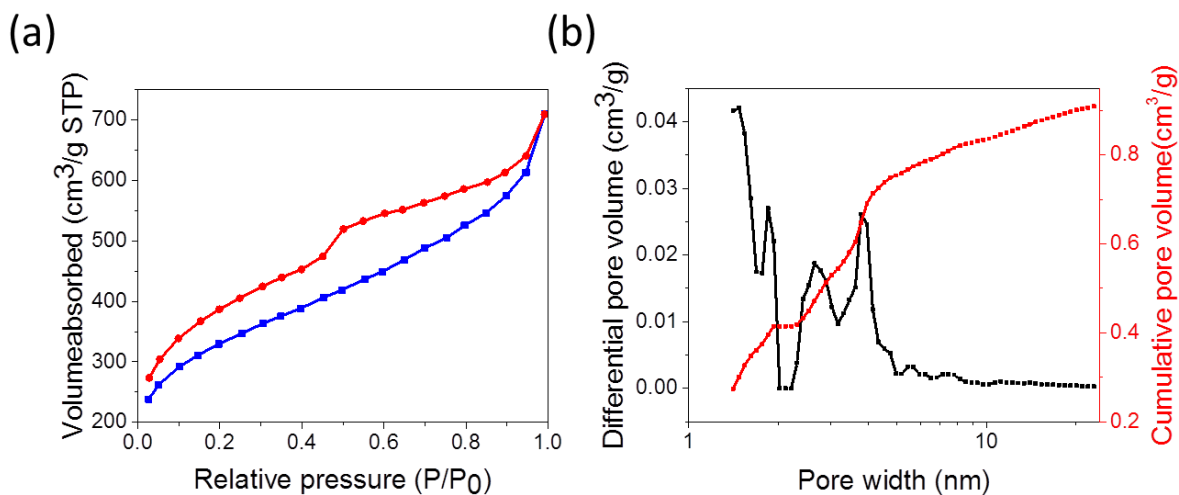


Figure 5.22 (a) N_2 sorption and desorption isotherms, and (b) pore size distributions of MOP-0.

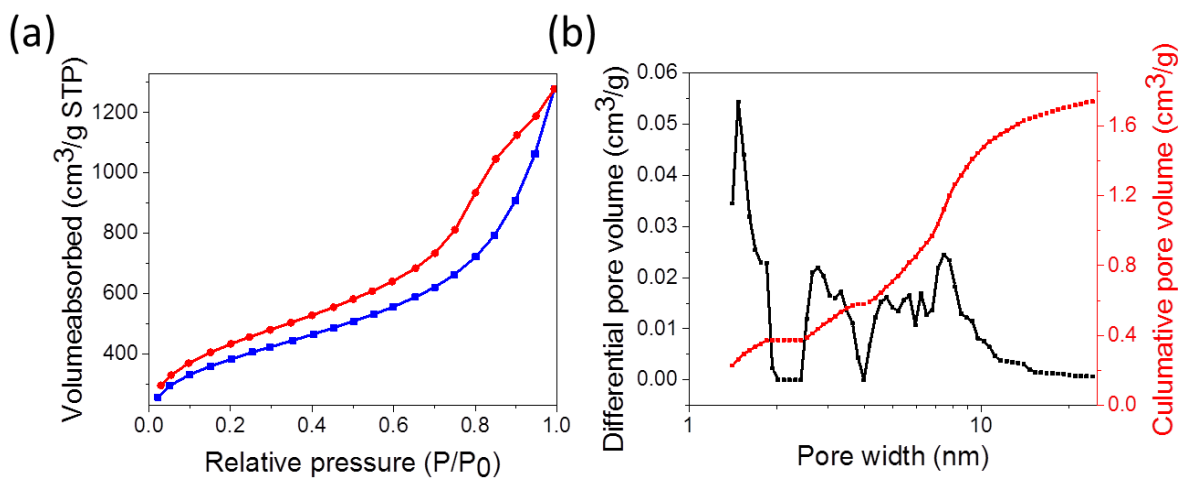


Figure 5.23 (a) N_2 sorption and desorption isotherms, and (b) pore size distributions of MOP-0b.

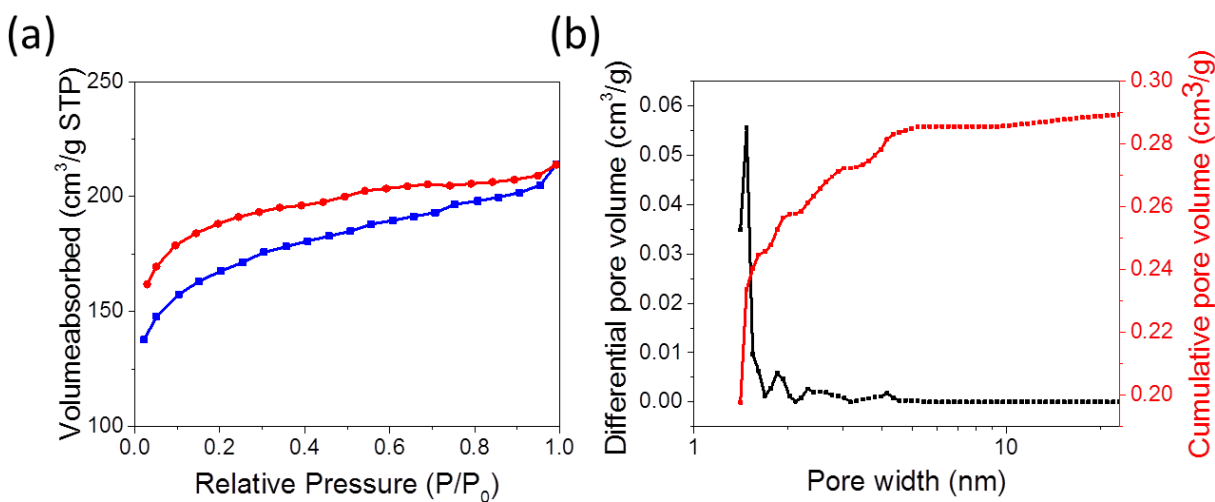


Figure 5.24 (a) N_2 sorption and desorption isotherms, and (b) pore size distributions of MOP-1.

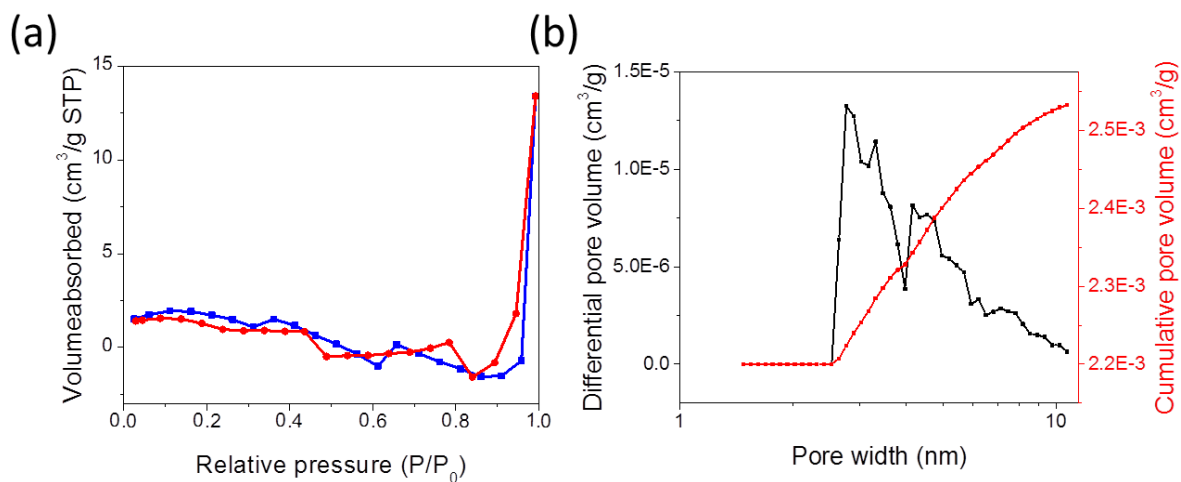


Figure 5.25 (a) N_2 sorption and desorption isotherms, and (b) pore size distributions of MOP-1b.

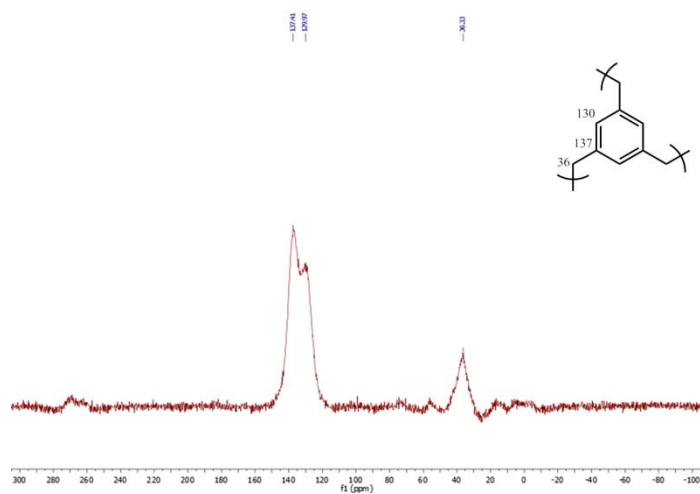


Figure 5.26 Solid state ^{13}C /MAS NMR spectrum with an idealized structure of MOP-0.

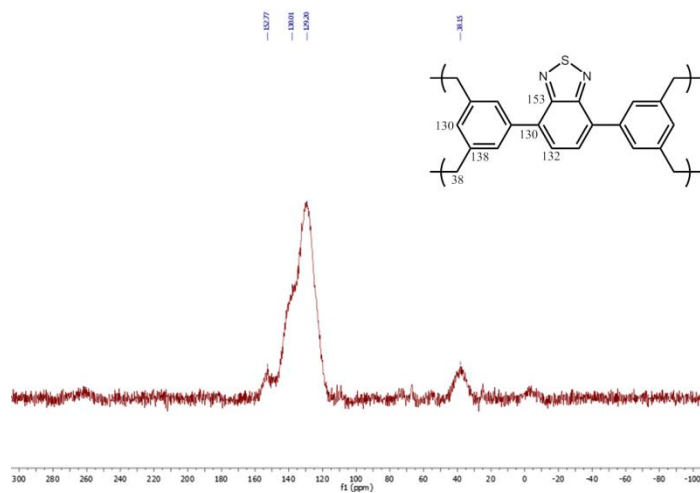


Figure 5.27 Solid state ^{13}C /MAS NMR spectrum with an idealized structure of MOP-1.

The FTIR spectra of the polymers were displayed in Figure 5.28(a). The signals at 1440, 1495 and 1595 cm^{-1} indicated the skeleton vibration of the aromatic rings in the polymers. The weak signals around 2930 and 1090 cm^{-1} could be attributed to C-H and C-O stretching mode, which could correspond to the structure of $-\text{CH}_2-$ and a minor amount of unreacted $-\text{CH}_2\text{OCH}_3$ remained in the polymer networks. In addition, the signals at 1348, 1377, 1567 and 1577 cm^{-1} were characteristic for the C=N and N-S stretching modes of the benzothiadiazole unit²⁵⁶.

The UV/Vis diffuse reflectance spectra (DRS) of the MOPs were displayed in Figure 5.28(b). Both polymers showed a broad absorption range. While MOP-0 showed broad absorption in the visible range up to 800 nm, the absorption band of MOP-1 ranged from the visible to the near infrared region (<1000 nm). Compared to their building blocks, the single phenyl unit and BT-Ph₂ (Figure 5.1), the absorption bands for both MOP-0 and MOP-1 exhibited a bathochromic shift. This could be caused by the formation of larger conjugated domains via direct oxidative coupling of the building blocks, which was likely an unavoidable side reaction in Fe(III)-catalyzed Friedel-Crafts alkylation reactions²⁵⁷. The red-shift of the absorption maximum for MOP-1 could be attributed to not only the introduction of acceptor unit but also the formation of larger conjugated domains.

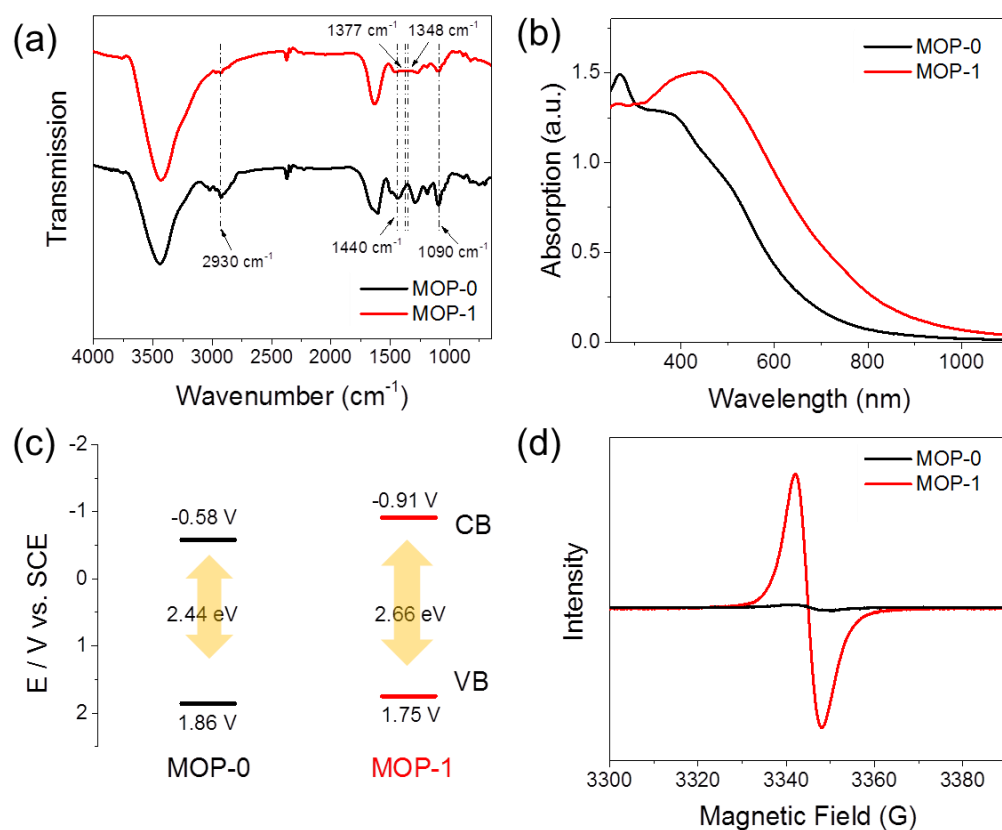


Figure 5.28 (a) FTIR spectra, (b) UV/vis DR spectra, (c) valence band (VB) and conduction band (CB) positions of the MOPs and (d) EPR spectra under light irradiation.

Cyclic voltammetry (CV) measurements revealed different oxidation and reduction onset potentials of the two polymers (Figure 5.28(c) and Figure 5.29-5.30), implying different valence band (VB) and conduction band (CB) positions of the MOPs. The VB and CB of MOP-0 lay at +1.86 V and -0.58 V vs. SCE, respectively. In comparison, the VB and CB positions of MOP-1 were at 1.75 V and -0.91 V vs. SCE. Additionally, the VB in the excited state for both MOP-0 and MOP-1 was further determined by ultraviolet photoelectron spectroscopy (UPS) measurement (Figure 5.31). The ionization potential for MOP-0 and MOP-1 were 5.76 eV and 6.67 eV, respectively, according to the calculation method in previous report²⁵⁸. Since the ionization potential was equivalent to the valence band of materials, giving an oxidation potential of 1.32 V vs. SCE for MOP-0 and 2.23 V vs. SCE for MOP-1, which were lower than value obtained from CV measurement, indicating low oxidation potentials in the excited state for both polymers. It was worth pointing out that the VB and CB positions of MOP-1, which contained the electron acceptor unit, benzothiadiazole, were comparable to the redox potentials of well-established transition metal complex photocatalysts such as $[\text{Ru}(\text{bpy})_3]^{3+}$ (+1.29 V vs. SCE) and $[\text{Ru}(\text{bpy})_3]^{2+}$ (-0.81 V vs. SCE)²⁵⁹. This might indicated a similar catalytic capability of the polymer for photoredox reactions.

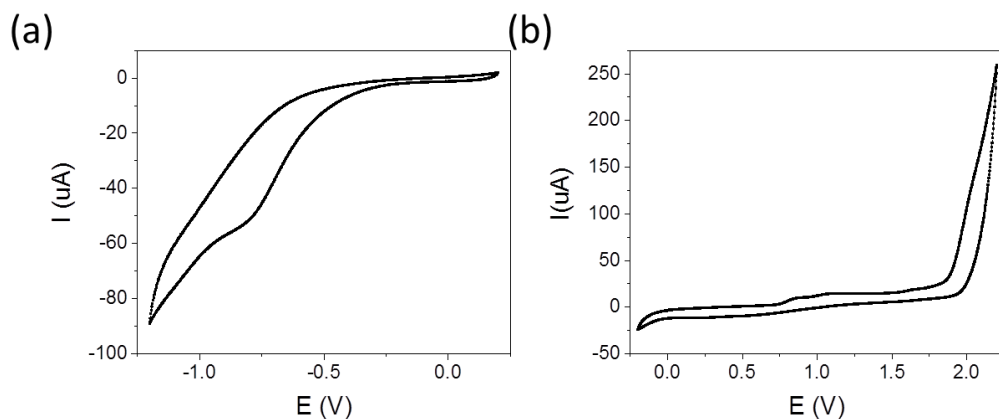


Figure 5.29 Cyclic voltammetry of MOP-0, (a) reduction cycle and (b) oxidation cycle.

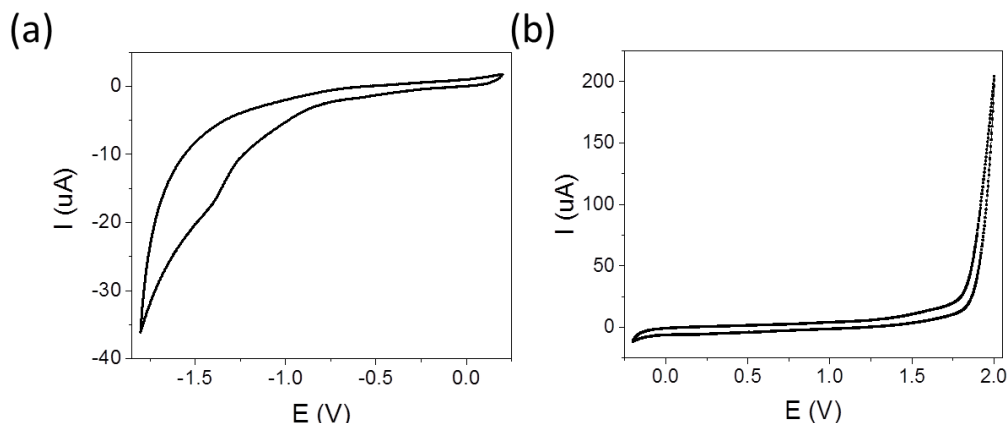


Figure 5.30 Cyclic voltammetry of MOP-1, (a) reduction cycle and (b) oxidation cycle.

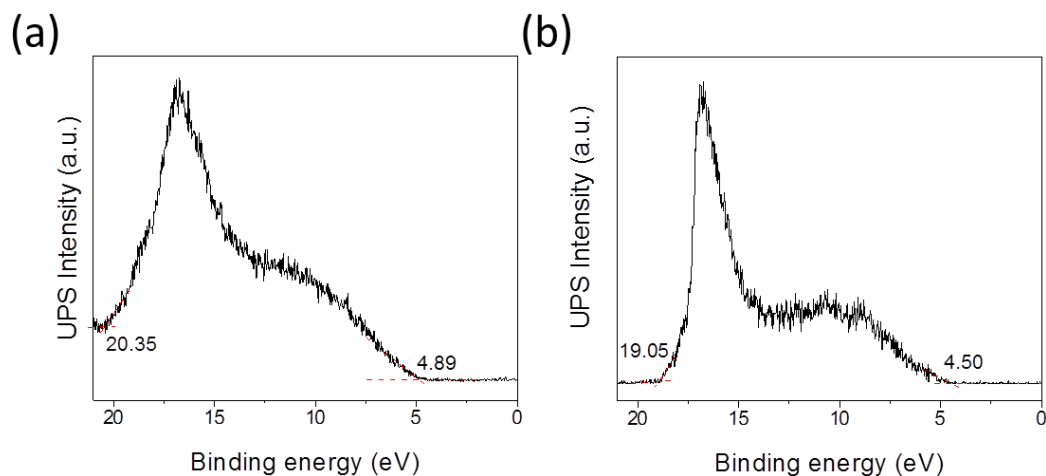


Figure 5.31 UPS spectra of MOP-0 (a) and MOP-1 (b). The dashed red lines mark the baseline and the tangents of the curve.

Electron paramagnetic resonance (EPR) spectra revealed a clear tendency of signal intensity for the two polymers both taken in dark and under light irradiation (Figure 5.28(d) and Figure 5.32). MOP-1 exhibited a more intense EPR signal than MOP-0, indicating that longer living electrons could be photogenerated in MOP-1 than in MOP-0. In addition, the EPR signals for MOP-1 gained a larger intensity increase (Figure 5.32(b)) under light irradiation compared to that taken in dark than that of MOP-0 (Figure 5.32(a)), demonstrating the structural influence on the stability of the photogenerated single electrons, i.e. radicals²⁶⁰. This indeed could lead to a more efficient catalytic activity of MOP-1 under light irradiation.

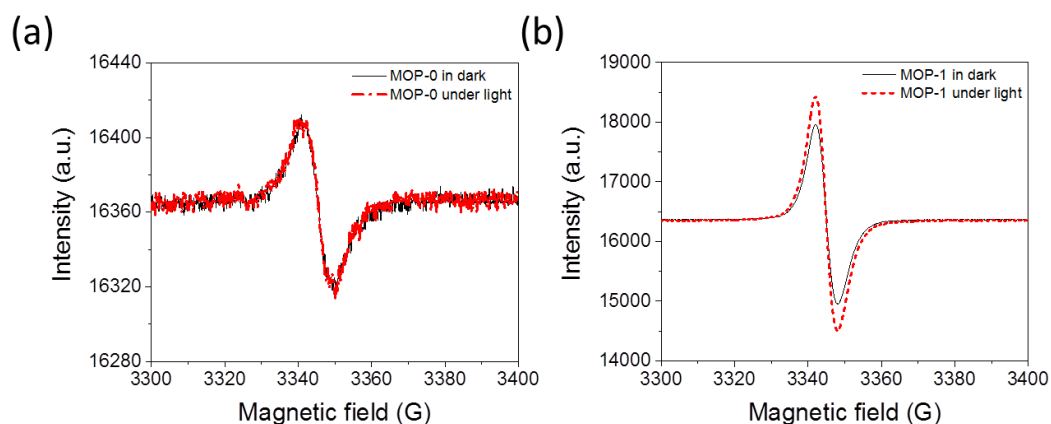


Figure 5.32 EPR spectra of MOP-0 taken in dark and under light irradiation.

Thermal gravimetric analysis (TGA) measurements showed that the polymer networks remained intact up to about 300°C under nitrogen (Figure 5.33). To note, the relatively high residual weight of the polymers of about 75% weight remained after heating to 800 °C, which could be a carbonized material.

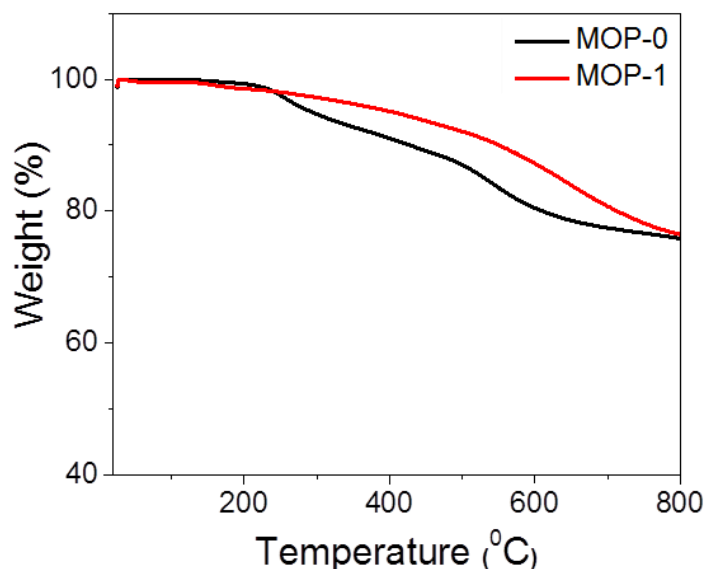


Figure 5.33 Thermogravimetric analysis of the MOPs.

5.2.3 Photocatalytic capacity test of MOPs for selective bromination on aromatic rings

For the photocatalytic bromination of aromatic compounds, we first chose 1, 2, 4-trimethoxybenzene (TMB) as the model substrate to investigate the catalytic activity of the two MOPs using HBr as the bromine source and molecular oxygen as a clean oxidant. As listed in Table 5.6, the bromination reaction of TMB catalyzed by MOP-1 achieved the higher conversion of over 90% (entry 2). As expected, the reaction catalyzed by MOP-0 only observed a low conversion of 35% (entry 1). The higher photocatalytic activity of MOP-1 also corresponded to the higher intensity of its EPR signal under light irradiation, which further proved that the longer living photogenerated electrons in MOP-1 played a vital role during the reaction. Additionally, the bulk-made polymer MOP-1b with a similar chemical structure as MOP-1 could only catalyze the bromination reaction with a conversion of 54% (entry 3), demonstrating that the high surface area of the MOPs as heterogeneous catalysts is mandatory to achieve a high catalytic efficiency.

To further study the reaction mechanism of the photocatalytic bromination reaction, several control experiments were conducted using MOP-1 as photocatalyst. As shown in Table 5.6, very low conversions of the reaction could be determined without using oxygen (entry 5) or light irradiation (entry 6), thus confirming the crucial role of light and oxygen during the reaction cycle. Under light, but without using MOP-1 as photocatalyst led to a reduced conversion of 16% (entry 4). To understand the specific role of the photochemical generated electron hole pairs during the catalytic bromination reaction, different hole and radical scavengers were added into the reaction mixture. The results were also listed in

Table 5.5. By adding KI as hole scavenger, only traces of the product was determined (entry 8). By adding CuCl₂ as electron scavenger, a reduced conversion of 40% was found (entry 7). This demonstrated the important role of photogenerated species in the MOPs. It was worth to mention that the photocatalytic bromination reactions tested here all achieved high selectivity.

Table 5.6 Screening and control experiments of the photocatalytic bromination of 1, 2, 4-trimethoxybenzene using the MOPs.^a

Entry	Catalyst	Light	Reaction condition variations	Conversion (%) ^b	Selectivity (%) ^b
1	MOP-0	+	-	35	>99
2	MOP-1	+	-	90	>99
3	MOP-1b	+	-	54	>99
4	-	+	no MOP	16	>99
5	MOP-1	+	No O ₂	14	>99
6	MOP-1	-	in dark	15	>99
7 ^c	MOP-1	+	electron scavenger	40	>99
8 ^d	MOP-1	+	hole scavenger	Trace	n.d.
9 ^e	MOP-1	+	superoxide scavenger	80	>99
10 ^f	MOP-1	+	singlet oxygen scavenger	29	>99
11 ^g	MOP-1	+	H ₂ O ₂ scavenger	94	>99
12 ^h	-	-	addition of H ₂ O ₂	94	>99

^aReaction conditions: [TMB] = 4 mM, [HBr] = 5 mM, acetonitrile 10 mL, MOPs 1 mg/ml, blue LED lamp (460 nm, 1.2 W/cm²), room temperature, 4 h. ^bConversion and selectivity determined by ¹H NMR. ^cCuCl₂ as electron scavenger. ^dKI as hole scavenger. ^e1,4-Benzoquinone as superoxide scavenger. ^fSodium azide as singlet oxygen scavenger. ^gCatalase as H₂O₂ scavenger. ^hEquivalent amount of H₂O₂ as TMB. n.d.: not determined.

According to previous reports, two active oxygen species, superoxide radical (O₂^{•-}) and singlet oxygen (¹O₂) could be generated using conjugated macromolecular systems as photocatalyst²⁶¹. To investigate the active oxygen species generated by using the MOPs, we then carried out the spin trap EPR experiments using 5,5-dimethyl-1-pyrroline N-oxide (DMPO) and 2,2,6,6-tetramethylpiperidine (TEMP) as superoxide and singlet oxygen trapping agents, respectively. As shown in Figure 5.34, both active oxygen species O₂^{•-} and ¹O₂ could be determined by using MOP-1 as photocatalyst. This could indicate that the two different oxygen species were generated by electrons of two possible excited states, i.e. the singlet and triplet states of the excited electrons, while O₂^{•-} was generated via singlet electron transfer (SET) of the singlet electrons and ¹O₂ was generated via energy transfer of the triplet electrons, respectively. To separately study the contribution of the two active oxygen species during the photocatalytic bromination reaction, we used first benzoquinone

as $O_2^{\bullet-}$ scavenger. A reduced conversion of 80% was determined (entry 9). The use of sodium azide as 1O_2 scavenger led to a conversion of 29% (entry 10). The results indicate that both activated oxygen species took part in the bromination process, with 1O_2 playing a significantly more dominant role than $O_2^{\bullet-}$ with a ratio of 70:20 for $^1O_2/O_2^{\bullet-}$ approximately. Based on our observations from the control experiments and mechanism study, we proposed a modified reaction mechanism similar to the literature¹²⁹.

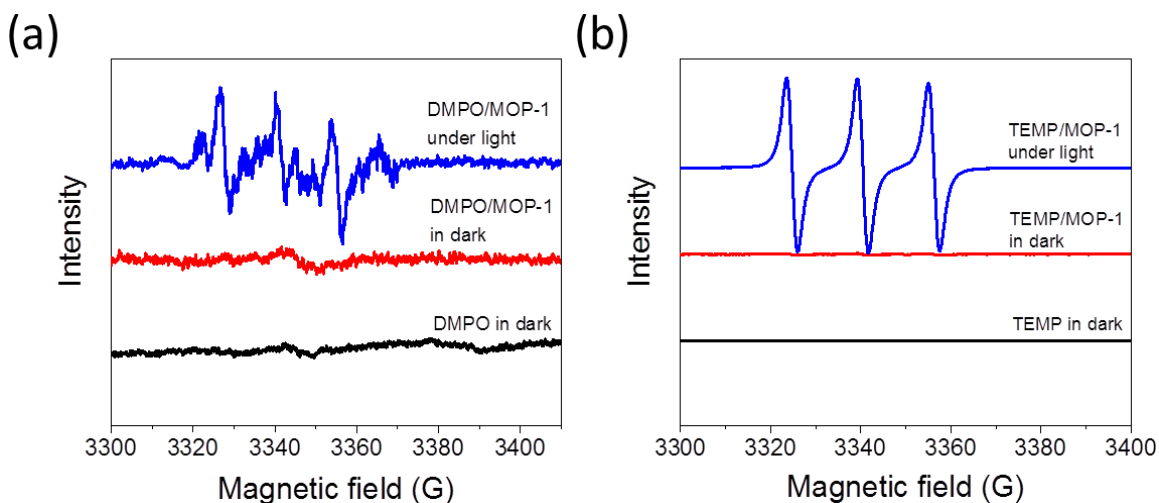


Figure 5.34 EPR spectra of DMPO- $O_2^{\bullet-}$ (a) and TEMP- 1O_2 adducts (b) using MOP-1 as photocatalyst in dark and under light irradiation.

The suggested reaction mechanism was illustrated in Figure 5.35. Under light irradiation, TMB was oxidized by the photogenerated hole of the MOPs and thus formed its cationic radical $TMB^{\bullet+}$, which reacted with the Br^- anion from HBr, leading to the formation of the $TMB^{\bullet}-Br$ radical as intermediate. Simultaneously, the photogenerated electron activated molecular oxygen to its active species $O_2^{\bullet-}$ and 1O_2 . The radical intermediate $TMB^{\bullet}-Br$ was then oxidized by both activate oxygen species separately, where $O_2^{\bullet-}$ likely formed first the highly reactive $\bullet O_2H$ species, which then oxidized the intermediate, while 1O_2 most likely oxidized the intermediate directly²⁶². The final bromide product 1-bromo-2,4,5-trimethoxybenzene and H_2O_2 as side product were formed. The formation of H_2O_2 could be determined by using the catalytic oxidation of N, N-diethyl-1,4-phenylenediammonium sulphate (DPD) by Horseradish peroxidase (POD)²⁶³. The concentration of H_2O_2 of about $94.5 \mu M$ in the original reaction mixture could be determined at a conversion of 50% (Figure 5.36). H_2O_2 , as reported previously, could also catalyze the bromination of TMB using HBr as the bromine source¹²⁹. This result showed that the obtained H_2O_2 could contribute to the oxidative bromination reaction of TMB as a minor side reaction. We then conducted another control experiment (entry 12) by adding extra H_2O_2 without photocatalyst. A high conversion of 94% for the brominated product was observed. By employing Catalase as H_2O_2 scavenger, the product was obtained with a similarly high

conversion of 94% (entry 11). To note, this was higher than the standard model reaction with a conversion of 90% (entry 2). This could be caused by the fact that the reaction equilibrium was shifted to the final product side while H_2O_2 as side product was “consumed” by the scavenger. The influenced of the equilibrium effect was rather predominant than the co-catalyzing effect of H_2O_2 itself. The oxidation onset potential of TMB was determined to be 0.89 V vs. SCE (Table 5.7), and the reduction potential of the $\text{O}_2/\text{O}_2^{\bullet-}$ lies at -0.57 V vs. SCE^{138,264}. The VB and CB positions of MOP-1 lay at 1.75 V and -0.91 V vs. SCE in the excited state, which were indeed sufficient for the photocatalytic oxidative bromination reaction of TMB. The monitoring experiment of the photocatalytic bromination reaction of TMB showed that the reaction rate slowed down after reaching a conversion of 80% after ca. 4 h. The exponential development indicated a reaction of second kinetic order (Figure 5.37). Additional experiments using HCl and HI as halide source were conducted. 1-chloro-2,4,5-trimethoxybenzene and 1-iodo-2,4,5-trimethoxybenzene were obtained as the chlorination and iodination products, demonstrating that the feasibility of the proposed reaction mechanism could be applied as a general photocatalytic halogenation method.

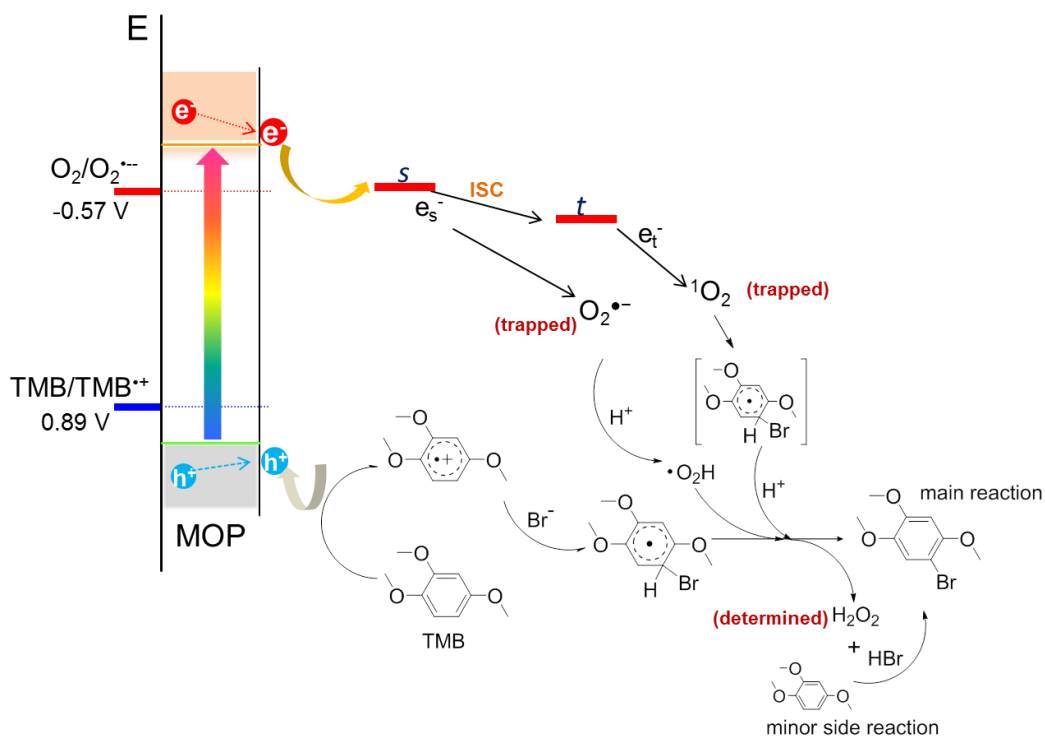


Figure 5.35 Suggested reaction mechanism of photocatalytic bromination of TMB using the MOPs as photocatalyst. s and t represent the singlet and triplet states of the excited electrons photogenerated in the MOPs. ISC: intersystem crossing.

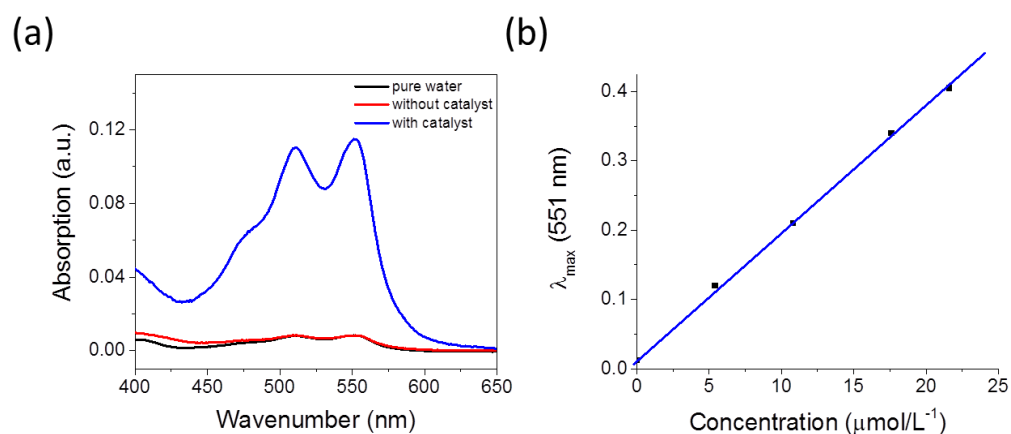


Figure 5.36 (a) UV-Vis absorption spectra of pure water and reaction system with or without catalyst after adding DPD and POD for H_2O_2 determination. (b) Standard curve of H_2O_2 concentration based on its absorption maximum at 551 nm. This method is based on the POD-catalyzed oxidation reaction of DPD by H_2O_2 , which gives the radical cation $\text{DPD}^{\bullet+}$. The radical cation can be easily determined by its two typical absorption peaks at ca. 510 and 551 nm.

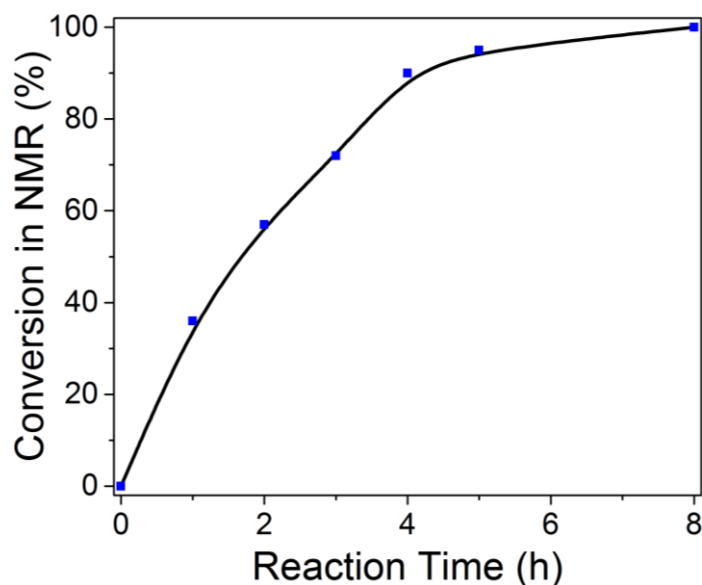


Figure 5.37 Monitoring experiment of the photocatalytic bromination reaction of TMB.

Additionally, repeating experiments were conducted using MOP-1 as photocatalyst and TMB as substrate. It showed that MOP-1 could be used for another 5 repeating cycles without significant change in its catalytic efficiency (Figure 5.38). Barely changes of the FTIR spectra of MOP-1 before and after the photocatalytic reaction were observed (Figure 5.39). Similar observation was obtained by the SEM and TEM images of MOP-1. It was

shown that the morphology of MOP-1 remained intact after the repeating experiments (Figure 5.40). This demonstrates the high stability and reusability of the polymer as heterogeneous photocatalyst.

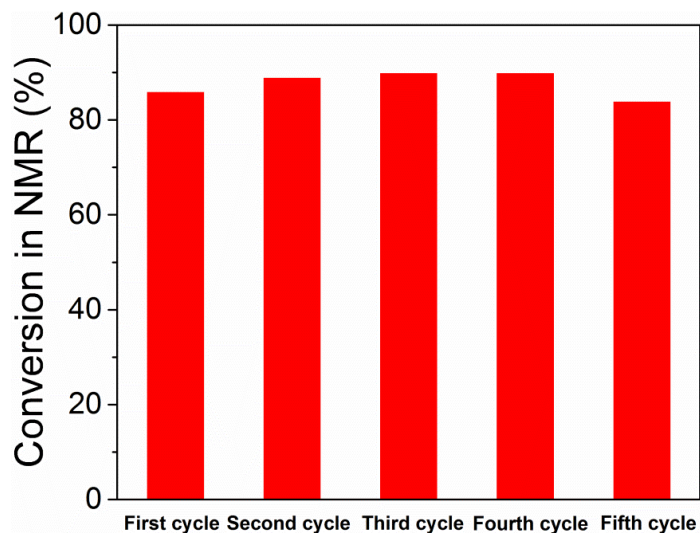


Figure 5.38 Repeating experiment of the photocatalytic bromination of TMB using MOP-1 as photocatalyst.

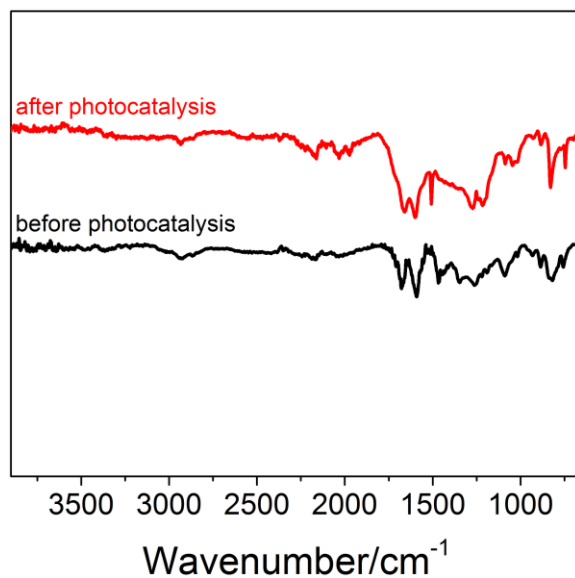


Figure 5.39 FTIR spectra of MOP-1 before (black) and after (red) 5 repeating cycles of the photocatalytic bromination of TMB.

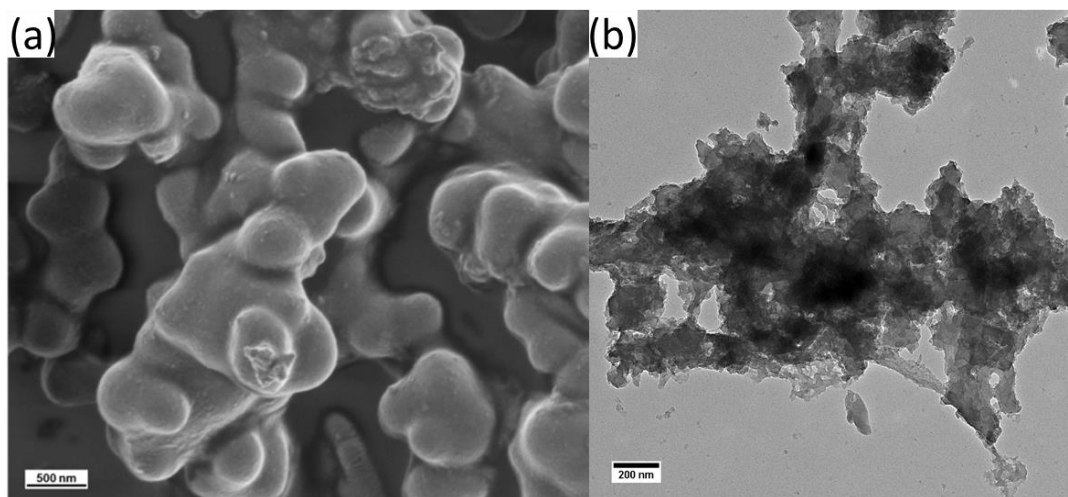
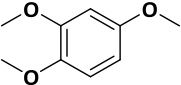
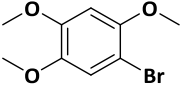
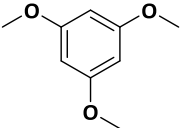
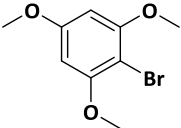
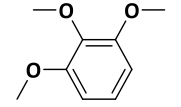
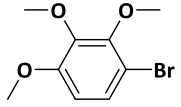
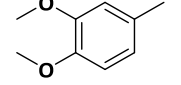
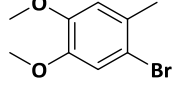
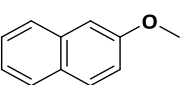
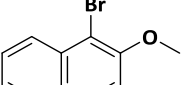
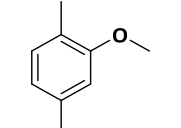
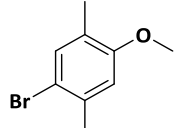
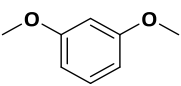
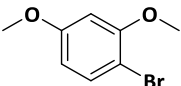
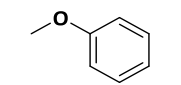
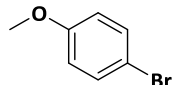
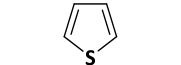
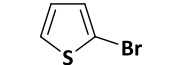
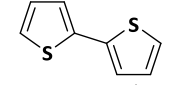
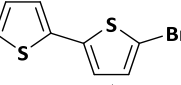
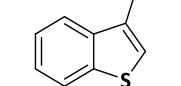
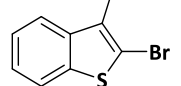
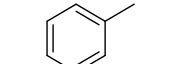
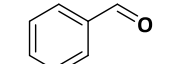


Figure 5.40 SEM and TEM images of MOP-1 after 5 repeating cycles of the photocatalytic bromination of TMB.

To further demonstrate the general feasibility of MOP-1 as photocatalyst, extensive investigation of the bromination reaction with various substituted phenyl rings and further electron-rich aromatic compounds thiophene derivatives was carried out under similar reaction conditions. Moreover, the oxidation onset potentials of the aromatic compounds were determined by cyclic voltammetry. The results were listed in Table 5.7. In most cases, high conversion and selectivity were achieved. The overall trend was that high oxidation potential of the aromatic compounds led to low conversion of the brominated products. For example, anisole ($E_{\text{oxi}} = 1.51 \text{ V vs. SCE}$) could be only brominated with a low conversion (63%) after an extended reaction time of 36 h (entry 8). However, an absolutely clear tendency of the oxidation potential to the reaction conversion or yield was not observed. The selectivity, in comparison, was found to be dependent on the substitute on the aromatic rings. It could be determined that methyl substitute on the aromatic ring led to lower selectivity of the bromination reaction (entry 4 and 6). Aromatic aldehydes were determined as a competitive side product. This could be caused by oxidation of toluene derivatives to the corresponding aldehyde by the active oxygen species, as previously reported¹²⁷. Other electron-rich thiophene derivatives such as thiophene and 3-methylbenzo[b]thiophene (entries 9 and 11) showed also high selectivity during the bromination reaction. With bithiophene (entry 10) with a rather low oxidation potential (1.18 V vs. SCE), dibromide was determined as a minor side product. The bromination reaction of toluene (entry 12) as an electron-deficient substrate did not occur, which could be caused by its high oxidation potential of ca. 1.98 V vs. SCE. The fact that only traces of benzaldehyde was determined as product could indicate that during the reaction only the methyl group was likely oxidized instead of the phenyl ring. This could lead to the reaction of its cation radical with oxygen, obtaining the final aldehyde product (Figure 5.41).

Table 5.7 Scope of the photocatalytic bromination of aromatic compounds using MOP-1 as photocatalyst under visible light.^a

Entry	Substrate	Product	Conversion (%) ^b	Yield (%) ^c	Selectivity (%)	Time (h)	E_{oxi} (V) ^d
1			96	89	>99	8	0.89
2			>99	82	90 ^e	12	1.34
3			58	50	>99	14	1.28
4			>99	75	80 ^f	10	1.15
5			>99	84	>99	15	1.26
6			>99	55	63 ^g	8	1.32
7			90	81	>99	10	1.32
8			63	55	>99	36	1.51
9			99	70	>99	14	1.63
10			>99	80	85 ^h	6	1.18
11			90	85	>99	18	1.35
12			4	-	>99	24	1.98

^aReaction conditions: [substrate] = 16 mM, [HBr] = 20 mM, acetonitrile 10 mL, MOP-1 10 mg, blue LED lamp, room temperature. ^bConversion determined by NMR measurement. ^cIsolated yield. ^d E_{oxi} (V vs. SCE) = oxidation onset potential of substrates determined by cyclic voltammetry. ^eMinor side product determined as the dibromide compound (ca. 10%). ^fSide product determined as 3,4-dimethoxy-benzaldehyde (ca. 20%). ^gMinor side products determined as aldehydes and dibromide. ^hMinor side product determined as the dibromide compound (ca. 15%).

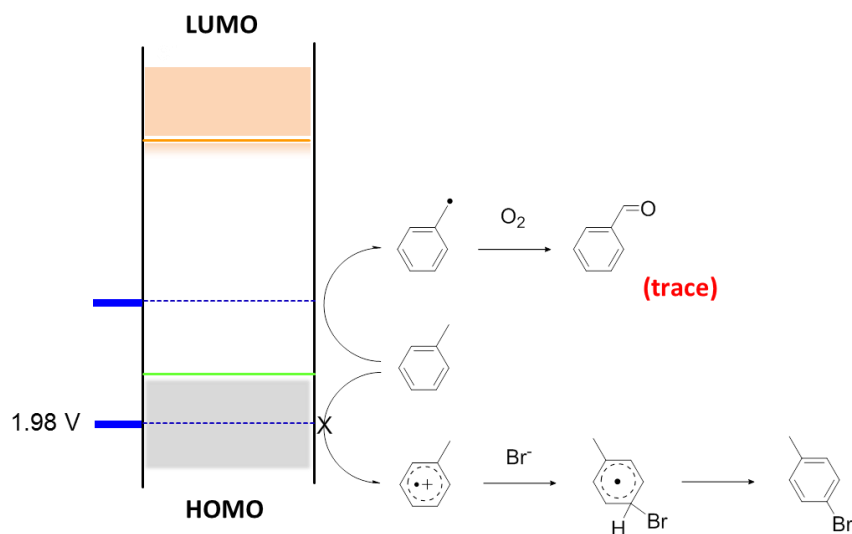


Figure 5.41 Suggested mechanisms for the formation of benzaldehyde instead of *p*-bromotoluene with toluene being as reactive substrate due to the high oxidation potential of toluene (1.98 V vs. SCE).

5.2.4 Conclusion and outlook

As a conclusion for this chapter, we demonstrated a simple, transition metal-free synthetic pathway to form highly porous crosslinked polymers containing photoactive conjugated organic semiconductor units as pure organic, heterogeneous photocatalysts for selective bromination of electron-rich aromatic compounds using HBr as the bromine source and oxygen as the clean oxidant under visible light irradiation. The polymers showed high catalytic efficiency and reusability. A mechanism study was carried out to demonstrate the mandatory roles of the photogenerated electron-hole pairs and both active oxygen species, superoxide and singlet oxygen during the catalytic cycle. We hope that this study can present this new class of pure organic, visible-light active, highly stable and reusable heterogeneous photocatalyst as an alternative to the metal-based catalytic systems with high potential in broader application fields.

5.3 Photocatalytic regio- and stereo-Selective [2+2] cycloaddition of styrene derivatives using a heterogeneous organic photocatalyst

This subchapter is based on the publication “Photocatalytic regioselective and stereoselective [2 + 2] cycloaddition of styrene derivatives using a heterogeneous organic”, *ACS Catalysis*, 2017, 7, 3097-3101. In the previous chapter, benzothiadiazole was introduced into non-conjugated microporous polymer matrix. In this subchapter, we knit the benzothiadiazole chromophore into a fully conjugated polymer system. The introduction of benzothiadiazole into a fully conjugated polymer matrix could not only endow the photocatalyst with heterogeneous nature but also tailor the energy band gap and promotes the separation of electron-hole pairs.

5.3.1 Motivation

Strained carbocyclic molecules, especially cyclobutane derivatives, have gained increasing attentions in the past decades due to their role as important molecular building motifs and intermediates for the synthesis of natural products and pharmaceuticals²⁶⁵⁻²⁶⁷. Certain cyclobutane derivatives such as endiandrin A, di-*O*-methylendiandrin A and magnosalin are regarded as potent binders for glucocorticoid receptor, which plays a critical role in the treatment of inflammatory conditions²⁶⁸. Up to now, various preparative strategies have been developed to obtain cyclobutane derivatives. Beside the ring expansion of cyclopropanes^{269,270}, [2+2] cycloaddition reaction of alkenes has been widely applied for the synthesis of cyclobutane-containing products. Conventionally, [2+2] cycloaddition is activated under thermal conditions, which also involves precisely designed catalysts such as Lewis acids²⁷¹, amines²⁷², or transition metals²⁷³. However, a disadvantage of the thermally activated [2+2] cycloaddition is that high reactions yields can only be obtained using polarized alkenes. More specifically, the two alkenes as cycloaddition partners should either be electrophile or nucleophile, respectively, to match the frontier molecular orbitals of reactants²⁷⁴. This requirement limits a wider application field of the thermal cycloaddition reactions.

Photocycloaddition, in comparison, has been successfully employed as a useful tool for the synthesis of cyclobutane-containing products in recent years^{275,276}. Especially low energetic visible light-driven [2+2] cycloaddition has been reported either for electron-rich alkenes⁷², or electron-deficient olefins²⁷⁷. So far, the photocatalytic systems used were mainly based on transition metal^{4,278}. Very few molecular organic photocatalysts have been reported for [2+2] cycloaddition reaction¹¹⁷. Nevertheless, considerable drawbacks are still associated to the noble metal-containing systems including rareness in the nature, toxicity, high price and common low stability due to photobleaching effect for small molecular metal

or non-metal catalytic systems. To overcome these limitations, an alternative photocatalytic system is indeed needed.

Organic semiconductor-based photocatalysts offer a more sustainable and environmentally friendly alternative due to their pure organic nature, highly tunable electronic and optical properties via molecular design or morphology engineering. Recent studies show that either small molecules^{189,212,279} or macromolecular^{147,151-153,161,162,168,170,176,183,216,252} systems have been employed as efficient photocatalysts for visible light-promoted reactions. Nevertheless, cycloaddition reactions using organic semiconductors are still unknown.

In this chapter, we report the use of a pure organic photocatalyst based on a conjugated microporous polymer network poly(benzothiadiazole) (B-BT) as photocatalyst for the [2+2] cycloaddition of styrene derivatives under the irradiation of visible light. Both homo- and unsymmetrical cycloaddition reactions could be performed with high conversion and selectivity. A mechanistic study on the reaction insights is described. In addition, some natural products, such as di-*O*-methylendiandrin A and endiandrin A are also synthesized with a high catalytic selectivity.

5.3.2 Synthesis and characterization of B-BT

B-BT (Figure 5.42(a)) was synthesized via Sonogashira-Hagihara cross-coupling of 4,7-dibromo-benzo[c][1,2,5]thiadiazole with 1,3,5-triethynylbenzene similar to a previous report¹⁶¹. The scanning electron (SEM) and transmission electron microscopy (TEM) images (Figure 5.42(b) and 5.42(c)) showed a fiber-shaped structure with a diameter of ca. 200 nm. The FTIR spectrum (Figure 5.42(d)) showed typical signals at 1348, 1377, 1567, and 1577 cm^{-1} , which were characteristic for C=N and N-S stretching modes in the benzothiadiazole moiety. The signals at around 2200 cm^{-1} and 3300 cm^{-1} indicated the C \equiv C and alkynyl C-H stretching modes, respectively. The signals at 1440, 1495, and 1600 cm^{-1} can be assigned to the skeleton vibration of aryl rings in the polymer. ¹³C solid-state cross-polarization magic angle spinning (CP/MAS) NMR spectrum (Figure 5.43) showed characteristic signals at 154 ppm, which can be assigned to the adjacent carbon to nitrogen atoms in the benzothiadiazole unit. The resonance peak between 110 and 140 ppm were attributed to aromatic carbons, and the signals from 80 to 100 ppm can be assigned to the carbon of the triple bond. The Brunauer-Emmet-Teller (BET) surface area of B-BT was found to be 120 m^2/g with a pore volume of 0.12 m^3/g (Figure 5.44).

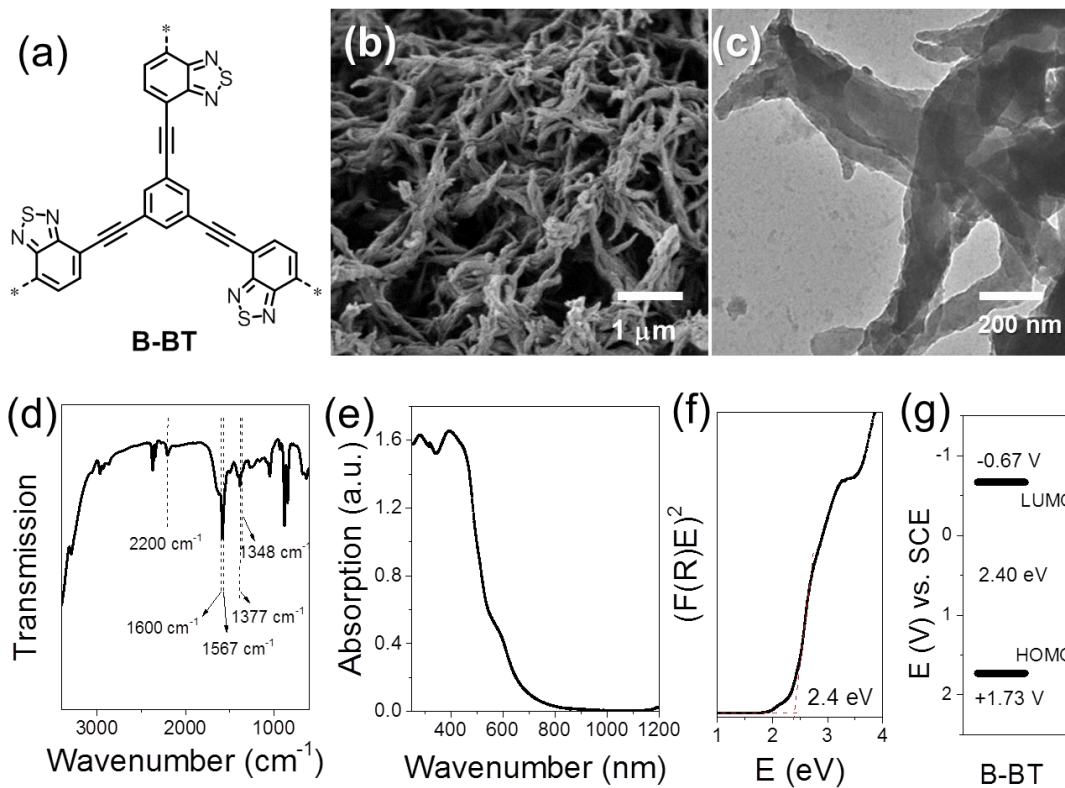


Figure 5.42 (a) Chemical structure, (b) SEM and (c) TEM image, (d) FTIR, (e) UV/Vis DR spectra, (f) Kubelka-Munk plot, and (g) HOMO and LUMO band positions of B-BT.

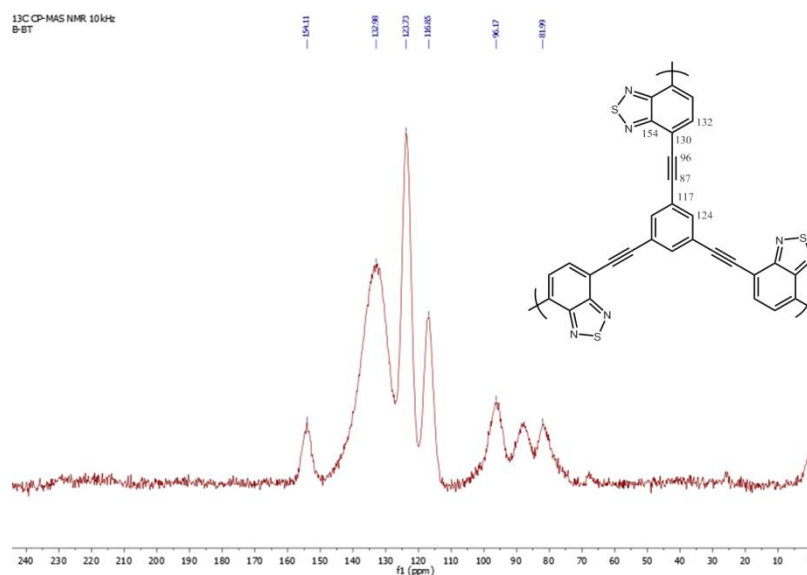


Figure 5.43 Solid-state ^{13}C CP-MAS NMR spectrum of B-BT.

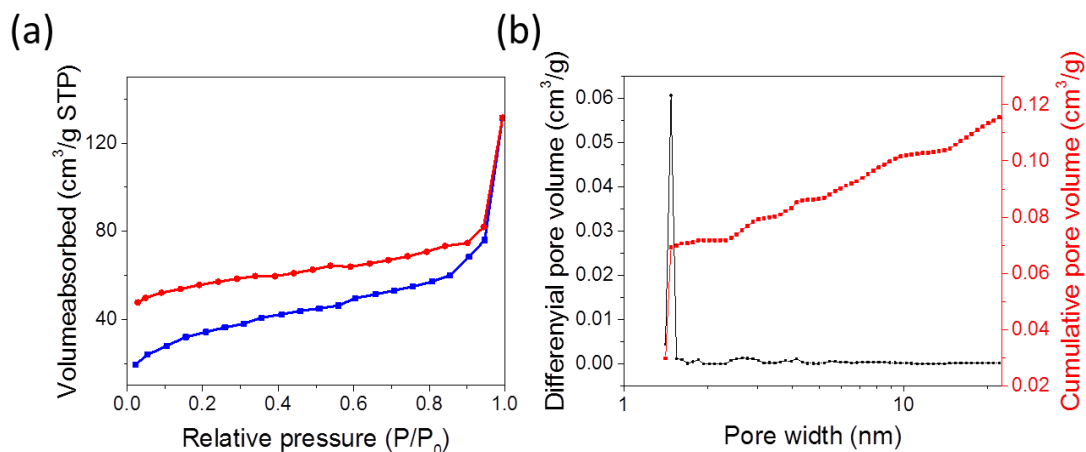


Figure 5.44 (a) N_2 sorption and desorption isotherms, and (b) pore size distributions of B-BT.

The UV/vis diffuse reflectance spectrum (DRS) of B-BT (Figure 5.42(e)) showed a maximum absorption at 395 nm with a broad absorption range up to 800 nm. An optical band gap of 2.4 eV could be derived from the Kubelka-Munk function (Figure 5.42(f)). Cyclic voltammetry measurement revealed the lowest occupied molecular orbital (LUMO) position of B-BT) at -0.67 V vs. SCE (Figure 5.45(a)). The highest unoccupied molecular orbital (HOMO) position at +1.73 V vs. SCE could be thus derived from the optical band gap. Additionally, the HOMO level in the excited state was determined via ultraviolet photoelectron spectroscopy (UPS) (Figure 5.45(b))²⁵⁸. An ionization potential could be calculated to be 7.07 eV, resulting in a HOMO level at 2.39 V vs. SCE in the excited state. This value was higher than that obtained from CV measurement, indicating a strong oxidizing character of the organic photo-catalyst B-BT. To study the photo-induced electron/hole charge separation, we then conducted electron paramagnetic resonance (EPR) and photocurrent measurements. The EPR spectra showed an enhanced signal after light irradiation compared to the signal reordered in dark (Figure 5.46(a)), indicating the existence of photo-generated single electrons (i.e. radicals)²⁶⁰. The photocurrent test illustrated a response for light-on and -off event, indicating an efficient light-induced electronic conductivity, as well as charge separation and charge transfer inside B-BT (Figure 5.46(b)). Furthermore, thermal gravimetric analysis (TGA) revealed that B-BT could remain intact up to 400 °C at nitrogen atmosphere (Figure 5.47). The residual weight of 75% might be attributed to the carbonized material.

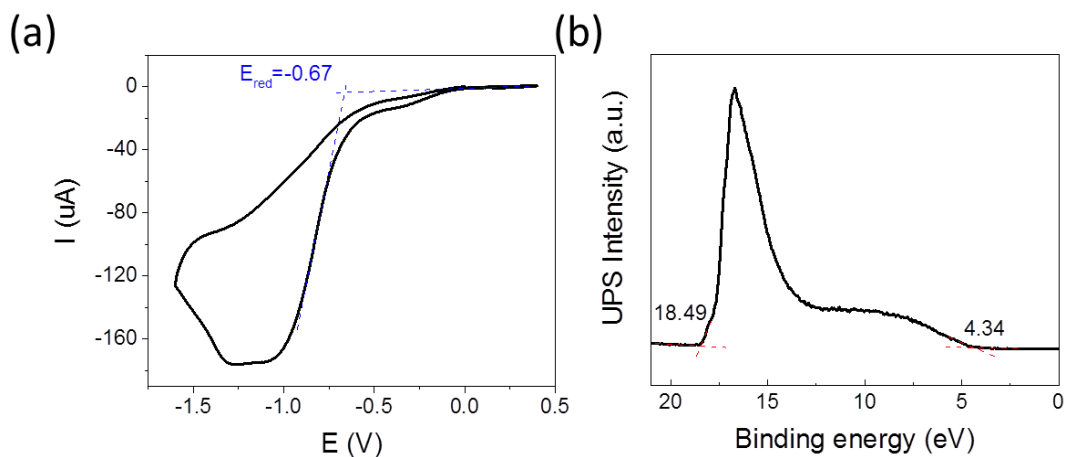


Figure 5.45 (a) Cyclic voltammetry of B-BT in the reduction cycle and (b) ultraviolet photoelectron spectroscopy (UPS) of B-BT. The dashed red lines mark the baseline and the tangents of the curve.

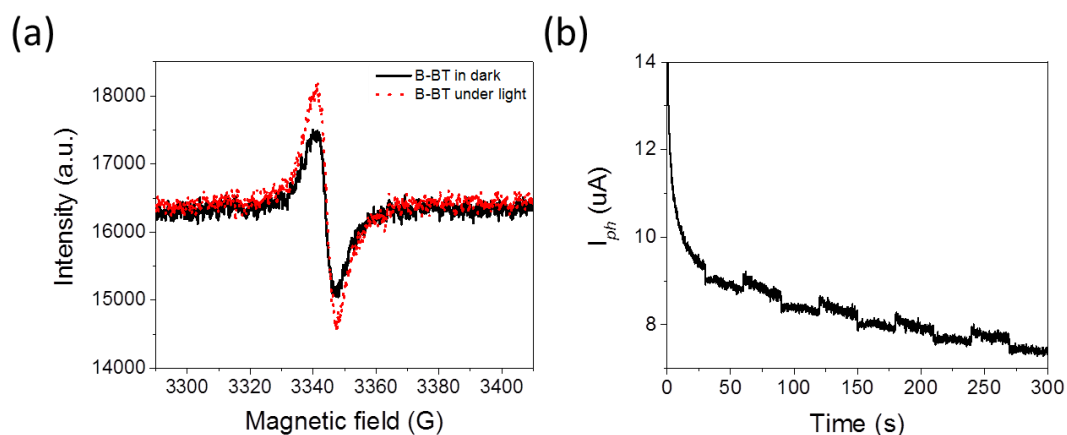


Figure 5.46 (a) EPR spectra of B-BT taken in dark and after light irradiation for 20 min, and (b) photocurrent responses upon switching the light on and off (blue LED, $\lambda=460$ nm).

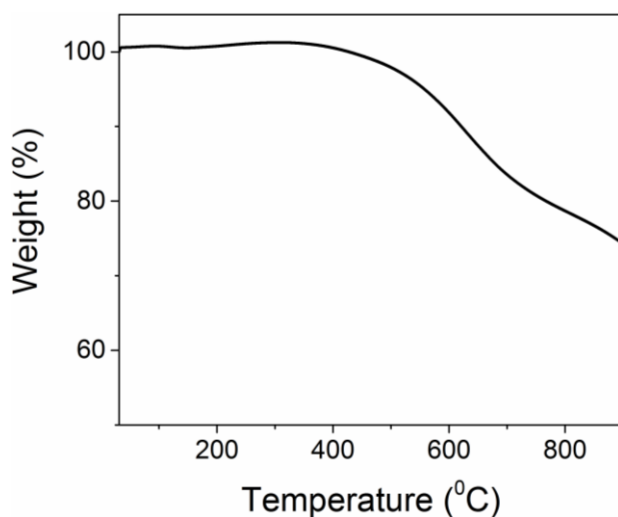
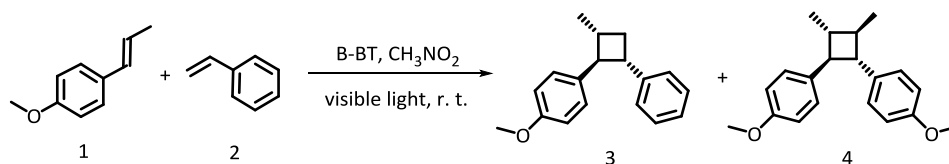


Figure 5.47 Thermogravimetric analysis of B-BT.

5.3.3 Photocatalytic [2+2] cycloaddition with the obtained photocatalyst B-BT

To test the visible light-promoted photocatalytic activity of B-BT, the [2+2] cycloaddition between (*E*)-1-methoxy-4-(prop-1-en-1-yl) benzene (commercial name: *trans*-anethole) was chosen as model reaction. Both homo- and unsymmetrical cycloaddition either with or without the addition of styrene as coupling partner were investigated respectively. As listed in Table 5.8, both homo- and unsymmetrical cycloaddition reactions showed a high conversion and selectivity (entries 1 and 7). Control experiments conducted in dark (entries 3 and 9), or without using B-BT as photocatalyst led only to trace conversions, demonstrating the essential roles of light and the photocatalyst. Furthermore, various solvents (entries 11-14) were investigated and nitromethane was found with highest conversion while in dimethyl sulfoxide and toluene no product was detected.

Table 5.8 Screening and control experiments of the [2+2] cycloaddition using B-BT as photocatalyst.^a



Entry	1	2	Light	Reaction condition variations	Ratio (3/4)	Conversion (%) ^b
1	+	-	+	-	-	86
2	+	-	+	No B-BT	-	5
3	+	-	-	In dark	-	Trace
4	+	-	+	In N ₂	-	40
5 ^c	+	-	+	Electron scavenger	-	38
6 ^d	+	-	+	Hole scavenger	-	Trace
7	+	+	+	-	>15:1	92
8	+	+	+	No B-BT	-	4
9	+	+	-	In dark	-	Trace
10	+	+	+	In N ₂	15:1	60
11	+	+	+	In DCM	>20:1	10
12	+	+	+	In acetonitrile	>20:1	15
13	+	+	+	In DMSO	-	Trace
14	+	+	+	In toluene	-	Trace
15 ^c	+	+	+	Electron scavenger	>15:1	56
16 ^d	+	+	+	Hole scavenger	-	trace

^aStandard reaction conditions: [anethole]=0.1 M, [styrene]=0.5 M, [B-BT]= 1 mg/ml, CH₃NO₂: 2.4 ml, blue LED lamp (460 nm, 0.26 W/cm²), room temperature, air, 8h. ^bConversion determined by GC-MS. ^cCuCl₂ as electron scavenger. ^dKI as hole scavenger.

To reveal the mechanistic insights and the specific roles of the photo-generated electron/hole pair during the [2+2] cycloaddition process, electron and hole scavengers were added into the reaction mixture for both homo- and asymmetry cycloadditions. With the addition of KI as hole scavenger, only trace conversion was observed for both reactions (entry 6 and 16), indicating the essential role of hole for formation of product²⁸⁰. By adding CuCl₂ as electron scavenger, reduced conversions were observed (entries 5 and 15). The same phenomenon was observed by excluding oxygen from the reaction atmosphere (entries 4 and 10). The result indicated that the electron-activated superoxide radical (O₂^{•-}) as active species could play an accelerating role for the cycloaddition, similar to previous reports²⁰⁸. An additional control experiment using 5,5-dimethyl-1-pyrroline N-oxide (DMPO) as superoxide radical trapping agent showed typical EPR patterns for DMPO-O₂^{•-} adducts (Figure 5.48(a)).

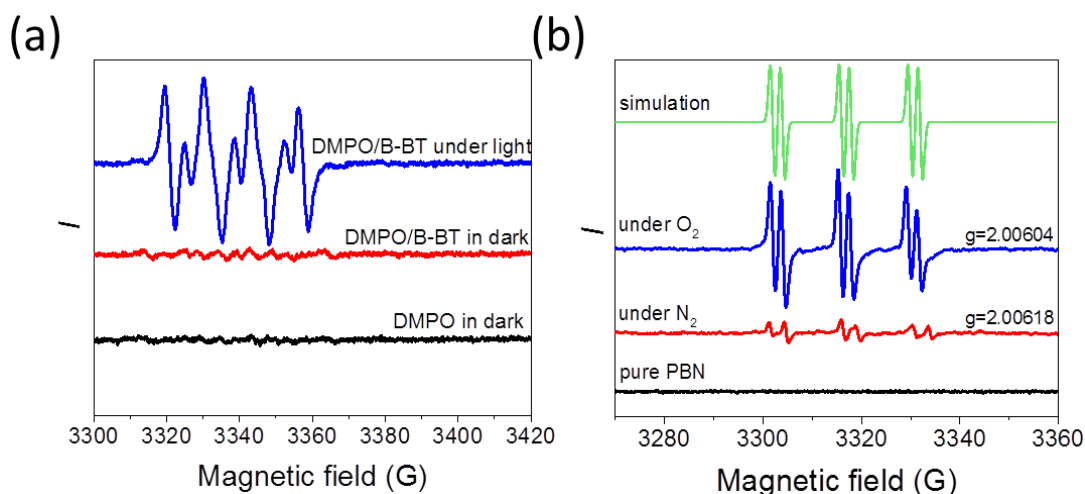


Figure 5.48 (a) EPR spectra of DMPO-O₂^{•-} adducts with B-BT as photocatalyst in dark or under blue light irradiation ($\lambda = 460$ nm, 1.2 W/cm²). (b) EPR spectra using PBN as radical trapping agent for the radical intermediate of anethole under light irradiation. Pure PBN (black); PBN with anethole and B-BT under N₂ atmosphere (red); and under O₂ (blue); simulated EPR pattern of the trapped radical (green).

Cyclic voltammetry measurement showed that the oxidation potential of anethole lay at 1.17 V vs. SCE, which made its direct oxidation by the photo-generated hole of B-BT ($E_{\text{oxi}} = 1.73$ V vs. SCE) possible²⁸¹. Based on the observations, we proposed a reaction mechanism similar to previous reports⁷². As illustrated in Figure 5.49, the catalytic process could occur via three different routes. Under visible light irradiation, *trans*-anethole was oxidized by the photo-generated hole of B-BT to form its cationic radical intermediate **a**, which then reacted with another equivalent olefin (anethole for homo- or styrene for unsymmetrical [2+2] cycloaddition) to generate the radical intermediate **b**. In the following three possible routes, the intermediate **b** can either receive one electron from the photo-generated electron (i), the activated superoxide O₂^{•-} (ii), or another anethole molecule (iii), and thus

led to the formation of the final product. According to previous reports^{72,282,283}, the reaction between the cationic radical **a** and alkene derivatives, here styrene, should first form a trapezoidal cyclobutane cation radical intermediate with a long-bond structure, where the σ bond was formed preferred to the β carbon rather than the α carbon of styrene. Therefore, the cycloaddition between the cation radical **a** and styrene is sterically more favored than that with another anethole unit. This would explain the favored selective formation of the unsymmetrical cycloaddition product in contrast to the minimal amount of the homo-cycloaddition of anethole. In addition, oxygen could also stabilize some specific intermediates which might part of reason that oxygen could facilitate the reaction conversion³⁹. Further proof of the formation of the radical intermediate **a** could be observed using N-tert-butyl- α -phenylnitron (PBN) as radical trapping agent (Figure 5.48(b)). A typical pattern for PBN-trapped radical could be recorded, which corresponded well to its simulation. The enhanced signal intensity taken under oxygen atmosphere indicates that oxygen played an important role within the photocatalytic cycle.

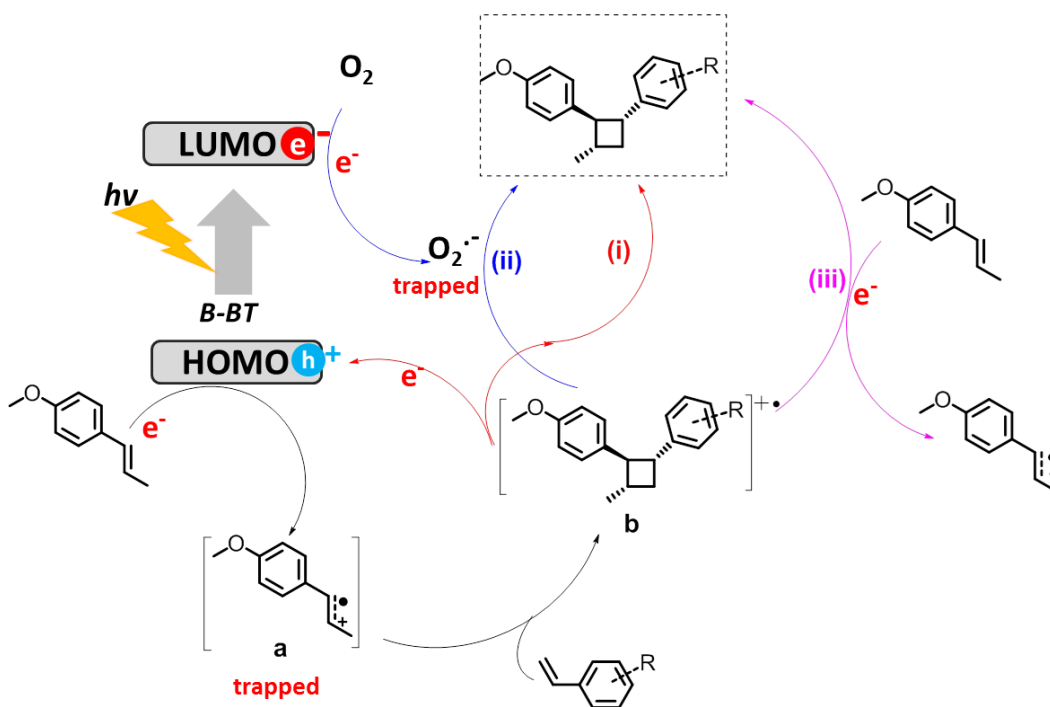


Figure 5.49 Proposed reaction mechanisms for the photocatalytic [2+2] cycloaddition using B-BT via 3 possible routes.

To further test the general feasibility of B-BT as photocatalyst, an extensive investigation of [2+2] cycloaddition with various styrene derivatives was conducted with the optimized reaction conditions. As illustrated in Figure 5.50(a), high conversion and selectivity were obtained in most cases. Both electron-donating substitution groups on the phenyl rings of the substrates such as methyl, methoxy, or dimethoxyl and electron-withdrawing

substitution groups such as ester or halides did not affect the conversion and selectivity. In addition, cycloaddition of anethole with methyl-substituted styrene on *ortho*, *meta*, or *para* positions generally occurred with high efficiency. Cycloaddition of other anethole derivatives with different substitution groups on the alkene such as isomethyleugenol also achieved with high conversion and selectivity. It was worth to note that the catalytic efficiency of the organic photocatalyst B-BT was comparable with that of the traditional transition metal complexes such as Ru(bpy)₃Cl₂ and *fac*-Ir(ppy)₃⁷². Moreover, the repeating experiment was also conducted for both homo- and crossed cycloaddition reactions with a slight decrease of conversion, which might be caused by the catalyst loss during recovery process (Figure 5.51). No considerable changes from the FTIR (Figure 5.52), SEM and TEM images (Figure 5.53) were observed, showing the stability of B-BT.

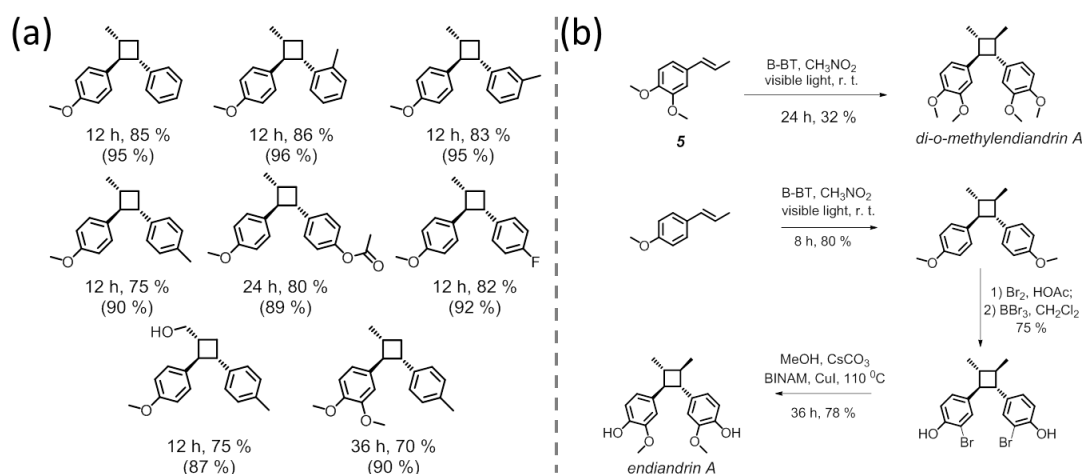


Figure 5.50 (a) Scope of the [2+2] cycloaddition reactions; the value in parentheses indicates the selectivity of unsymmetrical products compared with dimers. (b) Some natural products obtained.

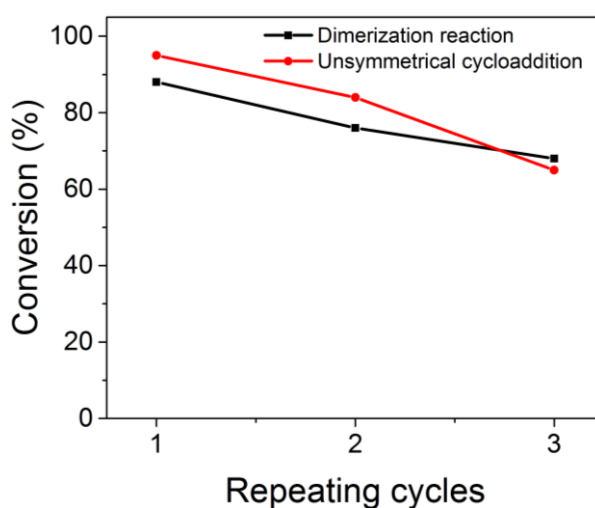


Figure 5.51 Repeating experiment of dimerization (black) and unsymmetrical cycloaddition (red) for 3 cycles.

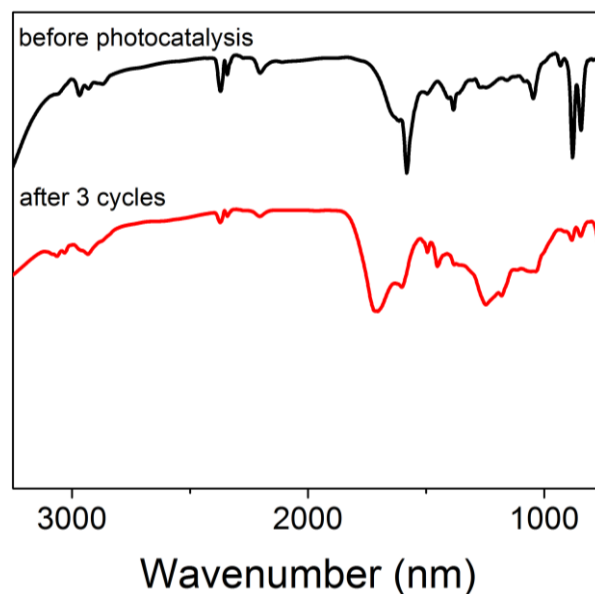


Figure 5.52 FTIR spectra of B-BT before photocatalysis reaction (black) and after 3 repeating cycles (red).

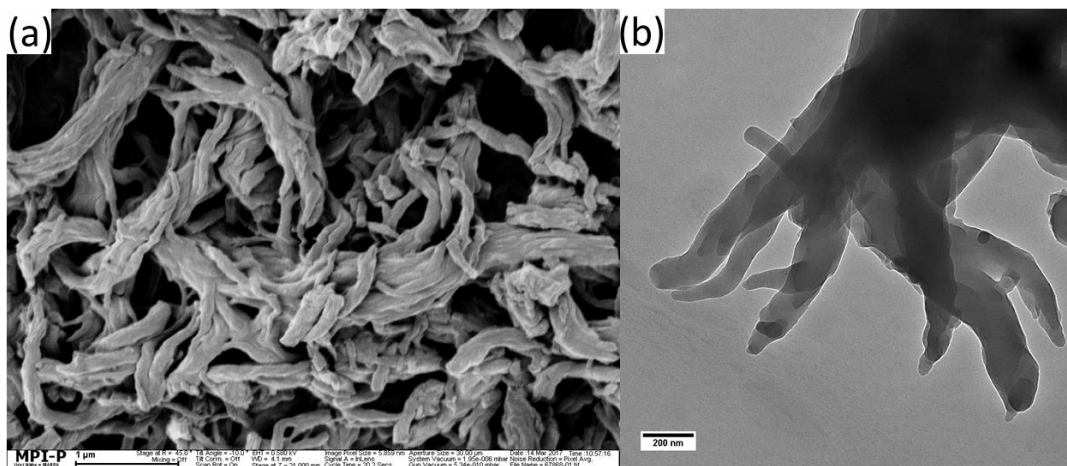


Figure 5.53 SEM image (a) and TEM image (b) of B-BT after 3 times repeating experiments.

Furthermore, the facile visible light-promoted photocatalytic protocol also allowed the preparation of important cyclobutane-containing natural products such as endiandrin A and di-*O*-methylenendiandrin A. As showed in Figure 5.50(b), di-*O*-methylenendiandrin A could be obtained with a moderate conversion but with high selectivity via the homo-cycloaddition of (*E*)-1,2-dimethoxy-4-(prop-1-en-1-yl)benzene (5), which has not been reported so far. In addition, endiandrin A could be synthesized from the homo-coupled product of *trans*-anethole, following by aryl bromination, demethylation and Ullmann-type coupling with a totally product yield of 47%, similar to literature¹¹⁷. The visible light-driven

approach offered a high regio- and stereo-selectivity for the synthesis of those cyclobutanes in a greener and novel way to obtain natural products.

5.3.4 Conclusion and outlook

As a conclusion for this subchapter, we demonstrated a visible light-promoted homo- and unsymmetrical [2+2] cycloaddition of styrene derivatives using a conjugated microporous polymer network as pure organic photocatalyst. The cycloaddition was achieved with high efficiency and regio- and stereo-selectivity. Additionally, cyclobutane-containing natural products such as di-*O*-methylandrin A and endiandrin A could be obtained via developed metal-free reaction route. We envisioned that the new class of organic photocatalysts ought not to be limited only on [2+2] cycloaddition. A broader range of cycloaddition reactions such as [3+2] or [4+2] cycloaddition reactions could also be catalyzed via the pure organic photocatalytic pathway.

5.4 Design of organic semiconductors with extreme long exciton life time for photocatalytic reduction of aryl and alkyl halides

This subchapter is based on the unpublished article “Design of molecular organic semiconductors with extreme long exciton life time and high reduction potential”. In the previous chapters, we show the high catalytic efficiency of benzothiadiazole derivatives including both small molecule and polymers. However, the reduction ability of photocatalyst is basically limited by their energy band structures, in particular, the LUMO level in the semiconducting range. This leads to the usually insufficiency of the organic semiconductor-based photocatalysts for specific challenging reactions, which requires extreme photoredox potentials. For example, the activation of the carbon-halogen bond demands extremely high bond-dissociation energy and reductive potential. In this chapter, we demonstrate a structure design of molecular semiconductors, which could be applied as photocatalysts for the activation of sp^2 and sp^3 carbon-halogen bonds.

5.4.1 Motivation

During the oxidative quenching cycle of photocatalyst, the electron accepting substrate could generate reactive radical anions and/or radicals after releasing specific functional groups, which is initiated by electron transfer from the photocatalyst. Known electron accepting substrates such as diazonium salts²⁸⁴, diaryliodonium salts²⁸⁵, sulfonyl chlorides²⁸⁶ and halides¹⁸⁰ have demonstrated high efficiency to provide reactive radicals via the PET process. In addition, halides, function as common source for C-C coupling, are prevalent in organic transformations due to its convenient storage, preparation, and low price¹⁸. However, the reduction potential of ~ -2.0 V for most halides is usually higher than the reduction potential of the frequently applied photocatalysts²¹⁹, which makes the electron transfer impossible from the photocatalysts to organic halides. Currently, many attempts have been taken to activate the carbon-halogen bond. Some transition metal photocatalysts with extremely negative reduction potential, such as iridium, have been reported for hydrogenation of aryl and alkyl halides^{182,287}. A few organic small molecules could also be applied for reduction of carbon-halogen bonds²⁸⁸⁻²⁹⁰. The visible-to-UV upconversion based on triplet-triplet annihilation (TTA) could be utilized for hydrogenation of unreactive aryl-bromine bond²⁹¹. Specific photoactive electron donor-acceptor (EDA) complexes have been introduced for alkylation between aldehydes and benzyl bromides^{292,293}. However, the photocatalysts with exceedingly high reduction potential have intrinsic drawbacks because they are either unstable under air condition or can only be excited by ultraviolet light. For the TTA involving multi-steps of electron transfer among sensitizer, annihilator and substrate, the reaction efficiency is usually very

low. For the use of the EDA complexes, the strong interactions between amino-containing compounds and the catalyst highly limit their application range. Since the bond dissociation energy of the carbon-halogen bonds is considerably higher than the maximum photonic energy of visible light, a new concept of the consecutive photo-induced electron transfer is introduced to activate those unreactive aromatic and aliphatic carbon-halogen bonds^{212,294,295}. Different from the conversional single photon initiation, consecutive photo-induced electron transfer is based on two consecutive photon absorption process, which makes the excitation of the electrons to an energetically higher level than the usually s1 state of the excited photocatalyst.

Recently, Adachi et al. reported various organic semiconductor molecules with the termed thermally activated delayed fluorescence characters^{296,297}. By tailoring the dihedral angle between the electron-withdrawing center and the electron-donating group, a narrow energy gap between the singlet state and triplet state (ΔE_{ST}) could be obtained, leading to a reverse intersystem-crossing process and the absorption of another photon. Extended fluorescence lifetime of several microseconds could be observed. The materials could be used in highly electroluminescent devices^{298,299}.

In this subchapter, a molecular photocatalyst containing benzothiadiazole (BT) and 9,9-dimethyl-9,10-dihydroacridine (DHA) is designed with a dihedral of $\sim 90^\circ$ between acceptor and donor units. The photocatalyst shows an outstanding intramolecular charge transfer and delayed fluorescence. It could be used for the activation of carbon-halogen bonds via the consecutive photo-induced charge transfer pathway.

5.4.2 Synthesis and characterization of photocatalyst BT-DHA

The synthesis of photocatalyst-4,7-bis(9,9-dimethylacridin-10(9H)-yl)benzo[c][1,2,5]thiadiazole (BT-DHA) was conducted via the Buchwald-Hartwig cross-coupling reaction between 4,7-dibromo-2,1,3-benzothiadiazole (BT-Br) and 9,9-dimethyl-9,10-dihydroacridine (DHA). The reaction pathway was demonstrated in Figure 5.54(a), accompanying with single-crystal image of the obtained BT-DHA. As expected, the acceptor-BT and donor-DHA units were almost perpendicular according to dihedral analysis of the obtained BT-DHA single-crystal (Figure 5.54(b)). In addition, the calculated electron density showed a clear charge separated characters in both HOMO and LUMO energy states (Figure 5.54(c)). The UV-Vis absorption spectrum of BT-DHA showed a very pronounced absorption band of the BT unit at ~ 320 nm at DHA unit at ~ 280 nm (Figure 5.55(a)). The broad absorption band centered at ~ 470 nm indicated a possible intramolecular charge transfer (ICT) within the molecule of BT-DHA (Figure 5.55(a)).

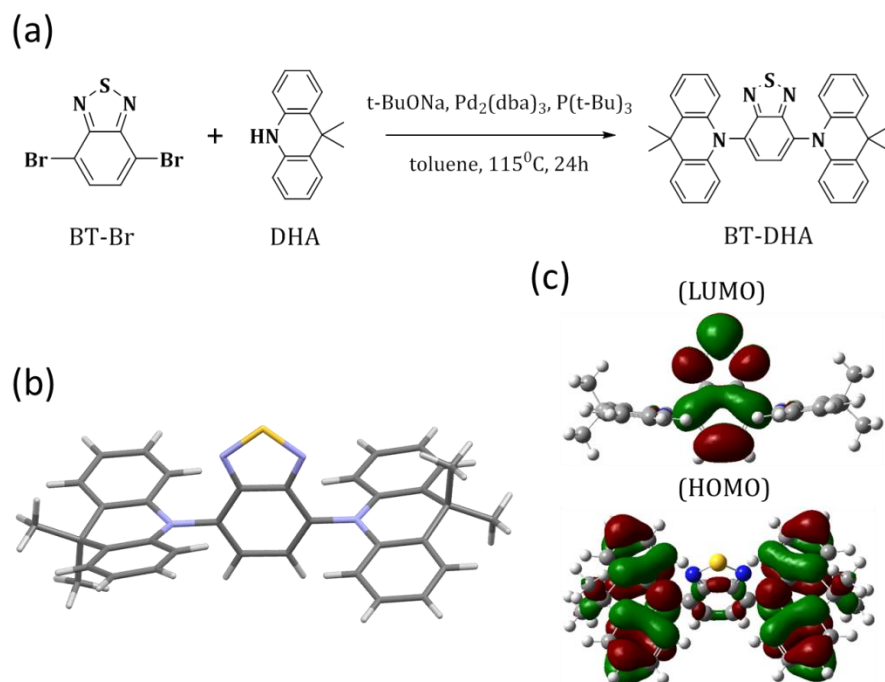


Figure 5.54 (a) General synthesis pathway of photocatalyst BT-DHA between BT-Br and DHA, (b) single crystal structure of the obtained BT-DHA and (c) calculated HOMO and LUMO state.

To further verify the intramolecular charge transfer properties, the solvatochromic effect of the UV-Vis absorption and fluorescence emission features of BT-DHA was investigated (Figure 5.55(b)-5.55(d)). The UV-Vis absorption spectra of BT-DHA appeared slightly solvent-dependent, with the absorption corresponding the ICT ranging from 482 nm to 470 nm (Figure 5.55(b)). The fluorescence spectra showed (Figure 5.55(c)) dual emissions located at ca. 400 nm and ca. 700 nm under the excitation of 320 nm. This could be attributed to the locally excited state (LE) and the ICT state, respectively. The fluorescence at ca. 700 nm demonstrated an obvious solvent-dependent emission behavior, showing a bathochromic shift as the polarity of solvent increased. The Lippert-Matage plots (Figure 5.55(d)) showed a clear difference with $r^2 = 0.850$ for all solvents tested and with $r^2 = 0.998$ for only polar solvents, respectively. The larger value for polar solvents indicated a larger dipolar change between the ground state and excited state in polar solvents than that in nonpolar solvents. This suggested that more effective charge transfer should occur in polar solvents^{300,301}. This phenomenon was also observed in solid state. As showed in Figure 5.56, the neat BT-DHA film and 10 wt% BT-DHA-doped *m*-bis(N-carbazolyl)benzene (*m*-CP) film exhibited similar absorption and emission ranges as that in solutions.

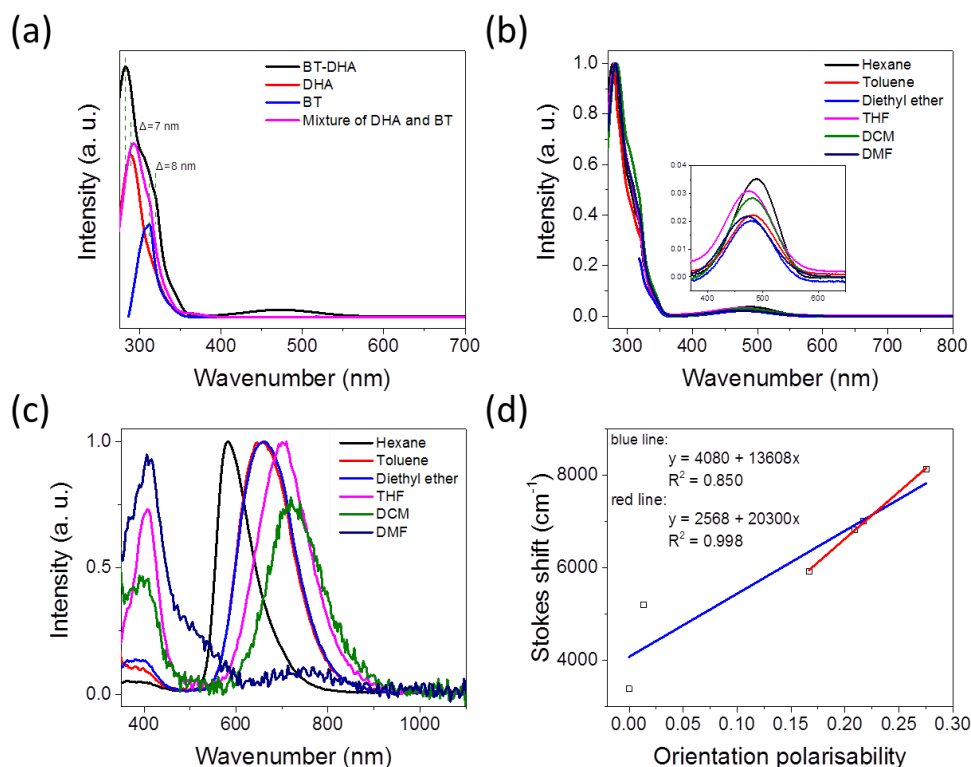


Figure 5.55 (a) UV-Vis spectra of BT-DHA (black), DHA (red), BT (blue) and mixture of DHA and BT with a molar ratio of 2/1 (magenta), normalized UV-Vis absorption spectra (b) and fluorescence spectra (c) of BT-DHA in different solvents. The solvents used are hexane (black), toluene (red), diethyl ether (blue), THF (magenta), DCM (olive) and DMF (navy). The insert of (b) shows the magnification of absorption between 380 nm and 650 nm. (d) Lippert-Mataga plots with simple line-of-best-fit for BT-DHA. There are two fitted-lines corresponding to all tested solvents (blue) and only polar solvents (red).

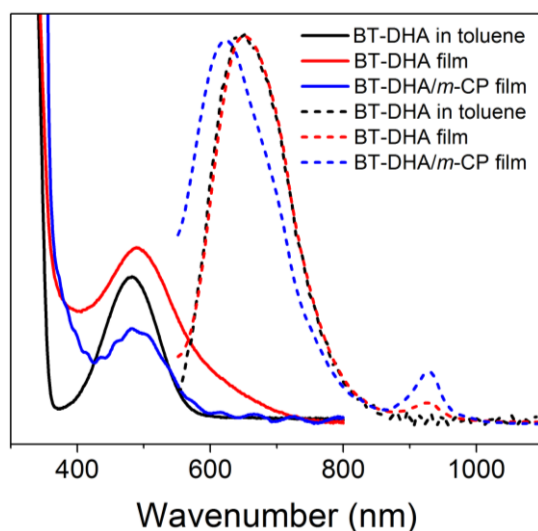


Figure 5.56 UV-Vis absorption (solid line) and fluorescence (dash line) spectra of BT-DHA in toluene solution (black), neat BT-DHA film (red), and BT-DHA 10 wt% doped *m*-CP film (blue).

To confirm the character of thermally activated delayed fluorescence (TADF) for BT-DHA, advanced photophysical methods were performed using the BT-DHA films in solid states. For the neat BT-DHA film, the fluorescence at 650 nm was observed with a lifetime of 12.6 ns (Figure 5.57). This value was comparable to the rather flat photocatalyst Ph-BT-Ph, as described in chapter 5.1. However, for the *m*-CP doped film, both fluorescence and phosphorescence were detectable with a ΔE_{ST} of 0.04 eV being determined from the high energy onsets of fluorescence and phosphorescence curves, a method for ΔE_{ST} calculation according to previous reports^{302,303}. In addition, in the photoluminescence decay curves (Figure 5.58), the intense emission and long tails after 20 μ s were attributed to prompt component and delayed component, respectively. The delayed lifetime for 77 K and 291 K were 37.7 μ s and 32.9 μ s, respectively. The fact that the intensity of delayed photoluminescence at 291 K was higher than that at 77 K indicated the presence of TADF characteristic^{303,304}. Furthermore, theoretical calculation was also conducted with a calculation module as previous report³⁰⁵, with a considerable small ΔE_{ST} of 0.15 eV being obtained, which was consistent to experimental results.

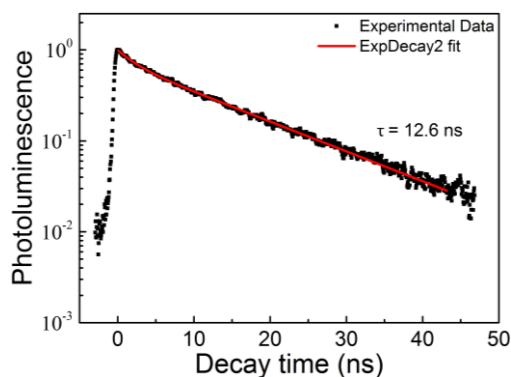


Figure 5.57 Photoluminescence decay of neat BT-DHA film at 291 K.

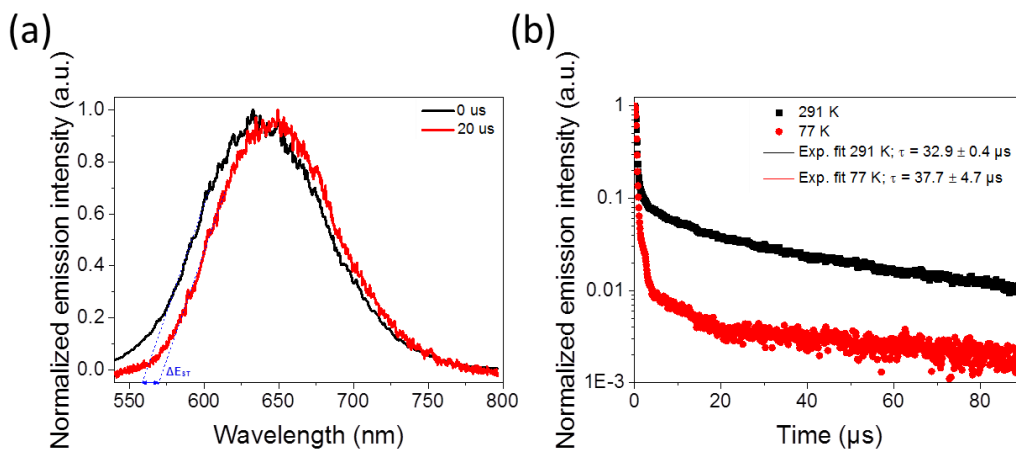
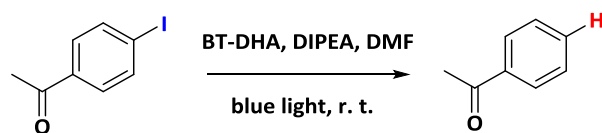


Figure 5.58 Photoluminescence spectra of 10 wt% BT-DHA/*m*-CP film measure at 77 K. the black and red curve show the fluorescence and phosphorescence spectra, respectively. (b) Photoluminescence decay of doped film at 291 K (black) and 77 K (red).

5.4.3 Photocatalytic activity test for BT-DHA

The photocatalytic activity of BT-DHA was studied with the deiodination reaction of 4-iodoacetophenone as model reaction. As expected, BT-DHA demonstrated an outstanding catalytic capacity for the activation of carbon-iodine bond (table 5.9, entry 1). The control experiments showed that without catalyst or without light, no conversion was detected (entry 2-3), indicating the critical role of both active components. In addition, neither isolated 2,1,3-benzothiadiazole nor 9,9-dimethyl-9,10-dihydroacridine could catalyze the reaction (entry 4-5). Moreover, various solvents were investigated. DMF was found with the highest conversion while acetonitrile and DMSO only showed a moderate conversion (entry 6-9). By using other amines such as trimethylamine and tris(4-methoxyphenyl)amine, only low conversions were obtained (entry 10-11). When the electron scavenger was added, no product was found (entry 12). In direct comparison with other state-of-art organic photocatalysts such as 9-Mesityl-10-methylacridinium, BT-DHA showed its superior photocatalytic efficiency while only a low conversion of 3% was determined by using 9-mesityl-10-methylacridinium as photocatalyst (entry 13).

Table 5.9 Screening and control experiments of the photocatalytic reduction of aryl halides using the model reaction.^a



Entry	Light	Reaction condition variations	Conversion (%) ^b
1	+	Standard conditions	> 99
2	-	In dark	trace
3	+	Without photocatalyst	3
4	+	With benzo[c][1,2,5]thiadiazole	trace
5	+	With DHA	trace
6	+	In acetonitrile	55
7	+	In DMSO	39
8	+	In THF	2
9	+	In toluene	trace
10	+	With trimethylamine	15
11	+	With tris(4-methoxyphenyl)amine	3
12 ^c	+	With electron scavenger	trace
13	+	With 9-mesityl-10-methylacridinium perchlorate	4

^aStandard reaction conditions: [4-Iodoacetophenone]=20 mM, [BT-DHA]=2.8 mg, [DIPEA]=174.2 μ L, dry DMF=5 mL, blue LED lamp (460 nm, 1.2 W/cm²), room temperature, argon, 24 h. ^bConversion determined by GC-MS. ^c1,4-benzoquinone as electron scavenger.

Using cyclic voltammetric measurement, a reductive potential of -1.08 V vs. SCE was determined for BT-DHA (Figure 5.59), which was slightly lower compared with its acceptor moiety BT (-1.31 V vs. SCE, Figure 5.60(a)) and reported transition metal photocatalysts, such as $\text{Ru}(\text{bpy})_3^{2+}$ (-1.33 V)^{7,306} and *fac*- $\text{Ir}(\text{ppy})_3$ (-2.19 V)^{7,182}. Significantly, it was clear that the reductive potential of BT-DHA lower than that of iodoacetophenone (-1.53 V vs. SCE), leading to a theoretically impossible electron transport from the LUMO level of BT-DHA to iodoacetophenone, as previous reports indicated^{101,182,188,189}. The fact that the reductive deiodination reaction of 4-iodoacetophenone was indeed successful, should lie on a new reaction mechanism other than the single electron transfer from the s1 state (LUMO) to the substrate. Here, the excited electron should not mainly populate on the s1 level, but rather on s2 of BT-DHA.

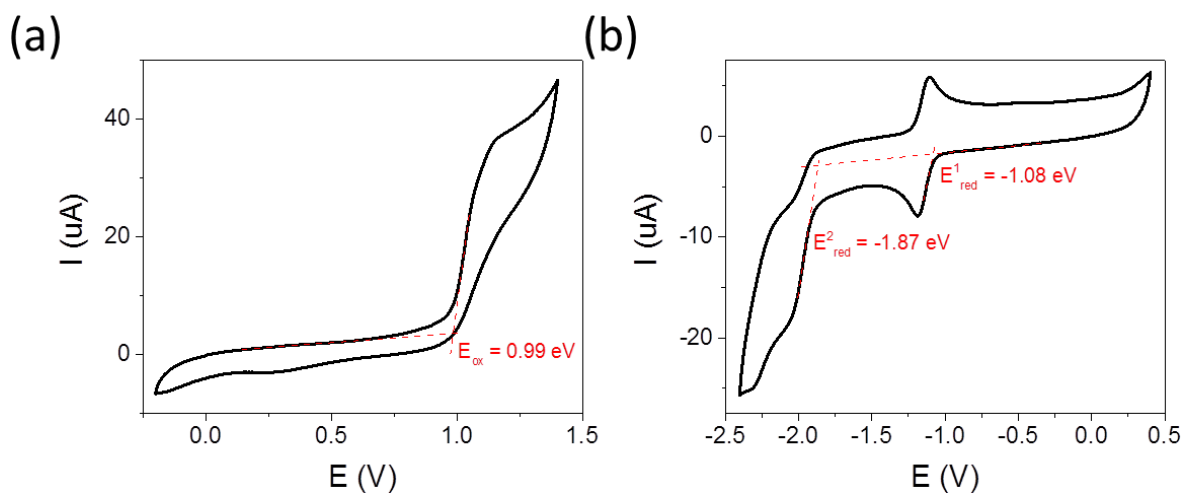


Figure 5.59 Cyclic voltammetry of BT-DHA for oxidative cycle (a) and reductive cycle (b).

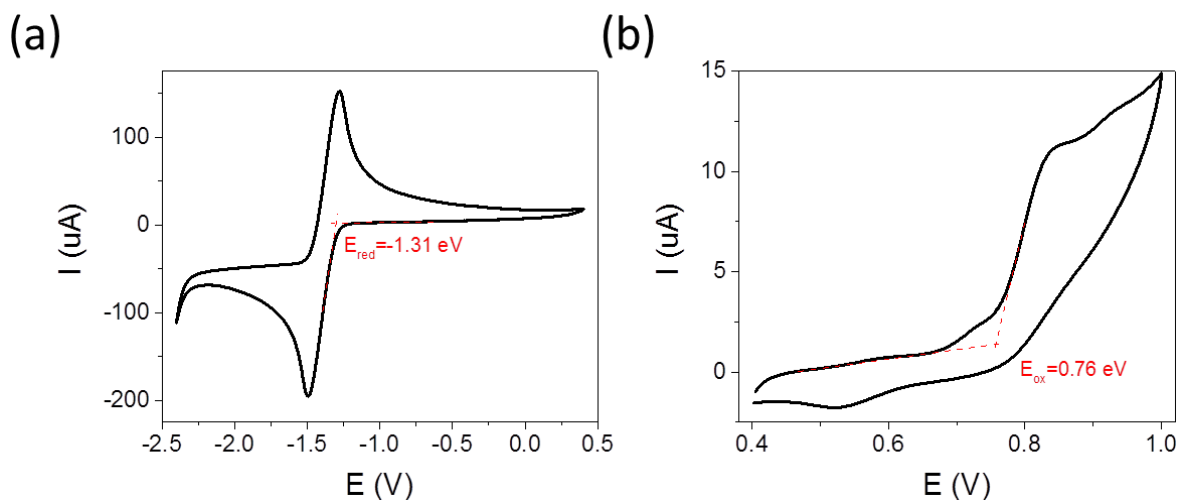


Figure 5.60 Reductive cycle of BT and oxidative cycle of DHA.

To evaluate the possible interactions in our reaction system, the UV-Vis absorption spectra of various mixtures consisting of BT-DHA, reactive halides, and amine additive were recorded as showed in Figure 5.61. No absorptions were found for both halide compounds and DIPEA solution in the visible region. The mixtures shared the similar absorption ranges as pure BT-DHA, indicating that no interactions between BT-DHA and halogenated acetophenone. However, DIPEA, working as sacrificed donor, could quench the fluorescence intensity of BT-DHA, indicating a possible electron transfer between BT-DHA and DIPEA (Figure 5.62).

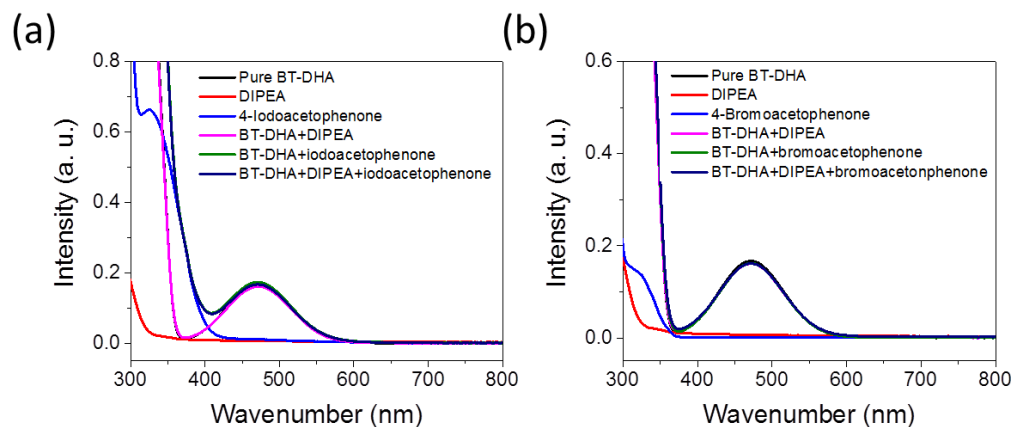


Figure 5.61 UV-Vis spectra of BT-DHA (black), DIPEA (red), halogenated acetophenone (blue), mixture of BT-DHA and DIPEA(magenta), BT-DHA and halogenated acetophenone (olive), and BT-DHA, DIPEA and halogenated acetophenone (navy). Halogenated acetophenone indicates 4-iodoacetophenone (a) and 4-bromoacetophenone (b).

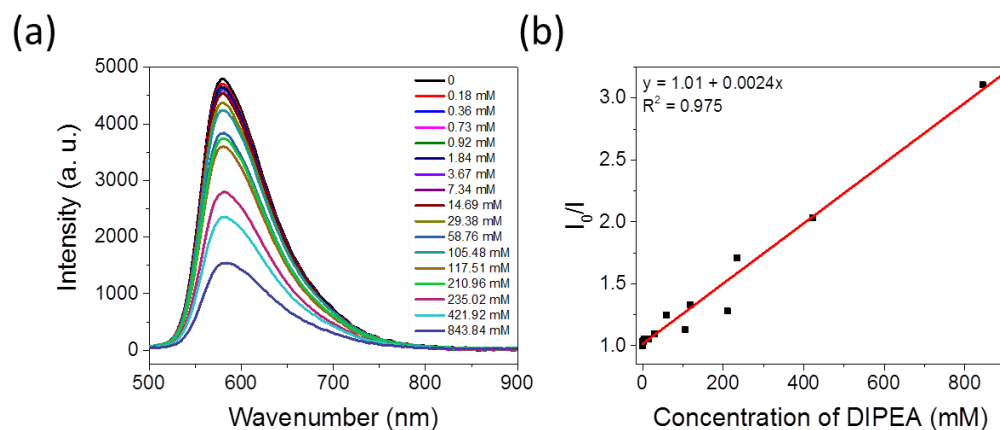


Figure 5.62 (a) The emission spectra of the BT-DHA after adding various amounts of DIPEA and (b) emission intensity as a function of DIPEA. I_0 for the emission intensity without DIPEA, and I for the emission intensity in the present of DIPEA.

Then, the characteristics of a possible consecutive photo-induced charge transfer of BT-DHA were tested by UV-Vis measurement (Figure 5.63) and cyclic voltammetry measurement (Figure 5.64). For the neat BT-DHA solution, the absorption position, the

intensity of the UV-Vis spectra and the reductive potential kept constant even under the irradiation of blue LED light for more than 1 h, indicating the high stability of the photocatalyst in its excited state. By adding DIPEA to the solution of BT-DHA, only limited influence on the optical and electrical properties of BT-DHA was observed in dark. However, when the mixture of DIPEA and BT-DHA was illuminated under light, the absorption peak of BT-DHA, which is related to the electron transfer state between 450 and 550 nm decreased clearly. The appearance of a new absorption peak at ca. 420 nm indicated the generation of an extra excited state of BT-DHA. The generated extra excited state of BT-DHA could be assigned to the higher reduction potential at ca. -1.9 V, as shown in the CV curves, ought to be responsible for the photocatalytic ability of BT-DHA to activate both sp^2 and sp^3 carbon-halogen bonds under light irradiation.

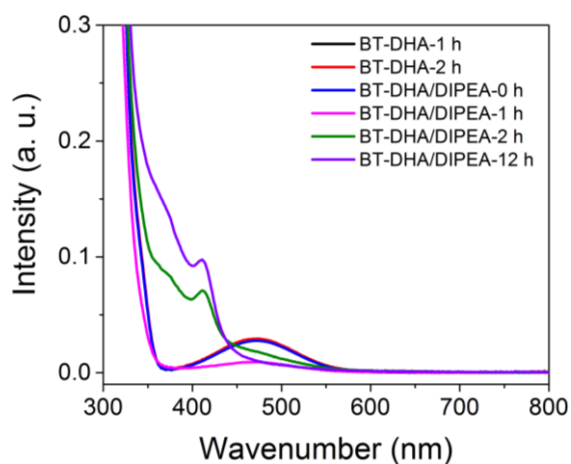


Figure 5.63 UV-Vis spectra of pure BT-DHA solution and BT-DHA/DIPEA mixture under the irradiation of blue light by given time durations.

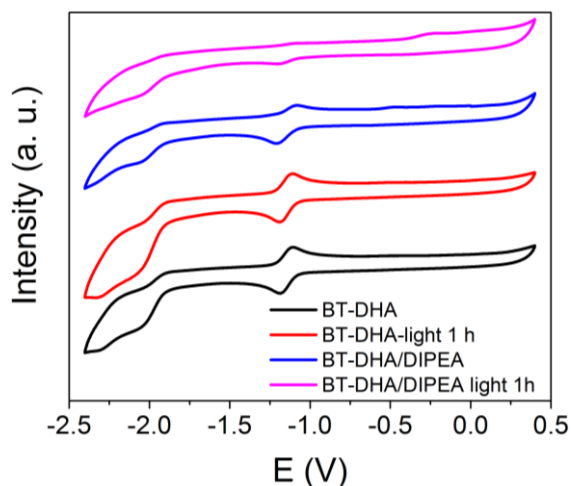


Figure 5.64 Cyclic voltammetry spectra of neat BT-DHA in dark (black), under the light irradiation for 1 h (red), mixture of BT-DHA and DIPEA in dark (blue), and under the light irradiation for 1 h (magenta).

Our proposed mechanism was illustrated in Figure 5.65. Under the light irradiation, the photo-generated hole could oxidize DIPEA as the electron-donating sacrificial reagent, resulting in the formation of the electrons in their excited state on the LUMO level (s_1) of BT-DHA. Due to the extremely long lifetime of BT-DHA in its excited state, the electrons on s_1 could absorb another photon for the next excitation step, resulting in the population on the s_2 level (LUMO+1 etc.). The higher reduction potential of the electrons from the s_2 level was able to reduce the carbon-halogen bond to form first the radical intermediate and halide anion. The radical intermediate could be hydrogenated after the hydrogen atom transfer (HAT) from either the solvent (DMF) (12%) or from the radical cation of DIPEA (88%). In addition, stable aryl radicals such as benzyl radicals could undergo the homo-coupling reaction and the dimer could become the major product.

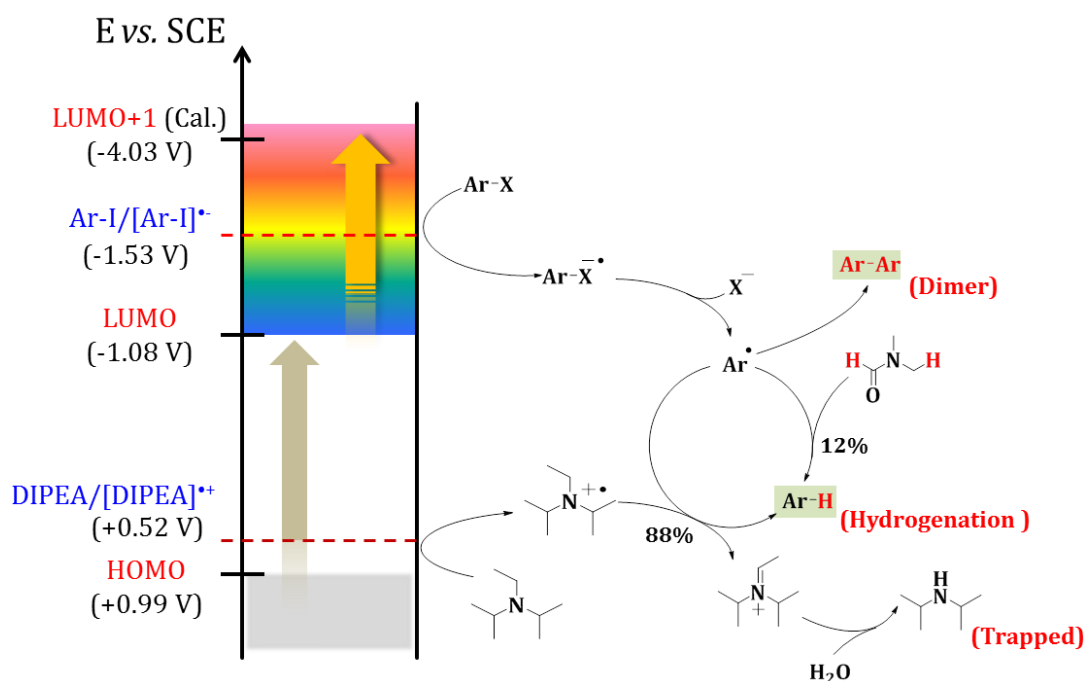
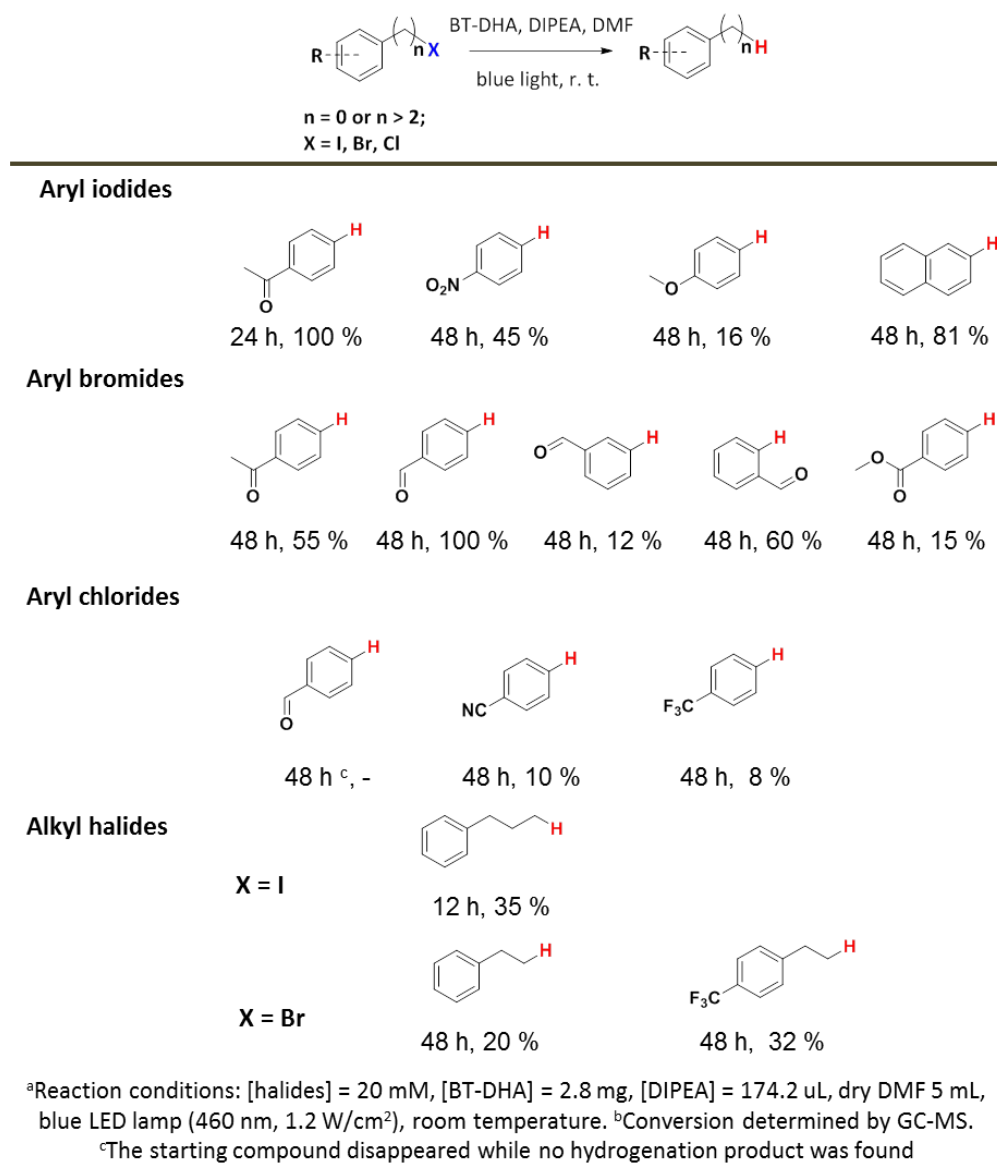


Figure 5.65 The proposed reaction mechanism. The value for LUMO+1 was obtained from theory calculation.

To further illuminate the feasibility of the designed photocatalyst, extensive investigations with various aryl halides containing different substitution groups were conducted under the optimal reaction conditions as listed in Figure 5.66. Aryl iodides with either electron-withdrawing group such as carbonyl and nitro or electron-donating group such as methoxy and naphthyl showed a moderate to high reactive conversion. In addition, aryl bromides with electron-withdrawing group such as carbonyl, aldehyde, and ester were tolerance with a medium conversion. Aldehyde group on *para* position demonstrated highest conversion, followed by *ortho* position and *meta* position, respectively. Moreover, aryl chlorine bond could also be cleaved while with a limited conversion due to extremely high

reductive potential and bond dissociation energy. Lastly, aliphatic carbon-halogen bond could also be activated with our photocatalytic system. Phenylpropyl iodide, phenylethyl bromide and trifluoromethylphenylethyl bromide transferred to corresponding hydrogenation compounds after dehalogenation with a high conversion and selectivity.

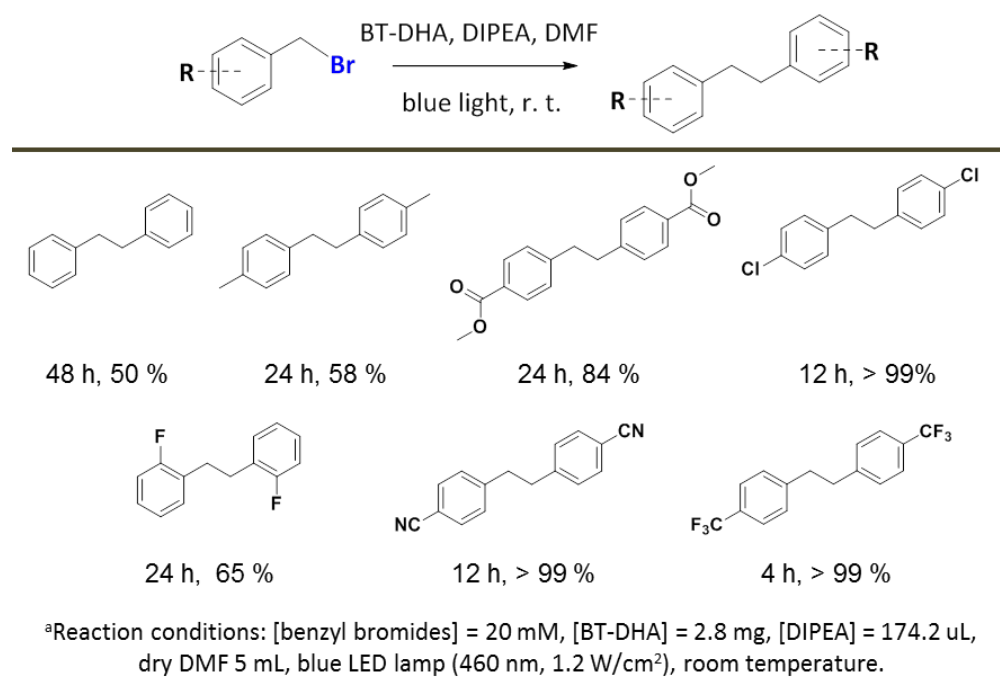
Figure 5.66 Scope of photoreduction of aryl and alkyl halides under visible light.^a



Interestingly, when benzyl bromides were used as substrate, the main product became the corresponding bibenzyl dimers via radical-radical coupling of their radical intermediates. Actually, the bibenzyl derivatives are important building blocks in natural products. They have been drawn much attention in recent years due to its potential biological and agricultural activities³⁰⁷⁻³⁰⁹. The preparation of bibenzyl compounds involved either traditional methods of alkene and alkyne reduction^{310,311} or currently reported homo-

coupling catalyzed by metal^{312,313} and inorganic salt³¹⁴. However, the synthesis of bibenzyl compounds via visible light-driven radical-radical coupling has barely been reported. To investigate the feasibility of BT-DHA as photocatalyst for the visible light-driven radical-radical-coupling reaction for the formation of bibenzyl derivatives, we extended our study for this purpose. As listed in Figure 5.67, the proposed reaction conditions exhibited an excellent compatibility to photoreduce benzyl bromides and formed the corresponding bibenzyl compounds. Various benzyl bromide derivatives containing methyl, ester, chlorine, fluorine, cyano and trifluoromethyl groups could be successfully photocatalytically reduced and homo-coupled into the corresponding bibenzyls with a high yield and selectivity. Benzyl bromides with electron-withdrawing function groups exhibited higher yields, which could lie on their lower reduction potentials.

Figure 5.67 Scope of dimerization of benzyl bromides after irradiating under visible light.^a



Furthermore, an extra example of the feasibility of our designed photocatalytic system for a “real life” application was undertaken as shown in Figure 5.68. Here, 1,2-bis(2-bromophenyl)ethane could be photocatalytically formed via selectively reducing 1-bromo-2-(bromomethyl)benzene using BT-DHA as photocatalyst. Using 1,2-bis(2-bromophenyl)ethane the starting compound, imipramine, a critical drug as tricyclic antidepressant and treatment of nocturnal enuresis³¹⁵, could be formed successfully after the ring formation via Buchwald-Hartwig amination.

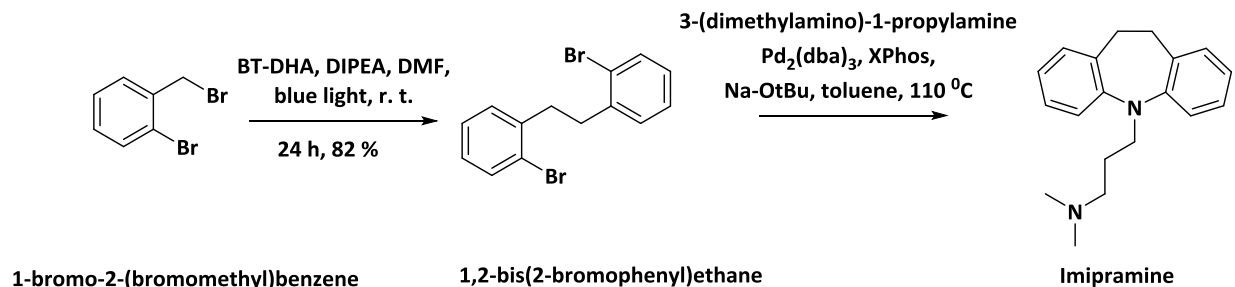


Figure 5.68 Synthetic route of imipramine.

5.4.4 Conclusion and outlook

In this chapter, a new structural design strategy of molecular organic semiconductors with extremely long exciton lifetime was presented. The donor and acceptor moieties, in particular, benzothiadiazole as acceptor and 9,9-dimethyl-9,10-dihydroacridine as donor, were designed to be perpendicular to each other on the molecular level. This structural design led to a narrow energy gap of the singlet and triplet states and enabled the reverse inter-system-crossing process in the excited state. The electron in excited state could absorb another photon and be excited again on the energetically higher level, probably LUMO+1 in the s_2 state, resulting in an extremely high reduction potential of the catalyst. The designed organic photocatalyst could activate both sp^2 and sp^3 carbon-halogen bonds, leading to either hydrogenated products from the alkyl halides or dimers from aryl halides. Furthermore, an important antidepressant, imipramine could be synthesized from the obtained dimers with high selectivity and yield.

6 Experimental Section

6.1 A metal-free, dually redox-active organic photocatalyst for visible light-promoted Diels-Alder reaction and direct conversion of aliphatic alcohols to bromides

6.1.1 Materials

All chemicals and solvents were purchased from commercial sources and used as received without further purification unless otherwise noted. For photocatalytic Diels-Alder reaction, all dienes and reaction solvents, including dichloromethane and acetonitrile, were purified by elution through neutral aluminium oxide (50-200 μm) and anhydrous CaCl_2 (w/w, 95/5). For photocatalytic bromination reaction, dry solvents, such as dry DMF, THF and acetonitrile were applied as the reaction solvent.

6.1.2 Methods and characterizations

UV-Vis absorption and fluorescence spectra were recorded on a Perkin Elmer Lambda 100 spectrophotometer and J&M TIDAS spectrofluorometer at ambient temperature, respectively. Electron paramagnetic resonance (EPR) spectrum was conducted on a Magnettech Miniscope MS200 spectrometer. Conditions for spin trap EPR: DMPO (0.1 M), catalyst (1 mg/ml) in acetonitrile. Cyclic voltammetry measurement was carried out on a Metrohm Autolab PGSTAT204 potentiostat/galvanostat with a three-electrode-cell system: glassy carbon electrode as the working electrode, Hg/HgCl_2 electrode as the reference electrode, platinum wire as the counter electrode, and Bu_4NPF_6 (0.1 M acetonitrile) as supporting electrolyte with a scan rate of 100 mV s^{-1} in the range of -2 V to 2 V. The redox potential of catalyst was obtained by dissolving compound into acetonitrile directly with a concentration of 1 mg/ml. GC-MS measurement was performed on Shimadzu GC-2010 plus gas chromatography and QP2010 ultra mass spectrometer with fused silica column (Phenomenx, Zebron 5-ms nonpolar) and flame ionization detector. ^1H and ^{13}C NMR spectra for all compounds were measured using Bruker AVANCE 300 MR (at 300 MHz) and are referenced to 0.00 ppm and 0.0 ppm for SiMe_4 .

Time-Resolved Photoluminescence: Time-resolved photoluminescence (TR-PL) spectra were taken with a C4742 Hamamatsu streak camera system in slow sweep mode. Excitation pulses at 400 nm were provided by frequency doubling the output of a commercial femtosecond amplifier laser system (Coherent LIBRA-HE).

Transient Absorption Spectroscopy: Transient absorption (TA) measurements were performed with a home-built pump-probe setup. To generate white light in the visible the output of commercial titanium: sapphire amplifier (Coherent LIBRA-HE, 3.5 mJ, 1 kHz, 100 fs) was used to pump a commercial optical parametric amplifier (Coherent OPerA Solo). The parametric amplifier (OPA) was used to generate the seed beam of 1300 nm for white-light generation. The 1300 nm seed of a few μJ was focused into a c-cut 3 mm thick sapphire window for white-light generation. Mostly reflective elements were used to guide the probe beam to the sample to minimize chirp. The excitation pulse was provided by an actively Q-switched Nd:YVO₄ laser (AOT Ltd. MOPA) at 355 nm with a resolution of 600 ps. The delay between pump and probe was controlled by an electronic delay generator (Stanford Research Systems DG535). The white-light pulses were dispersed onto a linear silicon photodiode array, which was read out at 1 kHz by home-built electronics. Adjacent diode readings corresponding to the transmission of the sample after an excitation pulse and without an excitation pulse were used to calculate $\Delta T/T$. TA measurements were performed at room temperature.

6.1.3 Synthesis of photocatalyst Ph-BT-Ph

A solution of 4, 7-dibromo-2, 1, 3-benzothiadiazole (2.94 g 10 mmol), phenylboric acid (3.05 g, 25 mmol) in toluene (50 mL) and a solution of potassium carbonate (5.52 g, 40 mmol) in H₂O (20 mL) were mixed. After degassing for 30 min, Pd(PPh₃)₄ (0.094 g, 0.08 mmol) was added and the reaction mixture was heated at 90 °C for overnight under N₂. After cooling to room temperature, the mixture was poured into water and extracted with dichloromethane. The organic layer was washed with water and dried with anhydrous Na₂SO₄. After removing the solvent on a rotary evaporator, the crude product was recrystallized from methanol. For further purification, the crude product was purified via column chromatography on silica using dichloromethane as eluent to afford Ph-BT-Ph as yellow solid. Yield: 2.54 g (88%).

¹H NMR (CDCl₃, 300 MHz): δ 7.99 (m, 4H), 7.79 (s, 2H, Ar H), 7.57 (m, 4H), 7.48 (t, J=7.3, 2H).

¹³C NMR (CDCl₃, 300 MHz): δ 128.13, 128.38, 128.64, 129.25, 133.38, 137.44, 154.11.

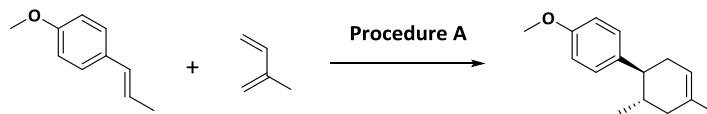
6.1.4 Photocatalytic redox reaction with Ph-BT-Ph

General Procedure A: Photocatalytic Diels-Alder Reaction

A flame dried 20 mL vial with a magnetic stir bar was added with Ph-BT-Ph (2.4 mg, 0.035 equiv), alkenes (0.24 mmol, 1.0 equiv), dienes (2.4 mmol, 10 equiv) and acetonitrile (2.4 ml). Then the vial was capped and placed under the irradiation of a blue or white LEDs lamp (1.2 W/cm²). The reaction mixture was stirred at room temperature until it was completely finished which was determined by GC-MS measurement. Afterwards, the mixture was poured into a separatory funnel containing the mixture of Et₂O and H₂O (v/v, 1/1). The organic layers were separated and extracted with Et₂O for 3 times. The combined organic layers were washed with water, dried over anhydrous MgSO₄ and concentrated with rotary evaporator. The residue crude product was purified via column chromatography on silica to afford the pure compound.

General Procedure B: Photocatalytic Bromination Reaction

A flame-dried 25 mL Schlenk flask with a magnetic stir bar was added with Ph-BT-Ph (10 mg, 0.065 equiv), corresponding alcohols (0.50 mmol, 1.0 equiv), sodium bromide (1.00 mmol, 2.0 equiv) carbon tetrabromide (1.00 mmol, 2.0 equiv) and dry DMF (10 mL). Then the flask was capped with rubber septum and degassed with nitrogen. The mixture was bubbled with nitrogen through freeze-thaw process for 3 times. Afterwards, the flask was placed under the irradiation of a blue or white LEDs lamp (1.2 W/cm²). The reaction mixture was stirred at room temperature until it was completely finished which was determined by GC-MS measurement. Subsequently, the mixture was poured into a separatory funnel containing the mixture of Et₂O (25 mL) and H₂O (25 mL). The organic layers were separated and extracted with Et₂O (25 mL) for 2 more times. The combined organic layers were washed with saturated Na₂S₂O₃, brine, and then dried over anhydrous MgSO₄. After removing the solvent with rotary evaporator, a crude product was obtained. The crude product was then purified with column chromatography on silica to afford the pure compound.



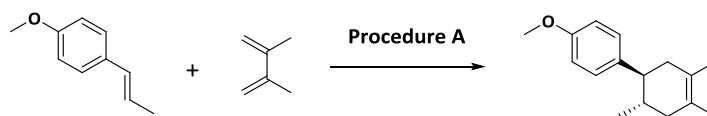
(1S,2S)-4'-Methoxy-2,4-dimethyl-1,2,3,6-tetrahydro-1,1'-biphenyl (Figure 5.5, 1a):

According to the general procedure A, a dried vial with a magnetic stir bar was charged with *trans*-anethole (35.6 mg, 0.24 mmol), isoprene (240 μ l, 2.4 mmol), Ph-BT-Ph (2.4 mg, 0.0083 mmol) and acetonitrile (2.4 mL). After the reaction was finished, the mixture was performed as the workup protocol and purified by chromatography on silica with hexane/ethyl acetate (12/1) as the elution to afford the pure cycloadduct as clear oil.

R_f (hexane/ethyl acetate 12/1): 0.76

^1H NMR (CDCl_3 , 300 MHz): δ 6.99 (d, $J=9$ Hz, 2H), 6.75 (d, $J=9$ Hz, 2H), 5.36 (bs, 1H), 3.71 (s, 3H), 2.21 (m, 1H), 2.11 (m, 1H), 2.04 (m, 1H), 1.98 (m, 1H), 1.81 (m, 1H), 1.71 (m, 1H), 1.61 (s, 3H), 0.62 (d, $J=6$ Hz, 3H);

^{13}C NMR (CDCl_3 , 300 MHz): δ 157.8, 138.2, 133.8, 128.5, 120.9, 113.7, 55.2, 47.0, 39.9, 35.3, 34.0, 23.4, 20.2.



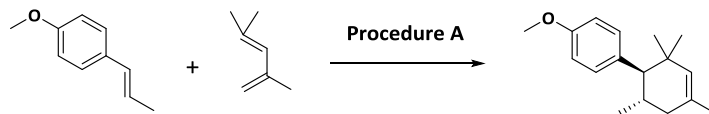
(1S,2S)-4'-Methoxy-2,4,5-trimethyl-1,2,3,6-tetrahydro-1,1'-biphenyl (Figure 5.5, 1b):

According to the general procedure A, a dried vial with a magnetic stir bar was charged with *trans*-anethole (35.6 mg, 0.24 mmol), 2,3-dimethylbuta-1,3-diene (81.5 μ l, 0.72 mmol), Ph-BT-Ph (2.4 mg, 0.0083 mmol) and acetonitrile (2.4 mL). After the reaction was finished, the mixture was performed as the workup protocol and purified by chromatography on silica with hexane/dichloromethane (1/1) as the elution to afford the pure cycloadduct as clear oil.

R_f (hexane/dichloromethane 1/1): 0.81

^1H NMR (CDCl_3 , 300 MHz): δ 7.02 (d, $J=9$ Hz, 2H), 6.78 (d, $J=12$ Hz, 2H), 3.71 (s, 3H), 2.33 (td, $J=6, 12$ Hz, 1H), 2.07 (m, 1H), 1.98 (m, 2H), 1.77 (m, 2H), 1.56 (s, 3H), 1.54 (s, 3H), 0.63 (d, $J=9$ Hz, 3H);

^{13}C NMR (CDCl_3 , 300 MHz): δ 157.6, 138.2, 128.5, 125.5, 125.4, 113.7, 55.2, 47.8, 41.9, 41.7, 34.3, 20.1, 18.8, 18.7.

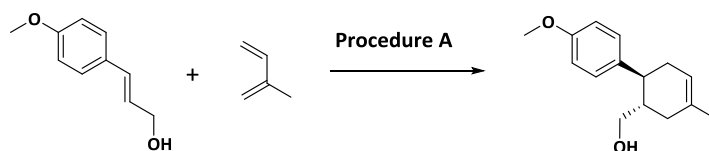


(1R,2S)-4'-Methoxy-2,4,6,6-tetramethyl-1,2,3,6-tetrahydro-1,1'-biphenyl (Figure 5.5, 1c): According to the general procedure A, a dried vial with a magnetic stir bar was charged with *trans*-anethole (35.6 mg, 0.24 mmol), 2,4-dimethylpenta-1,3-diene (93.1 μ l, 0.72 mmol), Ph-BT-Ph (2.4 mg, 0.0083 mmol) and acetonitrile (2.4 mL). After the reaction was finished, the mixture was performed as the workup protocol and purified by chromatography on silica with hexane/ethyl acetate (25/1) as the elution to afford the pure cycloadduct as clear oil.

R_f (hexane/ethyl acetate 25/1): 0.61

$^1\text{H NMR}$ (CDCl_3 , 300 MHz): δ 6.97 (dd, $J=6$, 18 Hz, 2H), 6.76 (dd, $J=9$, 18 Hz, 2H), 5.12 (s, 1H), 3.72 (s, 3H), 2.11 (d, 9 Hz, 1H), 2.05 (m, 1H), 1.98 (m, 1H), 1.70 (m, 1H), 1.59 (s, 3H), 0.75 (s, 3H), 0.70 (s, 3H), 0.64 (d, $J=6$ Hz, 3H);

$^{13}\text{C NMR}$ (CDCl_3 , 300 MHz): δ 157.7, 133.3, 130.3, 129.3, 113.2, 112.2, 57.4, 56.1, 40.5, 36.3, 30.0, 28.8, 24.6, 23.3, 20.8.



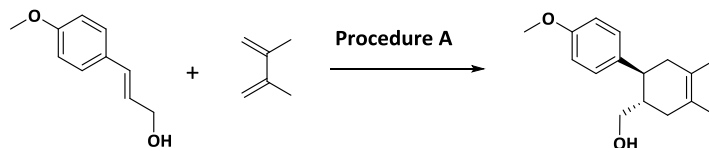
((1S,2S)-4'-Methoxy-4-methyl-1,2,3,6-tetrahydro-[1,1'-biphenyl]-2-yl)methanol

(Figure 5.5, 1d): According to the general procedure A, a dried vial with a magnetic stir bar was charged with (*E*)-3-(4-methoxyphenyl)prop-2-en-1-ol (39.4 mg, 0.24 mmol), isoprene (240 μ l, 2.4 mmol), Ph-BT-Ph (2.4 mg, 0.0083 mmol) and acetonitrile (2.4 mL). After the reaction was finished, the mixture was performed as the workup protocol and purified by chromatography on silica with hexane/ethyl acetate (4/1) as the elution to afford the pure cycloadduct as clear oil.

R_f (hexane/ethyl acetate 4/1): 0.56

$^1\text{H NMR}$ (CDCl_3 , 300 MHz): δ 7.06 (d, $J=9$ Hz, 2H), 6.78 (d, $J=9$ Hz, 2H), 5.37 (bs, 1H), 3.70 (s, 3H), 3.33 (dd, $J=3$, 9 Hz, 1H), 3.22 (dd, 6, 12 Hz, 1H), 2.45 (m, 1H), 2.14 (m, 1H), 2.12 (m, 1H), 2.03 (t, $J=12$ Hz, 1H), 1.93 (m, 1H), 1.90 (m, 1H), 1.64 (s, 3H);

$^{13}\text{C NMR}$ (CDCl_3 , 300 MHz): δ 158.1, 137.0, 133.4, 128.4, 120.6, 114.1, 65.9, 55.2, 42.2, 41.5, 34.7, 33.9, 23.5.



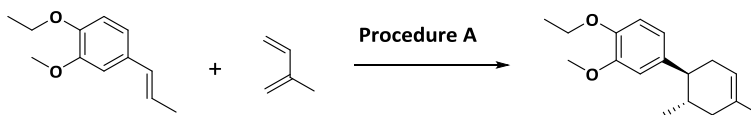
((1S,2S)-4'-Methoxy-4,5-dimethyl-1,2,3,6-tetrahydro-[1,1'-biphenyl]-2-yl)methanol

(Figure 5.5, 1e): According to the general procedure A, a dried vial with a magnetic stir bar was charged with (*E*)-3-(4-methoxyphenyl)prop-2-en-1-ol (39.4 mg, 0.24 mmol), 2,3-dimethylbuta-1,3-diene (271.6 μ l, 2.4 mmol), Ph-BT-Ph (2.4 mg, 0.0083 mmol) and acetonitrile (2.4 mL). After the reaction was finished, the mixture was performed as the workup protocol and purified by chromatography on silica with hexane/ethyl acetate (2/1) as the elution to afford the pure cycloadduct as clear oil.

R_f (hexane/ethyl acetate 2/1): 0.53

$^1\text{H NMR}$ (CDCl_3 , 300 MHz): δ 7.05 (d, $J=9$ Hz, 2H), 6.78 (d, $J=12$ Hz, 2H), 3.69 (s, 3H), 3.36 (dd, $J=6, 15$ Hz, 1H), 3.21 (dd, $J=6, 14$ Hz, 1H), 2.50 (m, 1H), 2.12 (m, 1H), 2.08 (m, 1H), 1.99 (m, 1H), 1.93 (m, 1H), 1.88 (m, 1H), 1.58 (s, 3H), 1.55 (s, 3H);

$^{13}\text{C NMR}$ (CDCl_3 , 300 MHz): δ 158.0, 137.0, 128.4, 125.2, 124.8, 114.0, 66.0, 55.2, 43.0, 41.8, 41.3, 35.7, 18.9, 18.7.



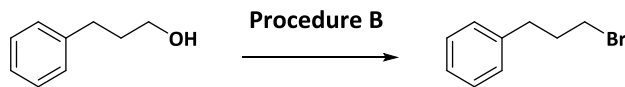
(1S,2S)-4'-Ethoxy-3'-methoxy-2,4-dimethyl-1,2,3,6-tetrahydro-1,1'-biphenyl (Figure

5.5, 1f): According to the general procedure A, a dried vial with a magnetic stir bar was charged with (*E*)-1-ethoxy-2-methoxy-4-(prop-1-en-1-yl)benzene (48.1 mg, 0.25 mmol), isoprene (250 μ l, 2.5 mmol), Ph-BT-Ph (2.5 mg, 0.0083 mmol) and acetonitrile (2.5 mL). After the reaction was finished, the mixture was performed as the workup protocol and purified by chromatography on silica with hexane/ethyl acetate (12/1) as the elution to afford the pure cycloadduct as clear oil.

R_f (hexane/ethyl acetate 12/1): 0.46

$^1\text{H NMR}$ (CDCl_3 , 300 MHz): δ 6.71 (m, 1H), 6.63 (m, 2H), 5.37 (bs, 1H), 4.02 (m, 2H), 3.78 (s, 3H), 2.21 (m, 1H), 2.14 (m, 1H), 2.09 (m, 1H), 1.99 (m, 1H), 1.83 (m, 1H), 1.72 (m, 1H), 1.62 (s, 3H), 1.38 (t, $J=6$ Hz, 3H), 0.66 (d, $J=6$ Hz, 3H);

$^{13}\text{C NMR}$ (CDCl_3 , 300 MHz): δ 149.1, 146.4, 138.8, 133.8, 120.8, 119.6, 112.6, 111.0, 64.3, 55.9, 47.4, 39.8, 35.2, 34.0, 23.4, 20.2, 14.9.

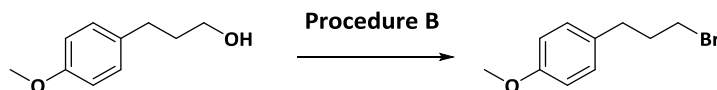


(3-Bromopropyl)benzene (Figure 5.15, 2a): According to the general procedure B, a flame-dried Schlenk flask with a magnetic stir bar was charged with 3-phenylpropan-1-ol (68.0 μ l, 0.5 mmol), NaBr (102.9 mg, 1 mmol), CBr₄ (331.6 mg, 1 mmol), Ph-BT-Ph (10 mg, 0.034 mmol) and dry DMF (10 mL). After the reaction was finished, the mixture was performed as the workup protocol and purified by chromatography on silica with hexane/dichloromethane (5/1) as the elution to afford the pure product as clear oil.

R_f (hexane/dichloromethane 5/1): 0.5

¹H NMR (CDCl₃, 300 MHz): δ 7.22 (m, 2H), 7.14 (m, 3H), 3.32 (t, *J*=7.5 Hz, 2H), 2.71 (t, *J*=7.5 Hz, 2H), 2.10 (p, *J*=6 Hz, 2H);

¹³C NMR (CDCl₃, 300 MHz): δ 140.5, 128.6, 128.5, 126.2, 34.2, 34.0, 33.1.

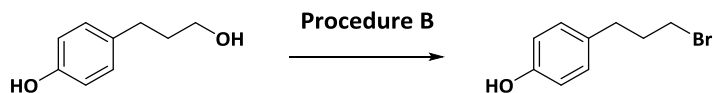


1-(3-Bromopropyl)-4-methoxybenzene (Figure 5.15, 2b): According to the general procedure B, a flame-dried Schlenk flask with a magnetic stir bar was charged with 3-(4-methoxyphenyl)propan-1-ol (83.1 mg, 0.5 mmol), NaBr (102.9 mg, 1 mmol), CBr₄ (331.6 mg, 1 mmol), Ph-BT-Ph (10 mg, 0.034 mmol) and dry DMF (10 mL). After the reaction was finished, the mixture was performed as the workup protocol and purified by chromatography on silica with hexane/dichloromethane (6/1) as the elution to afford the pure product as clear oil.

R_f (hexane/dichloromethane 6/1): 0.35

¹H NMR (CDCl₃, 300 MHz): δ 7.15 (d, *J*=6 Hz, 2H), 6.87 (d, *J*=6 Hz, 2H), 3.83 (s, 3H), 3.42 (t, *J*=6 Hz, 2H), 2.76 (t, *J*=6 Hz, 2 Hz), 2.17 (p, *J*=6 Hz, 2H);

¹³C NMR (CDCl₃, 300 MHz): δ 158.1, 132.6, 129.5, 113.9, 55.3, 34.4, 33.2, 33.1.

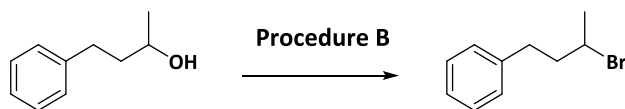


4-(3-bromopropyl)phenol (Figure 5.15, 2c): According to the general procedure B, a flame-dried Schlenk flask with a magnetic stir bar was charged with 4-(3-hydroxypropyl)phenol (76.1 mg, 0.5 mmol), NaBr (102.9 mg, 1 mmol), CBr₄ (331.6 mg, 1 mmol), Ph-BT-Ph (10 mg, 0.034 mmol) and dry DMF (10 mL). After the reaction was finished, the mixture was performed as the workup protocol and purified by chromatography on silica with hexane/ethyl acetate (5/1) as the elution to afford the pure product.

R_f (hexane/ethyl acetate 5/1): 0.35

¹H NMR (CDCl₃, 300 MHz): δ 7.07 (d, J=9 Hz, 2H), 6.79 (d, J=9 Hz, 2H), 3.41 (t, J=6 Hz, 2H), 2.73 (t, J=6 Hz, 2H), 2.14 (p, J=6 Hz, 2H),

¹³C NMR (CDCl₃, 300 MHz): δ 153.8, 132.8, 129.7, 115.4, 34.4, 33.2, 33.0.

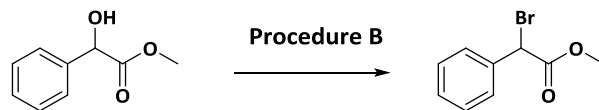


(3-bromobutyl)benzene (Figure 5.15, 2d): According to the general procedure B, a flame-dried Schlenk flask with a magnetic stir bar was charged with 4-phenylbutan-2-ol (77.4 μl, 0.5 mmol), NaBr (102.9 mg, 1 mmol), CBr₄ (331.6 mg, 1 mmol), Ph-BT-Ph (10 mg, 0.034 mmol) and dry DMF (10 mL). After the reaction was finished, the mixture was performed as the workup protocol and purified by chromatography on silica with hexane as the elution to afford the pure product as clear oil.

R_f (hexane): 0.45

¹H NMR (CDCl₃, 300 MHz): δ 7.35 (m, 2H), 7.26 (m, 3H), 4.14 (m, 1H), 2.93 (m, 1H), 2.82 (m, 1H), 2.19 (m, 1H), 2.11 (m, 1H), 1.79 (d, J=6 Hz, 3H);

¹³C NMR (CDCl₃, 300 MHz): δ 140.9, 128.6, 128.5, 126.1, 50.9, 42.7, 34.0, 26.6.

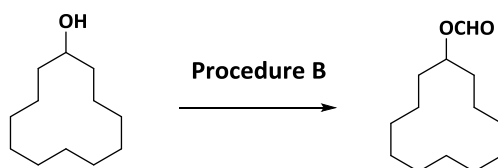


Methyl-2-bromo-2-phenylacetate (Figure 5.15, 2e): According to the general procedure B, a flame-dried Schlenk flask with a magnetic stir bar was charged with methyl-2-hydroxy-2-phenylacetate (83.1 mg, 0.5 mmol), NaBr (102.9 mg, 1 mmol), CBr₄ (331.6 mg, 1 mmol), Ph-BT-Ph (10 mg, 0.034 mmol) and dry DMF (10 mL). After the reaction was finished, the mixture was performed as the workup protocol and purified by chromatography on silica with hexane/ethyl acetate (10/1) as the elution to afford the pure product.

R_f (hexane/ethyl acetate 10/1): 0.44

¹H NMR (CDCl₃, 300 MHz): δ 7.46 (m, 2H), 7.28 (m, 3H), 5.29 (s, 1H), 3.71 (s, 3H);

¹³C NMR (CDCl₃, 300 MHz): δ 168.8, 135.7, 129.3, 128.9, 128.7, 53.4, 46.5.



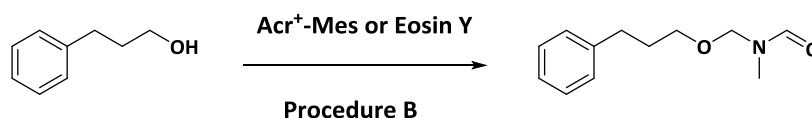
Cyclododecyl formate (Figure 5.15, 2f): According to the general procedure B, a flame-dried Schlenk flask with a magnetic stir bar was charged with cyclododecanol (92.2 mg, 0.5 mmol), NaBr (102.9 mg, 1 mmol), CBr₄ (331.6 mg, 1 mmol), Ph-BT-Ph (10 mg, 0.034 mmol) and dry DMF (10 mL). After the reaction was finished, the mixture was performed as the workup protocol and purified by chromatography on silica with hexane/dichloromethane (40/1) as the elution to afford the pure product.

R_f (hexane/dichloromethane 40/1): 0.12

¹H NMR (CDCl₃, 300 MHz): δ 7.98 (s, 1H), 5.07 (m, 1H), 1.66 (m, 2H), 1.48 (m, 2H), 1.28 (m, 18H);

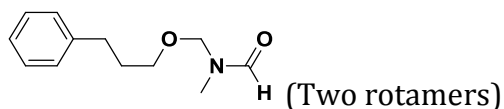
¹³C NMR (CDCl₃, 300 MHz): δ 161.0, 72.2, 29.1, 24.0, 23.8, 23.3, 23.2, 20.8.

6.1.5 Photocatalytic oxidation of DMF with organic photocatalysts



N-methyl-N-((3-phenylpropoxy)methyl)formamide: According to the general procedure B, a flame-dried Schlenk flask with a magnetic stir bar was charged with 3-phenylpropan-1-ol (68.0 μl , 0.5 mmol), NaBr (102.9 mg, 1 mmol), CBr_4 (331.6 mg, 1 mmol), 9-mesityl-10-methylacridinium perchlorate or eosin Y (10 mg) and dry DMF (10 mL). After the reaction was finished, the mixture was performed as the workup protocol and purified by chromatography on silica with methanol/dichloromethane (1/80) as the elution to afford the pure product as clear oil.

R_f (methanol/dichloromethane 1/80): 0.65



Major construction:

^1H NMR (CD_2Cl_2 , 500 MHz): δ 8.04 (s, 1H), 7.19 (m, 2H), 7.11 (m, 3H), 4.55 (s, 2H), 3.26 (t, $J=5$ Hz, 2H), 2.79 (s, 3H), 2.59 (t, $J=5$ Hz, 2H), 1.78 (m, 2H);

^{13}C NMR (CD_2Cl_2 , 500 MHz): δ 162.6, 141.8, 128.4, 128.3, 125.8, 80.2, 66.5, 32.2, 31.1, 28.7.

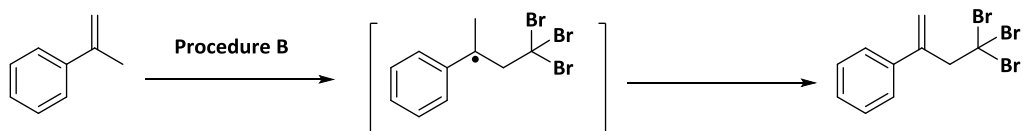
Minor construction:

^1H NMR (CD_2Cl_2 , 500 MHz): δ 8.02 (s, 1H), 7.19 (m, 2H), 7.09 (m, 3H), 4.69 (s, 2H), 3.33 (t, $J=5$ Hz, 2H), 2.86 (s, 3H), 2.58 (t, $J=5$ Hz, 2H), 1.78 (m, 2H);

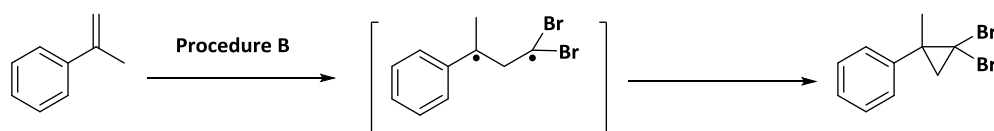
^{13}C NMR (CD_2Cl_2 , 500 MHz): δ 163.2, 142.0, 128.4, 128.3, 125.7, 73.5, 67.6, 32.9, 32.3, 31.2.

6.1.6 Insights of radical pathway for photocatalytic bromination reaction

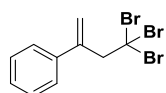
Major pathway (a)



Minor pathway (b)



According to general procedure B, a flame-dried Schlenk flask with a magnetic stir bar was charged with a-methylstyrene (65 μ L, 0.5 mmol), CBr_4 (331.6 mg, 1 mmol), Ph-BT-Ph (10 mg, 0.034 mmol) and dry DMF (10 mL). After the reaction was finished, the mixture was poured into a separatory funnel with 25 mL of Et_2O and 25 mL of H_2O . The aqueous layers were extracted with Et_2O (25 mL) for 2 times. The combined organic layers were washed with water and dried over MgSO_4 . Analysis of the crude product with GC-MS showed that there was only small amount of dibromocyclopropane species (Figure 5.13) generated in the reaction. The major product was (4,4,4-tribromobut-1-en-2-yl)benzene (Figure 5.13) with a conversion of 45%. Furthermore, the ratio between dibromo and tribromo is 1/8.8 according to peaks integrate in GC-MS. After purification by chromatography on silica with hexane as the elution, pure (4,4,4-tribromobut-1-en-2-yl)benzene was obtained as clear oil.



R_f (hexane): 0.65;

m/z: 367.823 (100.0%), 369.821 (97.3%), 365.825 (34.3%), 371.819 (31.5%), 368.827 (9.7%), 370.825 (8.4%), 366.829 (3.7%), 372.823 (3.4%), 370.825 (2.1%), 368.827 (1.1%);

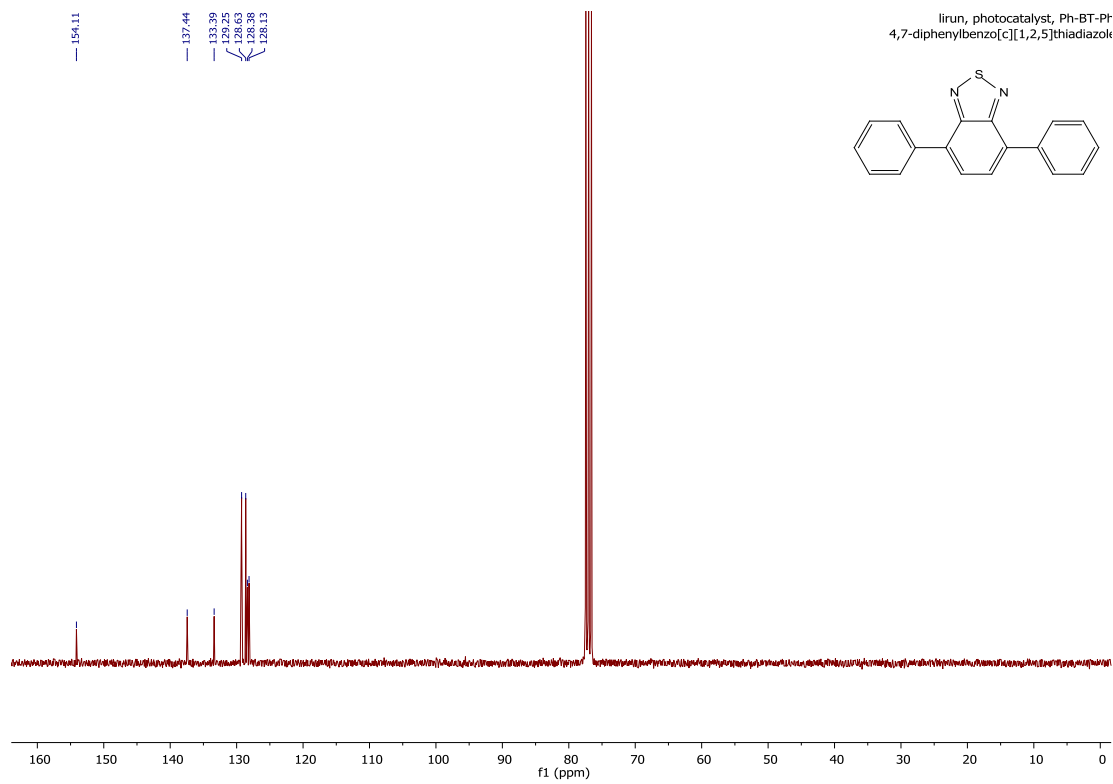
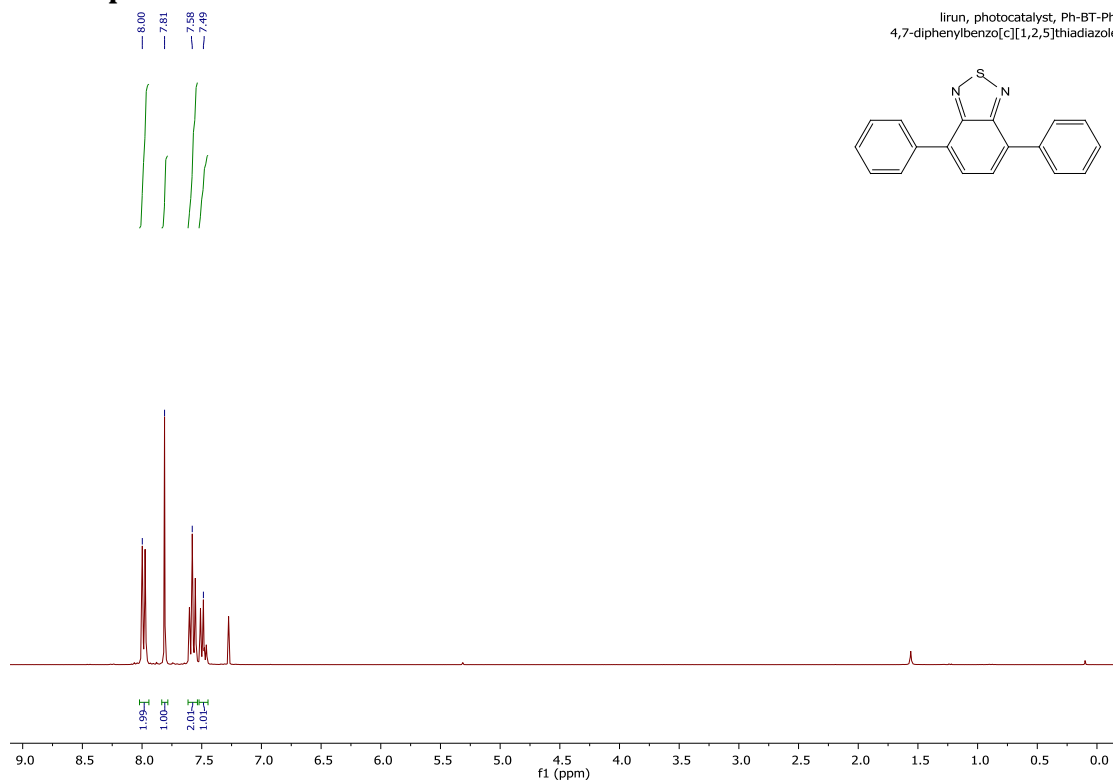
^1H NMR (CDCl_3 , 300 MHz): δ 7.35-7.16 (m, 5 H), 5.59 (s, 1 H), 5.49 (s, 1 H), 4.18 (s, 2 H);

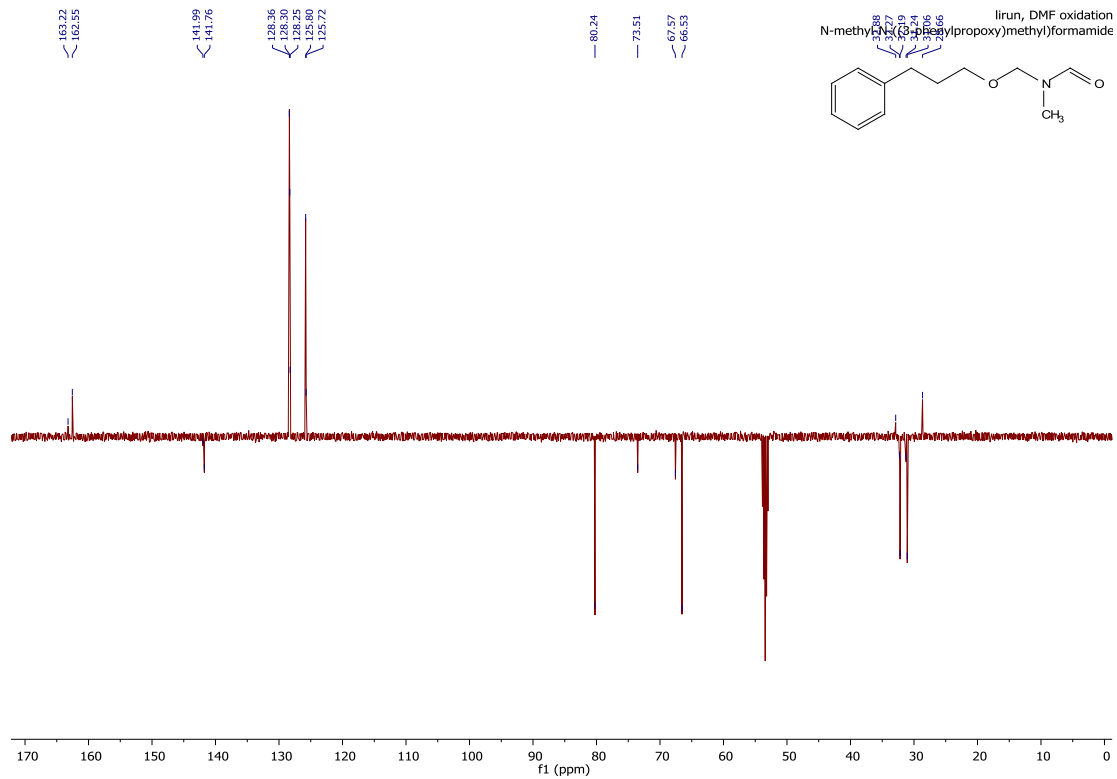
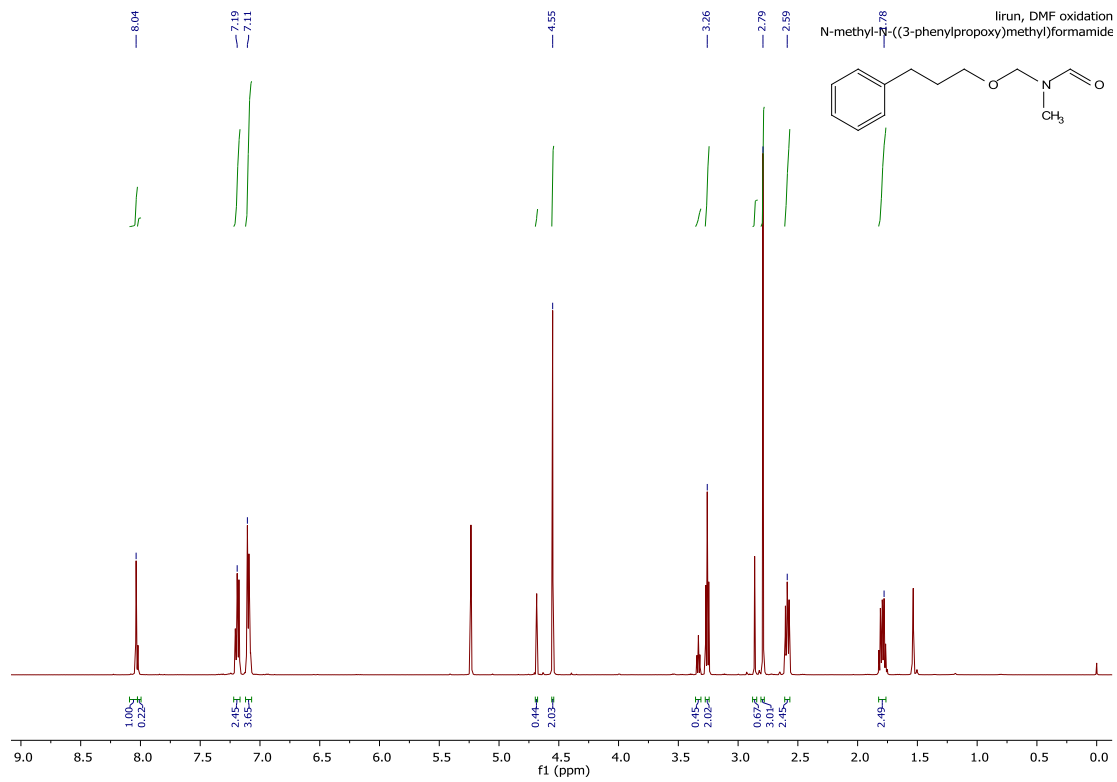
^{13}C NMR (CDCl_3 , 300 MHz): δ 144.1, 141.1, 128.4, 127.8, 127.0, 122.4, 62.7, 39.5.

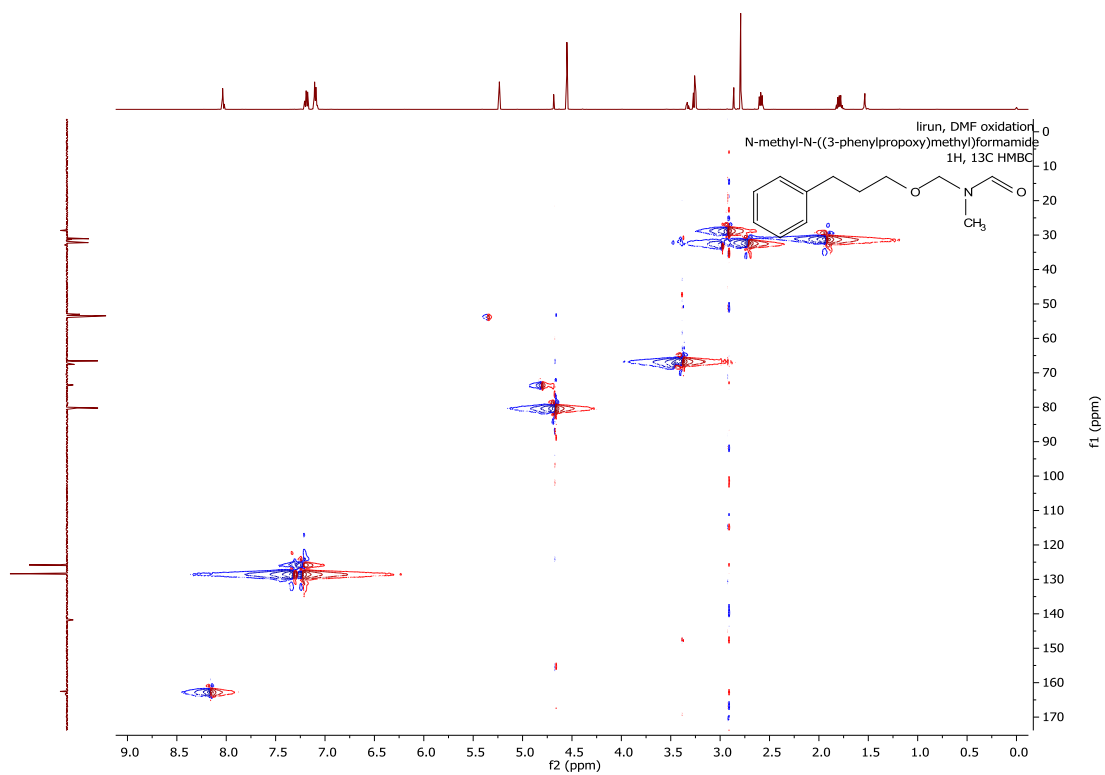
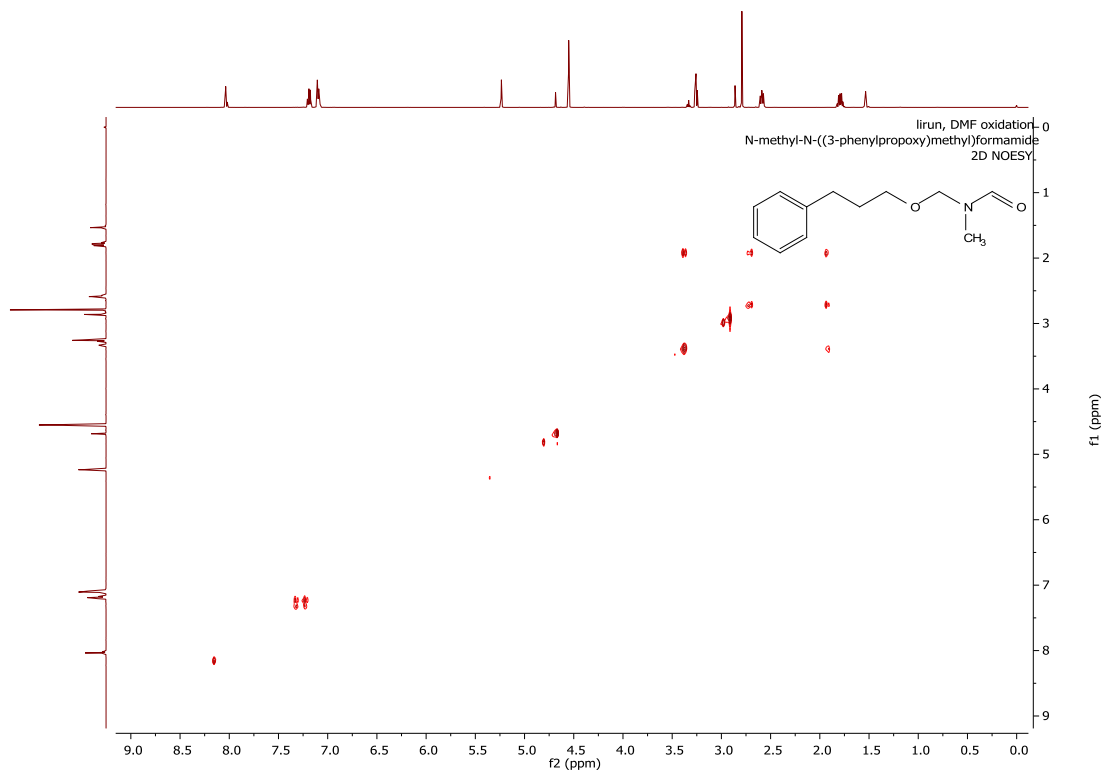
6.1.7 Repeating experiments for photocatalytic Diels-Alder reaction

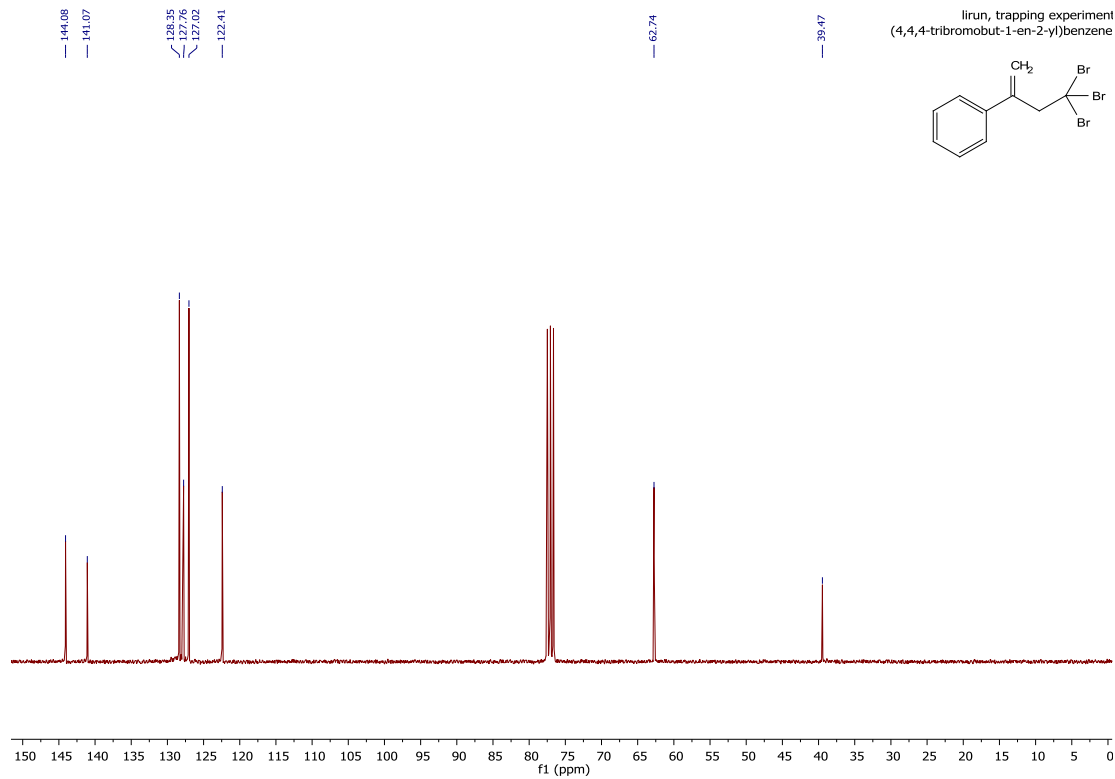
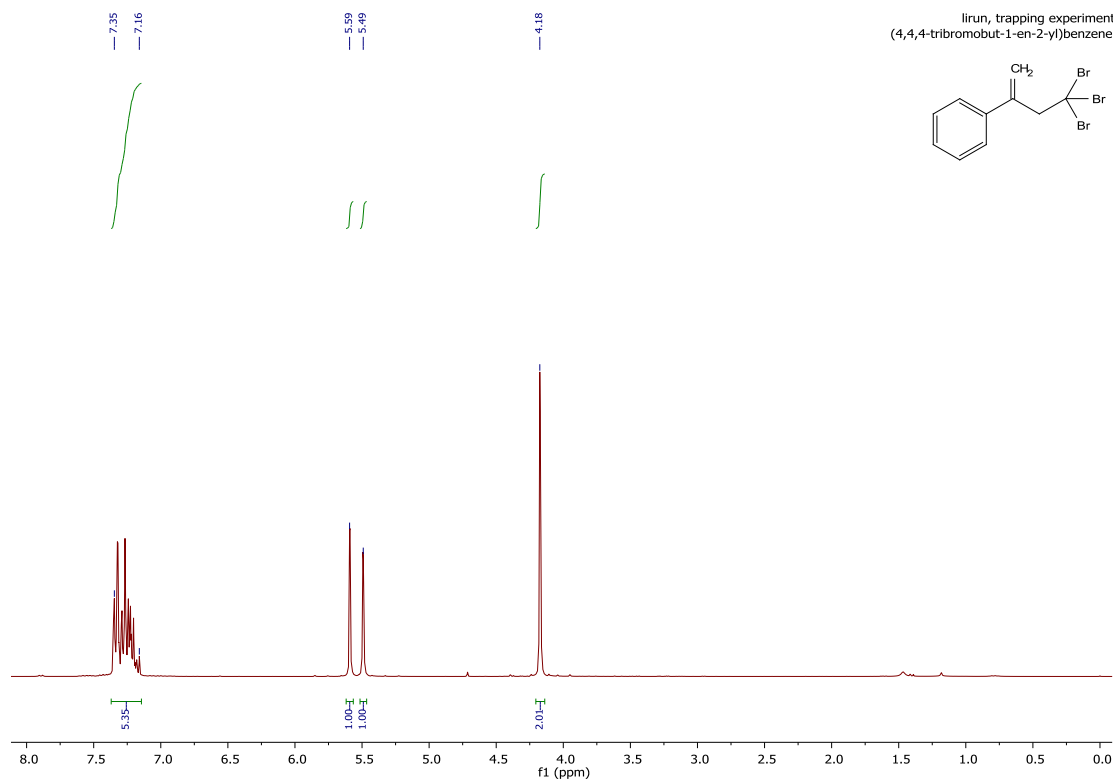
The recycling experiment was conducted similar to general procedure A without separating the photocatalyst after each cycle. Specifically, a dried vial with a magnetic stir bar was charged with *trans*-anethole (35.6 mg, 0.24 mmol), isoprene (240 μ l, 2.4 mmol), Ph-BT-Ph (2.4 mg, 0.0083 mmol) and acetonitrile (2.4 mL). After 10 min, 0.1 mL mixture was picked out by 1 mL syringe and the conversion for the reaction was obtained by GC-MS measurement after the mixture was washed with water and DCM for 3 times. Then without purification process, another *trans*-anethole (35.6 mg, 0.24 mmol) and isoprene (240 μ l, 2.4 mmol) were added into the mixture and the solution was irradiated under the blue light. After 10 min, 0.1 mL mixture was taken out and the conversion for the second cycle was gained by GC-MS measurement. The conversions for each cycle were received according the paralleled procedure.

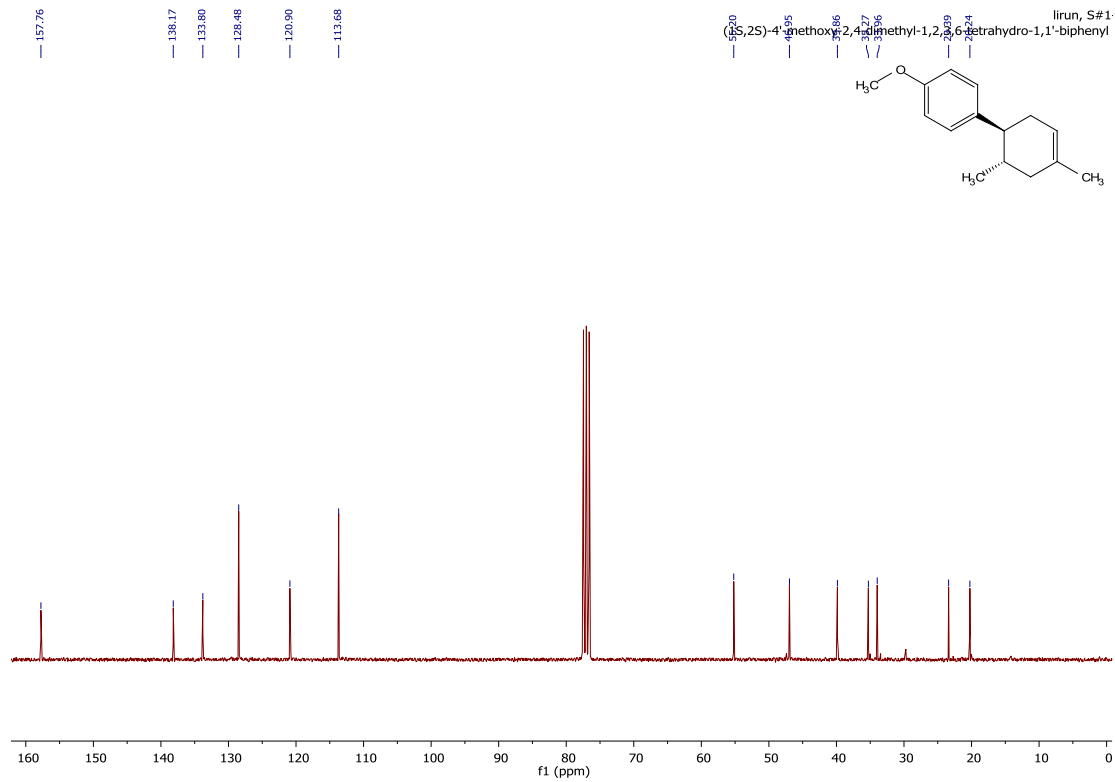
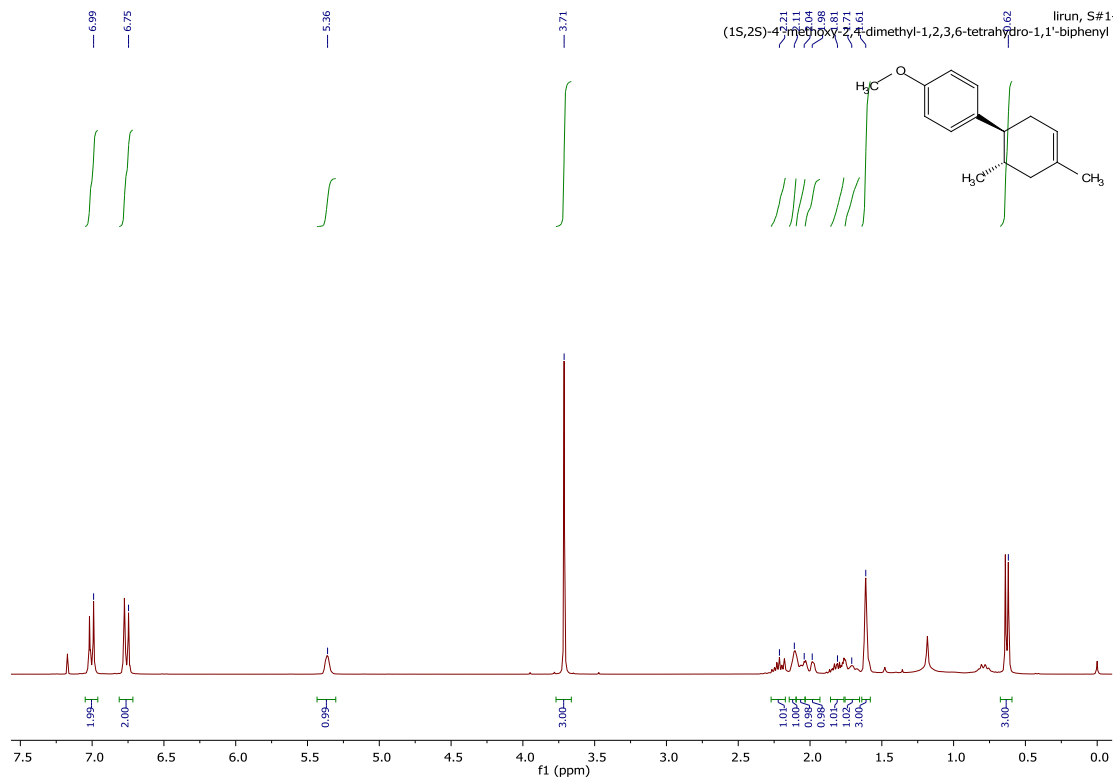
6.1.8 NMR spectra

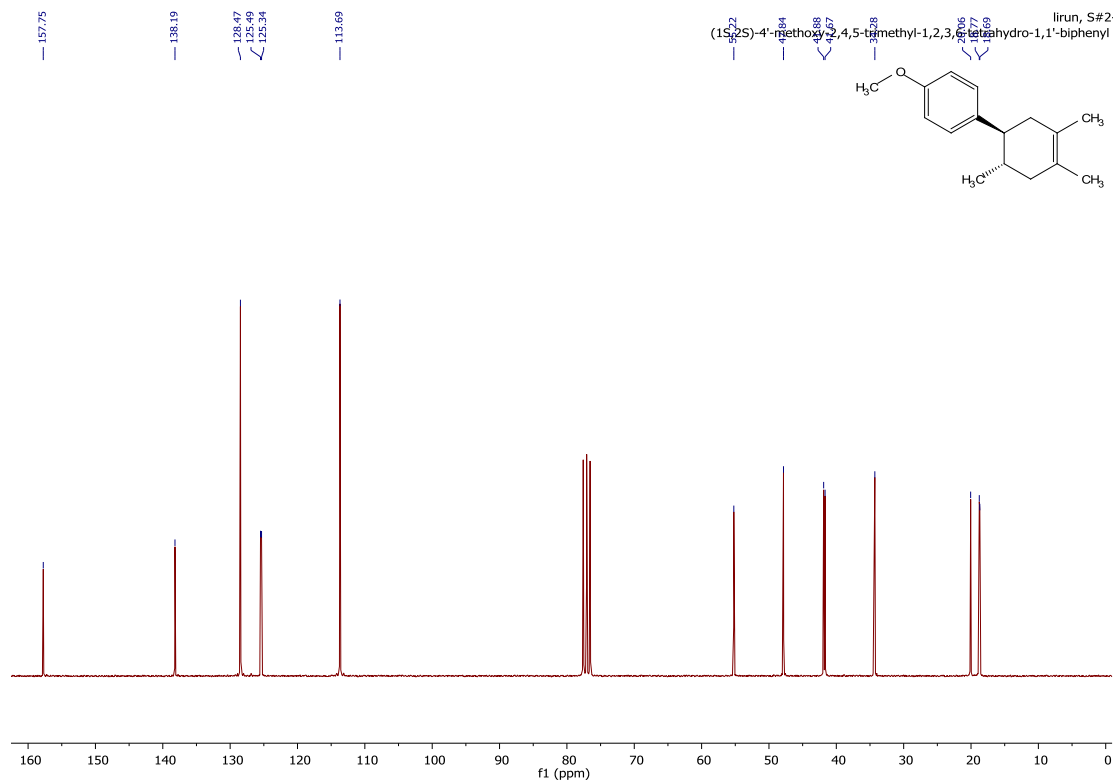
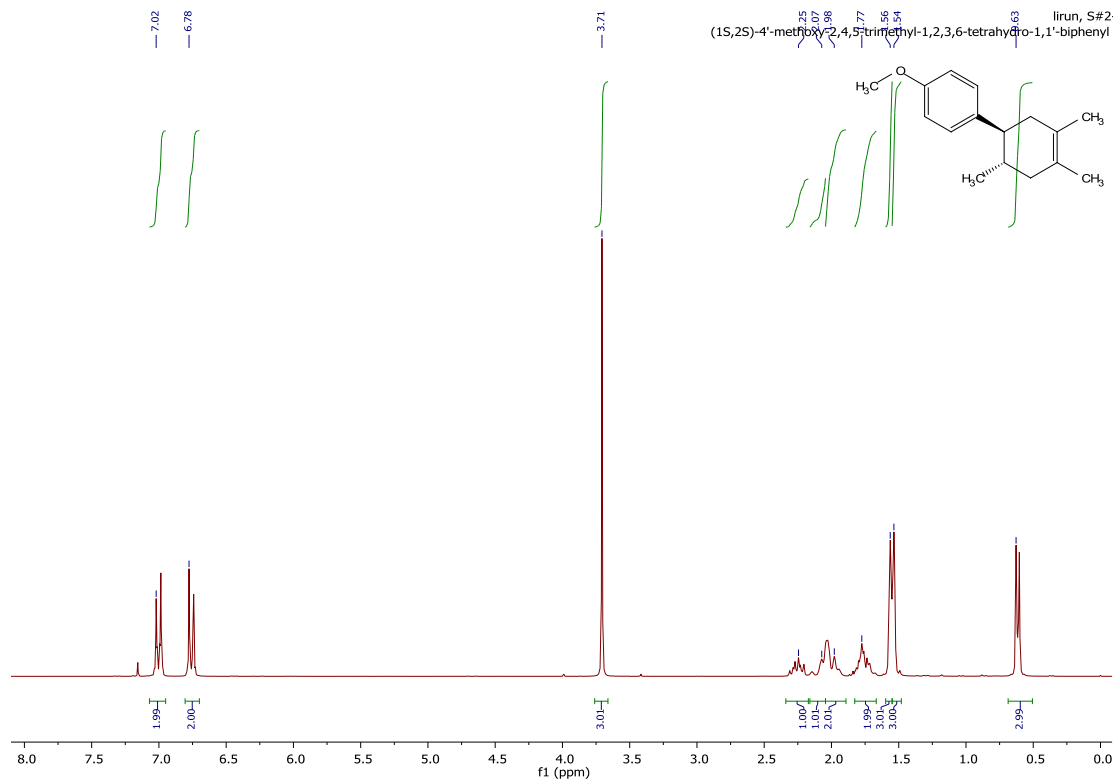


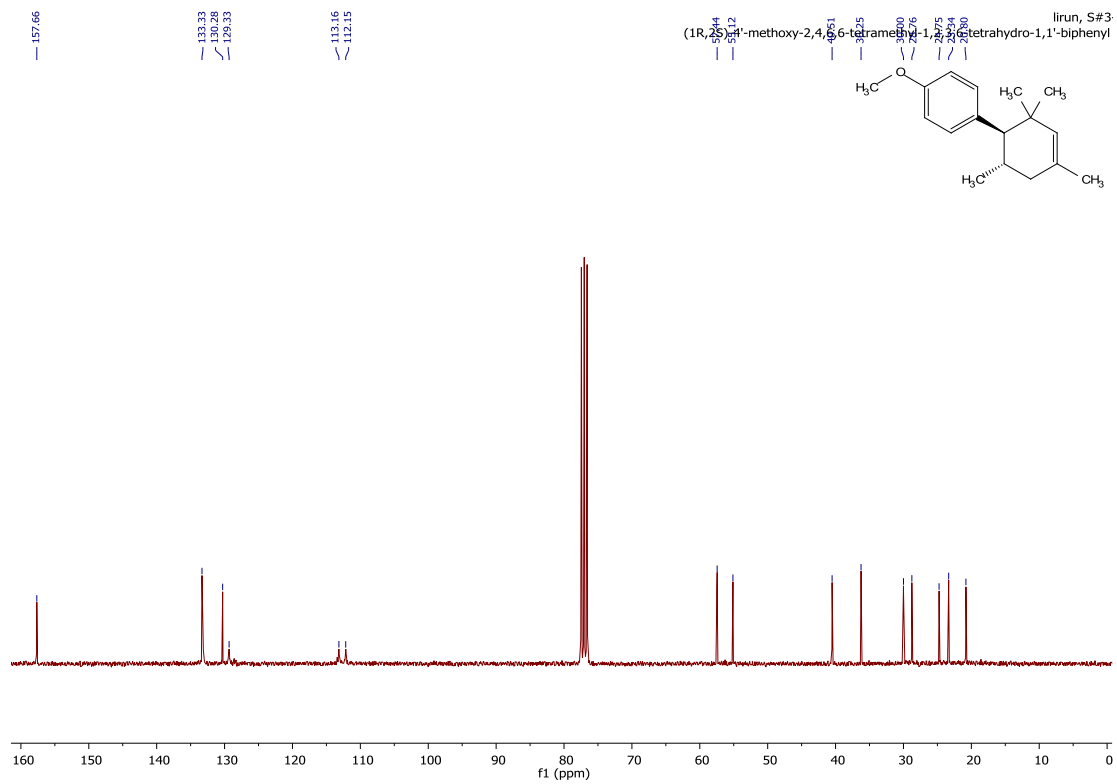
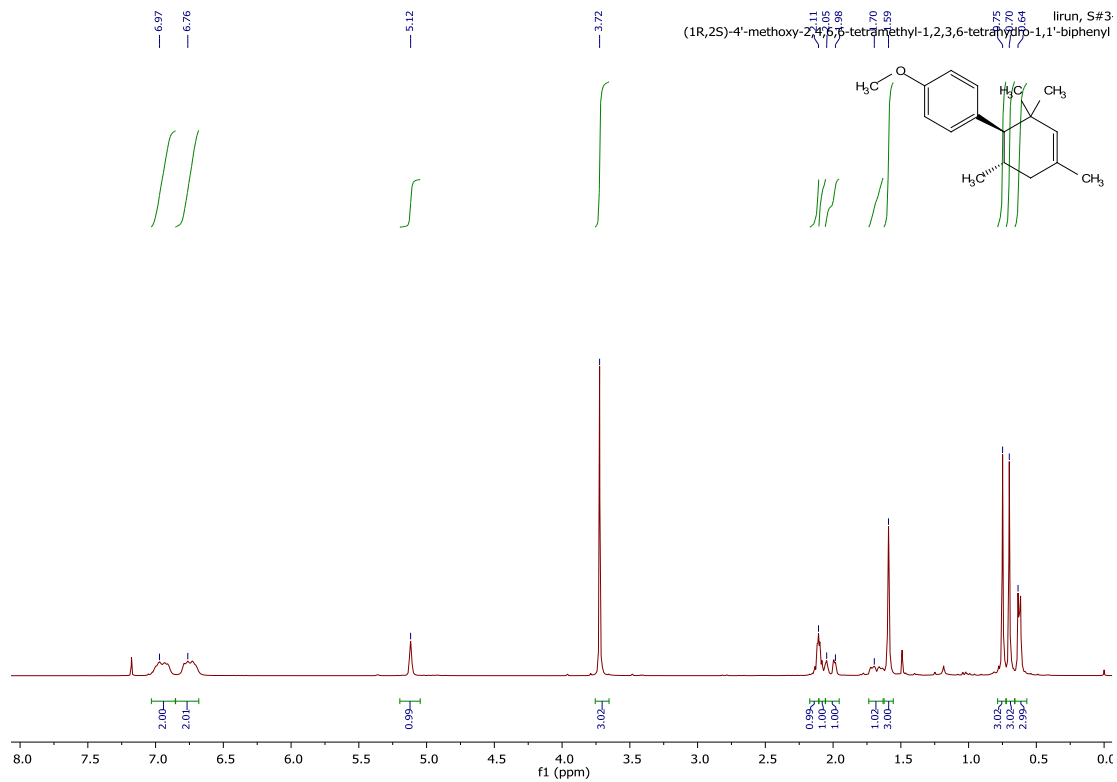


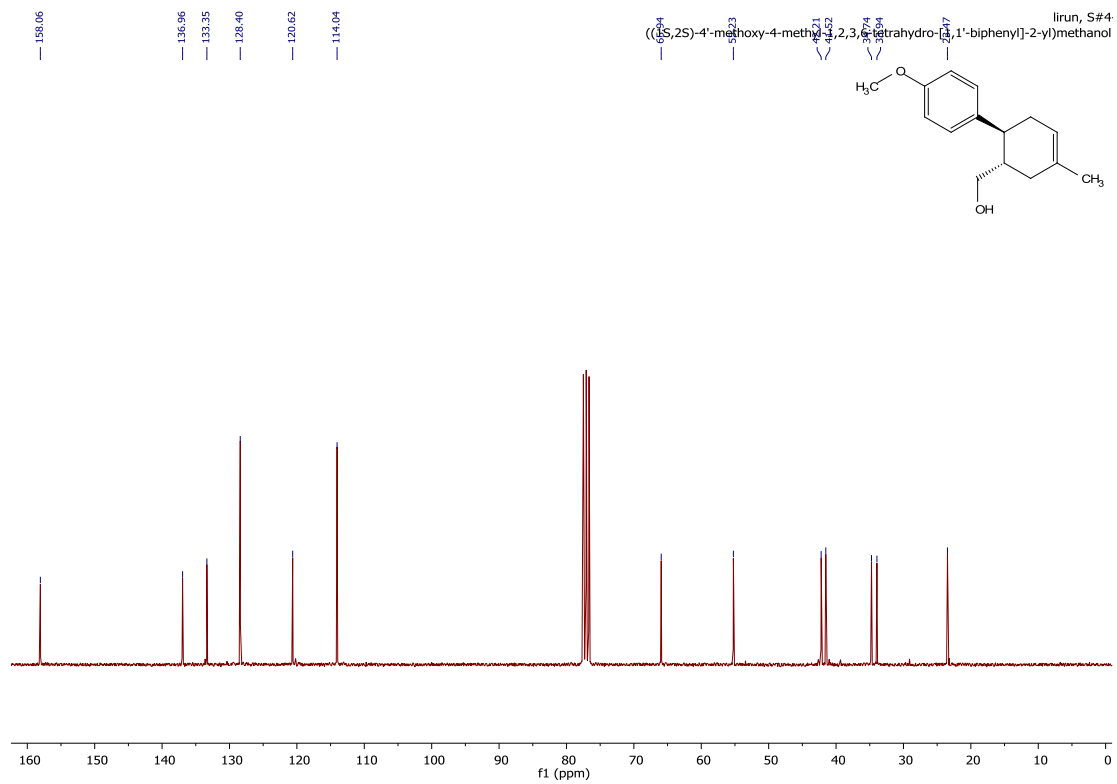
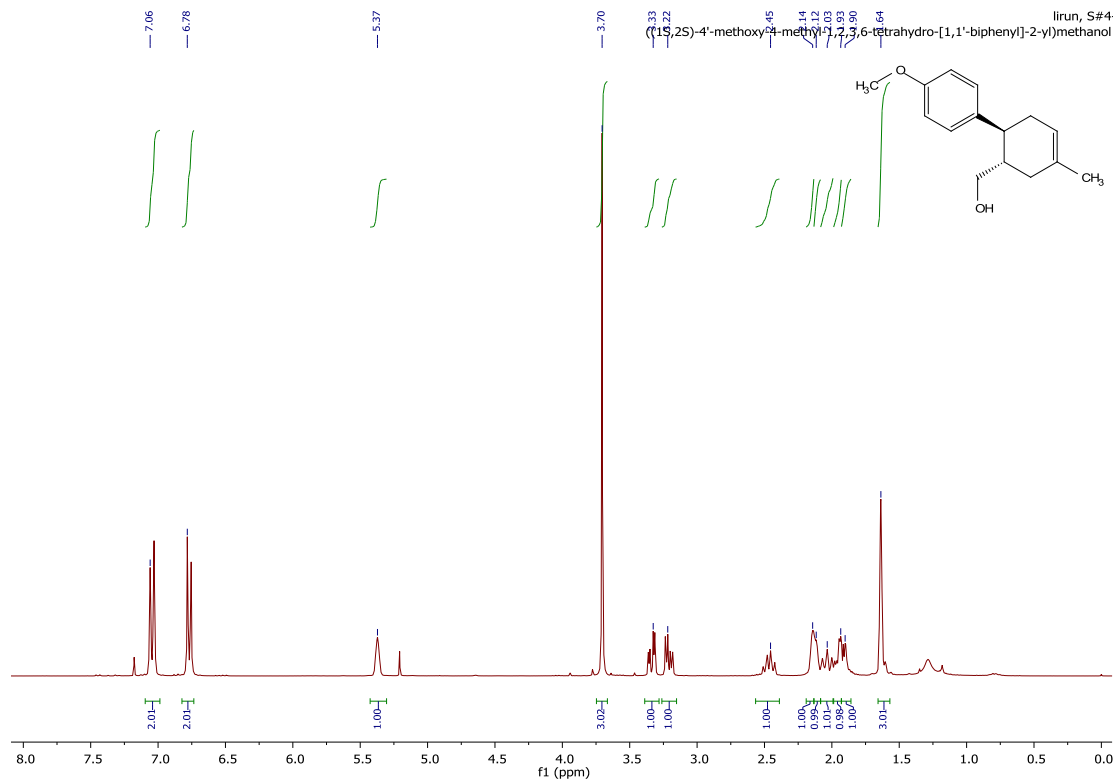


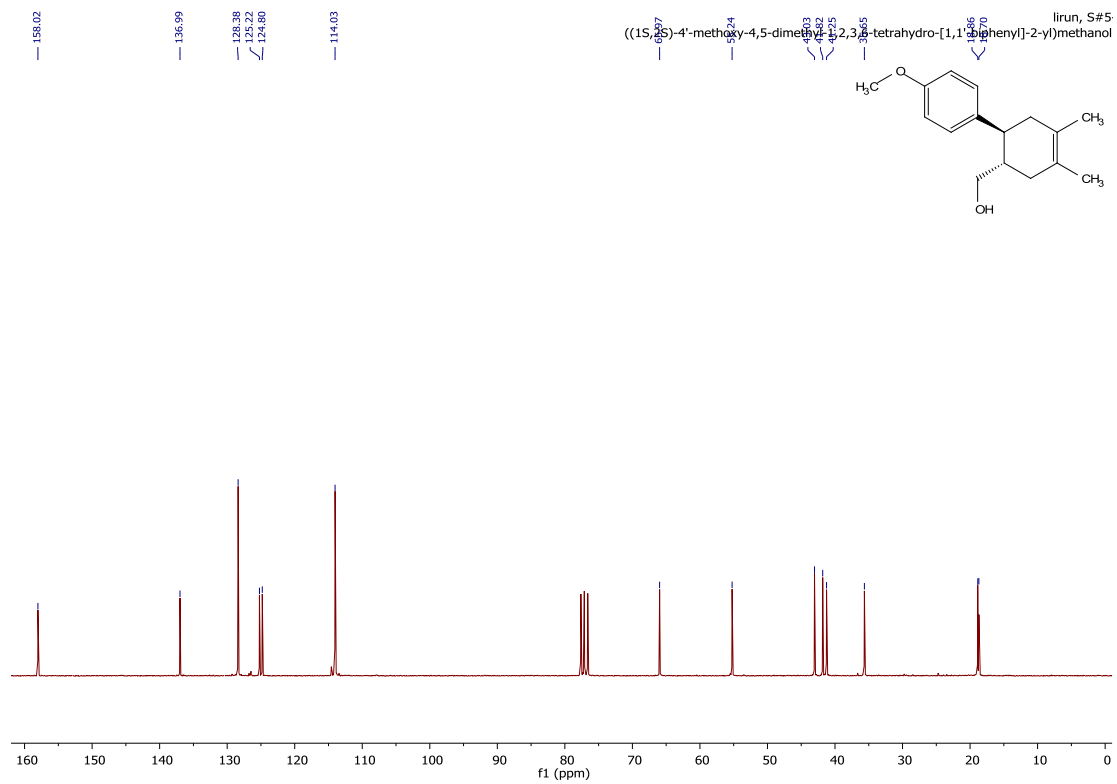
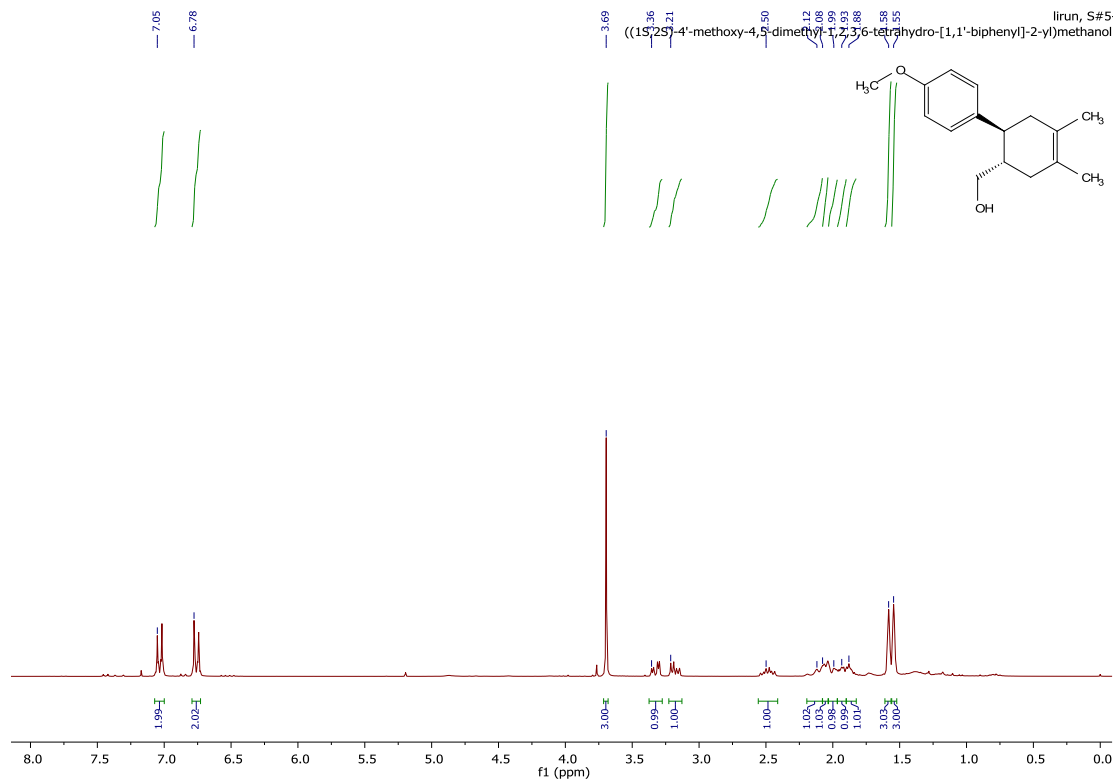


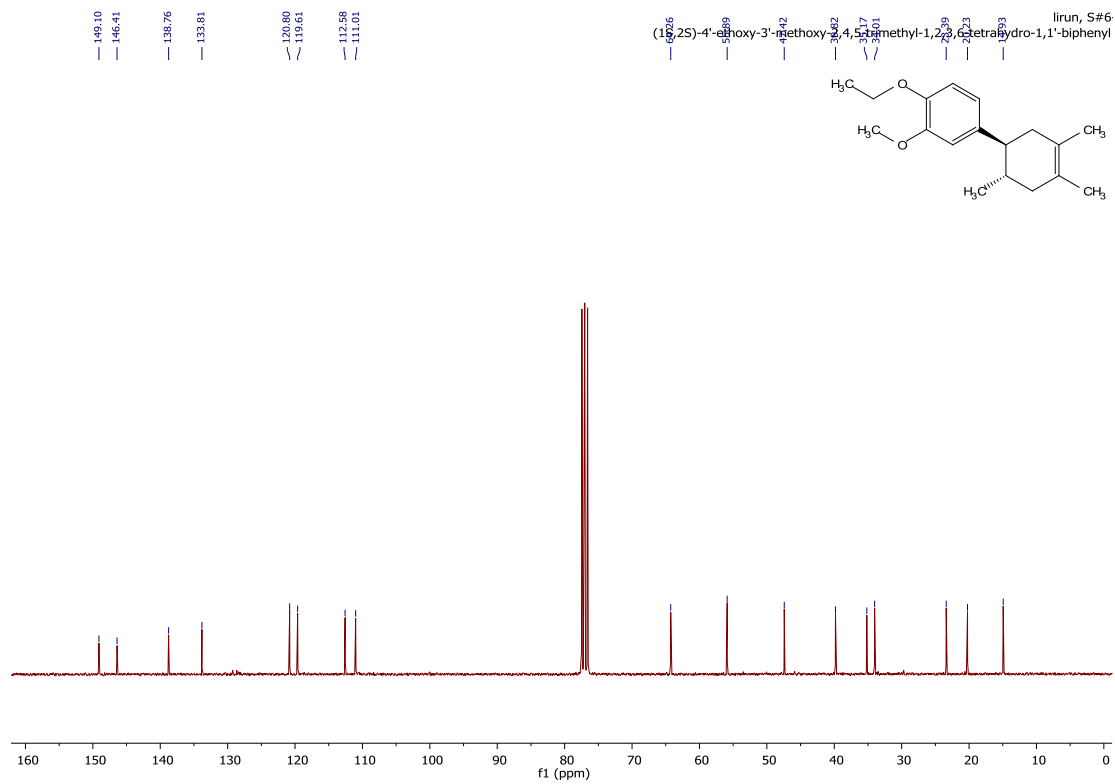
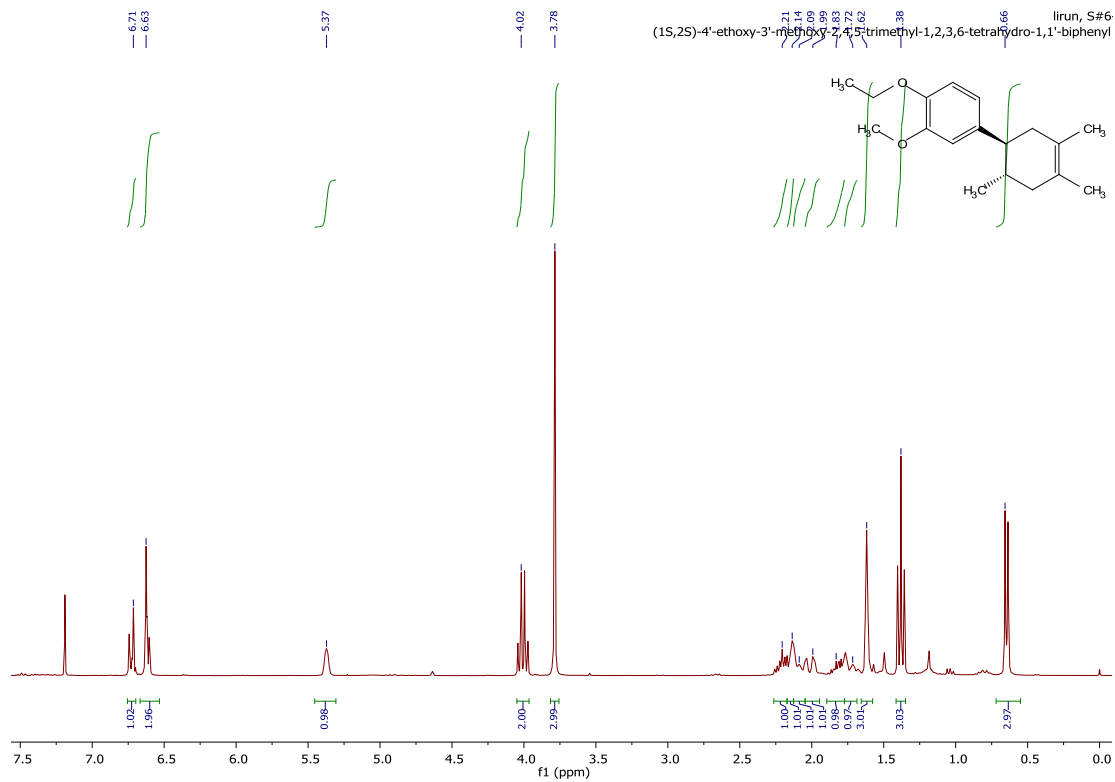


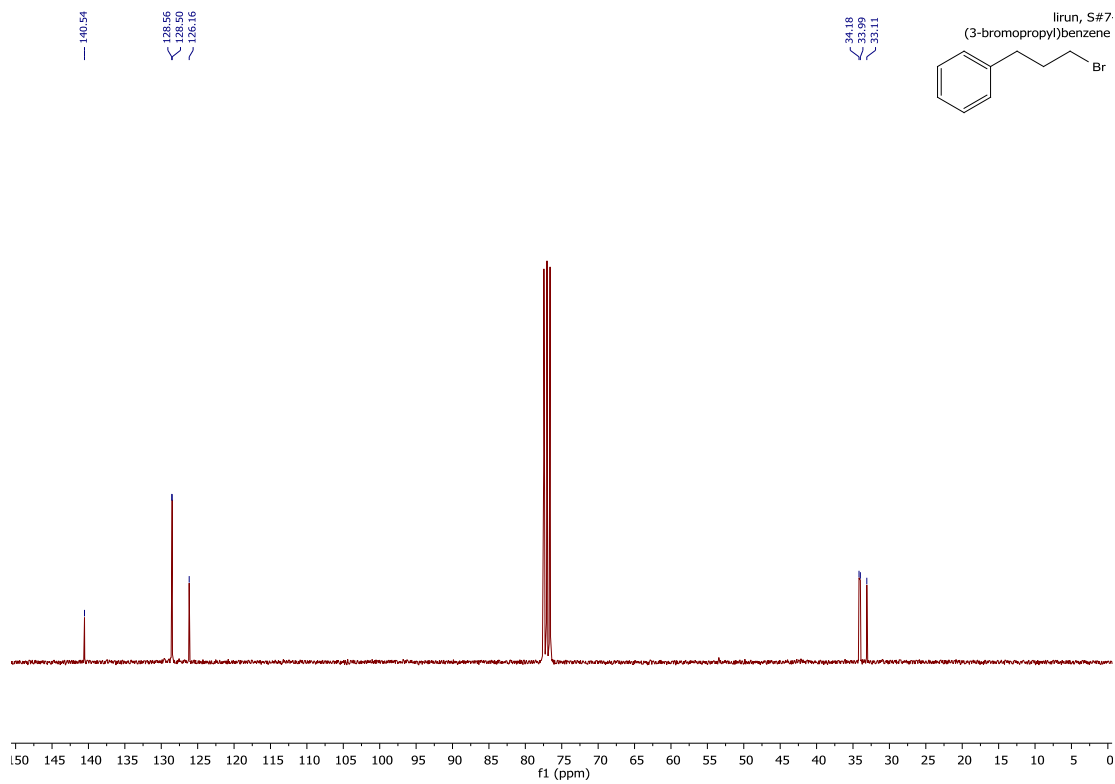
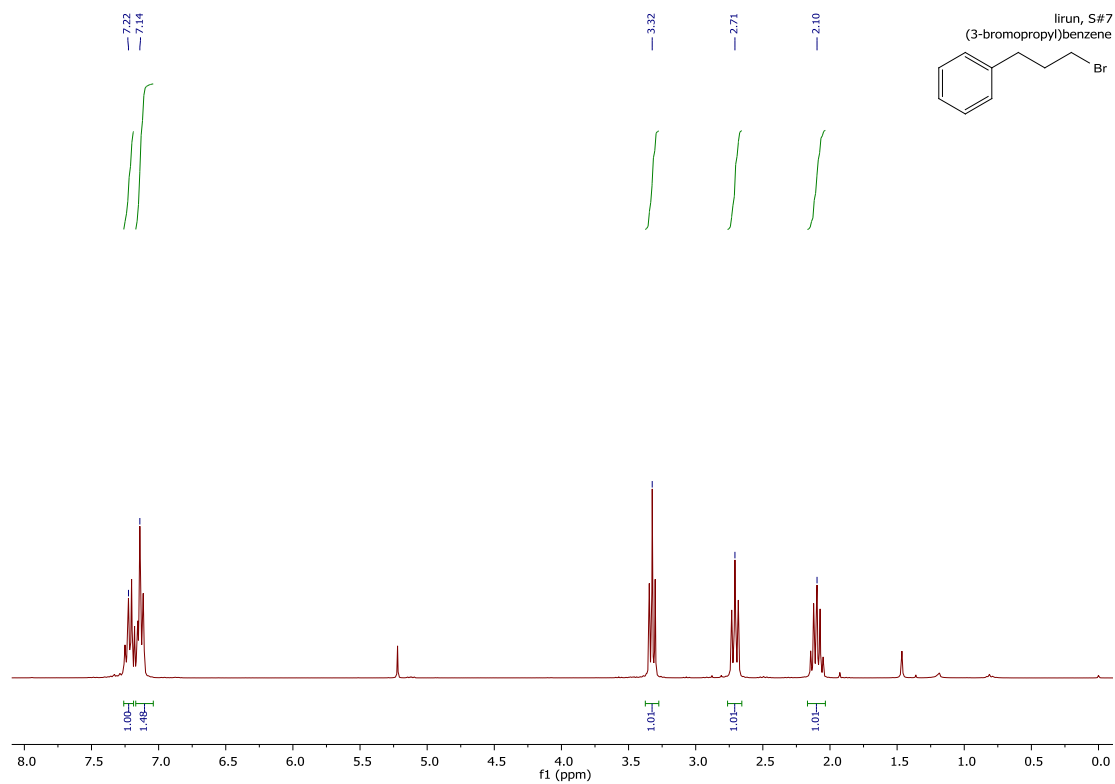


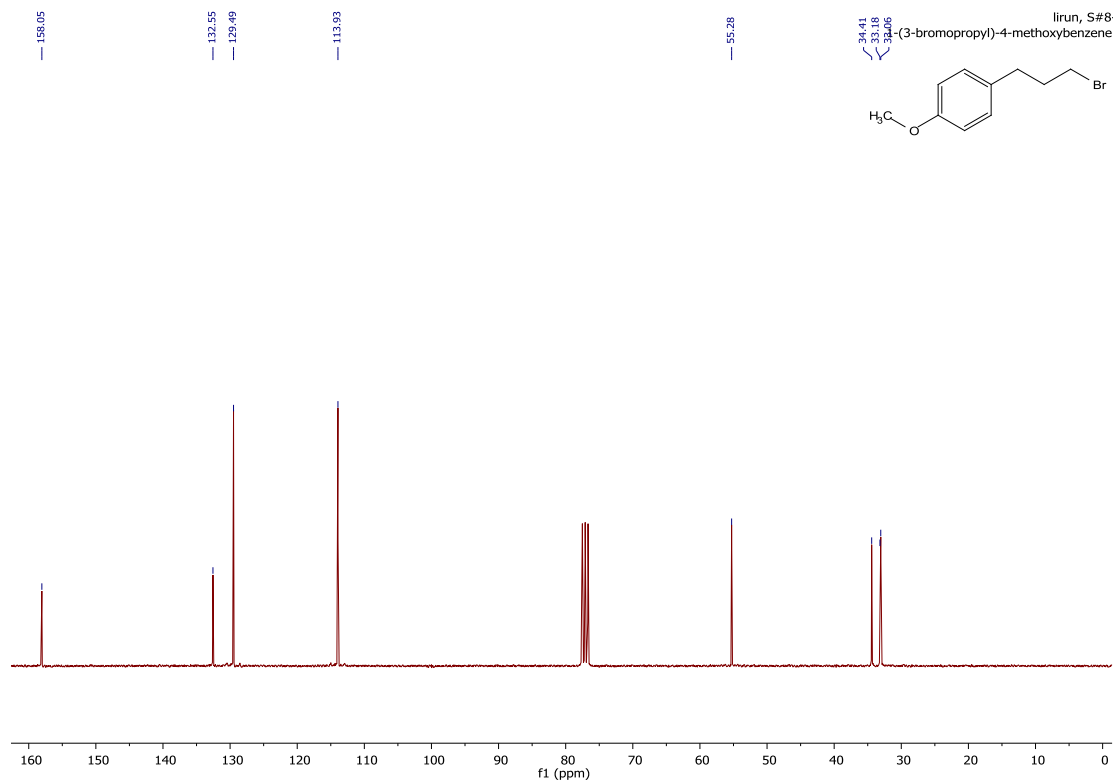
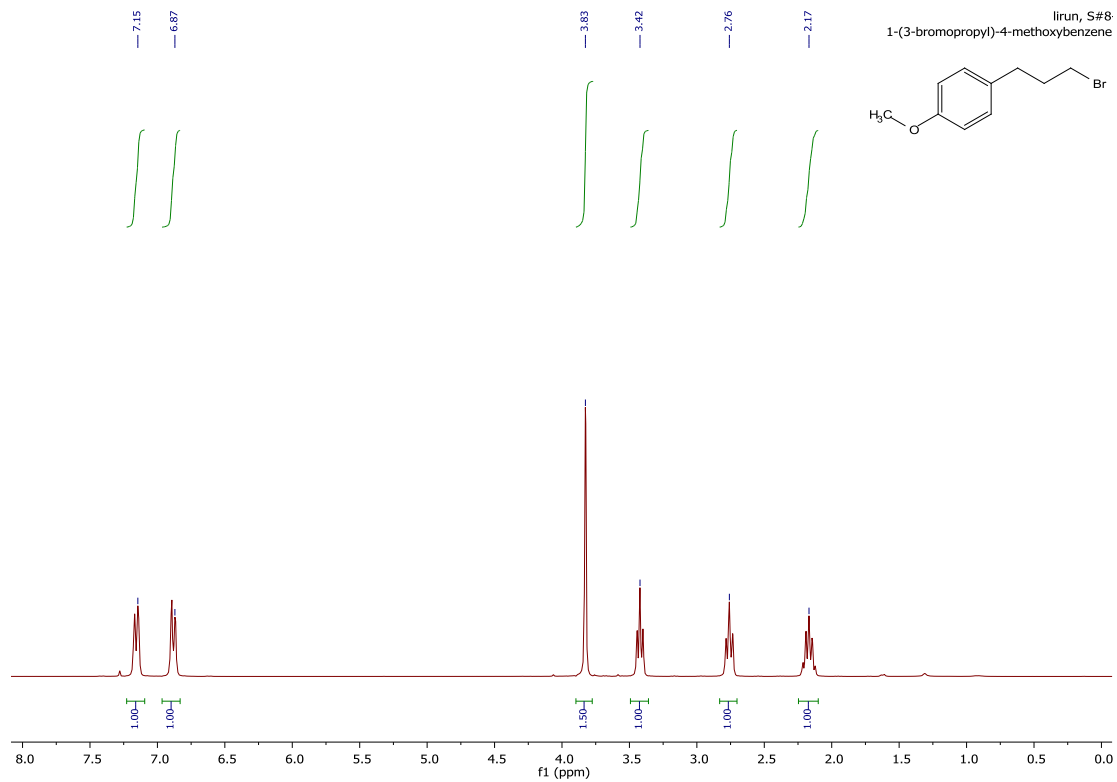


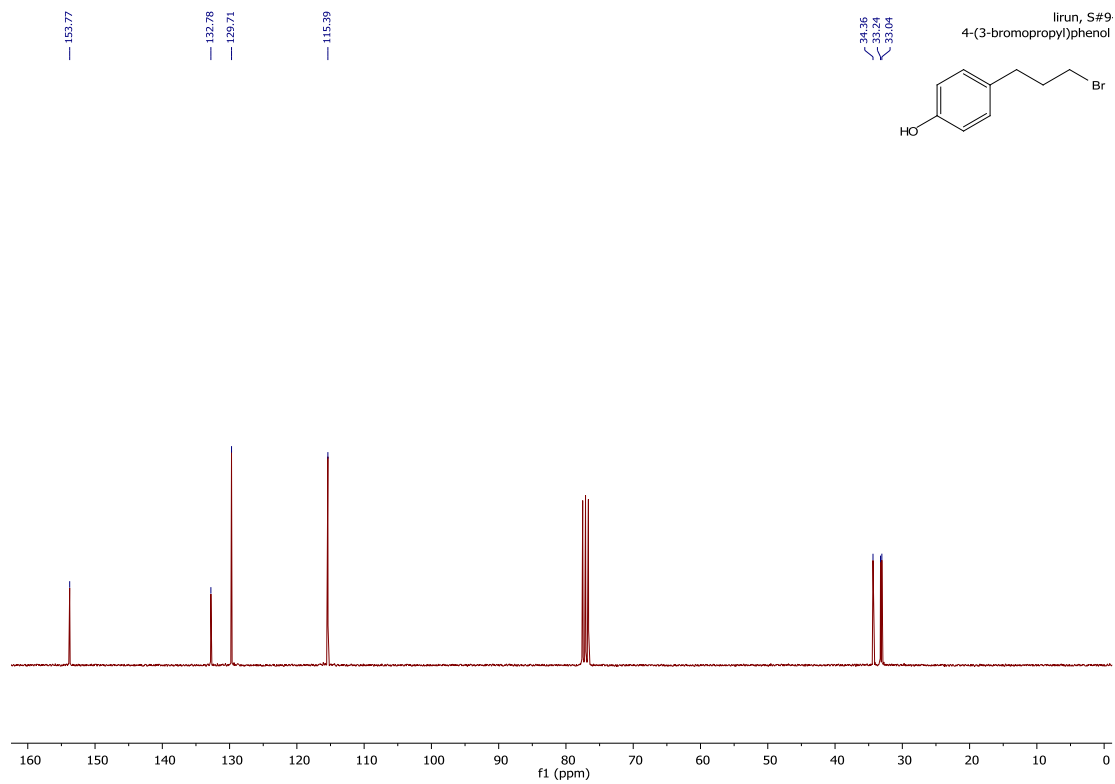
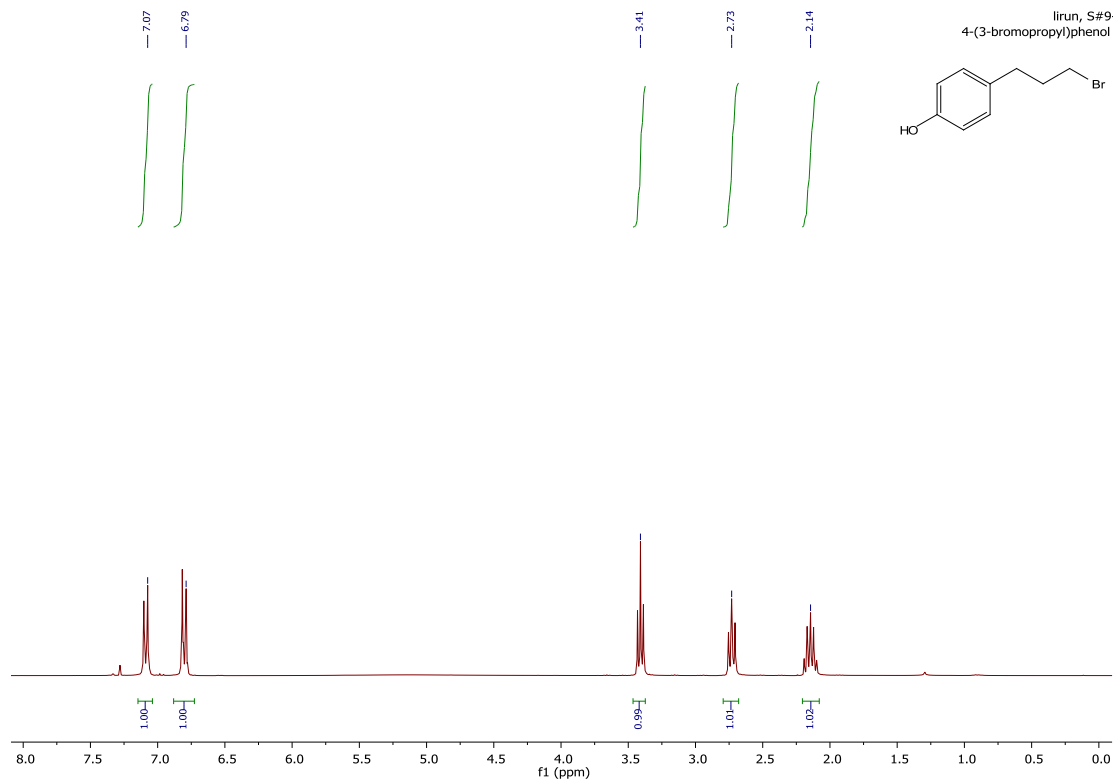


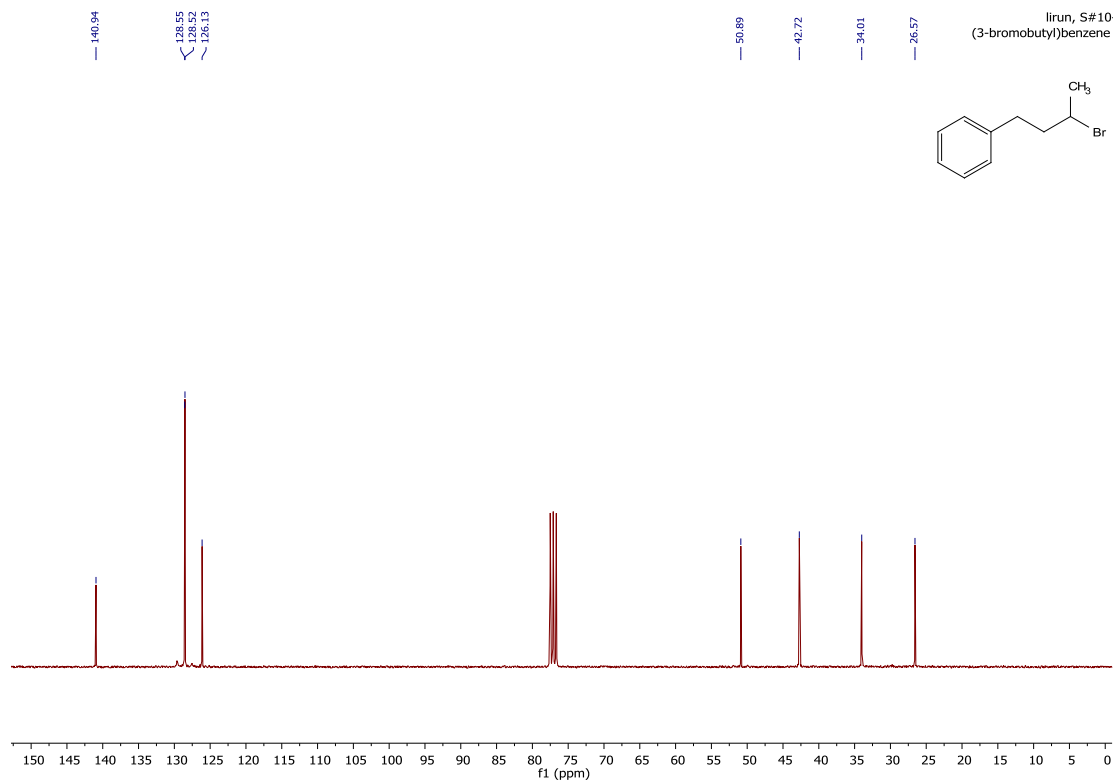
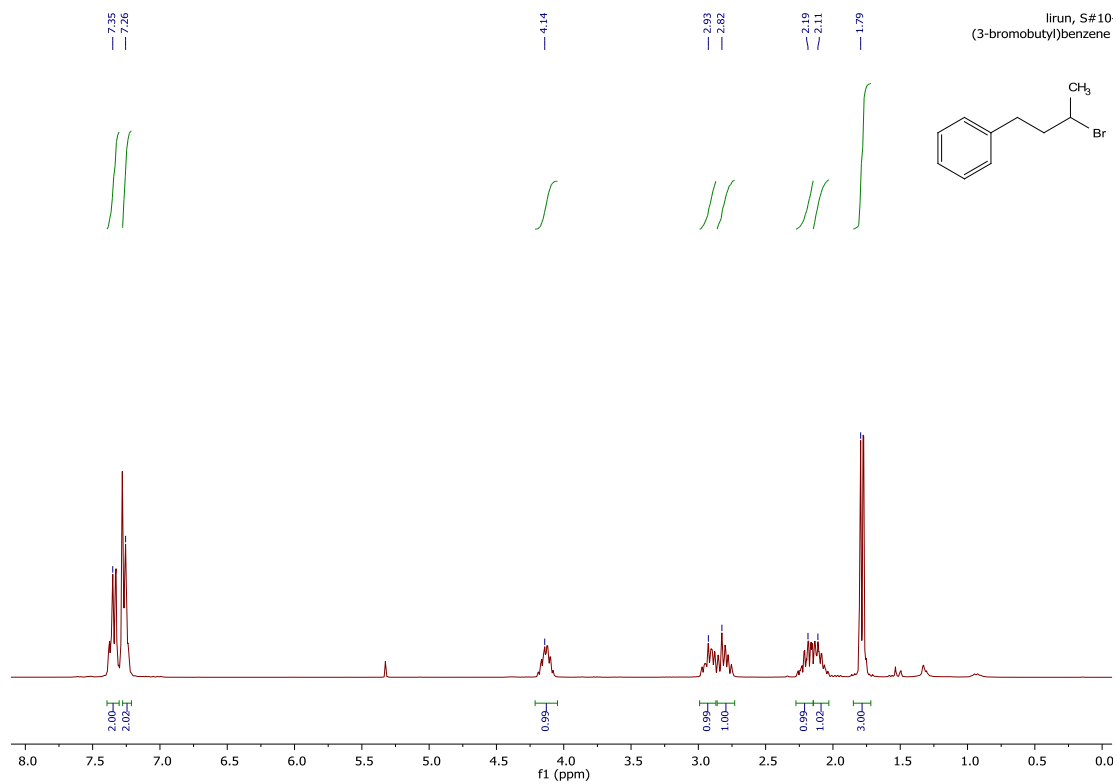


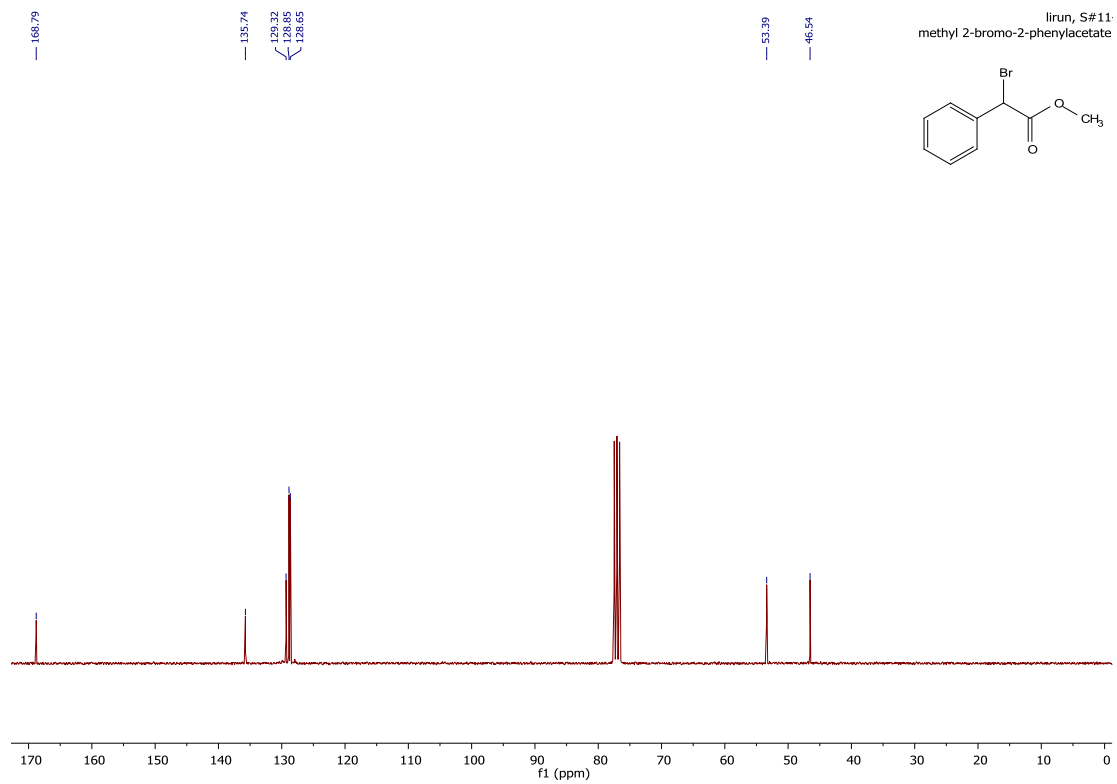
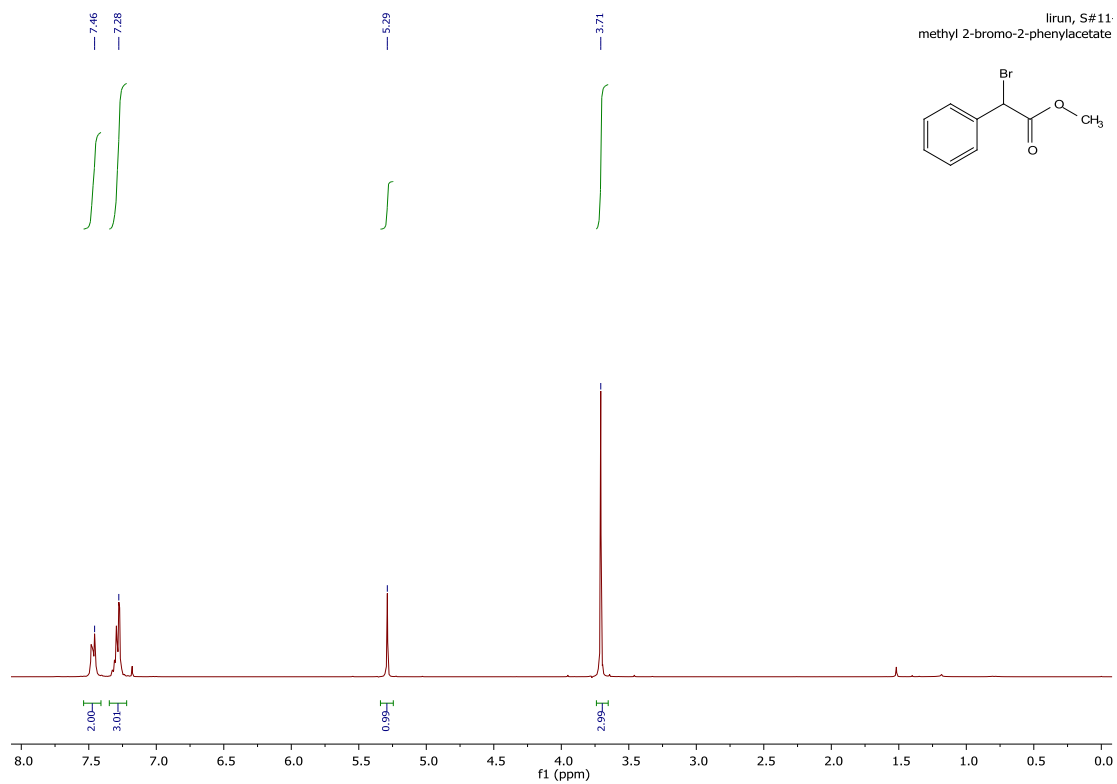


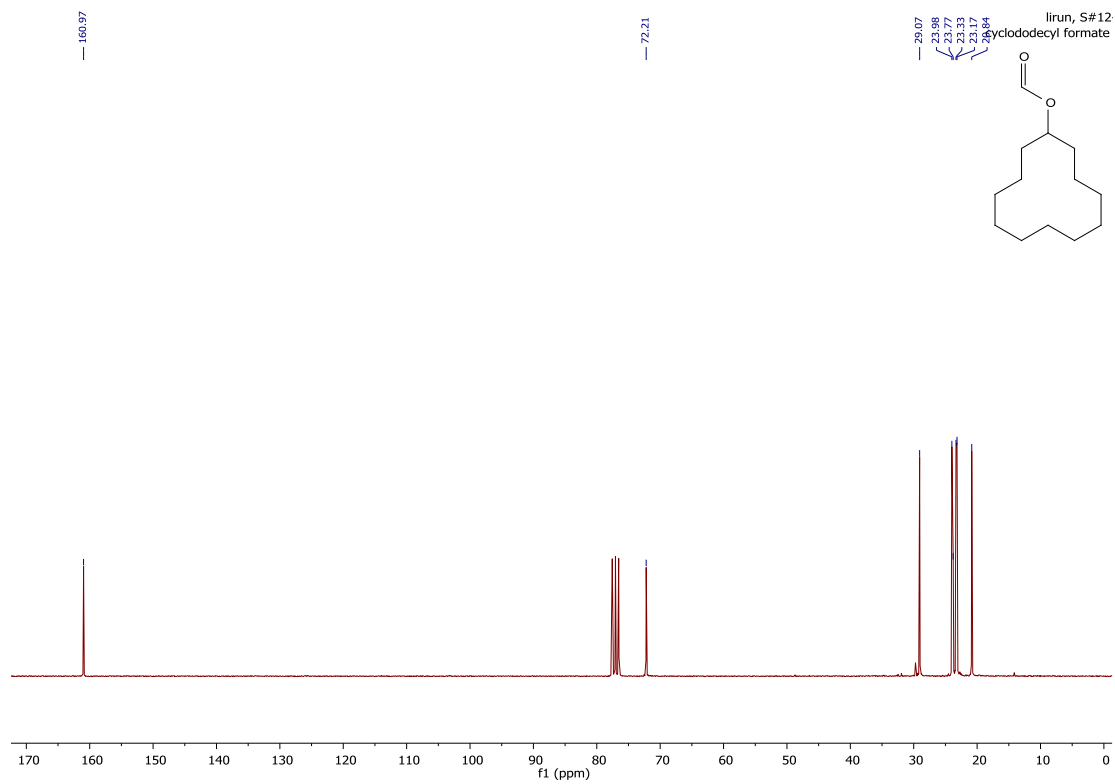
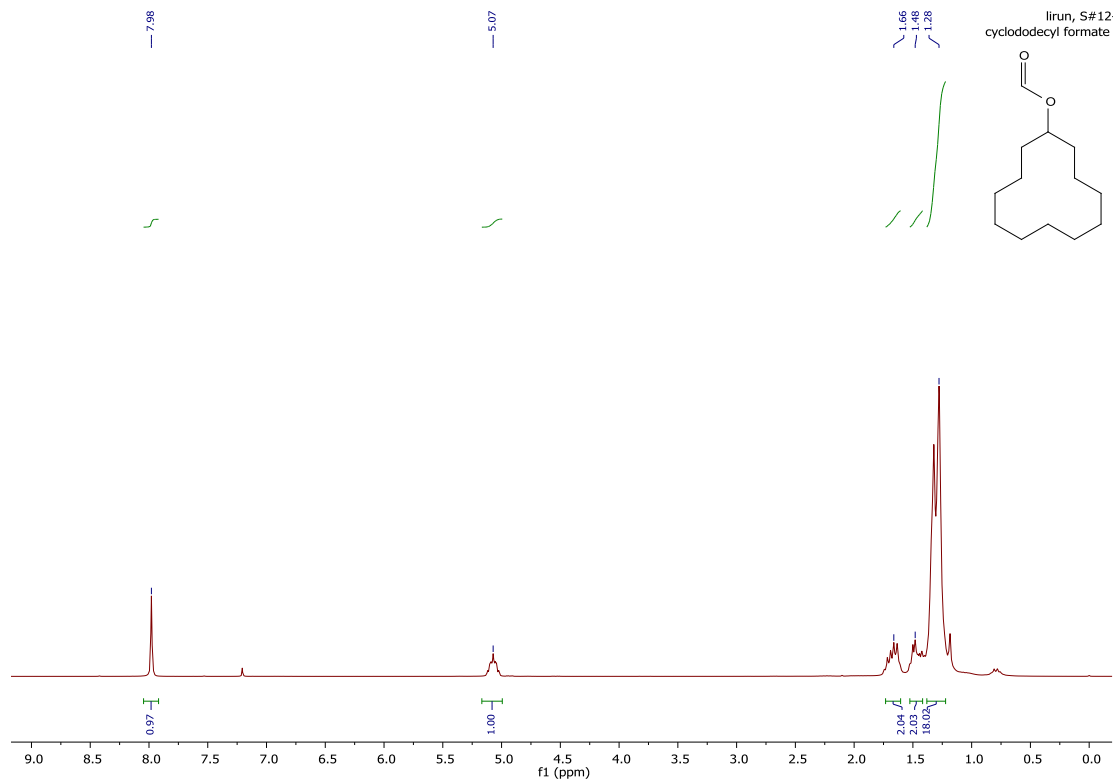












6.2 Photocatalytic selective bromination of electron-rich aromatic compounds using microporous organic polymers with visible light

6.2.1 Materials

All chemicals and solvents were purchased from commercial sources and used as received without further purification unless otherwise noted.

6.2.2 Methods and characterization

FTIR spectra were recorded on Varian 1000 FT-IR spectrometer. Solid state ^{13}C CP/MAS NMR spectra were measured with Bruker Avance II solid state NMR spectrometer under the condition of 300 MHz Larmor frequency coupled with a standard 4 mm magic angle spinning (MAS) double resonance probe head. UV-Vis absorption spectra were conducted on a Perkin Elmer Lambda 100 spectrophotometer at ambient temperature, respectively. The morphology was investigated on scanning electron microscope (SEM) (LEO Gemini 1530, Germany) with an in lens SE detector, and transmission electron microscope (TEM) (JEOL JEM-1400). Thermogravimetric analysis (TGA) was performed in a nitrogen atmosphere with temperature increasing from room temperature to 800 °C at a rate of 10 K/min. Electron paramagnetic resonance (EPR) spectra was recorded on a Magnettech Miniscope MS200 spectrometer. Conditions for spin trap EPR: DMPO (0.12 M), TEMP (0.12 M), MOP (1 mg/mL) in DMF, blue light 2 h. The mixture was separated by filtration and the supernatant was subjected to the ESR measurement. Cyclic voltammetry measurement was performed on a Metrohm Autolab PGSTAT204 potentiostat/galvanostat with a three-electrode-cell system): glassy carbon electrode drop-casted with MOPs as the working electrode, Hg/HgCl₂ electrode as the reference electrode, platinum wire as the counter electrode, and Bu₄NPF₆ (0.1 M Acetonitrile) as supporting electrolyte with a scan rate of 100 mV s⁻¹ in the range of -2 V to 2.5 V. The oxidation potential of substrates was obtained by dissolving substrates into acetonitrile directly with the similar measurement conditions. Surface areas and pore size distributions of MOPs were conducted by nitrogen adsorption and desorption at 77.3 K using Autosorb 1 (Quantachrome Instruments). Data was obtained using QuadraWin software from Quantachrome Instruments. Pore size distributions and pore volumes were calculated from the adsorption branches of the isotherms using Quenched Solid Density Functional Theory (QSDFT, N₂, evaluating carbon adsorbent with slit pores). The MOPs were degassed at 110 °C for 24 h under vacuum before analysis. The BET surface area was obtained based on data points received from $0 < P/P_0 < 0.25$ and the nonlinear density functional theory (NLDFT) equilibrium model was employed as the BET model fitting.

6.2.3 Synthesis of photocatalysts MOPs

Monomer synthesis: the preparation of 4,7-diphenyl-2,1,3-benzothiadiazole (Ph-BT-Ph) was the same as chapter 6.1.3

Polymer synthesis of MOP-0b and MOP-1b

FeCl₃ (4.87 mg, 30 μmol, anhydrous) was added to a solution of benzene (0.89 mL, 10 mmol) in 10 mL 1, 2-dichloroethane (DCE). After being stirred at room temperature for 30 min, formaldehyde dimethyl acetal (FDA, 2.67 mL) was added. Then the resulting mixture were stirred first at 45 °C for 5 h, and then at 80 °C for another 19 h to complete the cross-linking reaction. The obtained precipitate was washed with methanol for three times and then extracted in a Soxhlet extractor with methanol/dichloromethane for 24 h. The product MOP-0 was collected and dried under vacuum (60 °C).

MOP-1b was obtained in a similar manner using Ph-BT-Ph instead of benzene as monomer.

Polymer synthesis of MOP-0 and MOP-1

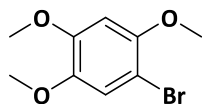
FeCl₃ (729.9 mg, 4.5 mmol, anhydrous) was added to a solution of Ph-BT-Ph (144.2 mg, 0.5 mmol) in 10 mL 1, 2-dichloroethane (DCE). After the resulting mixture being stirred at room temperature for 30 min, formaldehyde dimethyl acetal (FDA, 0.14 mL) was added. Then the reaction was took place at 45 °C for 5 h and 90 °C for 19 h to form the original network. After cooling to room temperature, FDA (0.13 mL) was added again and reacted with original polymer to get secondary network. Afterward, finally network was obtained by adding FDA in the third cycle. After cooling, 30 mL methanol was added to the reaction mixture and stirred for another 1 h. The resulting precipitate was washed with methanol for three times. After washing with methanol, the obtained solid was vigorously stirred in concentrated HCl for two hours. Then, the suspension was filtered and washed with water and methanol. After extraction with methanol/dichloromethane in a Soxhlet extractor for 24 h and with tetrahydrofuran for another 24 h, the MOP-1 was collected and dried in vacuum oven (60 °C).

For MOP-0, the same amount of the reactants as for MOP-0b was used, and under the same successive addition condition as for MOP-1.

6.2.4 Photocatalytic selective bromination of aromatic compounds using the MOPs as heterogeneous photocatalysts

General procedure:

In a flame-dried 25 mL Schlenk flask with a magnetic stir bar was charged with MOPs (10 mg), reactive substrates (0.16 mmol) and acetonitrile (10 mL). Then, 48% aqueous solution of HBr (22.5 μ L, 0.24 mmol) was added and the mixture was saturated with O₂ by bubbling O₂ for 5 min. The mixture was irradiated with a blue LED lamp (460 nm, 1.2 W/cm²) at room temperature. The conversion into the brominated compounds was determined by TLC and ¹H-NMR measurement. After the reaction was completed finished, the mixture was poured into a separatory funnel containing the mixture of hexane (25 mL) and H₂O (25 mL). The organic layer was separated and extracted with hexane for 2 more times and then the combined organic layers were washed with saturated Na₂S₂O₃, water and dried over anhydrous MgSO₄. The obtained crude product was further purified via column chromatography on silica to offer the final products.

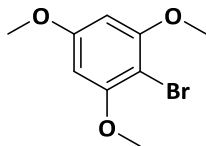


1-bromo-2,4,5-trimethoxybenzene (Table 5.7, 1):

According to the general procedure, a 25 mL Schlenk flask with a magnetic stir bar was charged with 1,2,4-trimethoxybenzene (22.7 μ L, 0.16 mmol), MOP-1 (10 mg), HBr (48%, 22.5 μ L, 0.24 mmol) and acetonitrile (10 mL). Then the mixture was saturated with O₂ for 5 min and irradiated under the blue LED light. After the reaction was completed, the mixture was performed as the workup protocol and purified by chromatography on silica with hexane/ethyl acetate (14/1) as the elution to afford the final pure bromides (yield: 89%).

¹H NMR (CDCl₃, 300 MHz): δ 7.05 (s, 1H), 6.58 (s, 1H), 3.90 (s, 3H), 3.89 (s, 3H), 3.85 (s, 3H);

¹³C NMR (CDCl₃, 300 MHz): δ 150.30, 149.09, 143.81, 116.45, 101.09, 98.89, 57.24, 56.65, 56.27.

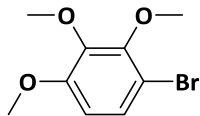


2-Bromo-1,3,5-trimethoxybenzene (Table 5.7, 2):

According to the general procedure, a 25 mL Schlenk flask with a magnetic stir bar was charged with 1,3,5-trimethoxybenzene (26.9 mg, 0.16 mmol), MOP-1 (10 mg), HBr (48%, 22.5 μ L, 0.24 mmol) and acetonitrile (10 mL). Then the mixture was saturated with O₂ for 5 min and irradiated under the blue LED light. After the reaction was completed, the mixture was performed as the workup protocol and purified by chromatography on silica with hexane/dichloromethane (6/1) as the elution to afford the final pure bromides (yield: 82%).

¹H NMR (CDCl₃, 300 MHz): δ 6.10 (s, 2H), 3.81 (s, 6H), 3.75 (s, 3H);

¹³C NMR (CDCl₃, 300 MHz): δ 161.48, 157.49, 92.05, 91.66, 56.38, 55.54.

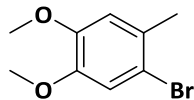


1-bromo-2,3,4-trimethoxybenzene (Table 5.7, 3):

According to the general procedure, a 25 mL Schlenk flask with a magnetic stir bar was charged with 1,2,3-trimethoxybenzene (26.9 mg, 0.16 mmol), MOP-1 (10 mg), HBr (48%, 22.5 μ L, 0.24 mmol) and acetonitrile (10 mL). Then the mixture was saturated with O₂ for 5 min and irradiated under the blue LED light. After the reaction was completed, the mixture was performed as the workup protocol and purified by chromatography on silica with dichloromethane as the elution to afford the final pure bromides (yield: 50%).

¹H NMR (CDCl₃, 300 MHz): δ 7.21 (d, J = 9 Hz, 1H), 6.59 (d, J = 9 Hz, 1H), 3.92 (s, 3H), 3.90 (s, 3H), 3.87 (s, 3H);

¹³C NMR (CDCl₃, 300 MHz): δ 153.34, 151.01, 143.55, 126.76, 108.63, 108.41, 61.12, 56.19.

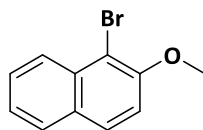


1-bromo-4,5-dimethoxy-2-methylbenzene (Table 5.7, 4):

According to the general procedure, a 25 mL Schlenk flask with a magnetic stir bar was charged with 1,2-dimethoxy-4-methylbenzene (23.2 μ L, 0.16 mmol), MOP-1 (10 mg), HBr (48%, 22.5 μ L, 0.24 mmol) and acetonitrile (10 mL). Then the mixture was saturated with O₂ for 5 min and irradiated under the blue LED light. After the reaction was completed, the mixture was performed as the workup protocol and purified by chromatography on silica with hexane/dichloromethane (3/1) as the elution to afford the final pure bromides (yield: 75%).

¹H NMR (CDCl₃, 300 MHz): δ 6.93 (s, 1H), 6.66 (s, 1H), 3.78 (s, 3H), 3.78 (s, 3H), 2.26 (s, 3H);

¹³C NMR (CDCl₃, 300 MHz): δ 148.16, 147.63, 129.62, 115.32, 114.42, 113.56, 56.18, 56.02.

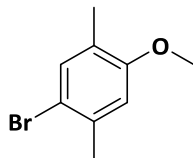


1-bromo-2-methoxynaphthalene (Table 5.7, 5):

According to the general procedure, a 25 mL Schlenk flask with a magnetic stir bar was charged with 2-methoxynaphthalene (23.8 μ L, 0.16 mmol), MOP-1 (10 mg), HBr (48%, 22.5 μ L, 0.24 mmol) and acetonitrile (10 mL). Then the mixture was saturated with O₂ for 5 min and irradiated under the blue LED light. After the reaction was completed, the mixture was performed as the workup protocol and purified by chromatography on silica with hexane as the elution to afford the final pure bromides (yield: 84%).

¹H NMR (CDCl₃, 300 MHz): δ 8.14 (m, 1H), 7.74 (m, 1H), 7.71 (m, 1H), 7.50 (ddd, J = 3, 9, 15 Hz, 1H), 7.33 (ddd, J = 3, 9, 15 Hz, 1H), 7.23 (d, J = 9 Hz, 1H), 3.97 (s, 3H);

¹³C NMR (CDCl₃, 300 MHz): δ 153.75, 133.13, 129.82, 128.96, 128.03, 127.74, 126.13, 124.32, 113.62, 108.67, 57.08.

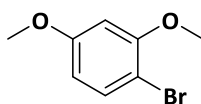


1-bromo-4-methoxy-2,5-dimethylbenzene (Table 5.7, 6):

According to the general procedure, a 25 mL Schlenk flask with a magnetic stir bar was charged with 2-methoxy-1,4-dimethylbenzene (22.6 μL , 0.16 mmol), MOP-1 (10 mg), HBr (48%, 22.5 μL , 0.24 mmol) and acetonitrile (10 mL). Then the mixture was saturated with O_2 for 5 min and irradiated under the blue LED light. After the reaction was completed, the mixture was performed as the workup protocol and purified by chromatography on silica with hexane/dichloromethane (3/1) as the elution to afford the final pure bromides (yield: 55%).

^1H NMR (CDCl_3 , 300 MHz): δ 7.18 (s, 1H), 6.60 (s, 1H), 3.72 (s, 3H), 2.28 (s, 3H), 2.08 (s, 3H);

^{13}C NMR (CDCl_3 , 300 MHz): δ 156.85, 135.66, 133.65, 126.06, 114.60, 112.50, 55.47, 22.89, 15.47.

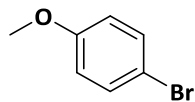


1-bromo-2,4-dimethoxybenzene (Table 5.7, 7):

According to the general procedure, a 25 mL Schlenk flask with a magnetic stir bar was charged with 1,3-dimethoxybenzene (21.0 μL , 0.16 mmol), MOP-1 (10 mg), HBr (48%, 22.5 μL , 0.24 mmol) and acetonitrile (10 mL). Then the mixture was saturated with O_2 for 5 min and irradiated under the blue LED light. After the reaction was completed, the mixture was performed as the workup protocol and purified by chromatography on silica with hexane/dichloromethane (5/1) as the elution to afford the final pure bromides (yield: 81%).

^1H NMR (CDCl_3 , 300 MHz): δ 7.43 (d, $J = 9$ Hz, 1H), 6.50 (d, $J = 3$ Hz, 1H), 6.43 (dd, $J = 3, 9$ Hz, 1H), 3.88 (s, 3H), 3.81 (s, 3H);

^{13}C NMR (CDCl_3 , 300 MHz): δ 160.23, 156.53, 133.13, 105.89, 102.41, 99.96, 56.13, 55.56.

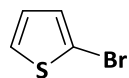


1-bromo-4-methoxybenzene (Table 5.7, 8):

According to the general procedure, a 25 mL Schlenk flask with a magnetic stir bar was charged with anisole (17.4 μ L, 0.16 mmol), MOP-1 (10 mg), HBr (48%, 22.5 μ L, 0.24 mmol) and acetonitrile (10 mL). Then the mixture was saturated with O₂ for 5 min and irradiated under the blue LED light. After the reaction was completed, the mixture was performed as the workup protocol and purified by chromatography on silica with hexane/dichloromethane (6/1) as the elution to afford the final pure bromides (yield: 55%).

¹H NMR (CDCl₃, 300 MHz): δ 7.32 (dd, J = 3, 6 Hz, 2H), 6.73 (dd, J = 3, 6 Hz, 2H), 3.72 (s, 3H);

¹³C NMR (CDCl₃, 300 MHz): δ 158.68, 132.22, 115.71, 112.80, 55.43.

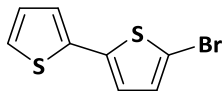


2-bromothiophene (Table 5.7, 9):

According to the general procedure, a 25 mL Schlenk flask with a magnetic stir bar was charged with thiophene (12.8 μ L, 0.16 mmol), MOP-1 (10 mg), HBr (48%, 22.5 μ L, 0.24 mmol) and acetonitrile (10 mL). Then the mixture was saturated with O₂ for 5 min and irradiated under the blue LED light. After the reaction was completed, the mixture was performed as the workup protocol and purified by chromatography on silica to afford the final pure bromides (yield: 70%).

¹H NMR (CDCl₃, 300 MHz): δ 7.25 (d, J = 6 Hz, 1H), 7.09 (m, 1H), 6.90 (m, 1H);

¹³C NMR (CDCl₃, 300 MHz): δ 129.88, 127.69, 127.03, 112.21.



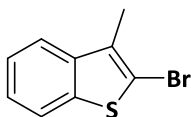
5-bromo-2,2'-bithiophene (Table 5.7, 10):

According to the general procedure, a 25 mL Schlenk flask with a magnetic stir bar was charged with 2,2'-bithiophene (26.6 mg, 0.16 mmol), MOP-1 (10 mg), HBr (48%, 22.5 μ L, 0.24 mmol) and acetonitrile (10 mL). Then the mixture was saturated with O₂ for 5 min and irradiated under the blue LED light. After the reaction was completed, the mixture was performed as the workup protocol and purified by chromatography on silica with hexane as the elution to afford the final pure bromides (yield: 80%).

R_f (hexane): 0.82

¹H NMR (CDCl₃, 300 MHz): δ 7.15 (dd, $J = 3, 6$ Hz, 1H), 7.03 (dd, $J = 1, 3$ Hz, 1H), 6.93 (dd, $J = 1.5, 3$ Hz, 1H), 6.88 (d, $J = 3$ Hz, 1H), 6.83 (d, $J = 3$ Hz, 1H);

¹³C NMR (CDCl₃, 300 MHz): δ 138.89, 136.40, 130.59, 127.88, 124.82, 124.05, 123.84, 110.91.



2-bromo-3-methylbenzo[b]thiophene (Table 5.7, 11):

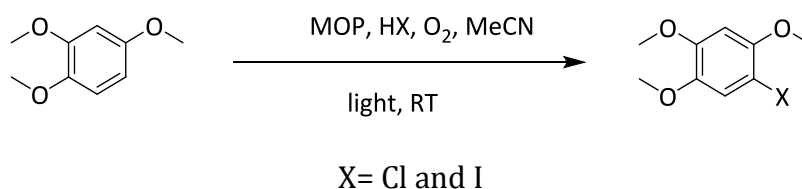
According to the general procedure, a 25 mL Schlenk flask with a magnetic stir bar was charged with 3-methylbenzo[b]thiophene (21.0 μ L, 0.16 mmol), MOP-1 (10 mg), HBr (48%, 22.5 μ L, 0.24 mmol) and acetonitrile (10 mL). Then the mixture was saturated with O₂ for 5 min and irradiated under the blue LED light. After the reaction was completed, the mixture was performed as the workup protocol and purified by chromatography on silica to afford the final pure bromides (yield: 85%).

¹H NMR (CDCl₃, 300 MHz): δ 7.62 (m, 1H), 7.56 (m, 1H), 7.27 (m, 2H), 2.29 (s, 3H);

¹³C NMR (CDCl₃, 300 MHz): δ 139.61, 138.91, 131.76, 124.52, 124.45, 121.75, 121.65, 112.46.

6.2.5 Investigation of Cl⁻ and I⁻ as halide source

According to the reaction mechanism, the interactions between Br⁻ and cationic radical of 1,2,4-trimethoxybenzene intermediate played an essential role for the formation of bromide product. Other halides, such as chloride and iodide, should share a similar nucleophile character for the halogenation reaction. Here, the additional experiments were conducted to demonstrate the general feasibility of the reaction mechanism by replacing **HBr** with **HCl** and **HI**, obtaining 1-chloro-2,4,5-trimethoxybenzene and 1-iodo-2,4,5-trimethoxybenzene as the chlorination and iodination products.



The chlorination of 1,2,4-trimethoxybenzene (TMB) was carried out in a similar procedure. Typically, MOPs (10 mg) and TMB (5.97 μ L, 0.04 mmol) were dissolved in 10 mL acetonitrile. 37% aqueous solution of HCl (32.85 μ L, 0.4 mmol) was added and the mixture was saturated with O₂ by bubbling O₂ for 5 min, and then irradiated with a blue LED lamp (460 nm, 1.2 W/cm²) at room temperature for overnight. After being extracted with brine and hexane, the crude product was purified via column chromatography. Yield: 70%

R_f (hexane/ethyl acetate 14/1): 0.15

¹H NMR (CDCl₃, 300 MHz): δ 6.82 (s, 1H), 6.50 (s, 1H), 3.81 (s, 3H), 3.80 (s, 3H), 3.76 (s, 3H);

¹³C NMR (CDCl₃, 300 MHz): δ 149.2, 148.4, 143.5, 113.7, 113.0, 99.1, 57.2, 56.6, 56.3.

The iodination of 1,2,4-trimethoxybenzene (TMB) was carried out in a similar procedure. Typically, MOPs (10 mg) and TMB (5.97 μ L, 0.04 mmol) were dissolved in 10 mL acetonitrile. 57% aqueous solution of HI (7.92 μ L, 0.06 mmol) was added and the mixture was saturated with O₂ by bubbling O₂ for 5 min, and then irradiated with a blue LED lamp (460 nm, 1.2 W/cm²) at room temperature for overnight. After being extracted with brine and hexane, the crude product was purified via column chromatography. Yield: 51%

R_f (hexane/ethyl acetate 5/1): 0.34

¹H NMR (CDCl₃, 300 MHz): δ 7.13 (s, 1H), 6.43 (s, 1H), 3.81 (s, 3H), 3.78 (s, 3H), 3.76 (s, 3H);

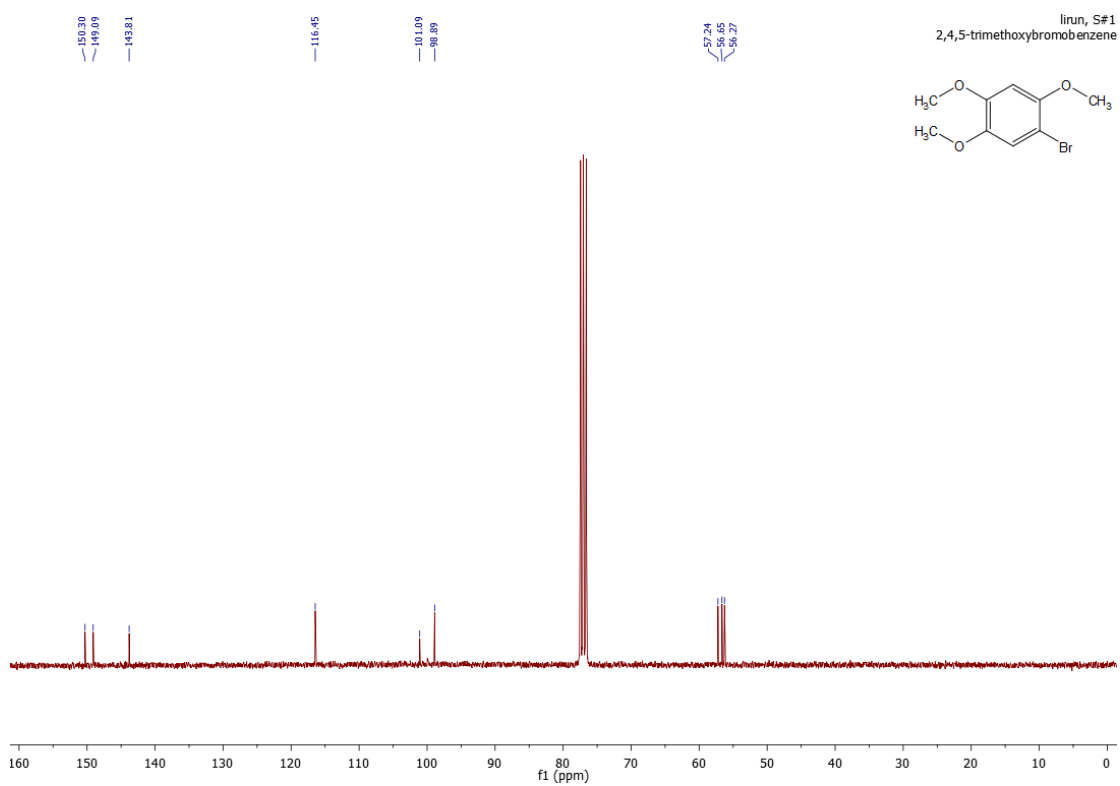
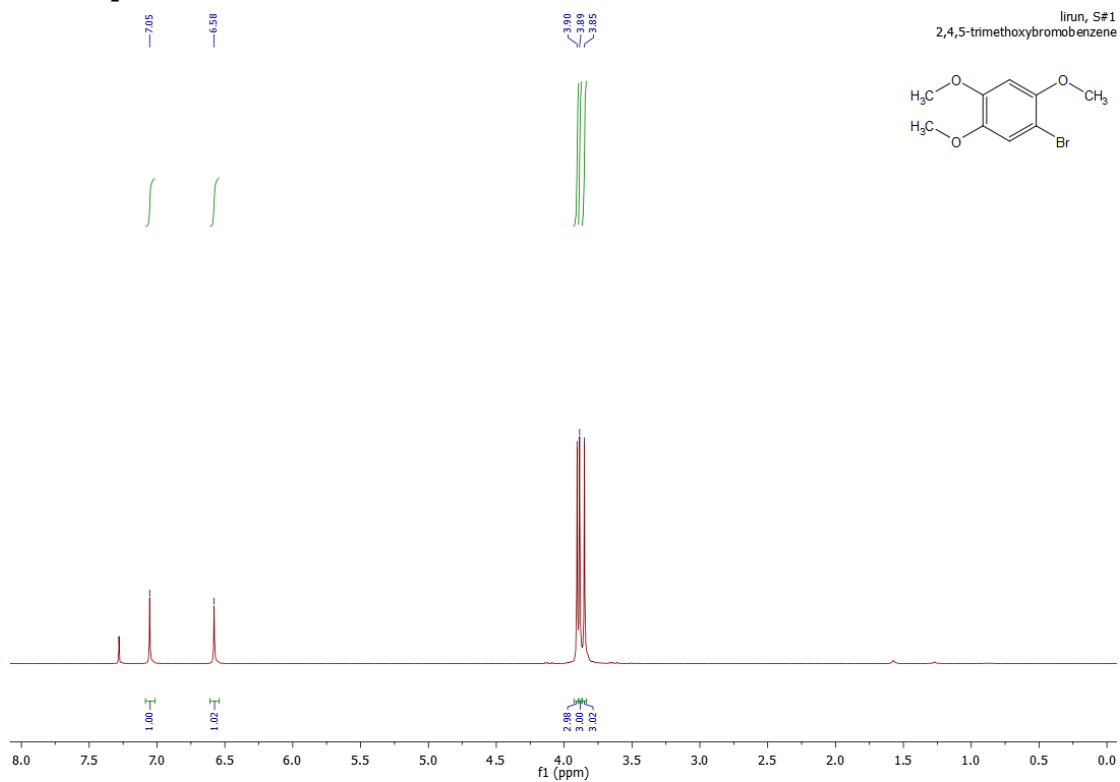
¹³C NMR (CDCl₃, 300 MHz): δ 153.0, 150.2, 144.2, 121.9, 97.8, 73.0, 57.3, 56.7, 56.2.

6.2.6 Determination of H₂O₂

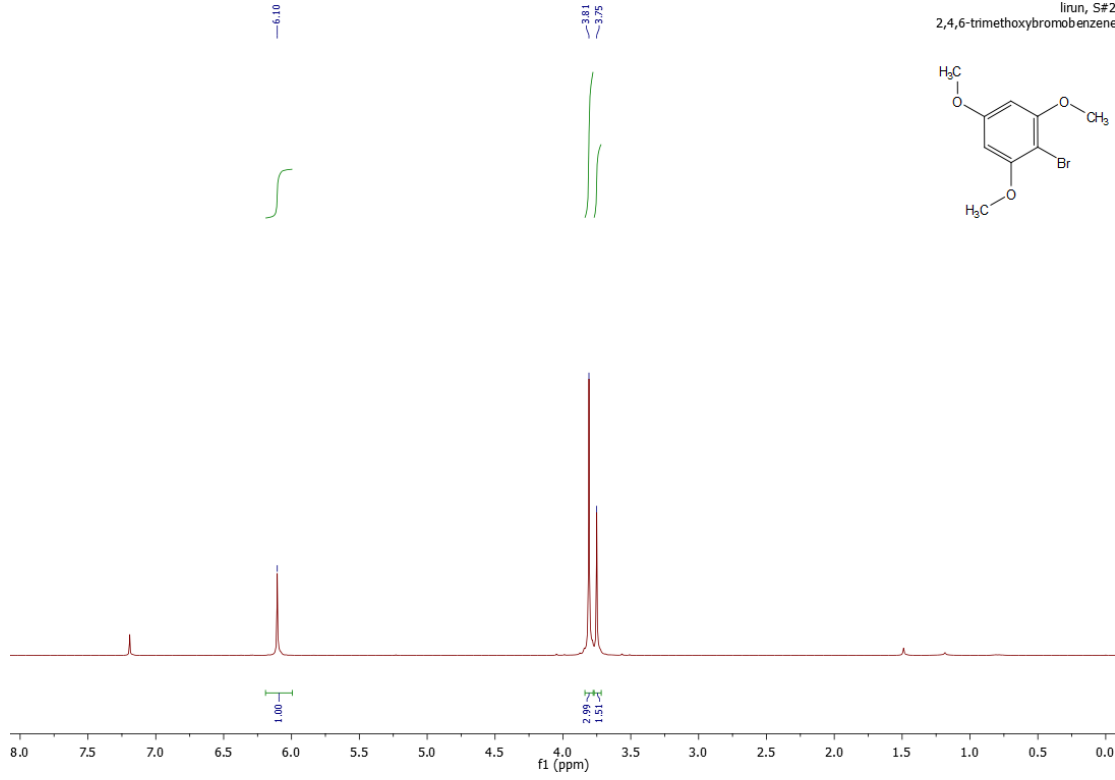
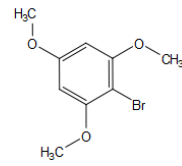
The DPD reagent was prepared by dissolving 0.1 g of DPD in 10 mL 0.05 M H₂SO₄ and the POD reagent was prepared by dissolving 10 mg peroxidase from horseradish in 10 mL of tridistilled water. Both standard solutions were prepared freshly on demand and stored in dark at low temperature (in fridge, ~ 4°C).

Typical procedure for the detection of H₂O₂: Photocatalyst (MOPs, 10 mg) and TMB (5.97 μL, 0.04 mmol) were dissolved in 10 mL acetonitrile. 48% aqueous solution of HBr (5.66 μL, 0.06 mmol) was added and the mixture was saturated with O₂ by bubbling O₂ for 5 min, and then irradiated with a blue LED lamp (1.2 W/cm²) at room temperature for 2 h. DI water was added to the solution and the mixture was extracted by hexane to remove the organic compounds. After purification process, the volume for the obtained water was 35 mL. 6 mL was taken out and diluted up to 30 mL by adding 24 mL DI water. 9 mL aqueous solution was added into the vessel and 1 mL PBS buffer (pH 7.4) was added into the vessel with stirring and used as the test sample. The UV-Vis spectra of the test sample were conducted after adding 20 μL DPD and 20 μL POD.

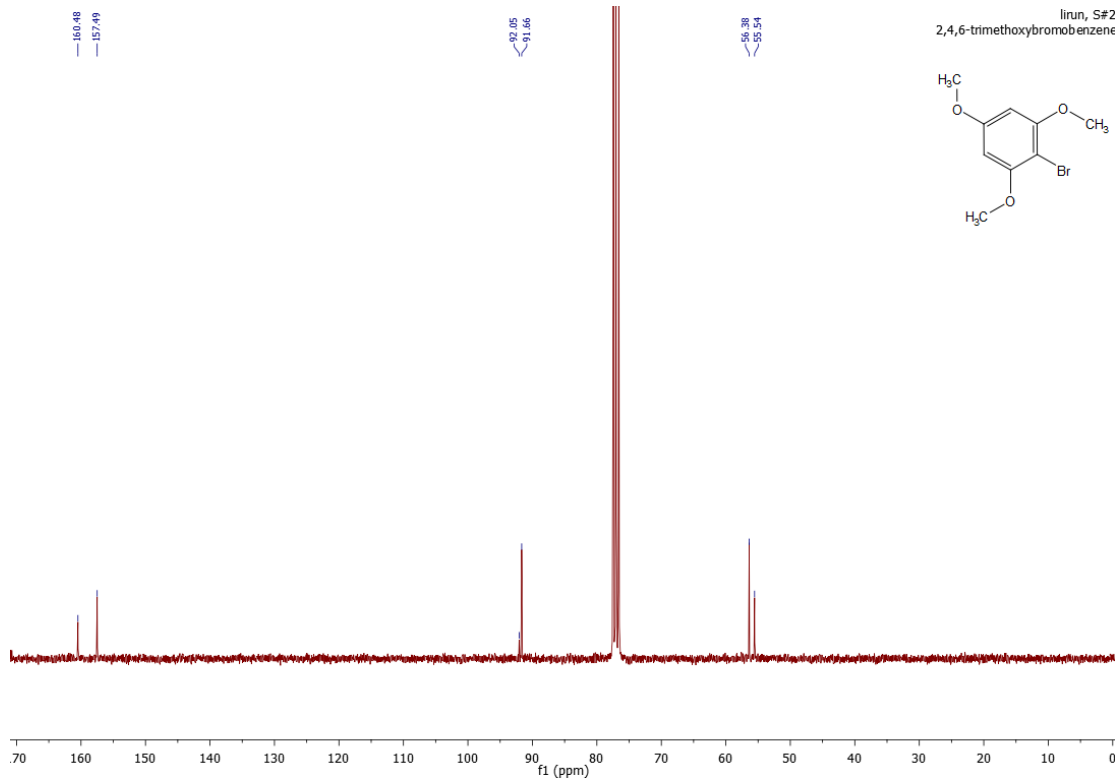
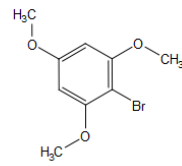
6.2.7 NMR spectra



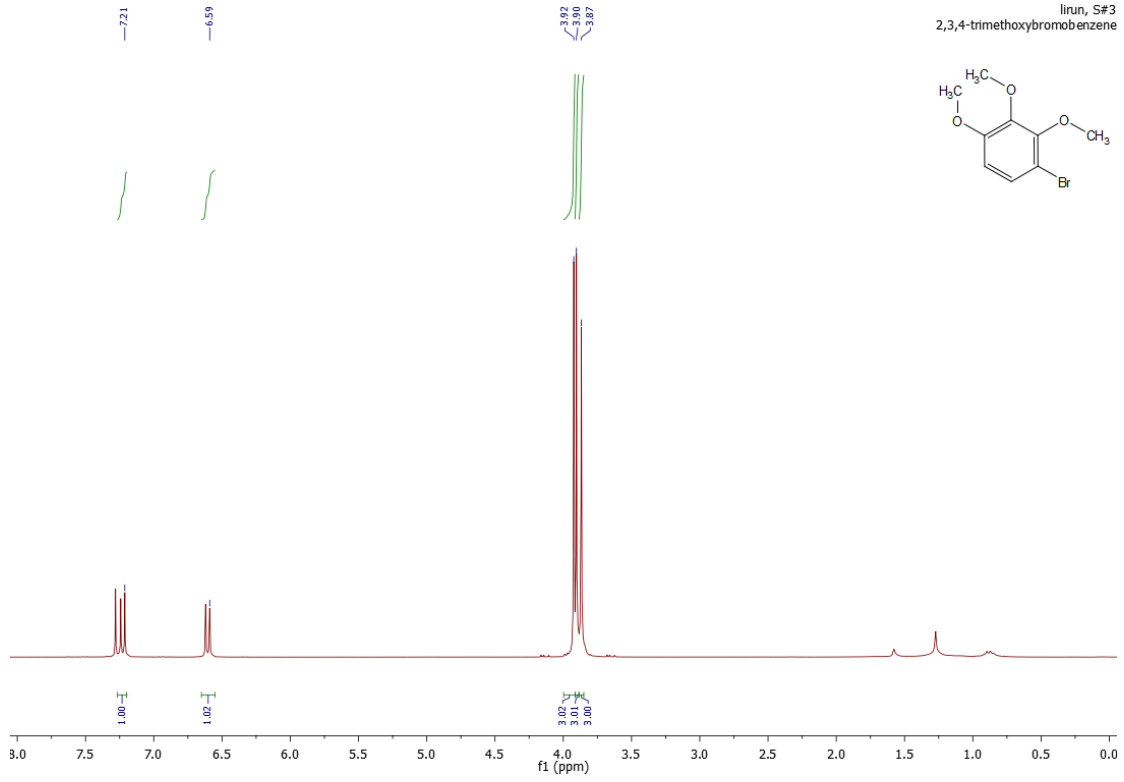
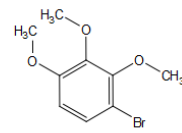
lirun, S#2
2,4,6-trimethoxybromobenzene



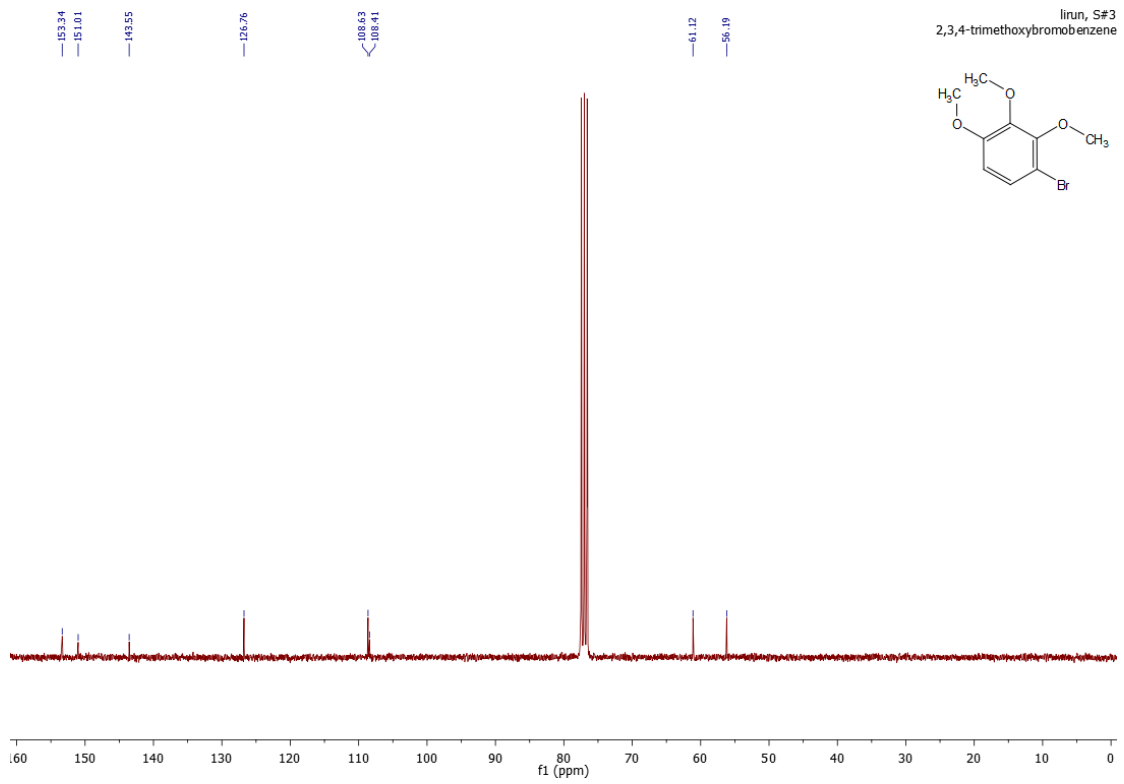
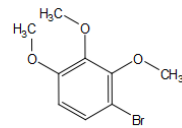
lirun, S#2
2,4,6-trimethoxybromobenzene

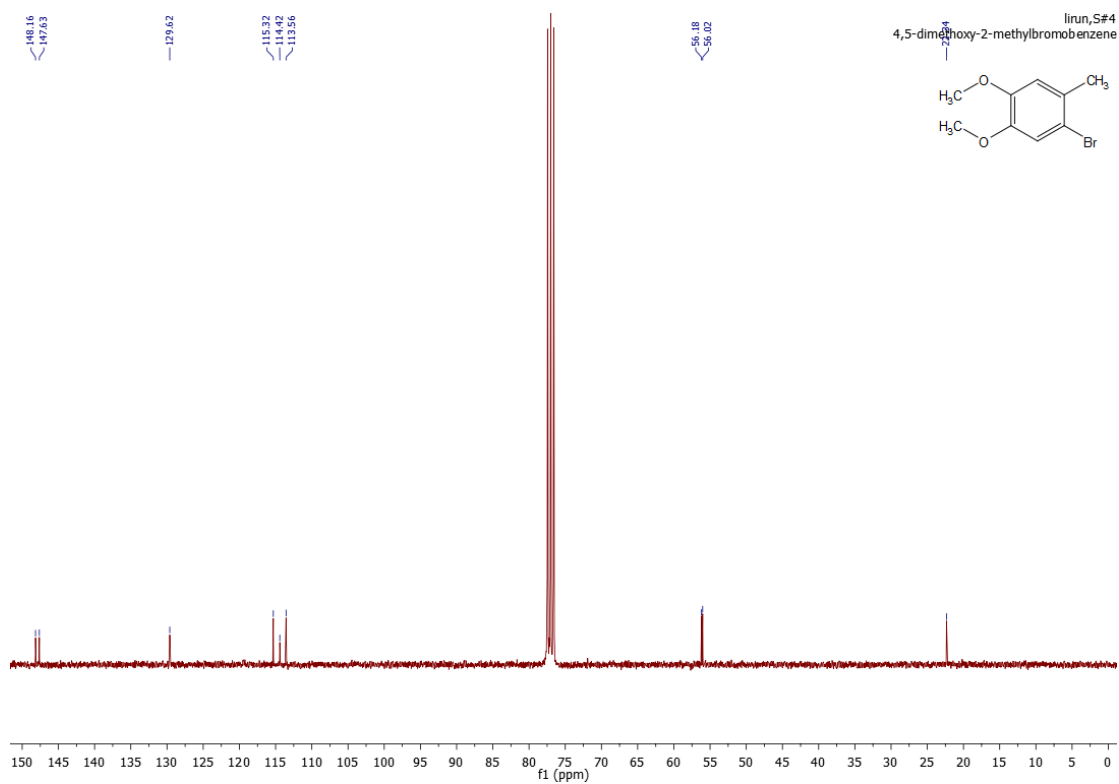
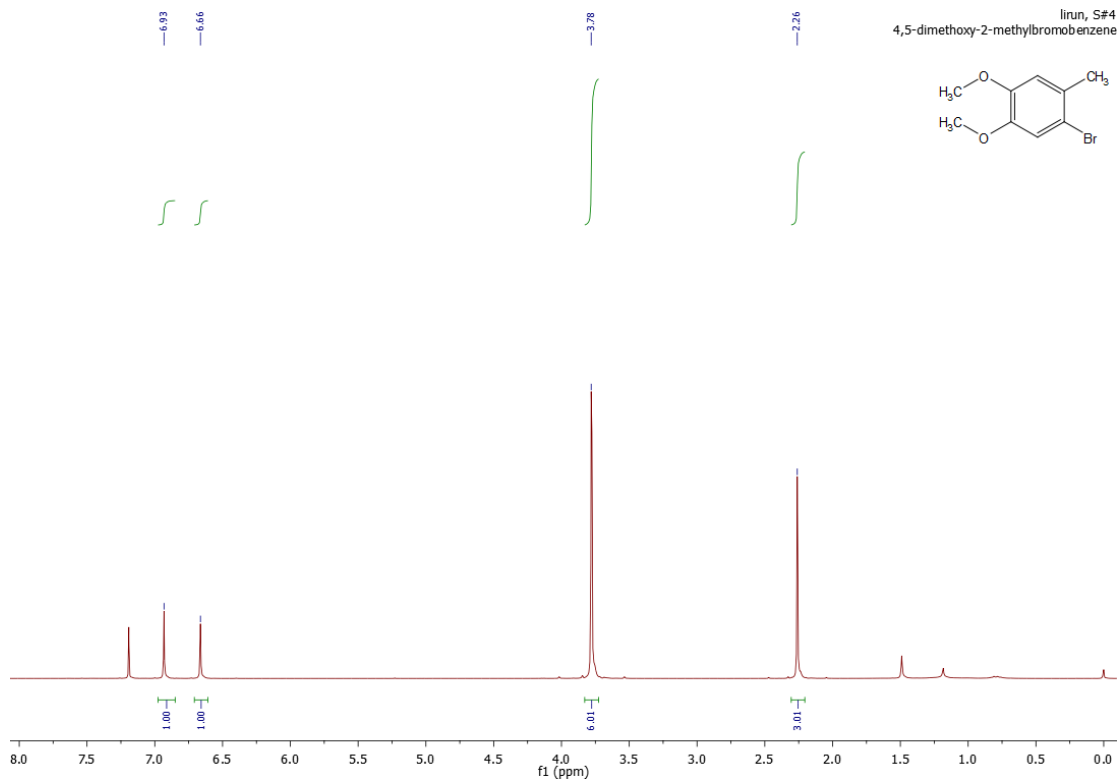


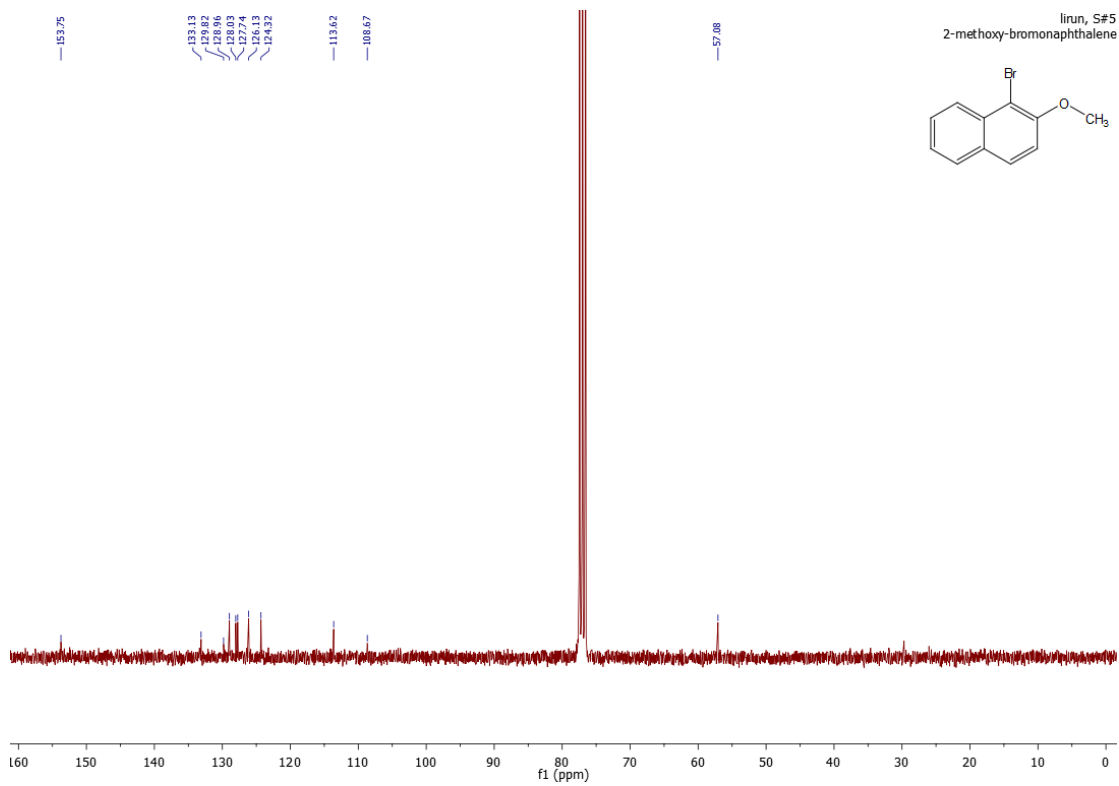
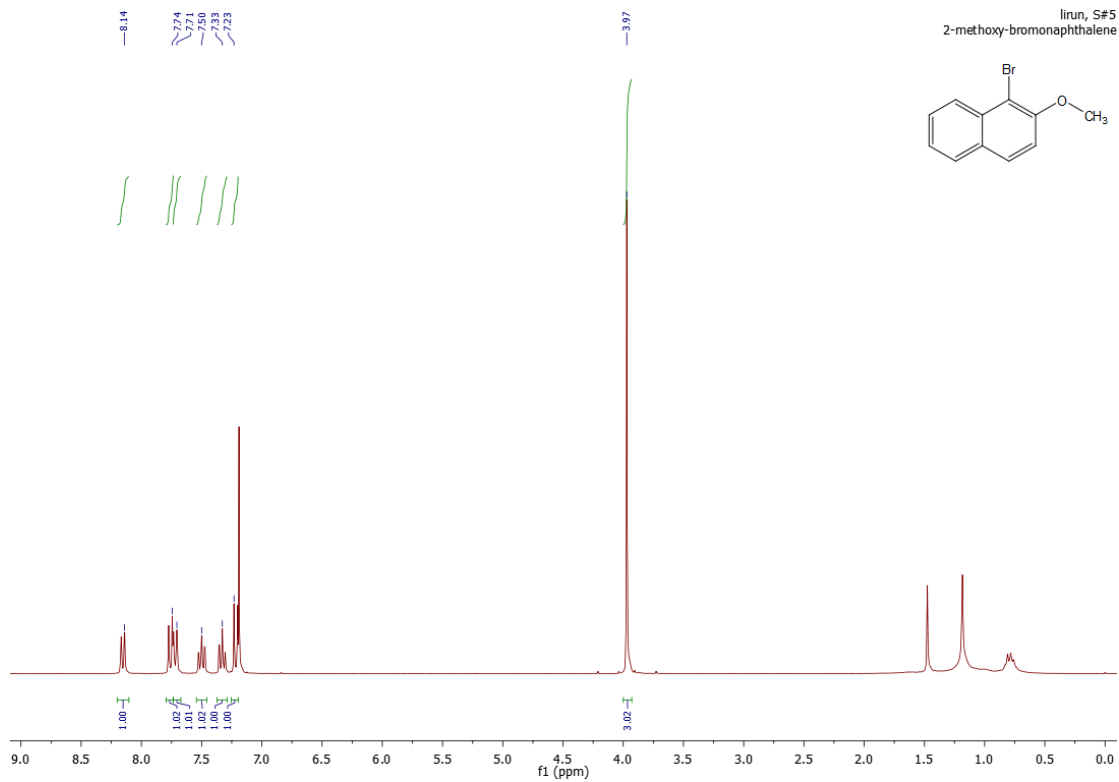
lirun, S#3
2,3,4-trimethoxybromobenzene

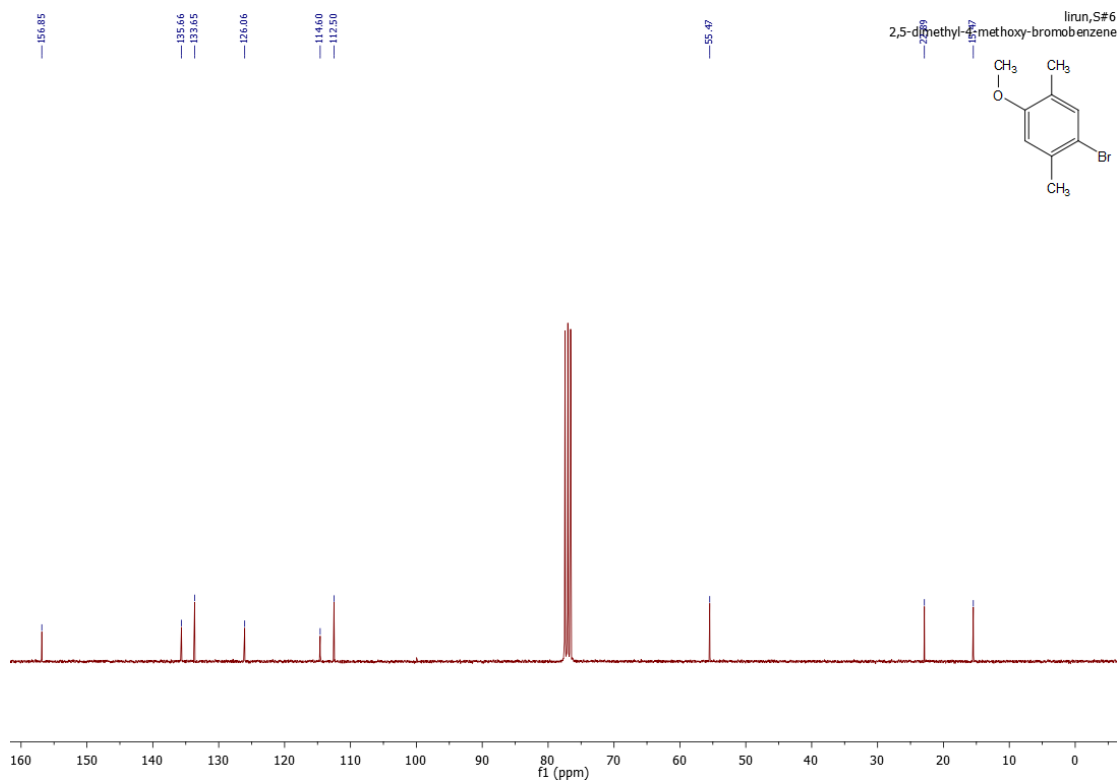
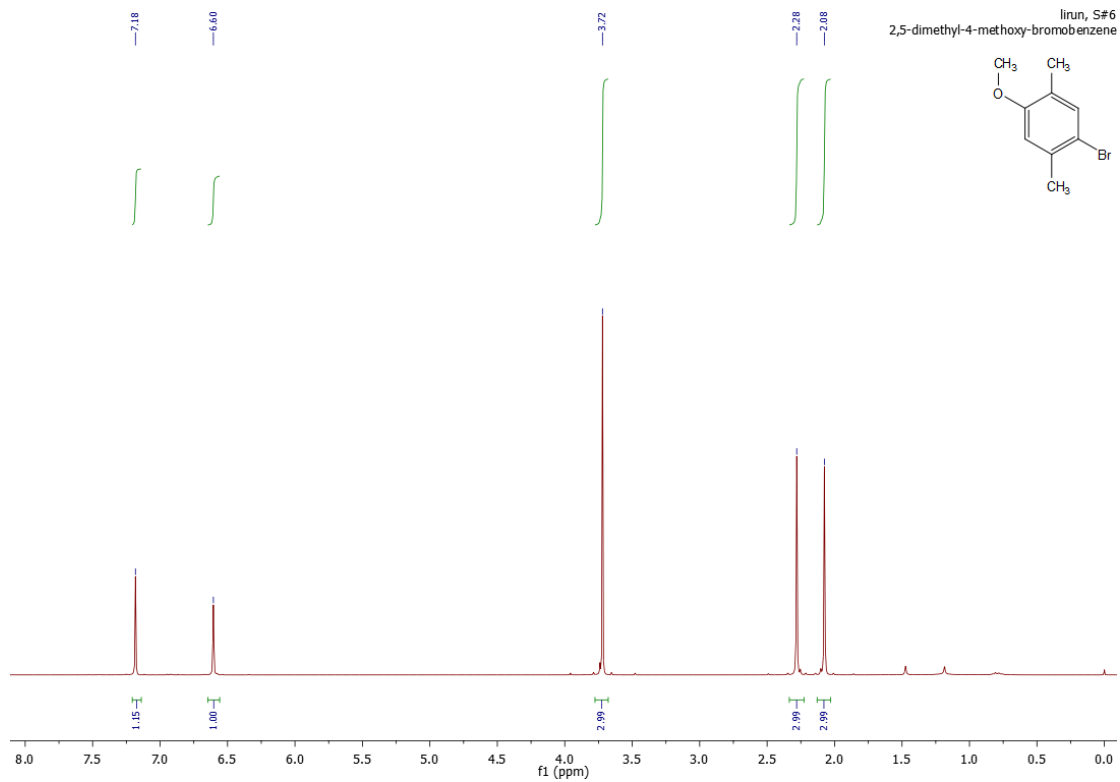


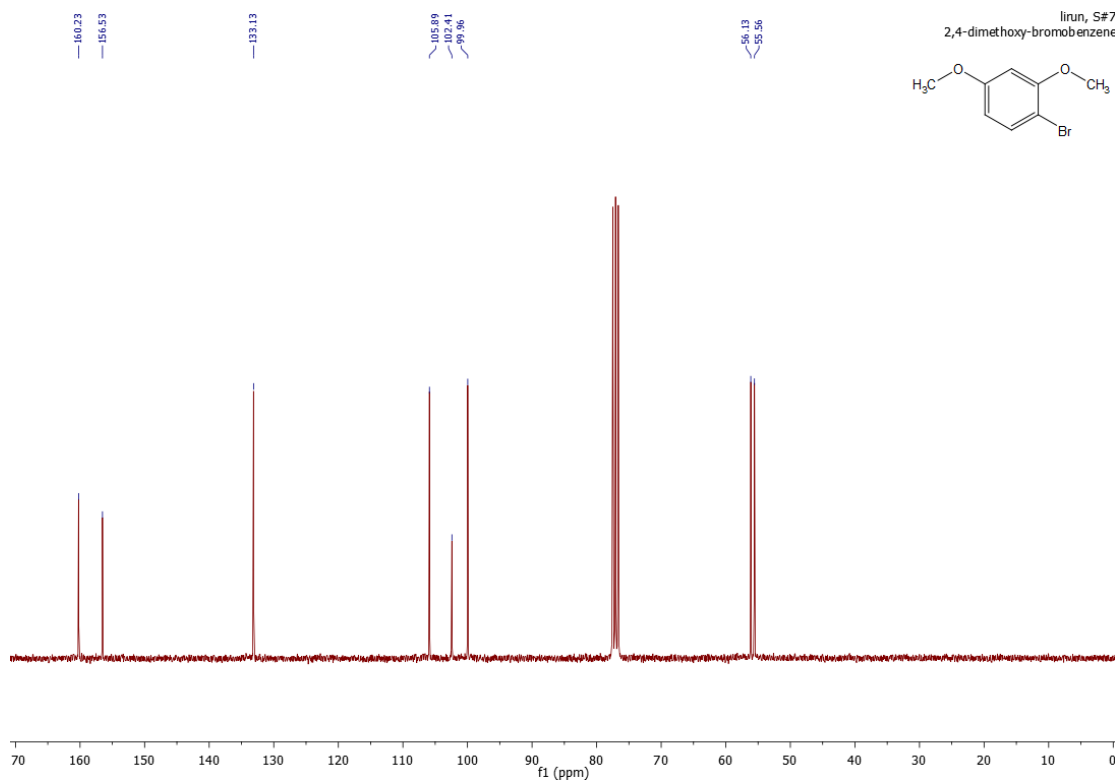
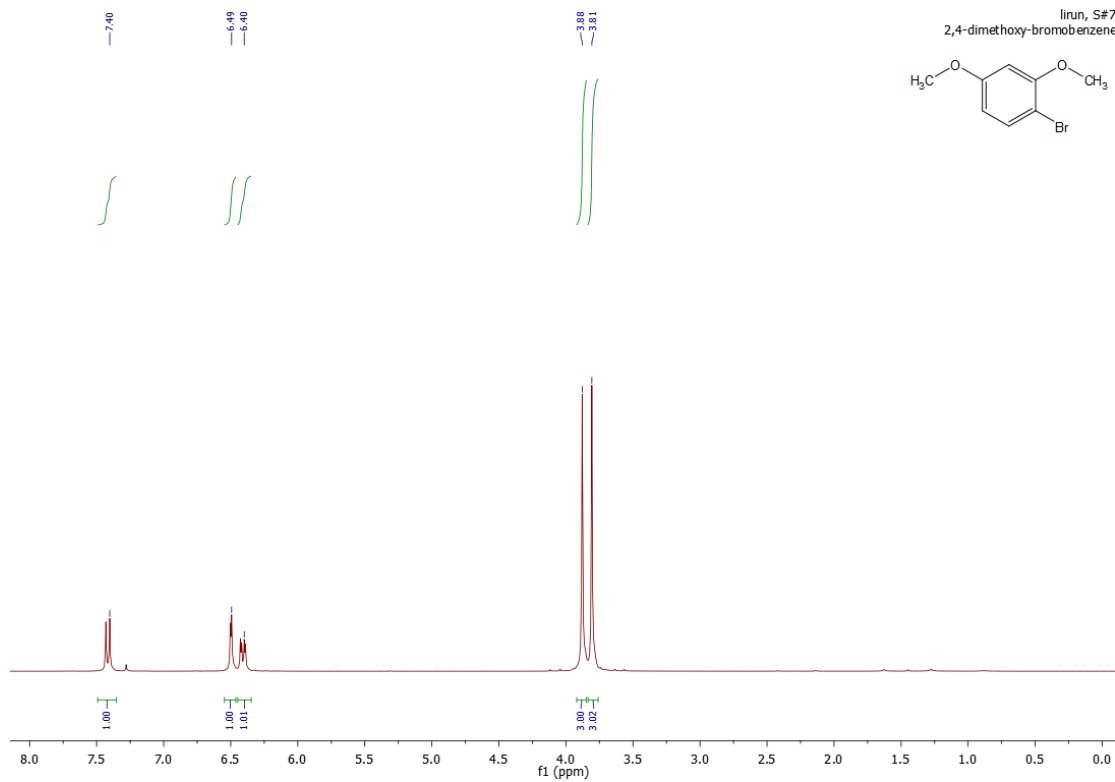
lirun, S#3
2,3,4-trimethoxybromobenzene

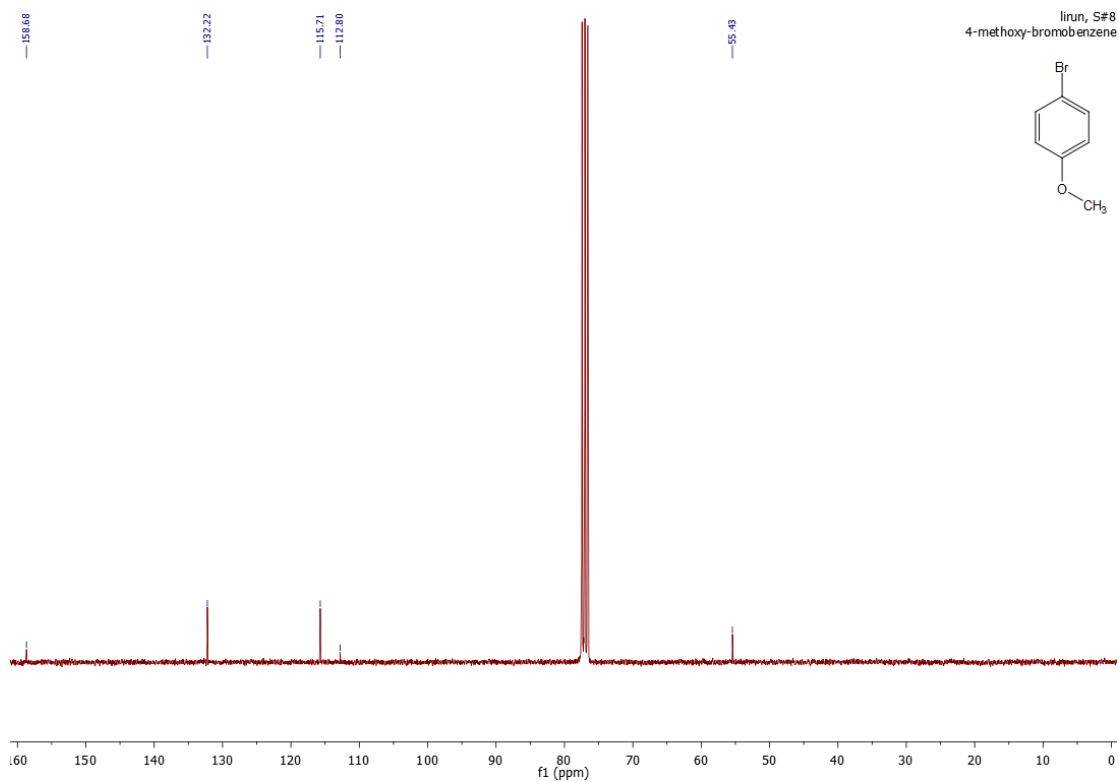
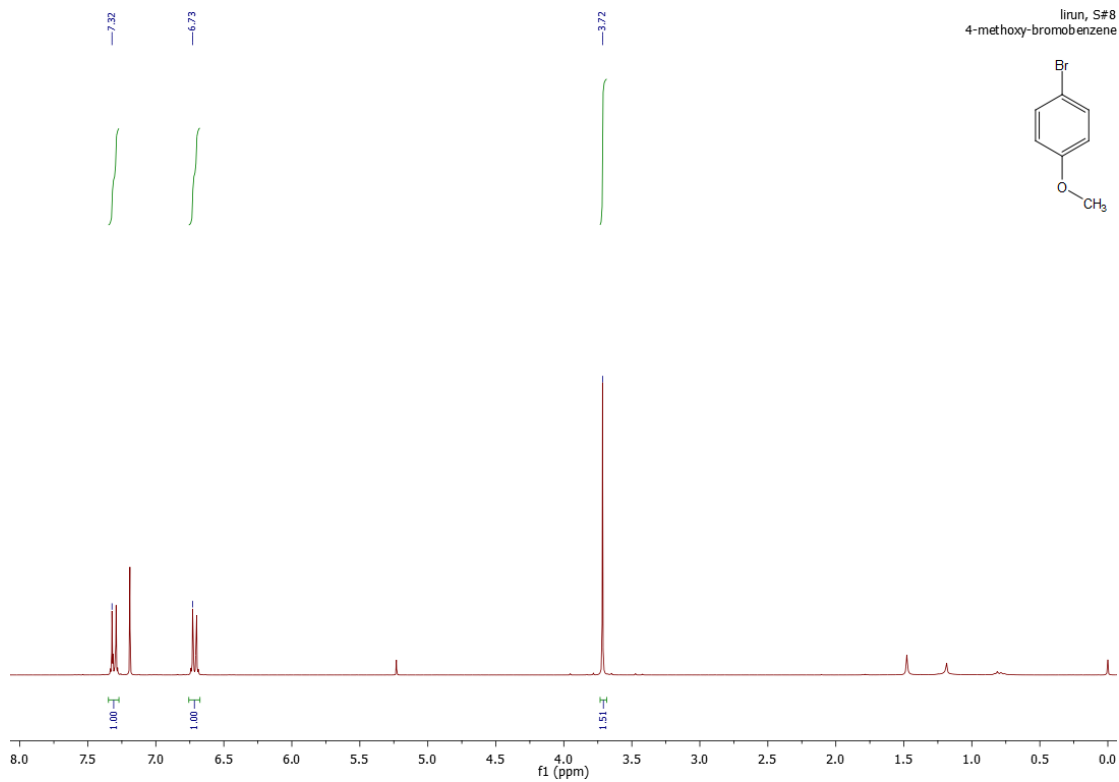




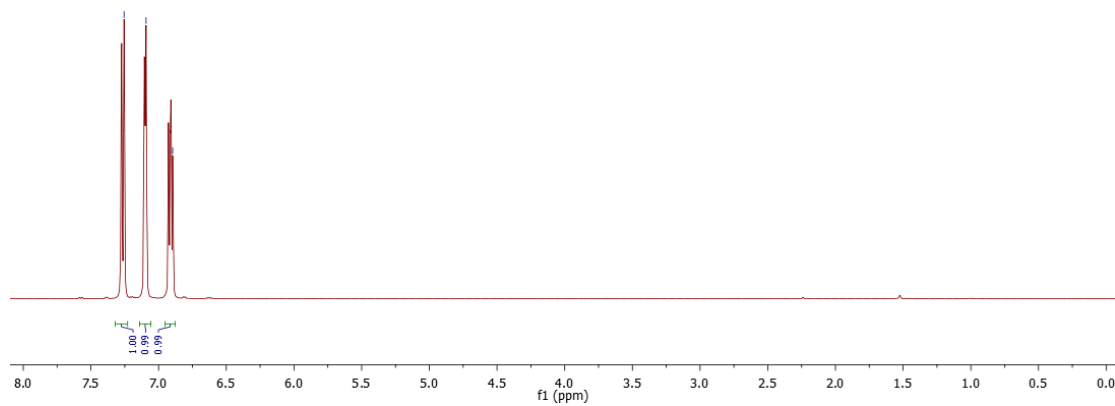




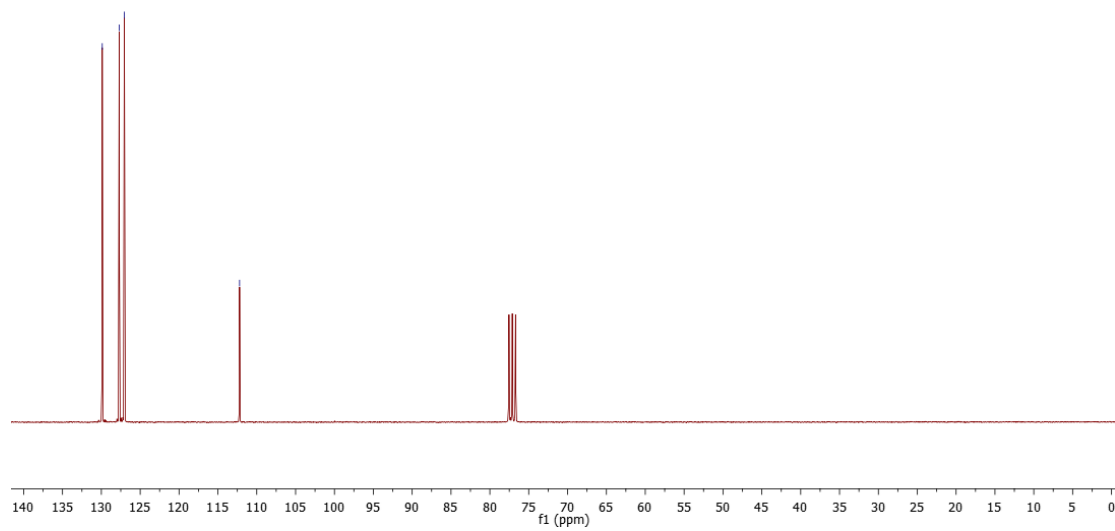


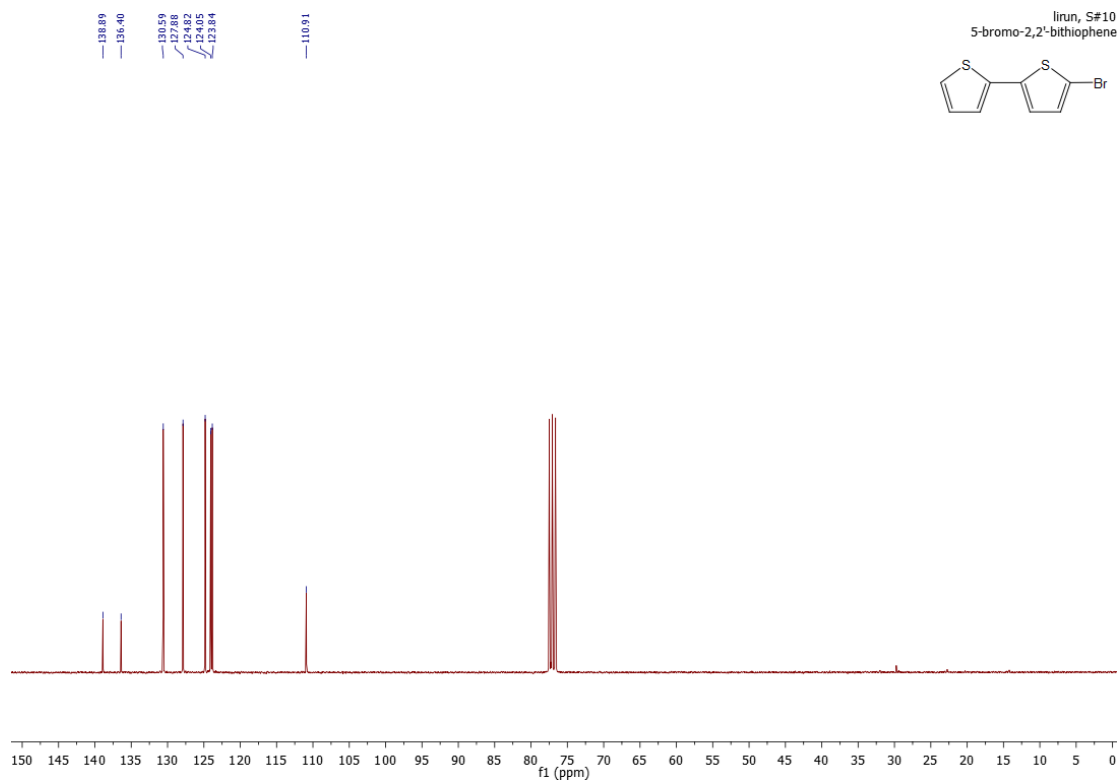
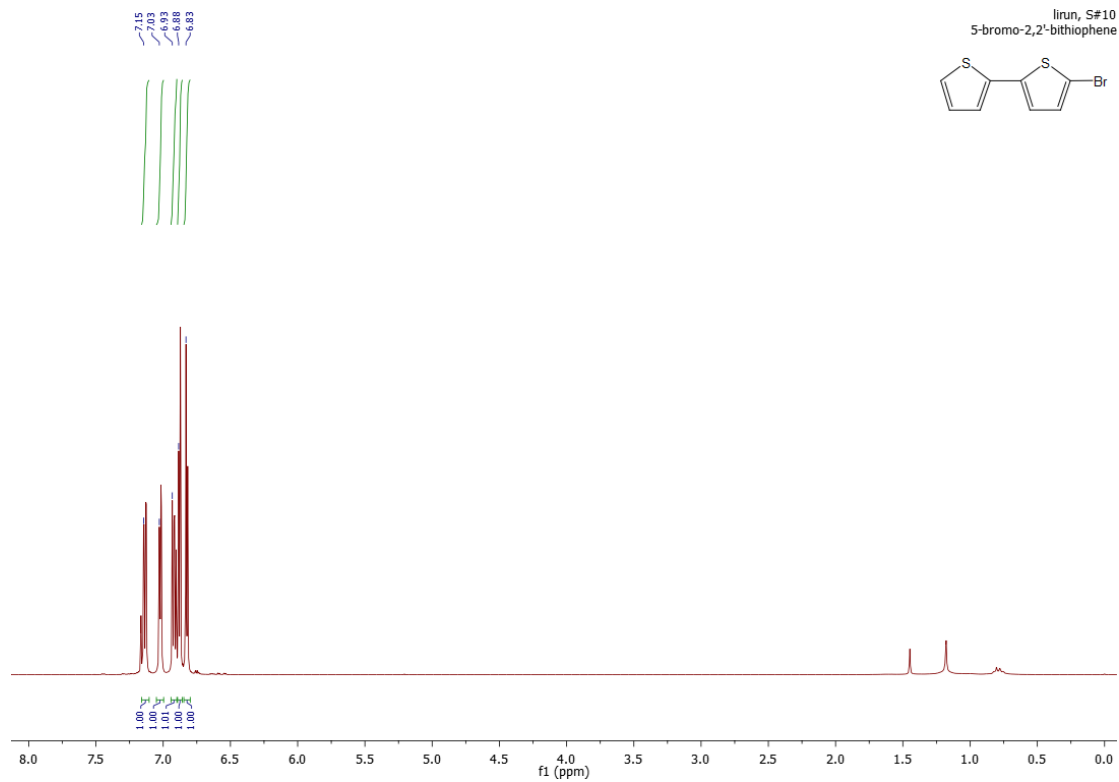


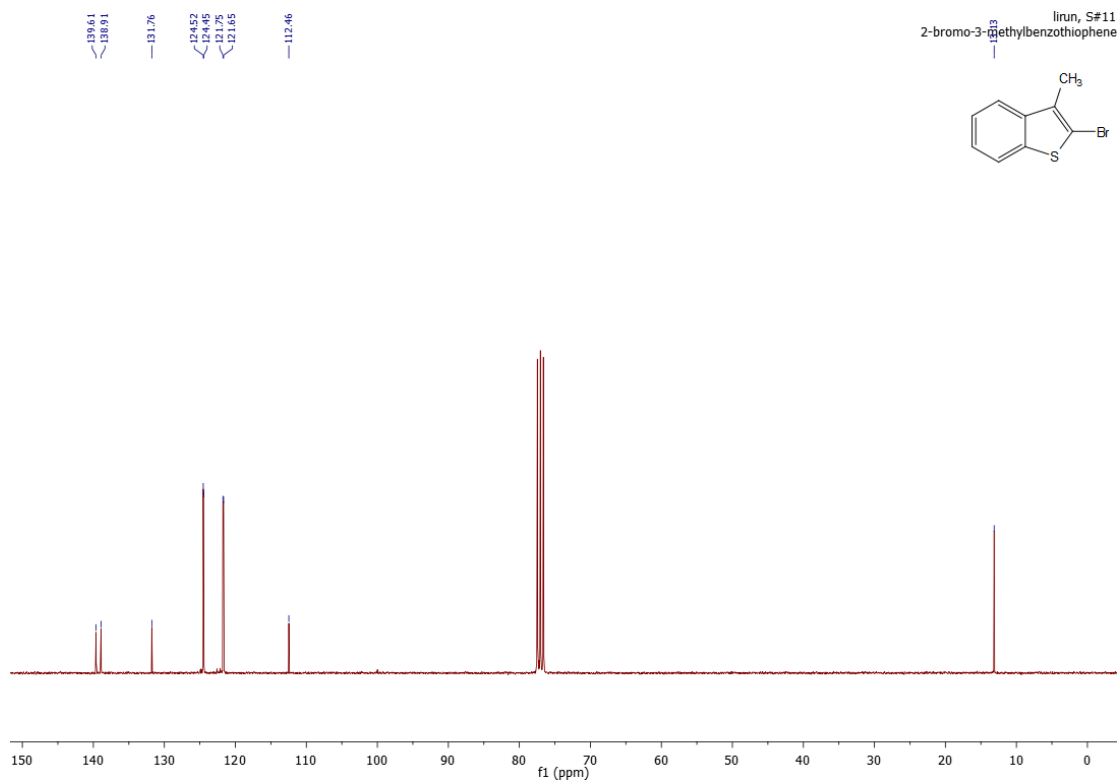
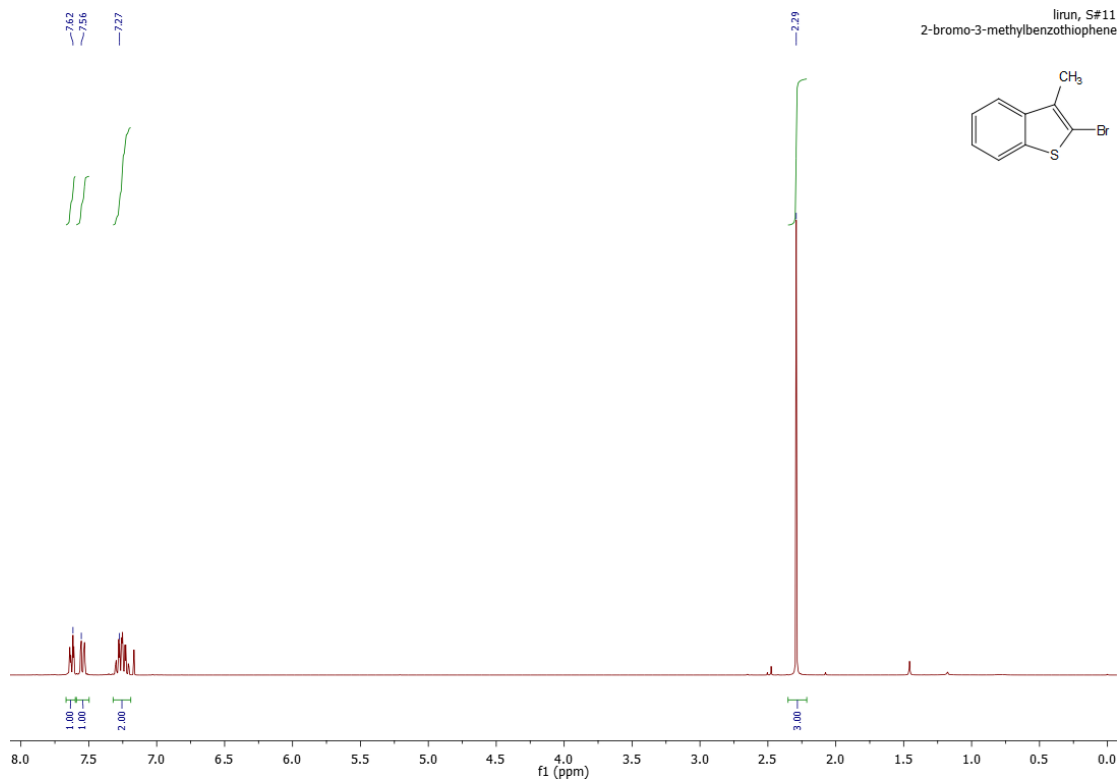
lirun, S#9
2-bromothiophene

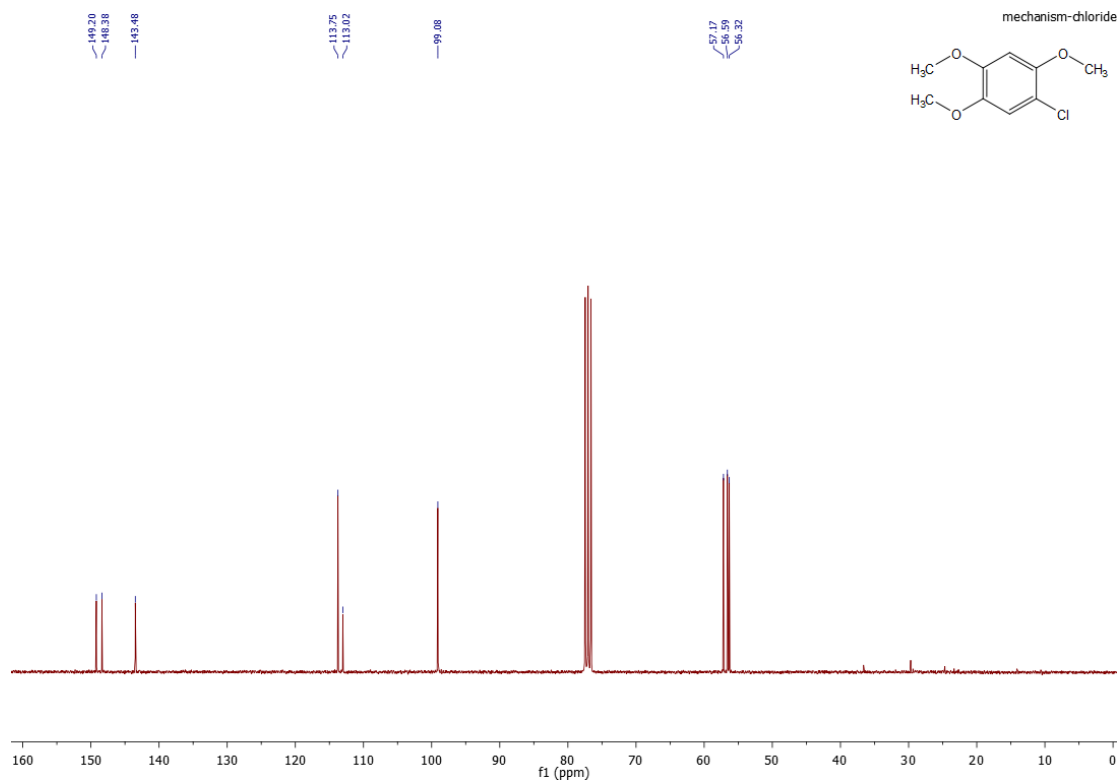
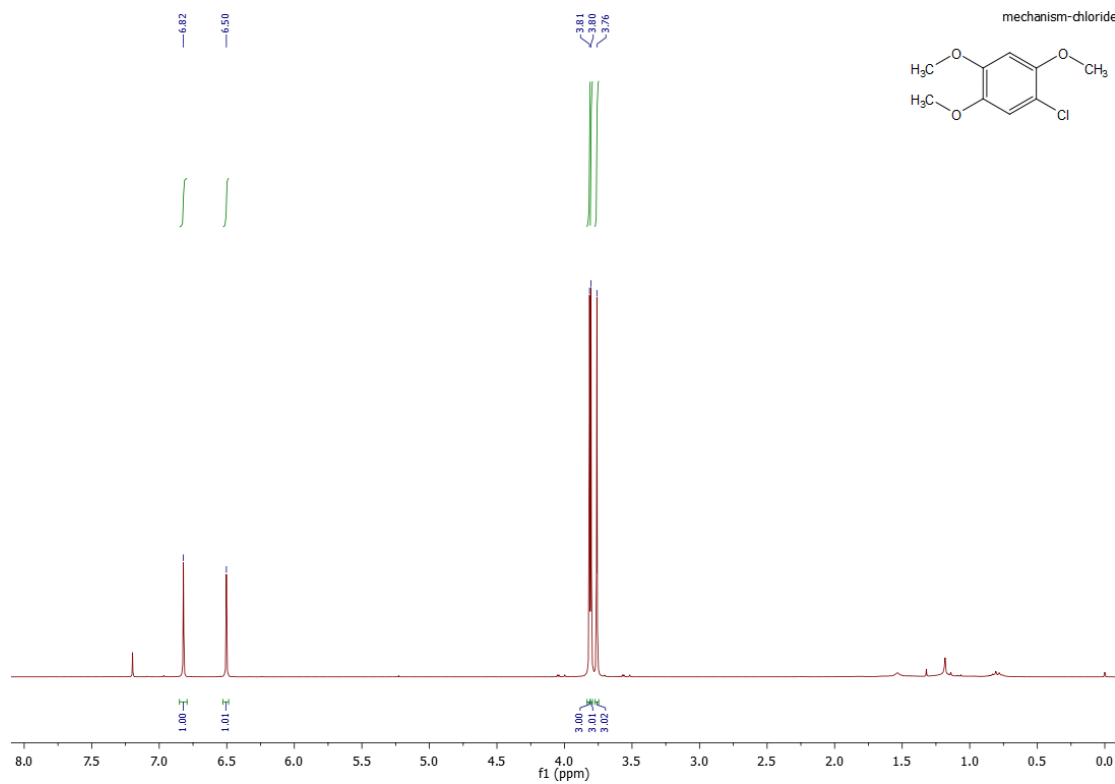


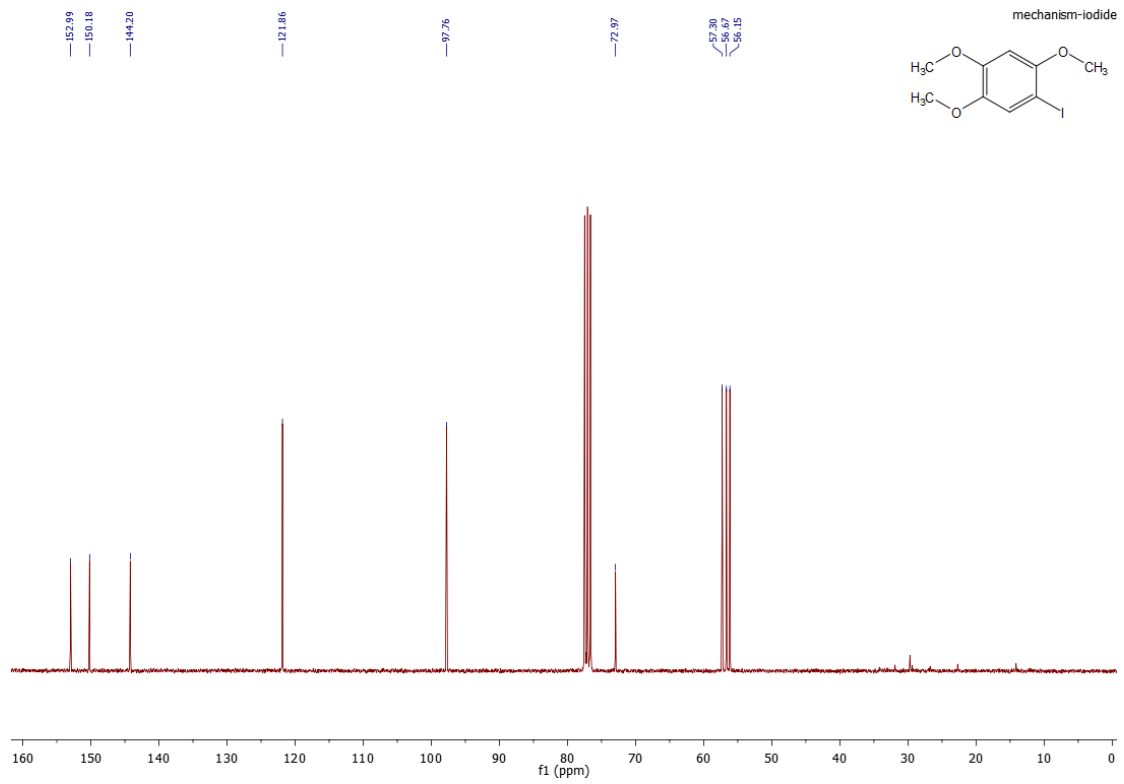
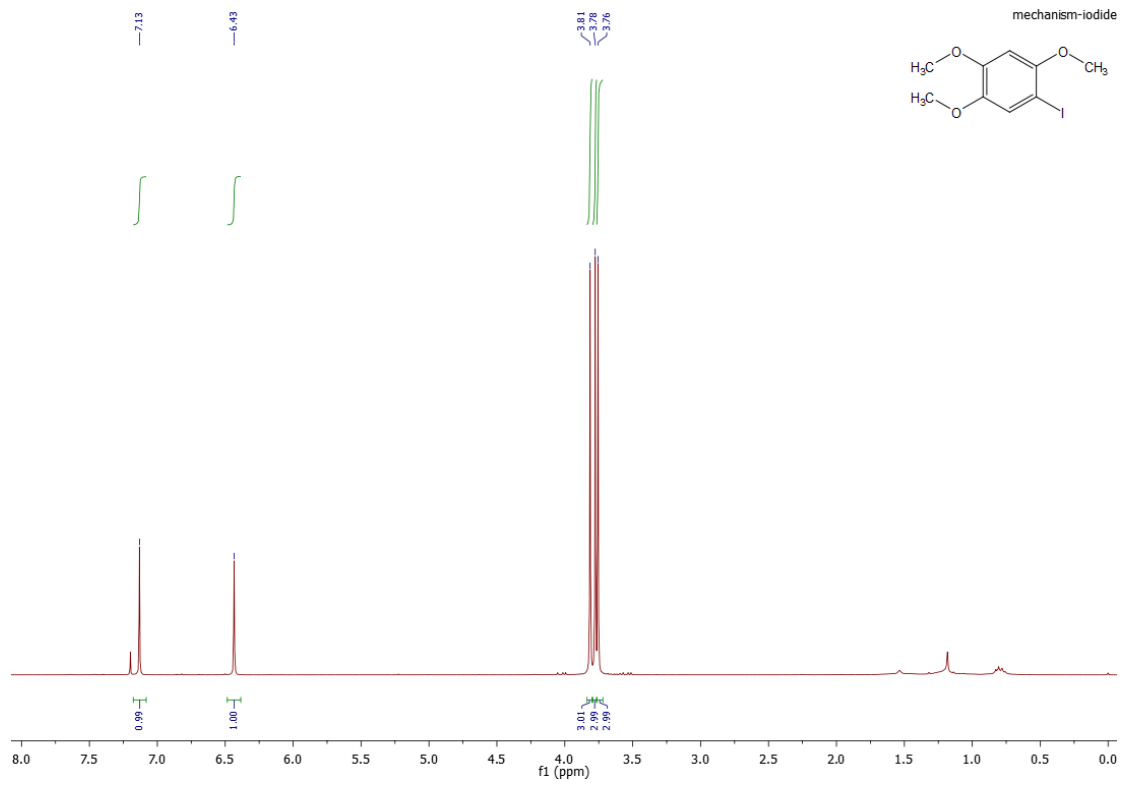
lirun, S#9
2-bromothiophene











6.3 Photocatalytic regio- and stereo-Selective [2+2] cycloaddition of styrene derivatives using a heterogeneous organic photocatalyst

6.3.1 Materials

All chemicals and solvents were purchased from commercial sources and used as received without further purification unless otherwise noted. *trans*-Anethole, and *trans*-isomethyleugenol were purchased from commercial sources and used without further purification. Other styrene derivatives were purified by elution through neutral aluminium oxide (50-200 μm) and anhydrous CaCl_2 (w/w, 95/5). The reactions conversions were monitored by GC-MS. Column flash chromatography was conducted with silica 60 (0.063-0.2 mm).

6.3.2 Methods and characterization

UV-Vis absorption and FTIR spectra were recorded on a Perkin Elmer Lambda 100 spectrophotometer and Varian 1000 FT-IR spectrometer at ambient temperature, respectively. Electron paramagnetic resonance (EPR) spectrum was performed on a Magnettech Miniscope MS200 spectrometer with spin trapping EPR at DMPO (0.1 M), catalyst (1 mg/mL) and anethole (0.1 M) in nitromethane. Another spin trapping EPR for PBN trapping experiment was conducted at PBN (0.1 M), catalyst (1 mg/mL) and anethole (0.1 M) in nitromethane on a Bruker EMX-plus spectrometer (Bruker B-VT 2000). The related simulation for the EPR spectrum was according to the condition: g factor was 2.00604. Frequency of measurement was 9.313456 (GHz) and B_c (magnetic center field) is 3317 (G). Cyclic voltammetry measurement was recorded on a Metrohm Autolab PGSTAT204 potentiostat/galvanostat in a three-electrode-cell system: glassy carbon electrode as the working electrode, Hg/HgCl₂ electrode as the reference electrode, platinum wire as the counter electrode, and Bu₄NPF₆ (0.1 M acetonitrile) as supporting electrolyte with a scan rate of 100 mV s⁻¹ in the range of -2 V to 2 V. The morphology was recorded by a scanning electron microscope (SEM) (LEO Gemini 1530, Germany) with an in lens SE detector and a transmission electron microscope (TEM) (JEOL JEM-1400). Thermogravimetric analysis (TGA) was conducted in a nitrogen atmosphere with temperature increasing from room temperature to 1000 °C at a rate of 10 K/min. GC-MS measurement was conducted on Shimadzu GC-2010 plus gas chromatography and QP2010 ultra mass spectrometer with fused silica column (122-5532, DB-5MS) and flame ionization detector. ¹H and ¹³C NMR spectra for all compounds were measured using Bruker AVANCE 300 MR (at 300 MHz) and are referenced to 0.00 ppm and 0.0 ppm for SiMe₄. Surface areas and pore size distributions were carried out by nitrogen adsorption and desorption at 77.3 K by Autosorb 1 (Quantachrome Instruments). Data were obtained using QuadraWin software from Quantachrome Instruments. Pore size distributions and pore volumes were

calculated from the adsorption branches of the isotherms using Quenched Solid Density Functional Theory (QSDFT, N₂, evaluating carbon adsorbent with slit pores). B-BT was degassed at 80 °C for 24 h under vacuum before analysis. The BET surface area was obtained based on data points received from $0 < P/P_0 < 0.25$ with the nonlinear density functional theory (NLDFT) equilibrium model being employed as the BET model fitting.

6.3.3. Synthesis of photocatalyst B-BT

The conjugated microporous polymer B-BT was prepared by palladium catalyzed Sonogashira-Hagihara cross coupling reactions. Typically, 4,7-dibromobenzo[c][1,2,5]thiadiazole (117.6 mg, 0.4 mmol), 1,3,5-triethynylbenzene (60.1 mg, 0.4 mmol), tetrakis(triphenylphosphine)palladium(0) (7 mg, 0.006 mmol), cooper(I) iodide (1.4 mg, 0.007 mmol) were dissolved in dry DMF (20 mL). Then, 0.8 mL trimethylamine was added following by degassing with N₂ for 30 min. After degassing process, the reactive mixture was heated at 80 °C for 72 h. The obtained precipitate was washed with chloroform, water and acetone for three times and then extracted in a Soxhlet extractor with acetone and THF for 48 h each, respectively. Finally, a yellow solid product was collected after dry in vacuum oven at 60 °C for 24 h.

6.3.4 Photocatalytic [2+2] cycloaddition reaction with B-BT

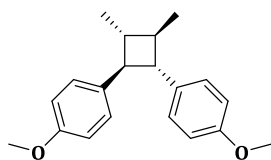
General procedure A: homo [2+2] cycloaddition

In a 40 mL vial was charged with 0.24 mmol alkene-1 (*trans*-Anethole, and *trans*-Isomethyleugenol), B-BT (2.4 mg) and CH₃NO₂ (2.4 mL). Then the vial was placed under air condition in front of a blue LED lamp (460 nm, 1.2 W/cm²). The conversion of alkene-1 was determined by GC-MS measurement. Upon consumption of alkene-1, the mixture was poured into a separatory funnel containing the mixture of Et₂O and water (v/v, 1/1). The organic layers was separated and extracted with Et₂O (30 mL). A crude product was obtained after drying over anhydrous MgSO₄ and concentrating with rotary evaporator. Finally, the cycloaddition products could be obtained after purification with flash-column chromatography.

General procedure B: unsymmetrical [2+2] cycloaddition

In a 40 mL vial was charged with 0.24 mmol alkene-1 (*trans*-Anethole and *trans*-Isomethyleugenol), 1.2 mmol alkene-2 (other styrene derivatives), B-BT (2.4 mg) and CH₃NO₂ (2.4 mL). Then the vial was placed under air condition in front of a blue LED lamp (460 nm, 1.2 W/cm²). The conversion of alkene-1 was determined by GC-MS measurement.

Upon consumption of alkene-1, the mixture was poured into a separatory funnel containing the mixture of Et₂O and water (v/v, 1/1). The organic layers was separated and extracted with Et₂O (30 mL). A crude product was obtained after drying over anhydrous MgSO₄ and concentrating with rotary evaporator. Finally, the cycloaddition products could be obtained after purification with flash-column chromatography.



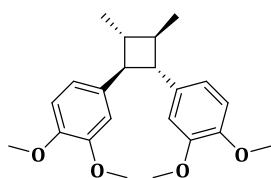
4,4'-((1S,2S,3R,4R)-3,4-dimethylcyclobutane-1,2-diyl)bis(methoxybenzene):

According to the general procedure A, a 40 mL vial with a magnetic stir bar was charged with *trans*-anethole (35.6 mg, 0.24 mmol), B-BT (2.4 mg) and CH₃NO₂ (2.4 mL). After the reaction was completed, the mixture was performed as the workup protocol and purified by chromatography on silica with hexane/ethyl acetate (15/1) as the elution to afford the pure cycloadduct as clear oil.

R_f (hexane/ethyl acetate 15/1): 0.12

¹H NMR (CDCl₃, 300 MHz): δ 7.07 (AA' of AA'BB', J = 9 Hz, 4H), 6.76 (BB' of AA'BB', J = 9 Hz, 4H), 3.69 (s, 6H), 2.74 (inverted d, 2H), 1.76 (m, 2H), 1.11 (d, J = 6 Hz, 6H).

¹³C NMR (CDCl₃, 300 MHz): δ 157.95, 135.94, 127.74, 113.71, 55.26, 52.50, 43.24, 18.90.



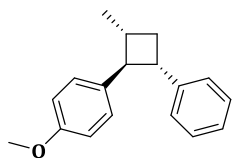
4,4'-((1S,2S,3R,4R)-3,4-Dimethylcyclobutane-1,2-diyl)bis(1,2-dimethoxybenzene):

According to the general procedure A, a 40 mL vial with a magnetic stir bar was charged with *trans*-isomethyleugenol (40.7 μL, 0.24 mmol), B-BT (2.4 mg) and CH₃NO₂ (2.4 mL). After the reaction was completed, the mixture was performed as the workup protocol and purified by chromatography on silica with hexane/ethyl acetate (3/1) as the elution to afford the pure cycloadduct as clear oil.

R_f (hexane/ethyl acetate): 0.41

^1H NMR (CDCl_3 , 300 MHz): δ 6.83 (d, J = 3 Hz, 2H), 6.79 (d, J = 1.5 Hz, 2H), 6.72 (m, 2H), 3.86 (s, 6H), 3.85 (s, 6H), 2.82 (d, J = 9 Hz, 2H), 1.87 (m, 2H), 1.22 (d, J = 6 Hz, 6H).

^{13}C NMR (CDCl_3 , 300 MHz): δ 148.82, 147.43, 136.47, 118.56, 111.23, 110.26, 55.93, 55.83, 53.01, 42.93, 18.89.

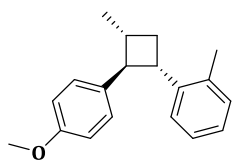


1-methoxy-4-((1S,2R,4S)-2-methyl-4-phenylcyclobutyl)benzene: According to the general procedure B, a 40 mL vial with a magnetic stir bar was charged with *trans*-anethole (35.6 mg, 0.24 mmol), styrene (138 μL , 1.2 mmol), B-BT (2.4 mg) and CH_3NO_2 (2.4 mL). After the reaction was completed, the mixture was performed as the workup protocol and purified by chromatography on silica with hexane/dichloromethane (6/1) as the elution to afford the pure cycloadduct as clear oil.

R_f (hexane/dichloromethane 6/1): 0.26

^1H NMR (CDCl_3 , 300 MHz): δ 7.33 (m, 2H), 7.22 (m, 5H), 6.93 (BB' of AA'BB', J = 9 Hz 2H), 3.84 (s, 3H), 3.44 (q, J = 12 Hz, 1H), 3.01 (t, J = 9 Hz, 1H), 2.56 (dt, J = 9 Hz, 15 Hz, 1H), 2.39 (m, 1H), 1.75 (q, J = 9 Hz, 1H), 1.26 (d, J = 6 Hz 3H).

^{13}C NMR (CDCl_3 , 300 MHz): δ 158.10, 144.69, 135.87, 128.27, 127.82, 126.66, 125.95, 113.79, 55.58, 55.28, 44.14, 35.55, 33.97, 20.52.



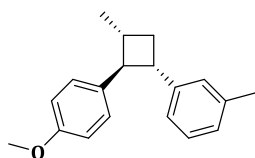
1-((1S,2S,3R)-2-(4-methoxyphenyl)-3-methylcyclobutyl)-2-methylbenzene:

According to the general procedure A, a 40 mL vial with a magnetic stir bar was charged with *trans*-anethole (35.6 mg, 0.24 mmol), 2-methylstyrene (154.8 μL , 1.2 mmol), B-BT (2.4 mg) and CH_3NO_2 (2.4 mL). After the reaction was completed, the mixture was performed as the workup protocol and purified by chromatography on silica with hexane/dichloromethane (6/1) as the elution to afford the pure cycloadduct as clear oil.

R_f (hexane/dichloromethane 6/1): 0.31

^1H NMR (CDCl_3 , 300 MHz): δ 7.22 (d, $J = 9$ Hz, 1H), 7.11 (AA' of AA'BB', $J = 9$ Hz, 2H), 7.06 (m, 1H), 6.99 (m, 2H), 6.75 (BB' of AA'BB', $J = 9$ Hz, 2H), 3.66 (s, 3H), 3.44 (q, $J = 12$ Hz, 1H), 3.03 (t, $J = 12$ Hz, 1H), 2.51 (q, $J = 12$ Hz, 1H), 2.24 (m, 1H), 2.09 (s, 3H), 1.47 (q, $J = 12$ Hz, 1H), 1.11 (d, $J = 6$ Hz, 3H).

^{13}C NMR (CDCl_3 , 300 MHz): δ 158.14, 142.39, 136.12, 136.02, 130.06, 127.85, 125.98, 125.91, 125.82, 113.82, 55.30, 53.44, 41.81, 35.77, 34.79, 20.71, 19.93.



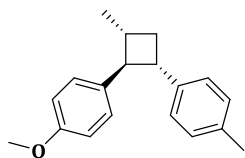
1-((1S,2S,3R)-2-(4-methoxyphenyl)-3-methylcyclobutyl)-3-methylbenzene:

According to the general procedure B, a 40 mL vial with a magnetic stir bar was charged with *trans*-anethole (35.6 mg, 0.24 mmol), 3-methylstyrene (157.6 μL , 1.2 mmol), B-BT (2.4 mg) and CH_3NO_2 (2.4 mL). After the reaction was completed, the mixture was performed as the workup protocol and purified by chromatography on silica with hexane/dichloromethane (10/1) as the elution to afford the pure cycloadduct as clear oil.

R_f (hexane/dichloromethane 10/1): 0.21

^1H NMR (CDCl_3 , 300 MHz): δ 7.24 (m, 3H), 7.09 (m, 3H), 6.94 (BB' of AA'BB', $J = 9$ Hz, 2H), 3.86 (s, 3H), 3.45 (q, $J = 9$ Hz, 1H), 3.03 (t, $J = 9$ Hz, 1H), 2.60 (dt, $J = 12, 6$ Hz, 1H), 2.42 (m, 1H), 2.39 (s, 3H), 1.78 (q, $J = 9$ Hz, 1H), 1.28 (d, $J = 6$ Hz, 3H).

^{13}C NMR (CDCl_3 , 300 MHz): δ 158.08, 144.66, 137.80, 135.99, 128.20, 127.82, 127.43, 126.75, 123.77, 113.78, 55.44, 55.28, 44.08, 35.55, 34.14, 21.54, 20.56.

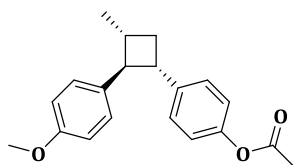


1-methoxy-4-((1S,2R,4S)-2-methyl-4-(p-tolyl)cyclobutyl)benzene: According to the general procedure B, a 40 mL vial with a magnetic stir bar was charged with *trans*-anethole (35.6 mg, 0.24 mmol), 4-methylstyrene (157.6 μL , 1.2 mmol), B-BT (2.4 mg) and CH_3NO_2 (2.4 mL). After the reaction was completed, the mixture was performed as the workup protocol and purified by chromatography on silica with hexane/dichloromethane (6/1) as the elution to afford the pure cycloadduct as clear oil.

R_f (hexane/dichloromethane 6/1): 0.35

^1H NMR (CDCl_3 , 300 MHz): δ 7.09 (AA' of AA'BB', $J = 9$ Hz, 2H), 7.00 (s, 4H), 6.77 (BB' of AA'BB', $J = 9$ Hz, 2H), 3.70 (s, 3H), 3.27 (q, $J = 9$ Hz, 1H), 2.84 (t, $J = 9$ Hz, 1H), 2.42 (q, $J = 9$ Hz, 1H), 2.25 (m, 1H), 2.22 (s, 3H), 1.60 (q, $J = 9$ Hz, 1H), 1.11 (d, $J = 6$ Hz, 3H).

^{13}C NMR (CDCl_3 , 300 MHz): δ 158.04, 141.67, 135.98, 135.40, 128.94, 127.78, 126.56, 113.75, 55.63, 55.27, 35.42, 34.13, 21.04, 20.54.

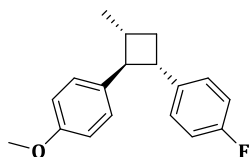


4-((1S,2S,3R)-2-(4-methoxyphenyl)-3-methylcyclobutyl)phenyl acetate: According to the general procedure B, a 40 mL vial with a magnetic stir bar was charged with *trans*-anethole (35.6 mg, 0.24 mmol), 4-vinylphenyl acetate (183.6 μL , 1.2 mmol), B-BT (2.4 mg) and CH_3NO_2 (2.4 mL). After the reaction was completed, the mixture was performed as the workup protocol and purified by chromatography on silica with hexane/diethyl ether (5/1) as the elution to afford the pure cycloadduct as clear oil.

R_f (hexane/diethyl ether 5/1): 0.40

^1H NMR (CDCl_3 , 300 MHz): δ 7.23 (AA' of AA'BB', $J = 6$ Hz, 2H), 7.20 (AA' of AA'BB', $J = 6$ Hz, 2H), 7.01 (BB' of AA'BB', $J = 9$ Hz, 2H), 6.89 (BB' of AA'BB', $J = 9$ Hz, 2H), 3.83 (s, 3H), 3.42 (td, $J = 12, 6$ Hz, 1H), 2.96 (t, $J = 9$ Hz, 1H), 2.54 (q, $J = 9$ Hz, 1H), 2.37 (m, 1H), 2.32 (s, 3H), 1.71 (q, $J = 9$ Hz, 1H), 1.21 (d, $J = 9$ Hz, 3H).

^{13}C NMR (CDCl_3 , 300 MHz): δ 169.73, 158.14, 148.79, 142.28, 135.60, 127.82, 127.57, 121.24, 113.82, 55.67, 55.27, 43.57, 35.59, 34.00, 21.15, 20.49.



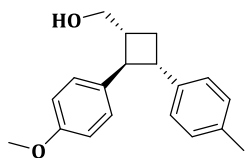
1-fluoro-4-((1S,2S,3R)-2-(4-methoxyphenyl)-3-methylcyclobutyl)benzene: According to the general procedure B, a 40 mL vial with a magnetic stir bar was charged with *trans*-anethole (35.6 mg, 0.24 mmol), 1-fluoro-4-vinylbenzene (143 μL , 1.2 mmol), B-BT (2.4 mg) and CH_3NO_2 (2.4 mL). After the reaction was completed, the mixture was performed as the

workup protocol and purified by chromatography on silica with hexane/dichloromethane (8/1) as the elution to afford the pure cycloadduct as clear oil.

R_f (hexane/dichloromethane 8/1): 0.35

^1H NMR (CDCl_3 , 300 MHz): δ 7.19 (m, 4H), 7.00 (t, $J = 6$ Hz, 3H), 6.92 (BB' of AA'BB', $J = 9$ Hz, 2H), 3.84 (s, 3H), 3.38 (q, $J = 9$ Hz, 1H), 2.93 (t, $J = 9$ Hz, 1H), 2.57 (q, $J = 9$ Hz, 1H), 2.38 (m, 1H), 1.72 (q, $J = 9$ Hz, 1H), 1.24 (d, $J = 6$ Hz, 3H).

^{13}C NMR (CDCl_3 , 300 MHz): δ 162.62 ($^1J_{\text{CF}} = 969$ Hz), 158.17, 140.30 ($^1J_{\text{CF}} = 12$ Hz), 135.54, 128.04 ($^3J_{\text{CF}} = 30$ Hz), 127.78, 115.09 ($^2J_{\text{CF}} = 84$ Hz), 113.84, 55.93, 55.26, 43.57, 35.45, 34.11, 20.46.

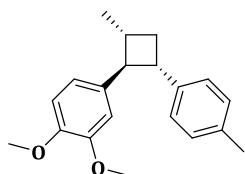


((1R,2R,3S)-2-(4-methoxyphenyl)-3-(p-tolyl)cyclobutyl)methanol: According to the general procedure B, a 40 mL vial with a magnetic stir bar was charged with (*E*)-3-(4-methoxyphenyl)prop-2-en-1-ol (39.4 mg, 0.24 mmol), 4-methylstyrene (157.6 μL , 1.2 mmol), B-BT (2.4 mg) and CH_3NO_2 (2.4 mL). After the reaction was completed, the mixture was performed as the workup protocol and purified by chromatography on silica with hexane/ethyl acetate (8/1) as the elution to afford the pure cycloadduct as clear oil.

R_f (hexane/ethyl acetate 8/1): 0.10

^1H NMR (CDCl_3 , 300 MHz): δ 7.11 (AA', $J = 9$ Hz, 2H), 7.01 (m, 4H), 6.76 (BB', $J = 9$ Hz, 2H), 3.68 (s, 3H), 3.66 (m, 1H), 3.62 (m, 1H), 3.32 (td, $J = 9, 6$ Hz, 1H), 3.12 (t, $J = 9$ Hz, 1H), 2.46 (m, 1H), 2.36 (m, 1H), 2.22 (s, 3H), 1.81 (q, $J = 9$ Hz, 1H), 1.61 (br s, 1H).

^{13}C NMR (CDCl_3 , 300 MHz): δ 158.14, 141.25, 135.66, 135.51, 129.02, 127.94, 126.57, 113.85, 66.03, 55.28, 50.21, 43.97, 41.61, 28.66, 21.06.



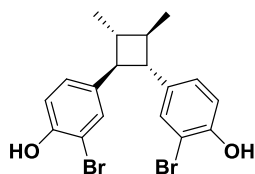
1,2-dimethoxy-4-((1S,2R,4S)-2-methyl-4-(p-tolyl)cyclobutyl)benzene: According to the general procedure B, a 40 mL vial with a magnetic stir bar was charged with (*E*)-1,2-dimethoxy-4-(prop-1-en-1-yl)benzene (40.7 μL , 0.24 mmol), 4-methylstyrene (157.6 μL ,

1.2 mmol), B-BT (2.4 mg) and CH_3NO_2 (2.4 mL). After the reaction was completed, the mixture was performed as the workup protocol and purified by chromatography on silica with hexane/dichloromethane (1/1) as the elution to afford the pure cycloadduct as clear oil.

R_f (hexane/dichloromethane 1/1): 0.31

^1H NMR (CDCl_3 , 300 MHz): δ 7.01 (m, 4H), 6.72 (m, 2H), 6.67 (m, 1H), 3.77 (s, 6H), 3.26 (q, $J = 9$ Hz, 1H), 2.82 (t, $J = 9$ Hz, 1H), 2.43 (dt, $J = 3, 9$ Hz, 1H), 2.27 (m, 1H), 2.23 (s, 3H), 1.62 (q, $J = 9$ Hz, 1H), 1.12 (d, $J = 6$ Hz, 3H).

^{13}C NMR (CDCl_3 , 300 MHz): δ 148.86, 147.49, 141.59, 136.55, 135.43, 128.93, 126.52, 118.67, 111.24, 110.24, 56.15, 55.94, 55.84, 43.82, 35.40, 33.88, 21.01, 20.55.



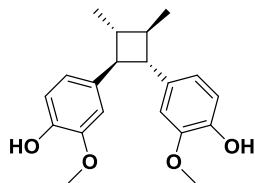
4,4'-((1R,2R,3S,4S)-3,4-dimethylcyclobutane-1,2-diyl)bis(2-bromophenol):

The compound was obtained via two steps methods, including bromination process and demethylation procedure, which was similar to previous reports^{117,316}. Typically, a 40 mL vial with a magnetic stir bar was charged with anethole dimer (94 mg, 0.3193 mmol) and acetic acid (2 mL), and was cooled at 0 °C. Then, Br_2 (42 μL , 2.5 equiv.) was added dropwise and the reactive solution was kept stirring at room temperature for another 30 min. After that, the reaction was quenched with $\text{Na}_2\text{S}_2\text{O}_3$, extracted with dichloromethane for 3 times, washed with brine, water, dried over MgSO_4 , and concentrated *in vacuo*. The crude product was used for next step without further purification. More precisely, after dried in over for overnight, the crude mixture was added with anhydrous DCM (14 mL) at 0 °C. Then, a solution of BBr_3 (6.4 mM, 1 M in DCM) was added dropwise and the reaction was kept at 0 °C for 2 h. Finally, the reactive solution was stirred at room temperature for 24 h. After the reaction finished, the mixture was cooled to 0 °C, and quenched with water, then extracted with DCM, wash with brine, water, dried over MgSO_4 , and concentrated *in vacuo*. After purified by chromatography on silica with hexane/acetone (8/1) as the elution, a pure product of light red oil (101 mg) was obtained with the yield of 75% over two steps.

R_f (hexane/acetone 8/1): 0.21

^1H NMR (CDCl_3 , 300 MHz): δ 7.23 (d, $J = 2$ Hz, 2H), 6.98 (dd, $J = 3, 9$ Hz, 2H), 6.88 (d, $J = 9$ Hz, 2H), 5.33 (bs, 2H), 2.66 (dd, $J = 3, 6$ Hz, 2H), 1.78 (m, 2H), 1.12 (d, $J = 6$ Hz, 6H).

^{13}C NMR (CDCl_3 , 300 MHz): δ 150.64, 137.01, 129.95, 127.64, 115.93, 110.20, 52.28, 43.23, 18.68.



4,4'-((1S,2S,3R,4R)-3,4-Dimethylcyclobutane-1,2-diyl)bis(1,2-dimethoxybenzene):

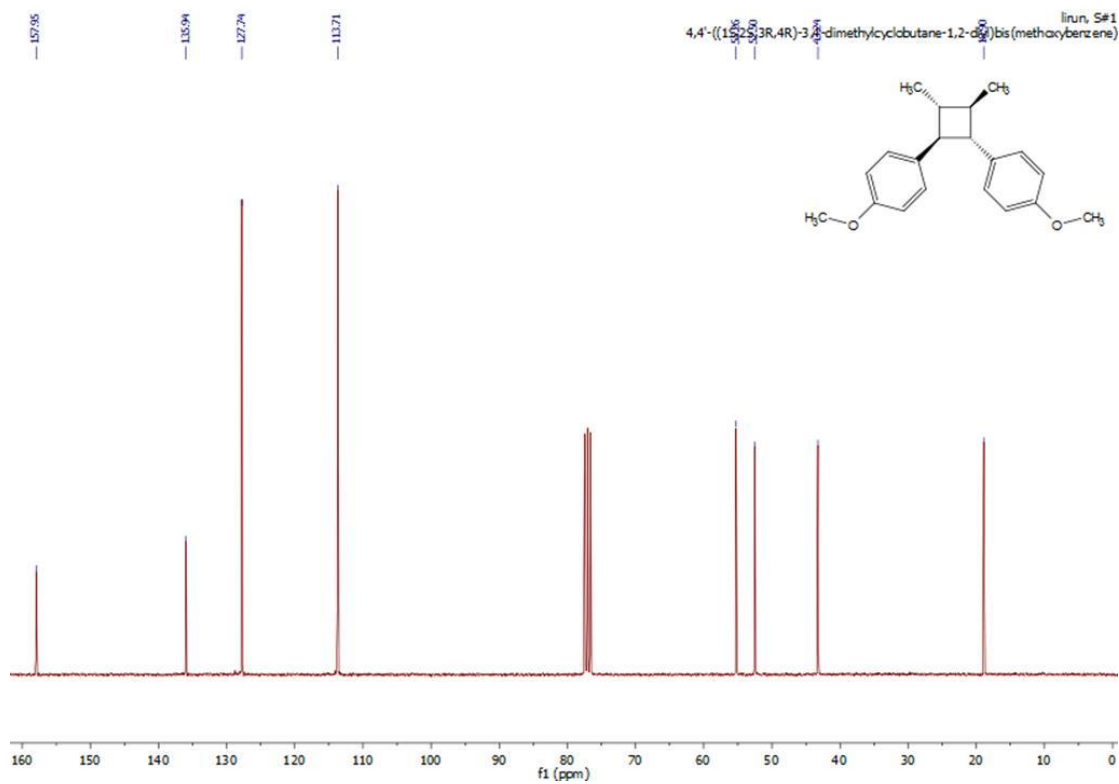
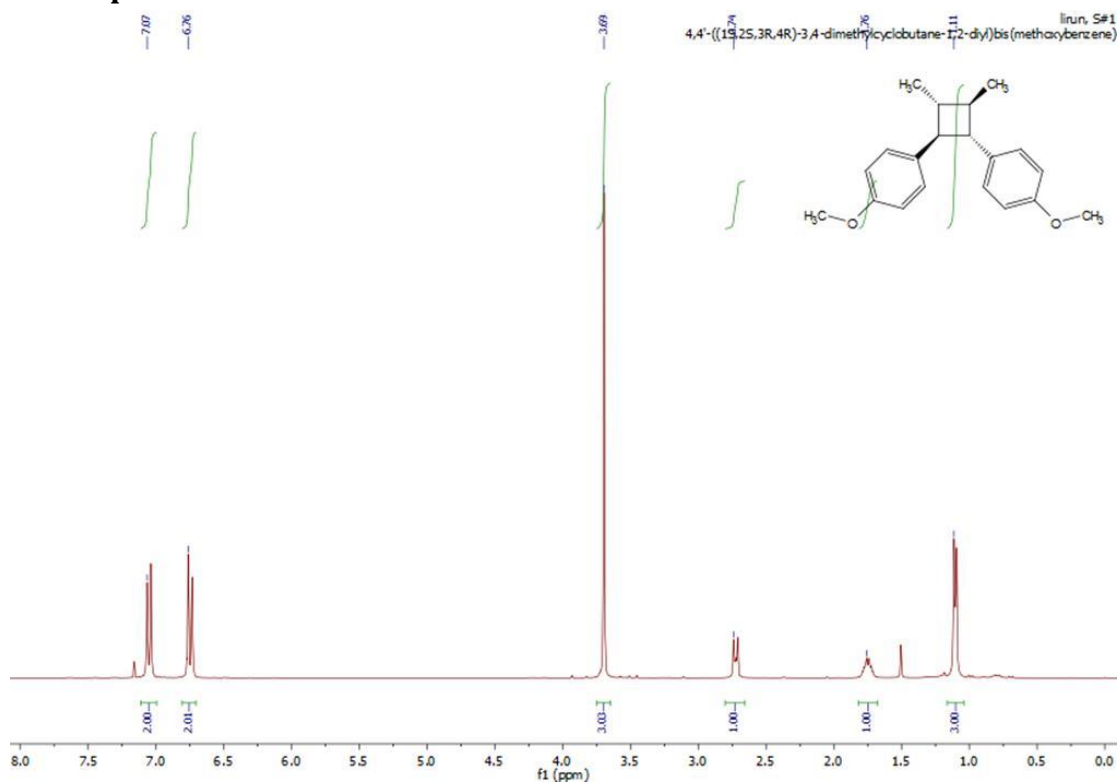
The compound was obtained via BINAM-copper (I) catalyzed Ullmann-type coupling, which was similar to previous reports^{117,317}. Typically, a 25 mL Schlenk flask was charged with the starting compound (94 mg, 0.22 mmol), Cs_2CO_3 (287.5 mg, 4 equiv.), CuI (16.8 mg, 0.04 equiv.), and BINAM (25.1 mg, 0.04 equiv.). The Schlenk flask was evacuated and back-filled with anhydrous argon for three times. Then sparged MeOH (1.5 mL) was added under the argon bath, and the reaction mixture was stirring at 110 °C for 36 h. Then the mixture was allowed to cool to room temperature and diluted with water. After quenched with 3 M HCl at 0 °C, the mixture was extracted with DCM for 3 times, dried over MgSO_4 and concentrated *in vacuo*. After purified by chromatography on silica with hexane/acetone (6/1) as the elution, a pure product of yellow oil (56 mg) was obtained with the yield of 78%.

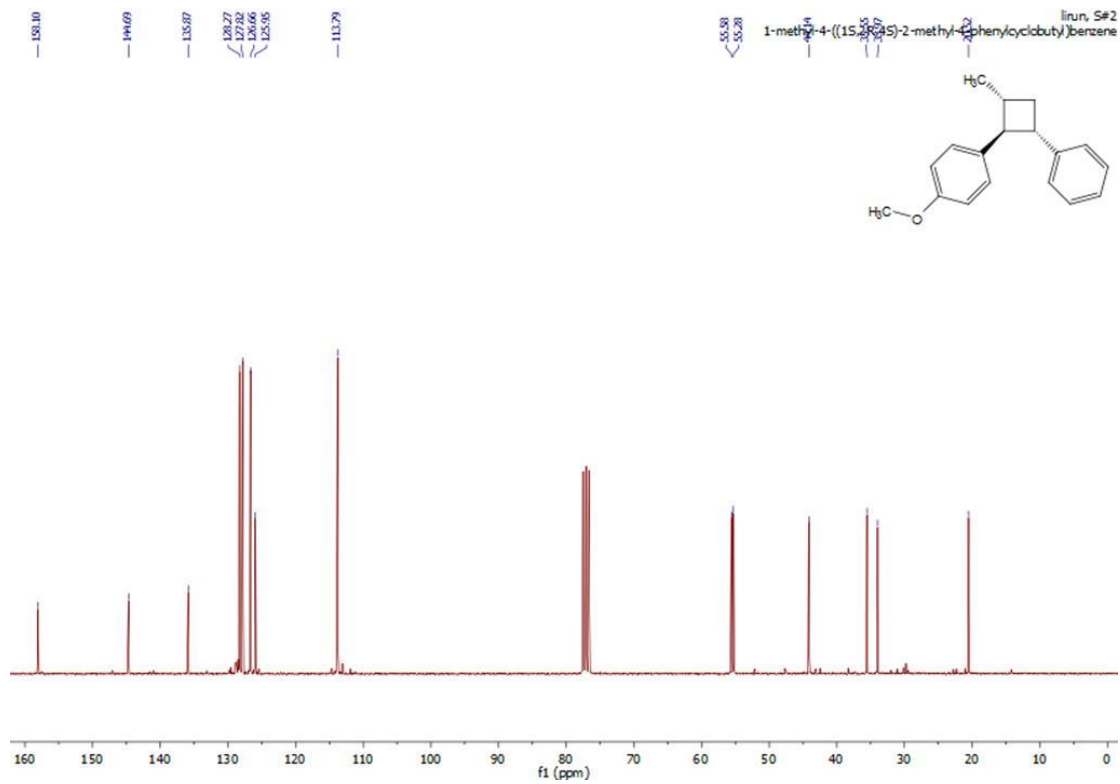
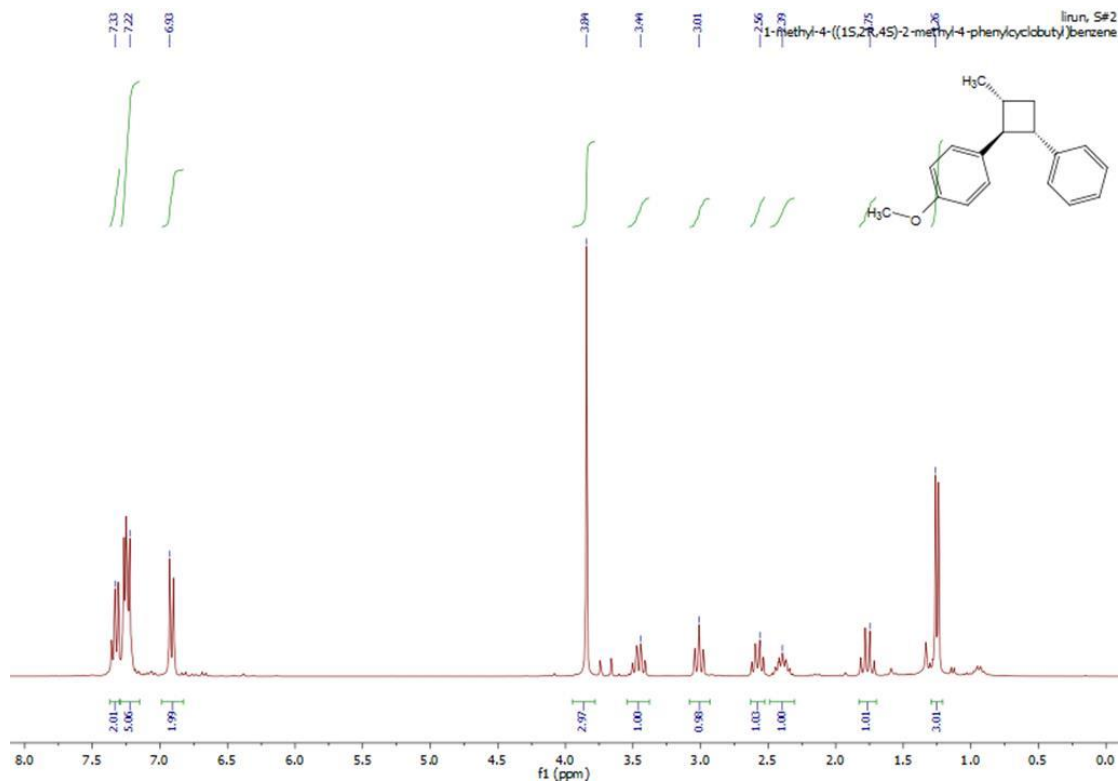
R_f (hexane/acetone 6/1): 0.07

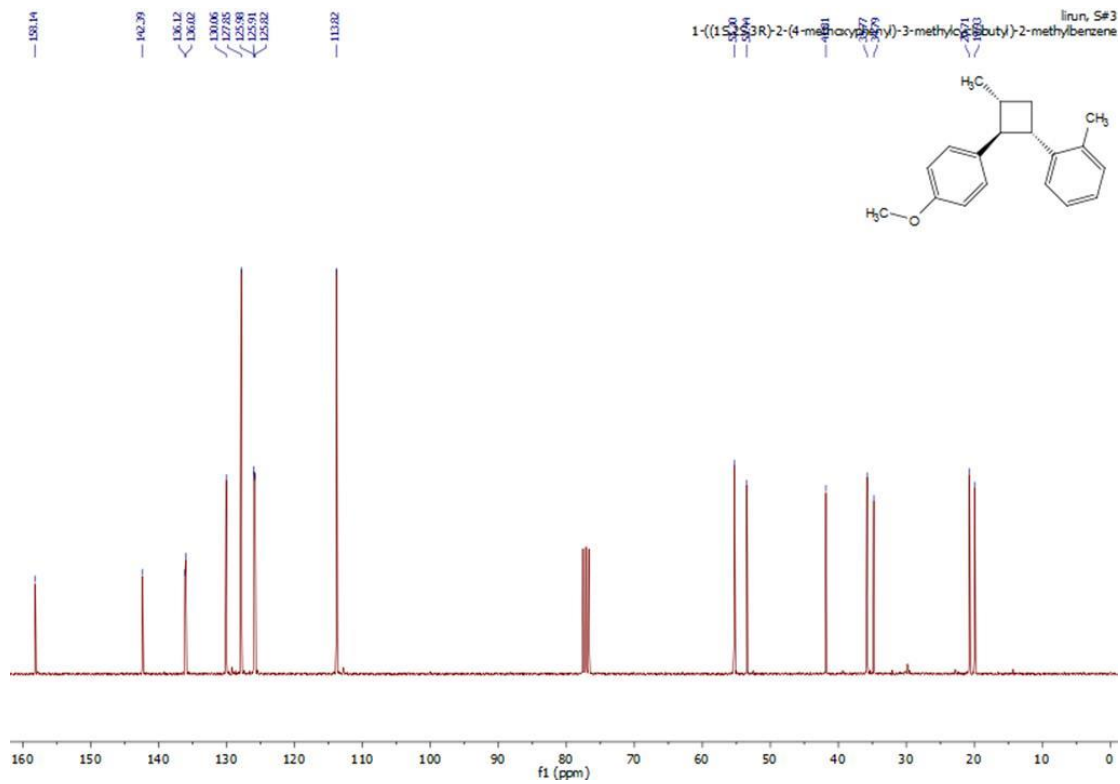
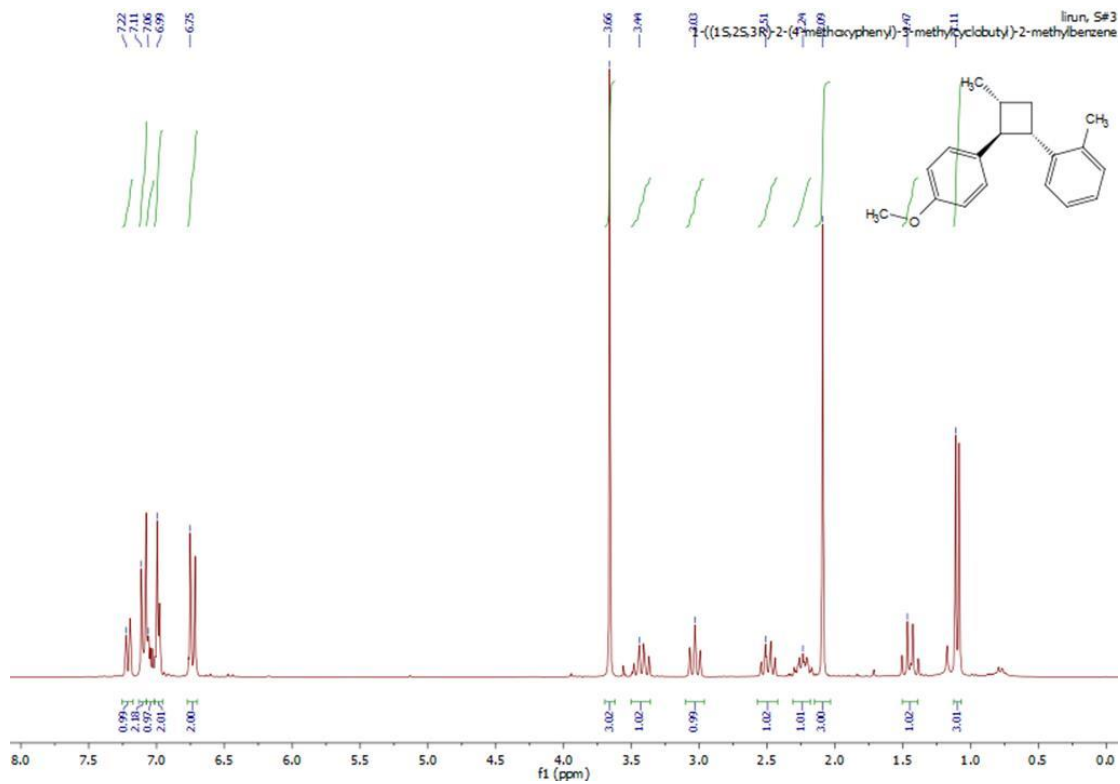
^1H NMR (CDCl_3 , 300 MHz): δ 6.76 (d, $J = 6$ Hz, 2H), 6.67 (dd, $J = 3, 6$ Hz, 2H), 6.60 (d, $J = 3$ Hz, 2H), 5.40 (bs, 2H), 3.78 (s, 6H), 2.67 (dd, $J = 3, 6$ Hz, 2H), 1.76 (m, 2H), 1.11 (d, $J = 2.1$ Hz, 6H).

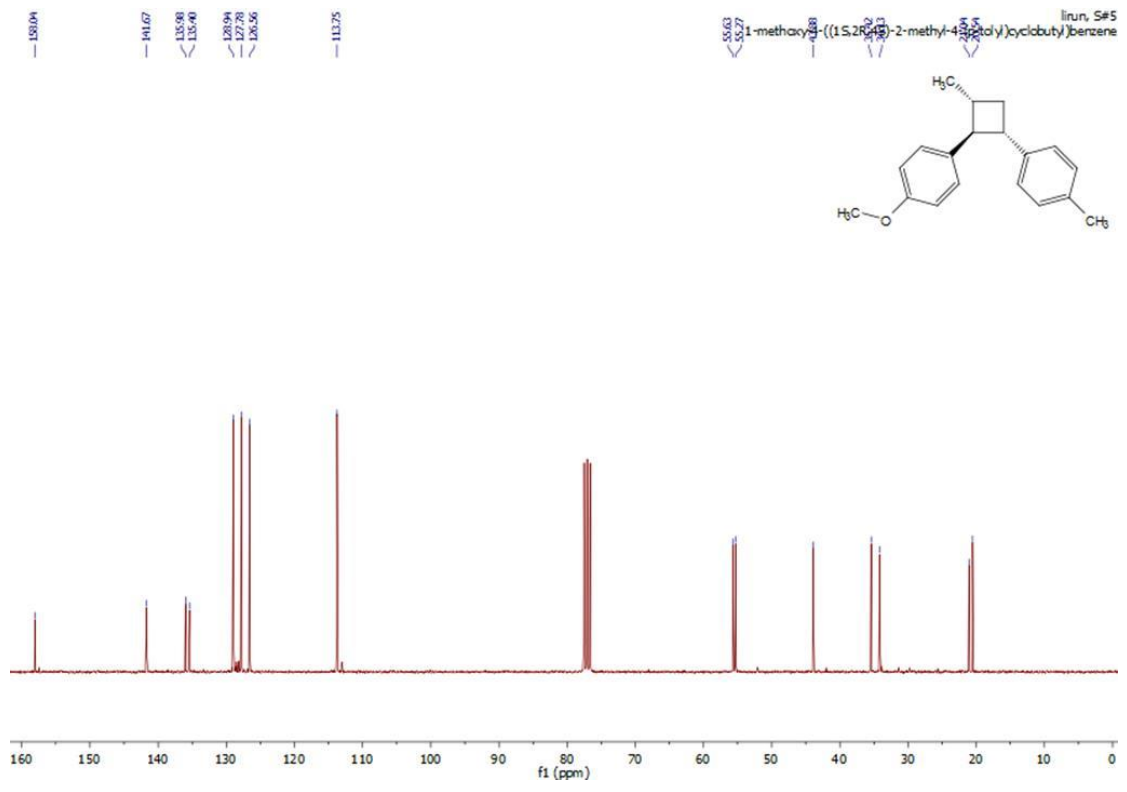
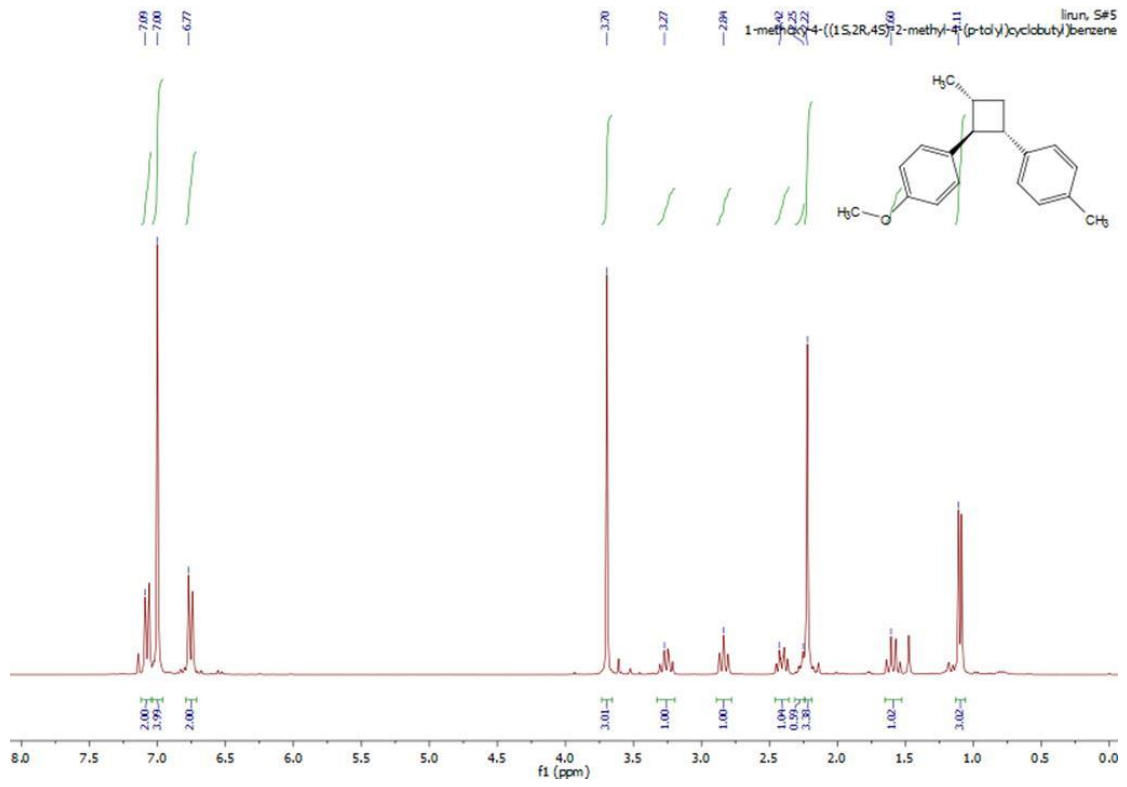
^{13}C NMR (CDCl_3 , 300 MHz): δ 146.34, 143.94, 135.81, 119.33, 114.17, 109.41, 55.86, 53.22, 43.00, 18.87.

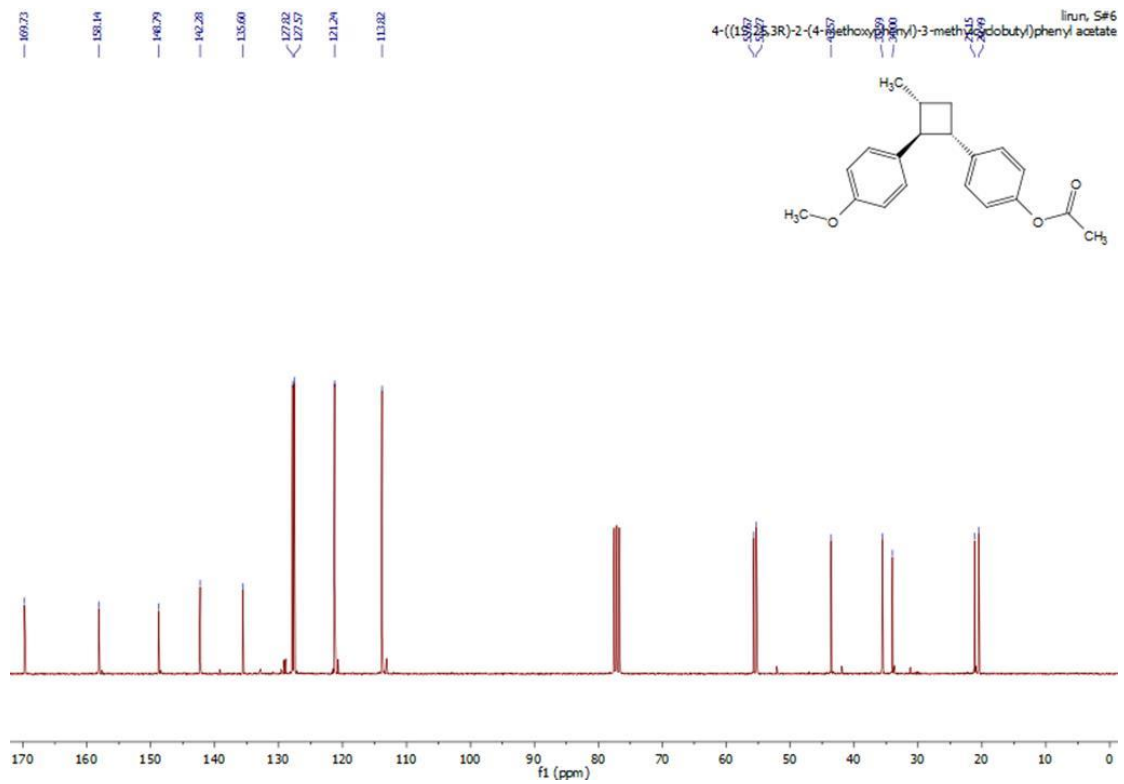
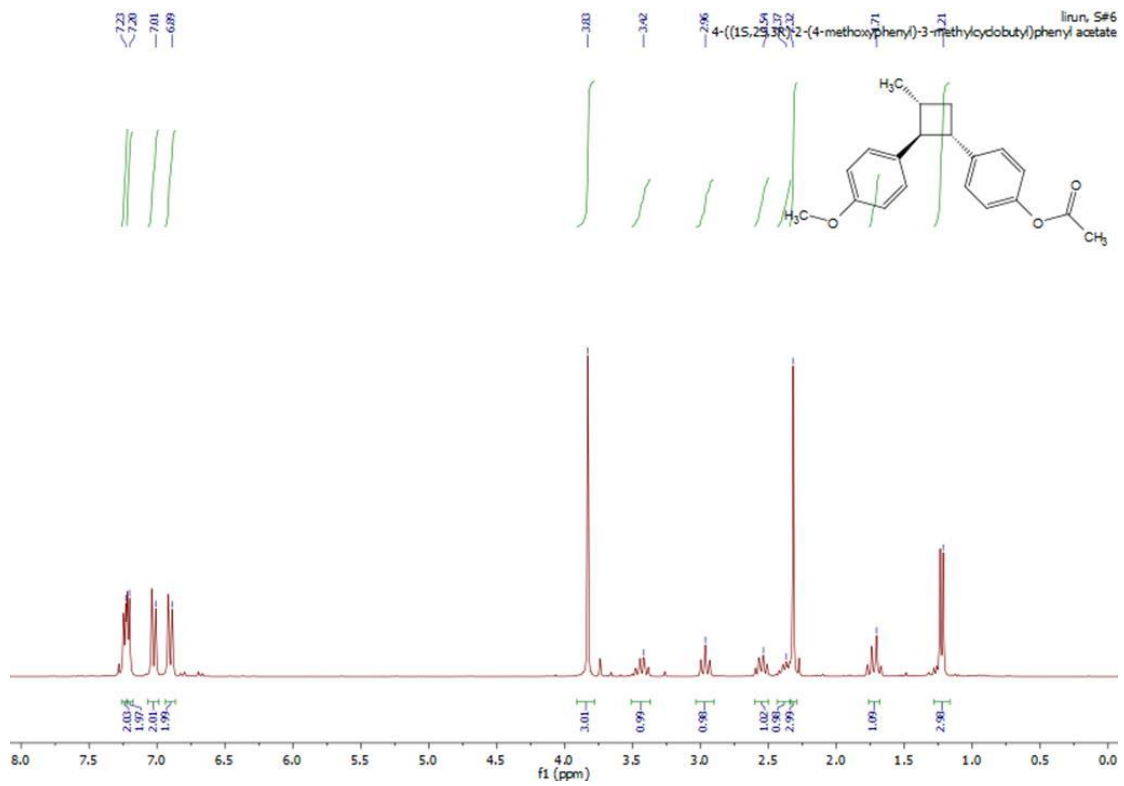
6.3.5 NMR spectra

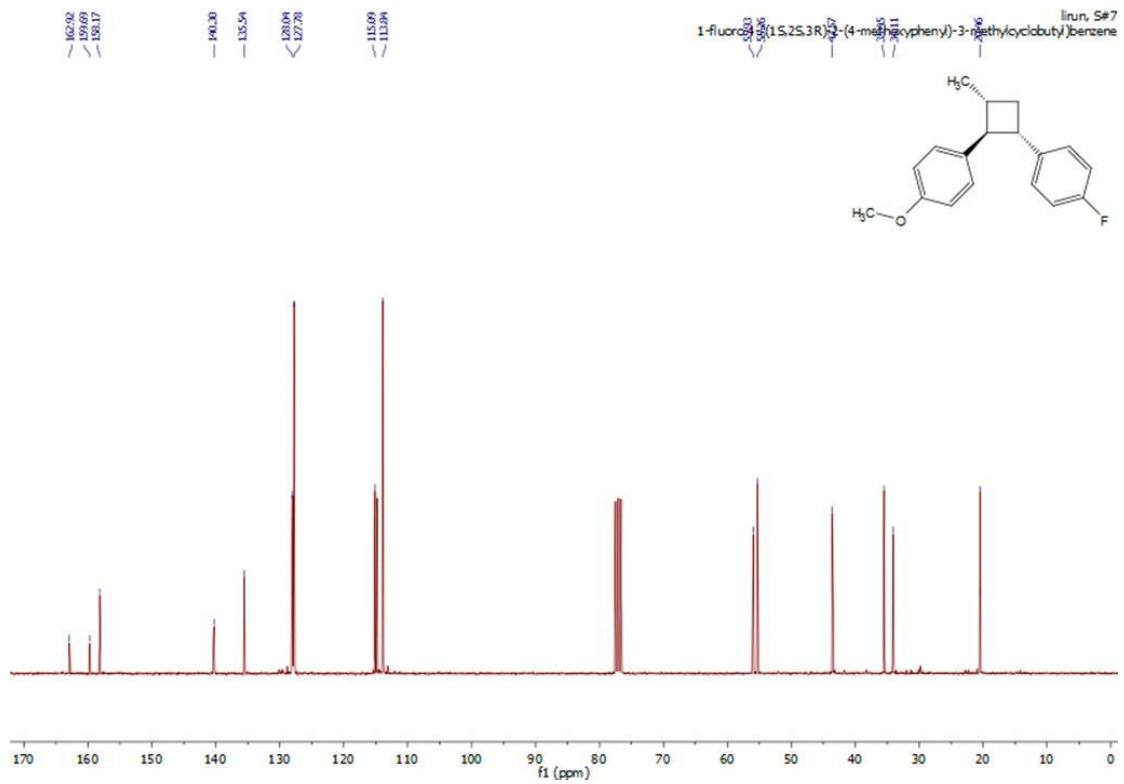
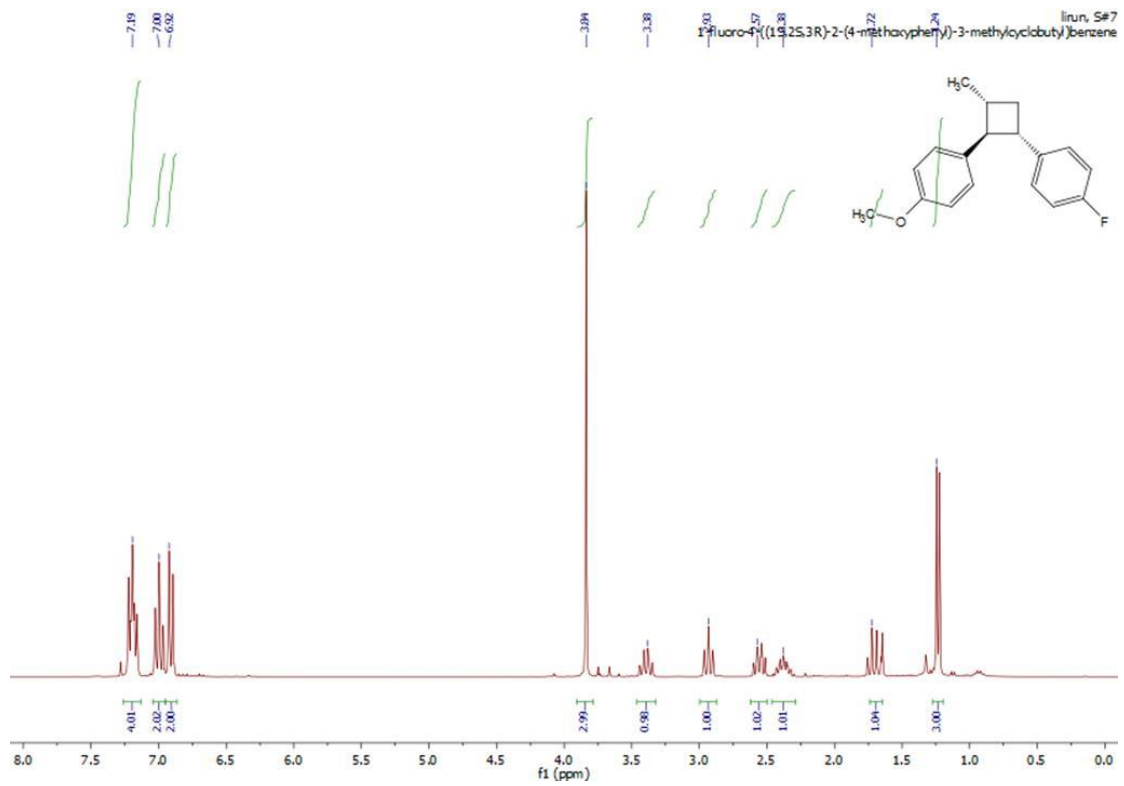


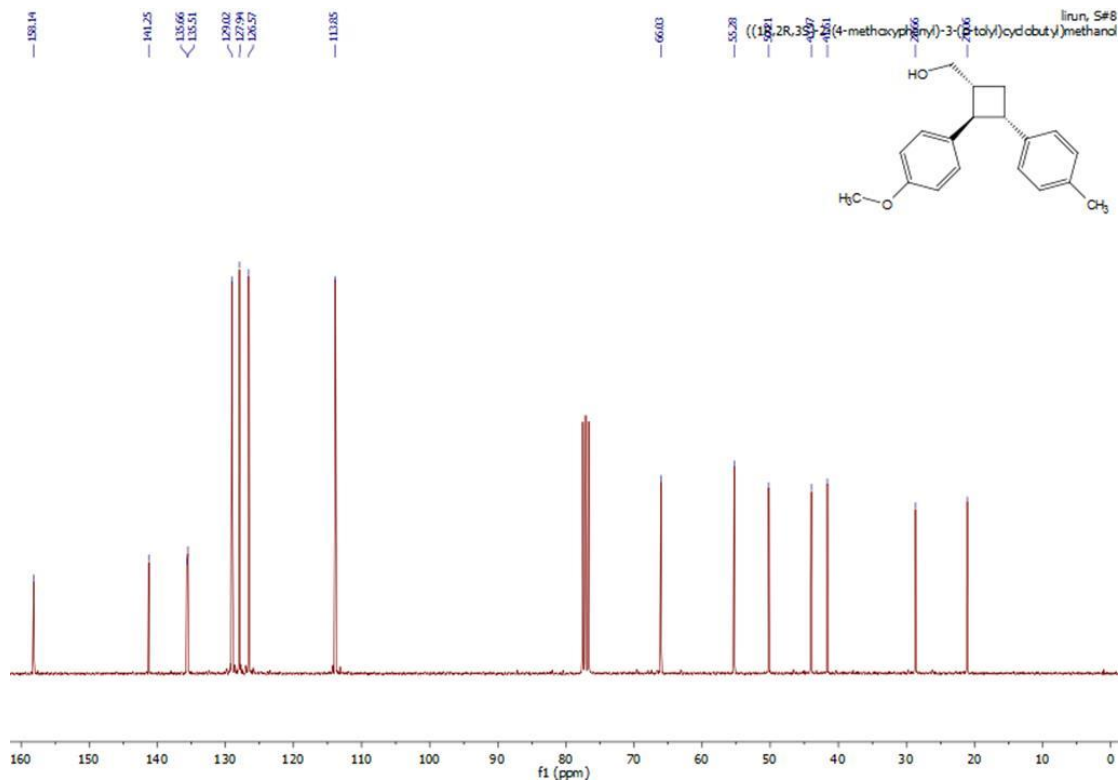
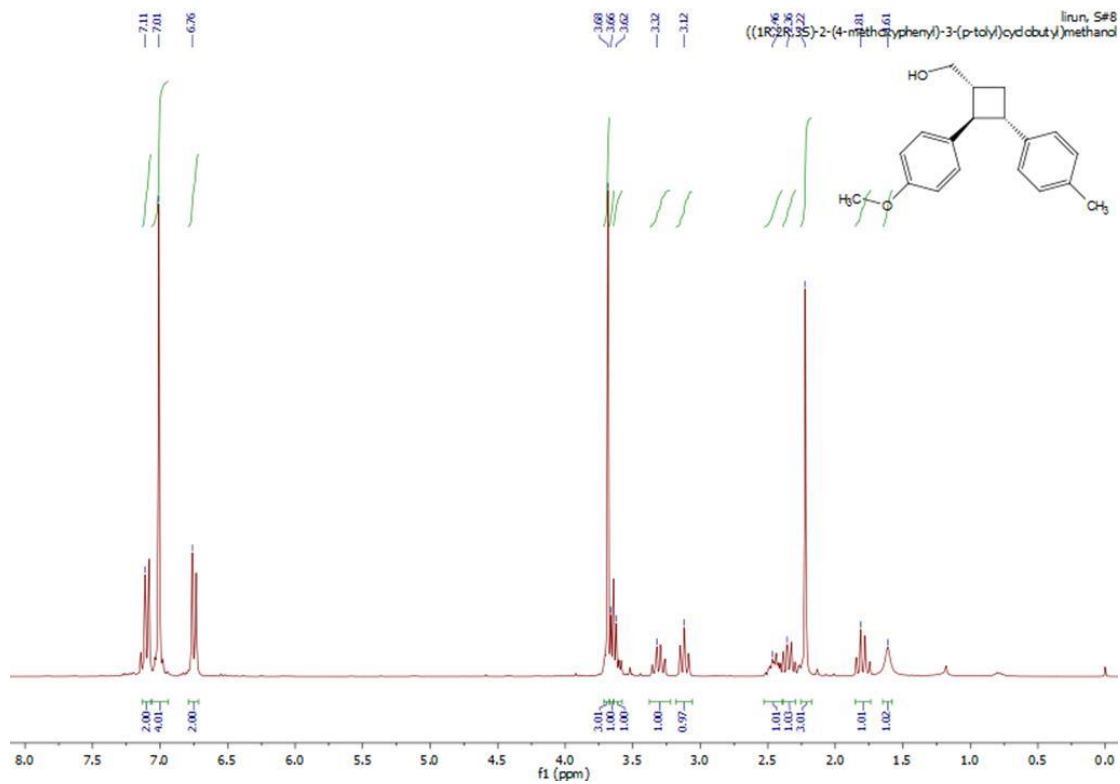


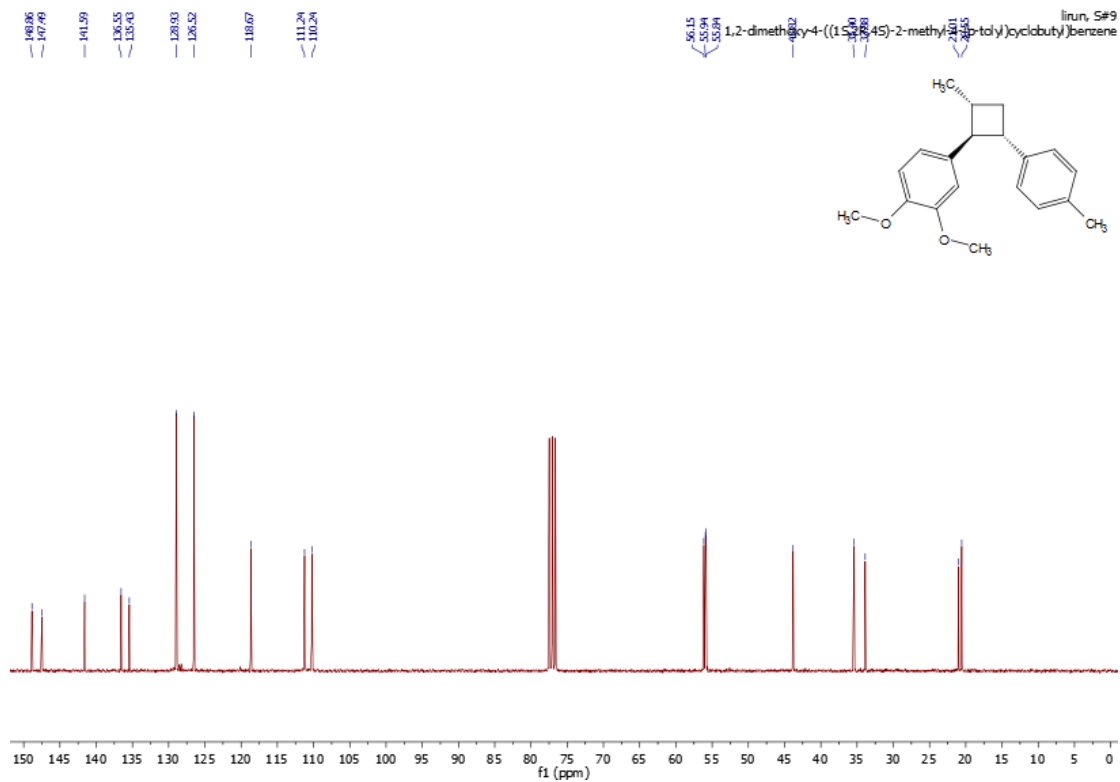
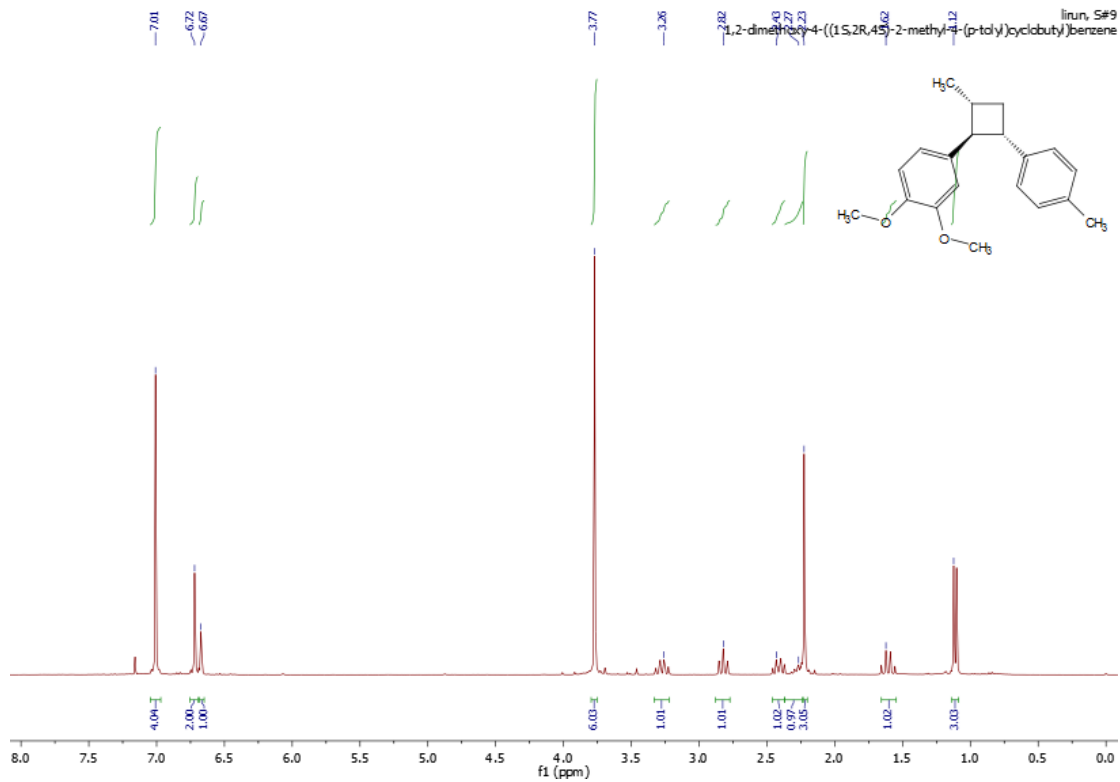


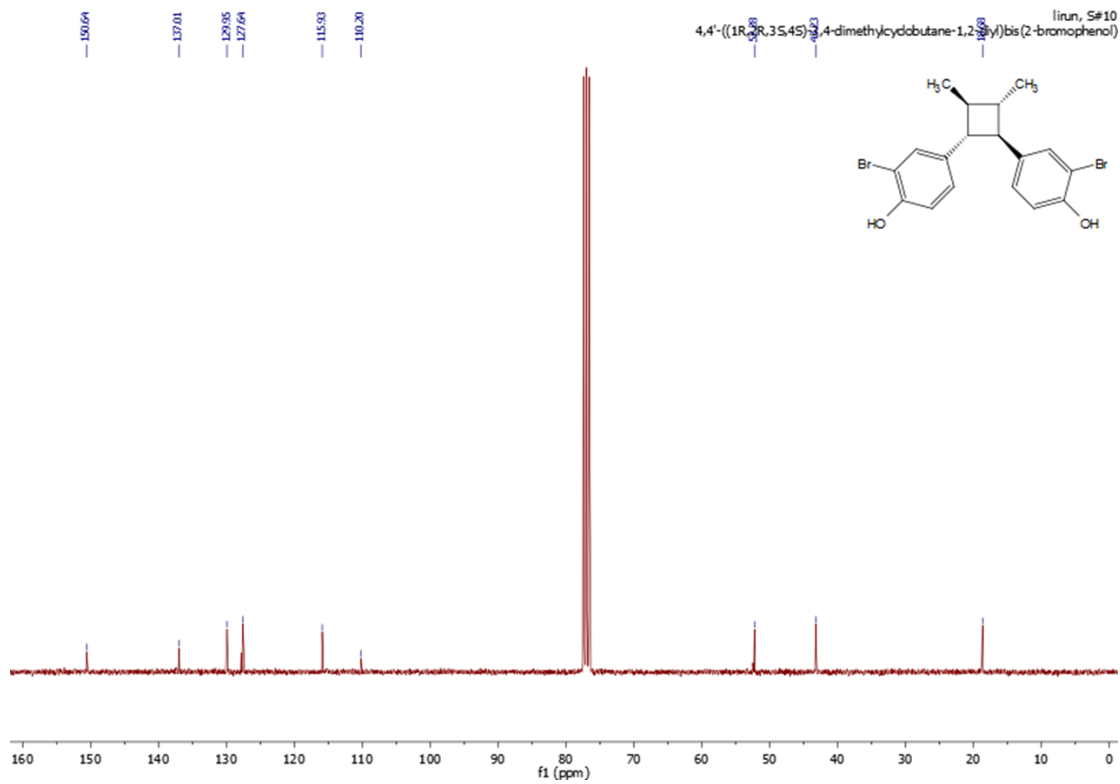
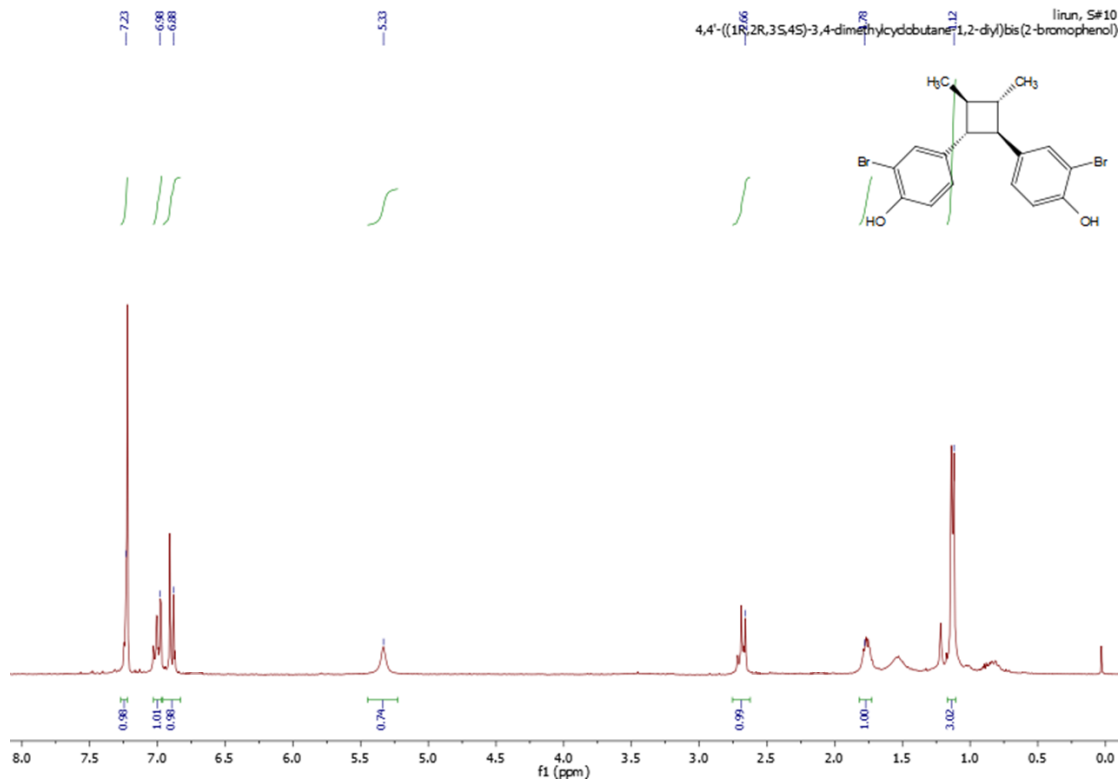


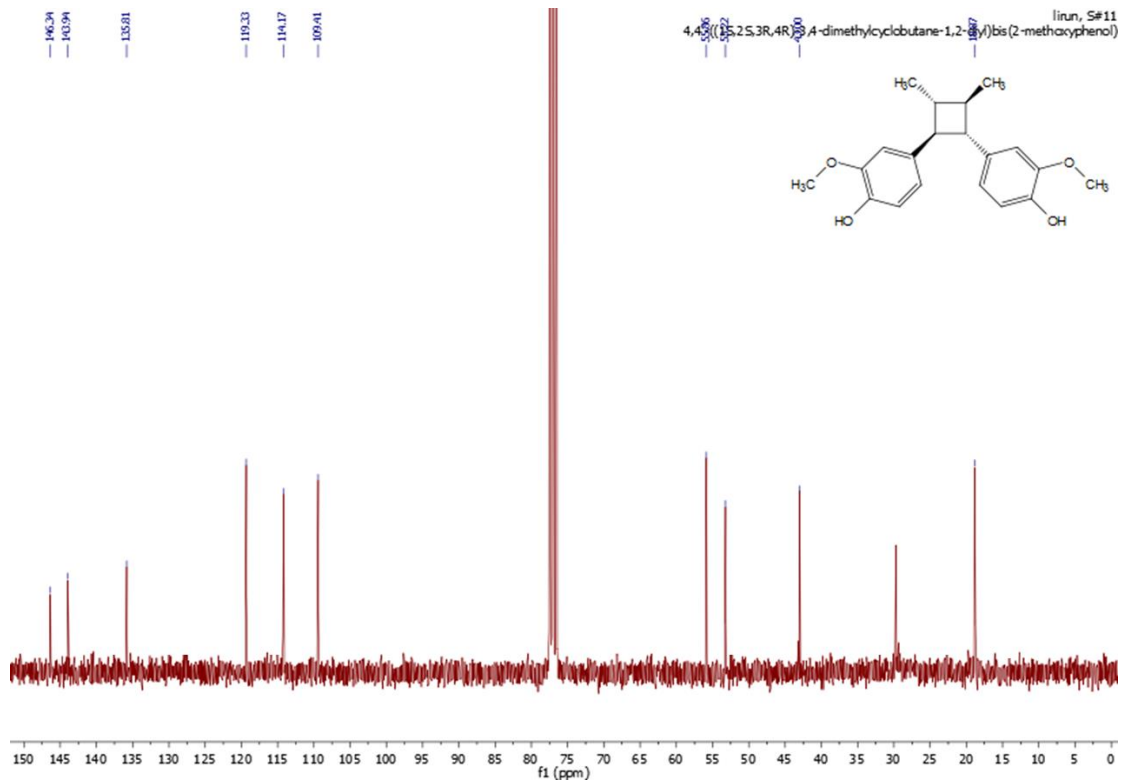
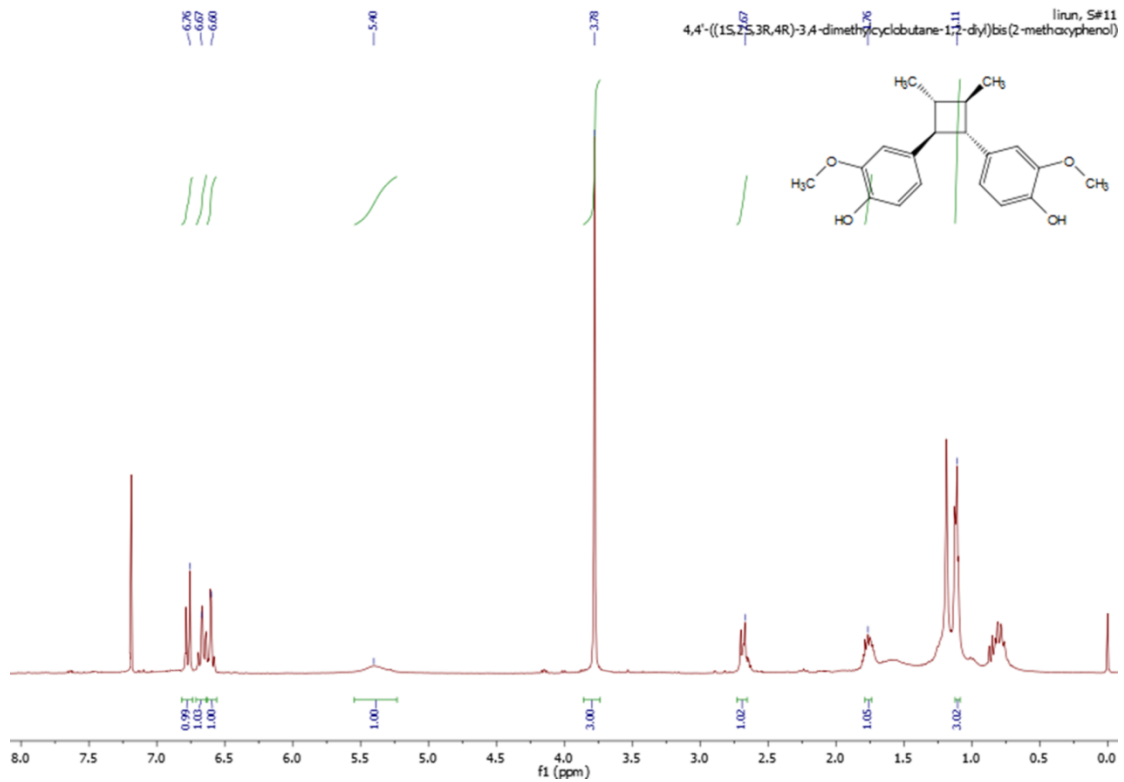


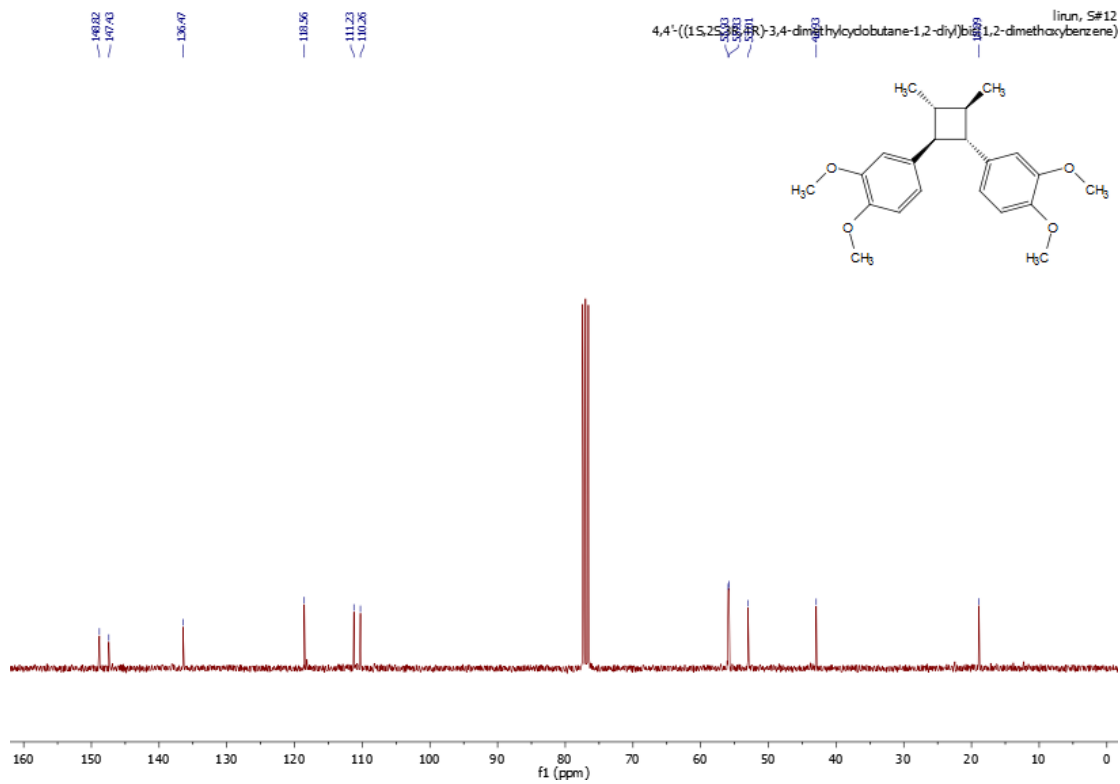
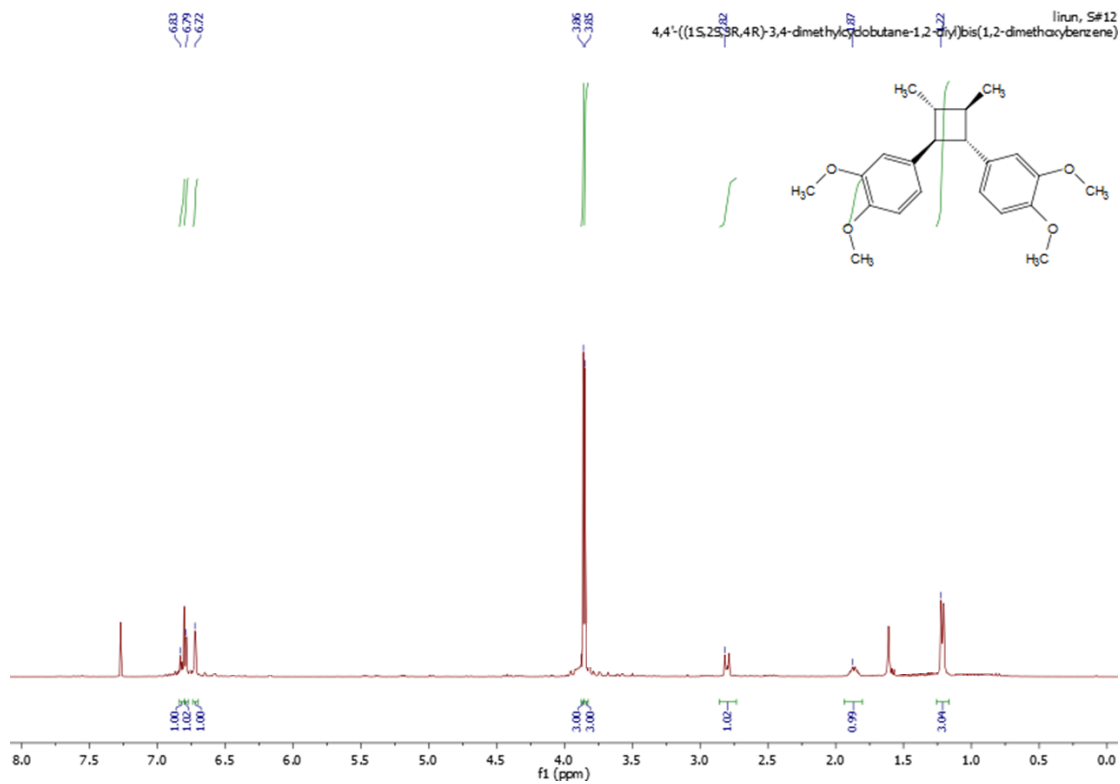












6.4 Design of twisted structure with thermally activated delayed fluorescence characteristic and its catalytic application for reduction of aryl and alkyl halides via consecutive visible light-induced charge transfer

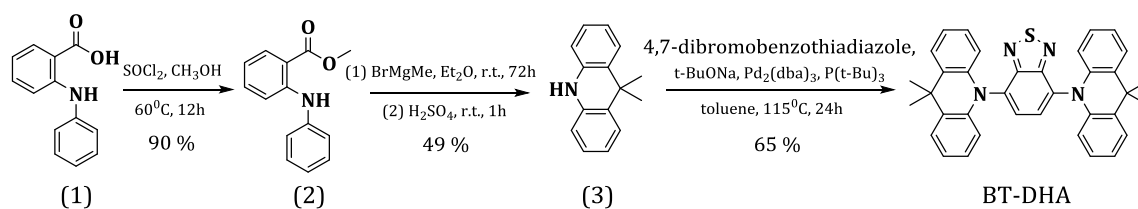
6.4.1 Materials

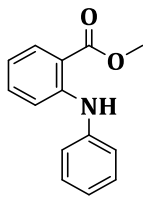
All chemicals and solvents were purchased from commercial sources and used as received unless otherwise noted. Column flash chromatography was conducted with silica 60 (0.063-0.2 mm). Reaction yield refer to pure compound after being purified with column.

6.4.2 Methods and characterization

UV-Vis absorption and fluorescence spectra were recorded on a Perkin Elmer Lambda 100 spectrophotometer and J&M TIDAS spectrofluorometer at ambient temperature, respectively. Cyclic voltammetry measurement was carried out on a Metrohm Autolab PGSTAT204 potentiostat/galvanostat with a three-electrode-cell system: Hg/HgCl₂ electrode as the reference electrode, platinum wire as the counter electrode, glassy carbon electrode as the working electrode, and Bu₄NPF₆ (0.1 M acetonitrile) as supporting electrolyte with a scan rate of 100 mV s⁻¹ in the range of -2 V to 2 V. GC-MS measurement was carried out on Shimadzu GC-2010 plus gas chromatography and QP2010 ultra mass spectrometer with fused silica column (Phenomenex, Zebron 5-ms, unpolar) and flame ionization detector. ¹H and ¹³C NMR spectra for all compounds were measured using Bruker AVANCE 300 MR (at 300 MHz) and are referenced to 0.00 ppm and 0.0 ppm for SiMe₄.

6.4.3 Preparation of photocatalyst BT-DHA



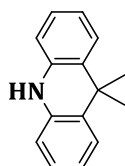


Methyl 2-(phenylamino)benzoate (2): the synthesis of (2) was similar to previous report²⁹⁸. Typically, a two-neck flask was charged with N-phenylanthranilic acid (9.98 g, 0.047 mol) and methanol (57 mL, 1.4 mol). After the temperature was stabilized at 60 °C, thionyl chloride (6.15 mL, 0.084 mol) was added dropwise and the reaction was stirring at 60 °C for overnight. Then, the reactive mixture was concentrated directly by rotary evaporator. The concentrated mixture was then extracted with toluene (30 mL) and saturated sodium hydrogen carbonate solution (30 mL), dried over anhydrous MgSO₄ and concentrated. The crude product was further purified by column chromatography with chloroform to offer the final product as yellow solid (9.61 g, 90%).

*R*_f (chloroform): 0.97

¹H NMR (CDCl₃, 300 MHz): δ 9.38 (bs, 1H), 7.91 (m, 1H), 7.21 (m, 3H), 7.16 (m, 3H), 7.01 (t, J = 7.5 Hz, 1H), 6.66 (t, J = 7.5 Hz, 1H), 3.83 (s, 3H).

¹³C NMR (CDCl₃, 300 MHz): δ 168.93, 147.93, 140.74, 134.09, 131.61, 129.35, 123.55, 122.51, 117.09, 114.02, 111.89, 51.79.

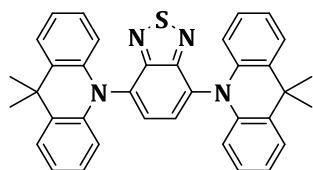


9,9-dimethyl-9,10-dihydroacridine (DHA, 3): the preparation of (3) was similar to previous report³¹⁸. More precisely, a flame-dried flask was charged with methyl 2-(phenylamino)benzoate (1.0 g, 4.4 mmol) and dry Et₂O (45 mL). the solution was cooled down to 0 °C in ice bath and degassed with argon for 20 min. then, 5.2 mL Grignard reagent in Et₂O (3.0 M methylmagnesium bromide in Et₂O, 3.5 equiv.) was added dropwise and the reaction mixture was stirring at room temperature for 3 days. After the mixture was quenched with saturated ammonium chloride, the organic part was collected, washed with brine and water, dried over MgSO₄ and concentrated. The crude tertiary alcohol was conducted for the next step reaction without further purification. For the crude material in the previous step was added 2 mL concentrated H₂SO₄ under the argon surroundings and the reaction mixture was stirring at ambient temperature for 1 h. after diluted with 30 mL water, the mixture was poured into 10% (v/v) ammoniacal solution and then extracted

with diethyl ether for several times. The organic layer was washed with saturated sodium bicarbonate, brine and water, dried over MgSO_4 , and concentrated. The crude product was further purified with column chromatography (hexane/dichloromethane from 9/1 to 2/1) for offer the final product as white solid (451 mg, 49%).

^1H NMR (CDCl_3 , 300 MHz): δ 7.32 (d, J = 9 Hz, 2H), 7.03 (m, 2H), 6.84 (m, 2H), 6.63 (d, J = 6 Hz, 2H), 6.05 (bs, 1H), 1.51(s, 6H).

^{13}C NMR (CDCl_3 , 300 MHz): δ 138.46, 129.13, 126.70, 125.47, 120.62, 113.40, 36.20, 30.51.



4,7-bis(9,9-dimethylacridin-10(9H)-yl)benzo[c][1,2,5]thiadiazole (BT-DHA): the photocatalyst was obtained via Buchwald-Hartwig cross coupling reaction. Typically, a flame-dried Schlenk flask was charged with 4,7-dibromo-2,1,3-benzothiadiazole (338.1 mg, 1.15 mmol), 9,9-dimethyl-9,10-dihydroacridine (506.5 mg, 2.42 mmol), sodium tert-butoxide (331.6 mg, 3.45 mmol), $\text{Pd}_2(\text{dba})_3$ (52.7 mg, 0.0575 mmol) and dry toluene (30 mL). After degassing with argon for 20 min, tri-tert-butyl phosphine (55.8 μL , 0.23 mmol) was added into flask under the argon bath. The reaction mixture was degassed for another 20 min and then increased the temperature to 115 $^\circ\text{C}$ and reacted for overnight. After cooled down to room temperature, the mixture was extracted with dichloromethane and saturated NH_4Cl solution. The organic layers was collected, dried over MgSO_4 and concentrated. The crude product was purified with column chromatography (hexane/dichloromethane 4/1) to provide the final product as orange solid (410 mg, 65%).

R_f (hexane/dichloromethane 4/1): 0.03

^1H NMR (CDCl_3 , 300 MHz): δ 7.99 (s, 1H), 7.60 (m, 2H), 7.05 (m, 2H), 7.02 (m, 2H), 6.36 (m, 2H), 1.84 (s, 6H).

^{13}C NMR (CDCl_3 , 300 MHz): δ 154.93, 140.15, 133.69, 133.35, 130.90, 126.52, 125.47, 113.67, 36.23, 30.88.

6.4.4 Photocatalytic reduction of aryl and alkyl halides

General procedure

A flame-dried Schlenk flask with a magnetic stirring bar was charged with halides (0.1 mmol), photocatalyst (0.005 mmol, 2.8 mg) and dry DMF (5 mL). After bubbling with argon for 5 min, DIPEA (1 mmol, 174.2 μ L) was added and the mixture was degassed with argon for another 5 min. Then the reaction mixture was placed under the irradiation of blue LED lamp (1.2 W/cm²) at the ambient temperature. The reaction conversion was determined by GC-MS measurement. When the reaction was finished, the mixture was extracted with Et₂O and water (v/v, 1/1) and the organic layers was collected, dried over MgSO₄ and concentrated. The residue crude product was purified with column chromatography to offer the final product.

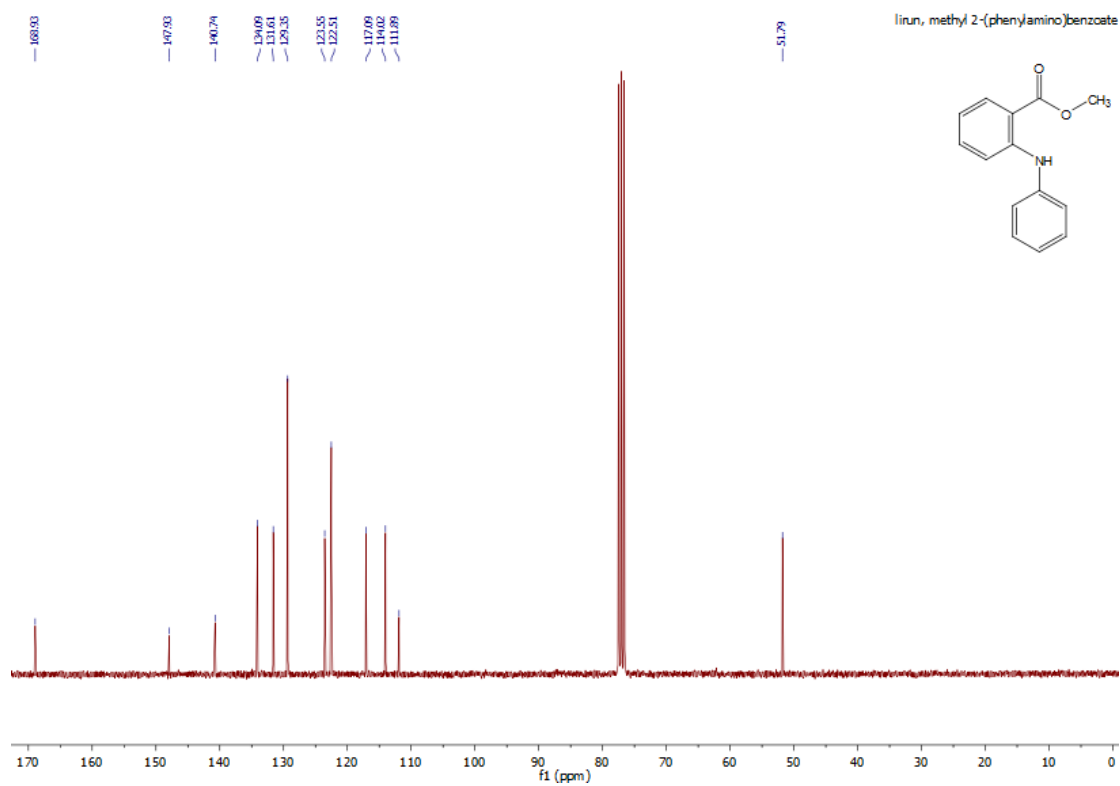
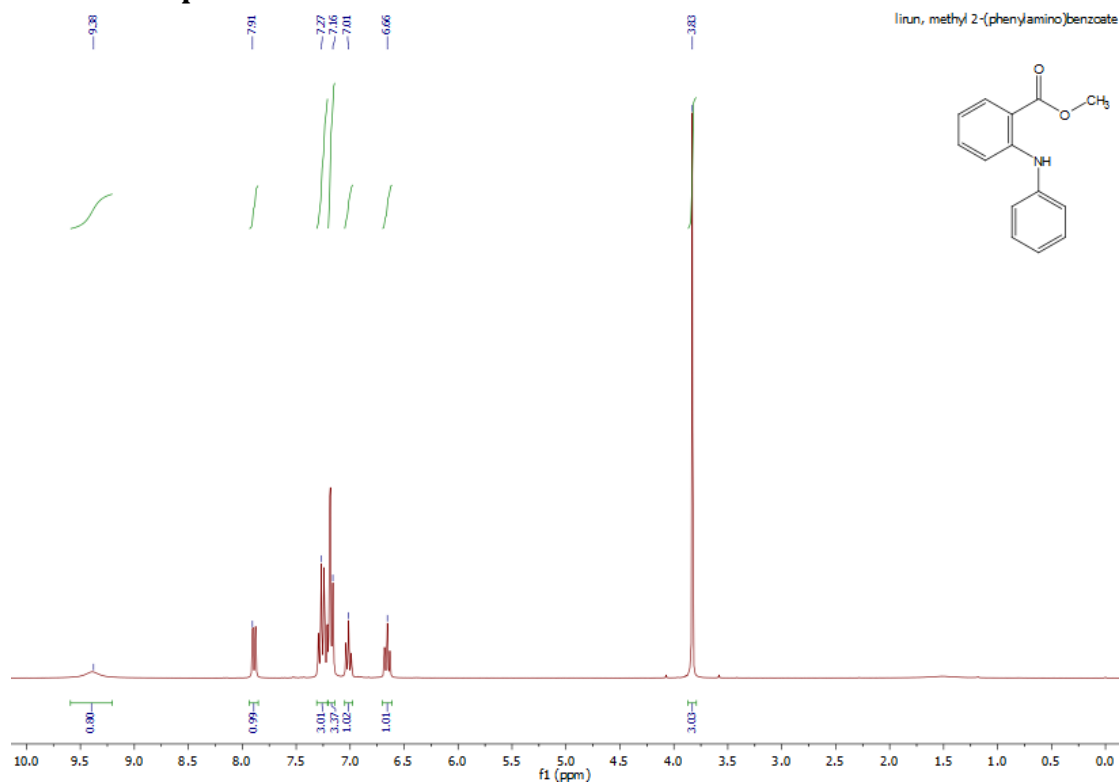
6.4.5 Deuterium labeling experiment

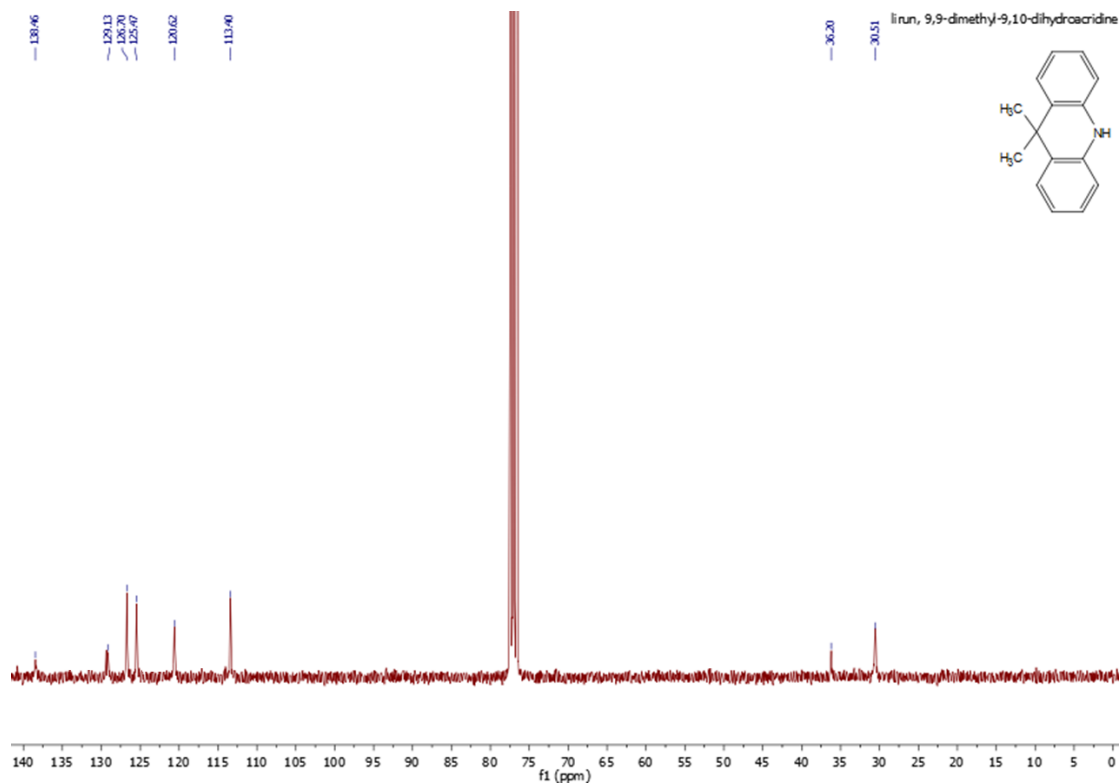
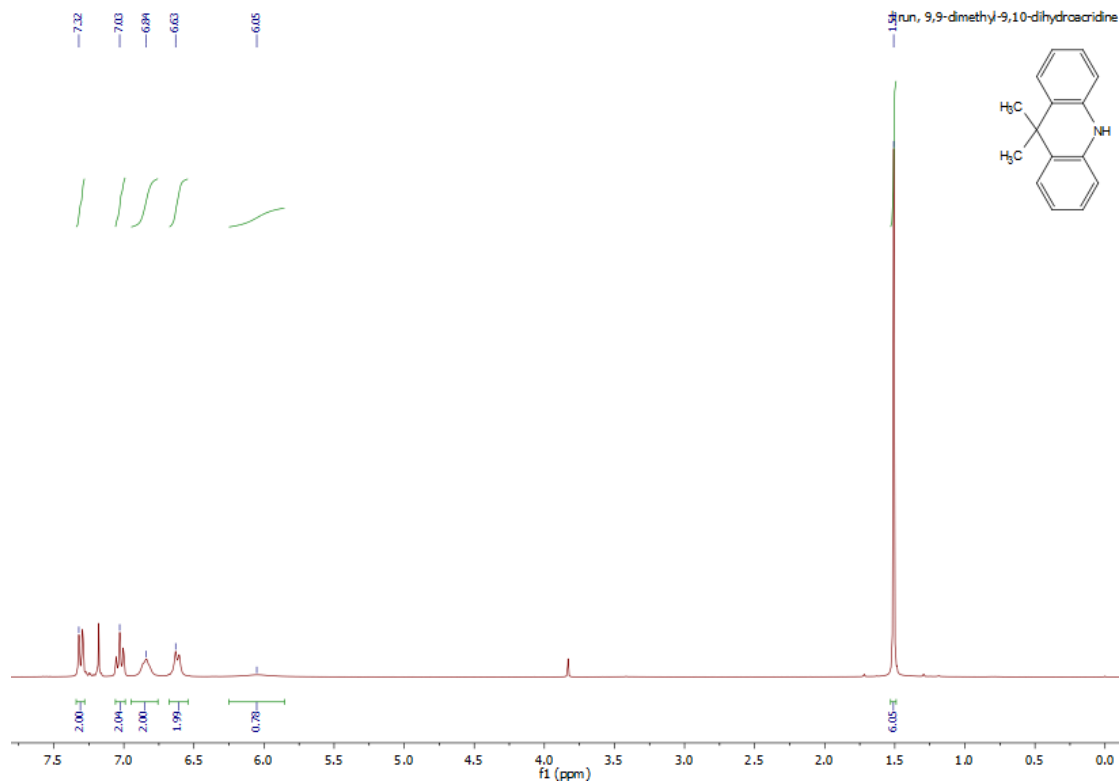
The deuterium labeling experiment was conducted according to the general procedure with d-DMF as the reaction solvent. More precisely, a flame-dried Schlenk tube with magnetic stir bar was charged with 4-iodoacetophenone (24.6 mg, 0.1 mmol), photocatalyst (2.8 mg, 0.005 mmol), DIPEA (174.2 μ L, 1 mmol) and d-DMF (2 mL). After bubbling with argon for 5 min, the mixture was under the irradiation of blue LED light for 24 h. Then, the reaction mixture was quenched with water and extracted with DCM for 3 times. The combined organic layers were dried over anhydrous MgSO₄ and concentrated with rotary evaporator. A pure product (10.8 mg, 90%) was obtained after being purified via column chromatography with hexane/dichloromethane (4/1) as the elution. The NMR spectrum was recorded at 700 MHz with d-DCM as the solvent.

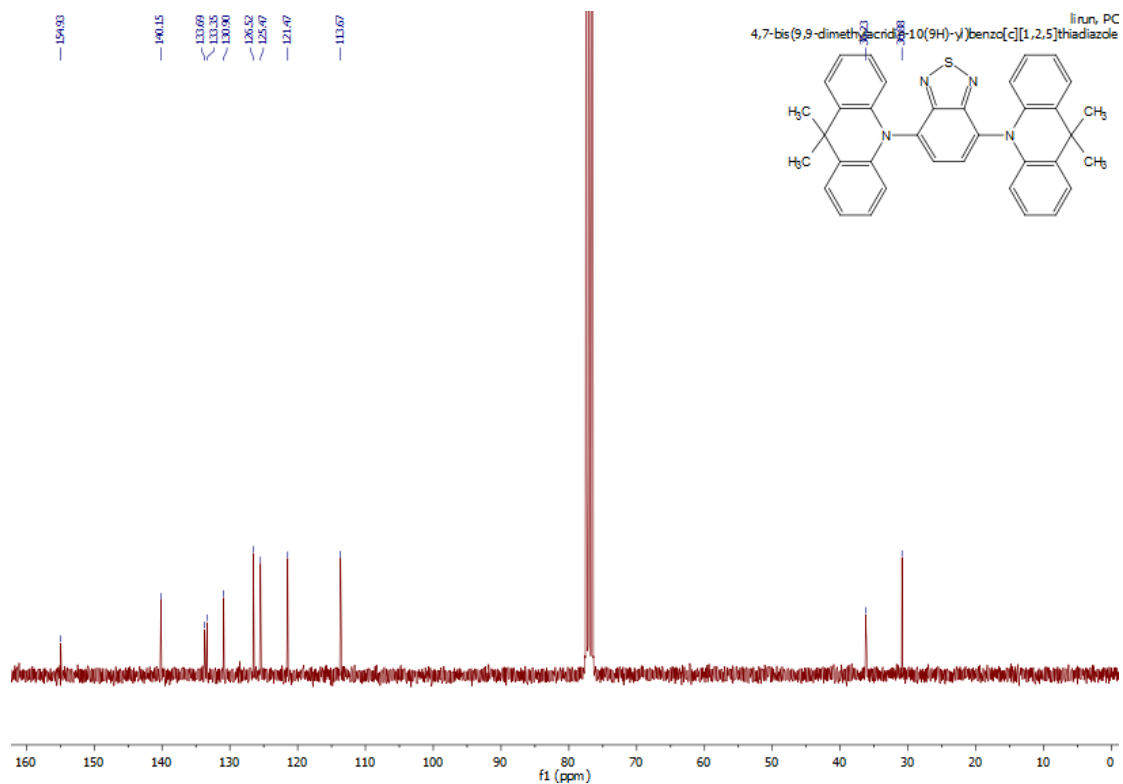
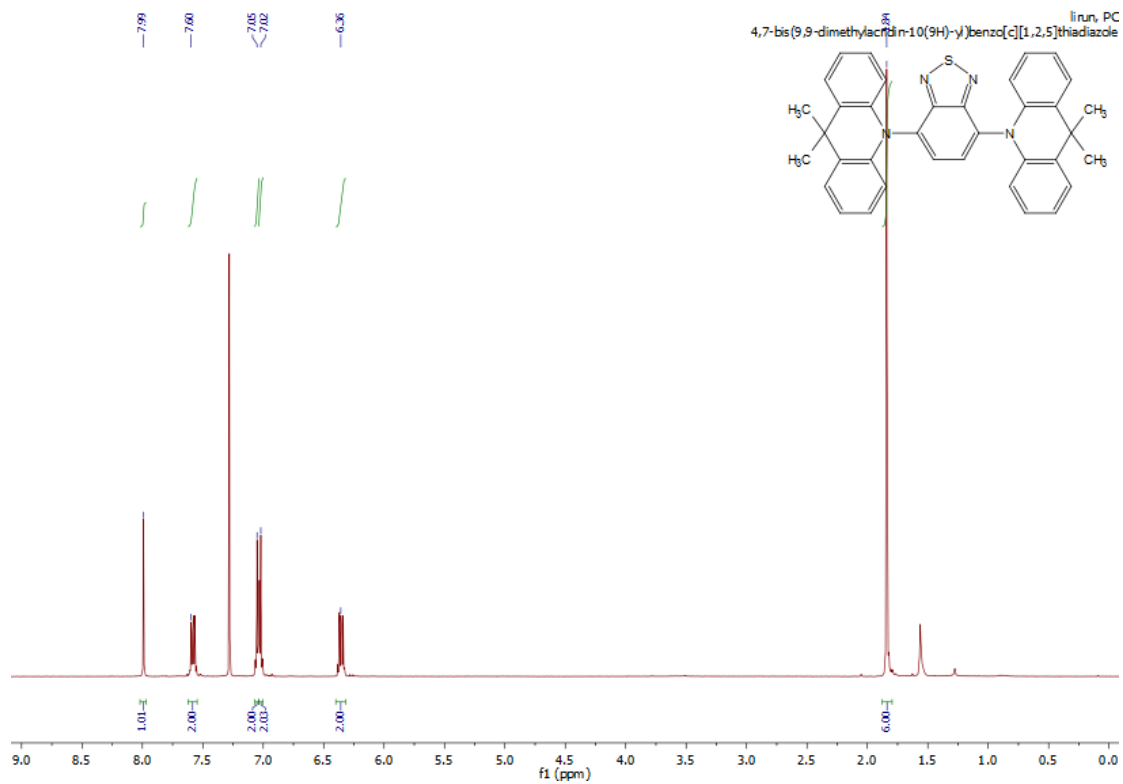
*R*_f (hexane/dichloromethane 4/1): 0.12

¹H NMR (700 MHz, CDCl₂): δ 7.88 (dd, *J* = 7.3, 9.2 Hz, 2H), 7.50 (t, *J* = 7.4 Hz, 1H), 7.40 (m, 2H), 2.51 (s, 3H)

6.4.6 NMR spectra







7 Overall summary and Outlook

In this thesis, benzothiadiazole- (BT)-containing molecular and macromolecular systems, embracing advantages of excellent visible light absorption and emission, strong electron-withdrawing properties, tunable energy band structures, and tailorable excited state lifetime, have been successfully introduced as high efficient photocatalysts for organic photoredox reactions. Challenging organic redox reactions have been successfully conducted with the obtained benzothiadiazole photocatalysts. Various chemical and photophysical characterization methods have been applied for a deeper understanding in the nature of the benzothiadiazole photocatalysts. The kinetics of the photocatalytic reactions, accompanying with the observation of the reactive intermediates, have been investigated to reveal the majorly radical character of the reactive intermediates in most photo-induced redox reactions.

In the first project, a simple donor-acceptor-type molecular semiconductor containing the BT and phenyl units was prepared and applied as a pure organic, dually redox-active photocatalyst for organic transformation reactions. Photocatalytic cationic Diels-Alder reaction and direct conversion of alcohols into bromides have been investigated based on the reductive and oxidative quenching processes, respectively. The molecular photocatalyst demonstrated a comparable catalytic efficiency with the state-of-art transition metal and organic photocatalysts such as $[\text{Ru}(\text{bpy})_3]^{2+}$, *fac*- $[\text{Ir}(\text{ppy})_3]$, eosin Y, and 9-mesityl-10-methylacridinium ($\text{Acr}^+\text{-Mes}$). Advanced photophysical methods as time-resolved photoluminescence decay and transient absorption spectroscopy were carried out to precisely study the electron transfer process between the photocatalyst and reactive substrates.

In the second project, the photoactive BT-containing molecular photocatalyst from the previous study was knitted in a polymer matrix with highly microporous organic polymers (MOPs) via the simple Friedel-Crafts alkylation-based cross-linking method. High surface areas larger than $1000 \text{ m}^2/\text{g}$ were obtained. The highly porous polymer was successfully used for the selective bromination of electron-rich aromatic compounds with HBr as bromine source and oxygen as oxidant under visible light irradiation. Various aromatic rings, including benzene, thiophene, bithiophene and benzothiophene, were tolerable for the reaction condition. The mechanism study demonstrated the details of the electron transfer, radical generation, and bromides formation. The polymer photocatalyst showed a high stability and reusability without suffering the catalytic efficiency.

In the third project, benzothiadiazole was introduced in the conjugated microporous polymer (CMP) network via Sonogashira-Hagihara cross-coupling. The [2+2] cycloaddition reaction between styrene derivatives could be accomplished using the BT-containing CMP.

The reactive substrates bearing both electron-donating groups and electron-withdrawing groups could be catalyzed successfully for the [2+2] cycloaddition reaction with high conversion and excellent region- and stereo-selectivity. Furthermore, examples of natural products such as di-*O*-methlendiandrin A and endiandrin A could be synthesized in the photocatalytic approach using the polymer photocatalyst.

In the last project, a BT-containing molecular photocatalyst with an extremely long excited state lifetime and high photoredox potential was designed via molecular twist between the donor and acceptor units. The designed twisted photocatalyst exhibited an extremely long fluorescence lifetime of 37 μ s. Furthermore, the excited electron on the LUMO level could undergo the second excitation process and was transferred from LUMO to LUMO+X level. This led an unexpected high reduction potential of the photocatalyst. As model reactions, both sp^2 and sp^3 carbon-halogen bonds could be successfully activated with the formation of dehalogenated products.

This comprehensive study demonstrated that benzothiadiazole-containing organic semiconductors could be used as highly efficient photocatalysts for visible light-driven organic photoredox reactions. Different structural designs were introduced for the improvement of the catalytic efficiency, stability or reusability. For outlook, this class of materials will have a broader application range in the field of chemical synthesis and catalysis.

8 References

- (1) Roth, H. D. *Angew. Chem. Int. Ed. Engl.* **1989**, *28*, 1193.
- (2) Ciamician, G. *Science* **1912**, *36*, 385.
- (3) Nicewicz, D. A.; MacMillan, D. W. C. *Science* **2008**, *322*, 77.
- (4) Ischay, M. A.; Anzovino, M. E.; Du, J.; Yoon, T. P. *J. Am. Chem. Soc.* **2008**, *130*, 12886.
- (5) Narayanam, J. M. R.; Tucker, J. W.; Stephenson, C. R. J. *J. Am. Chem. Soc.* **2009**, *131*, 8756.
- (6) Teplý, F. *Collect. Czech. Chem. Commun.* **2011**, *76*, 859.
- (7) Koike, T.; Akita, M. *Inorg. Chem. Front.* **2014**, *1*, 562.
- (8) Shaw, M. H.; Twilton, J.; MacMillan, D. W. C. *J. Org. Chem.* **2016**, *81*, 6898.
- (9) Reiser, O. *Acc. Chem. Res.* **2016**, *49*, 1990.
- (10) Bonin, J.; Robert, M.; Routier, M. *J. Am. Chem. Soc.* **2014**, *136*, 16768.
- (11) Mintrop, L.; Windisch, J.; Gotzmann, C.; Alberto, R.; Probst, B.; Kurz, P. *J. Phys. Chem. B* **2015**, *119*, 13698.
- (12) Romero, N. A.; Nicewicz, D. A. *Chem. Rev.* **2016**, *116*, 10075.
- (13) Nicewicz, D. A.; Nguyen, T. M. *ACS Catal.* **2014**, *4*, 355.
- (14) Hari, D. P.; Konig, B. *Chem. Commun.* **2014**, *50*, 6688.
- (15) Yoon, T. P.; Ischay, M. A.; Du, J. *Nat. Chem.* **2010**, *2*, 527.
- (16) Bach, T.; Hehn, J. P. *Angew. Chem. Int. Ed.* **2011**, *50*, 1000.
- (17) Esser, P.; Pohlmann, B.; Scharf, H.-D. *Angew. Chem. Int. Ed. Engl.* **1994**, *33*, 2009.
- (18) Ghosh, I.; Marzo, L.; Das, A.; Shaikh, R.; König, B. *Acc. Chem. Res.* **2016**, *49*, 1566.
- (19) Majek, M.; Jacobi von Wangelin, A. *Acc. Chem. Res.* **2016**, *49*, 2316.
- (20) Studer, A. *Angew. Chem. Int. Ed.* **2012**, *51*, 8950.
- (21) Alonso, C.; Martínez de Marigorta, E.; Rubiales, G.; Palacios, F. *Chem. Rev.* **2015**, *115*, 1847.
- (22) Beatty, J. W.; Stephenson, C. R. J. *Acc. Chem. Res.* **2015**, *48*, 1474.
- (23) Shi, L.; Xia, W. *Chem. Soc. Rev.* **2012**, *41*, 7687.
- (24) Yoon, U. C.; Mariano, P. S. *Acc. Chem. Res.* **1992**, *25*, 233.
- (25) Skubi, K. L.; Blum, T. R.; Yoon, T. P. *Chem. Rev.* **2016**, *116*, 10035.
- (26) DiRocco, D. A.; Rovis, T. *J. Am. Chem. Soc.* **2012**, *134*, 8094.
- (27) Hopkinson, M. N.; Sahoo, B.; Li, J.-L.; Glorius, F. *Chem. Eur. J.* **2014**, *20*, 3874.
- (28) Allen, A. E.; MacMillan, D. W. C. *Chem. Sci.* **2012**, *3*, 633.
- (29) Kisch, H. *Angew. Chem. Int. Ed.* **2013**, *52*, 812.
- (30) Sang, Y.; Liu, H.; Umar, A. *ChemCatChem* **2015**, *7*, 559.
- (31) Scaiano, J. C. *J. Photochem.* **1973**, *2*, 81.
- (32) Protti, S.; Fagnoni, M.; Ravelli, D. *ChemCatChem* **2015**, *7*, 1516.
- (33) Ravelli, D.; Montanaro, S.; Zema, M.; Fagnoni, M.; Albini, A. *Adv. Synth. Catal.* **2011**, *353*, 3295.
- (34) Tzirakis, M. D.; Lykakis, I. N.; Orfanopoulos, M. *Chem. Soc. Rev.* **2009**, *38*, 2609.
- (35) Turro, N. J. In *Pure and Applied Chemistry* 1977; Vol. 49, p 405.

- (36) Lu, Z.; Yoon, T. P. *Angew. Chem. Int. Ed.* **2012**, *51*, 10329.
- (37) Zhao, J.; Brosmer, J. L.; Tang, Q.; Yang, Z.; Houk, K. N.; Diaconescu, P. L.; Kwon, O. *J. Am. Chem. Soc.* **2017**.
- (38) Stevenson, S. M.; Higgins, R. F.; Shores, M. P.; Ferreira, E. M. *Chem. Sci.* **2016**.
- (39) Stevenson, S. M.; Shores, M. P.; Ferreira, E. M. *Angew. Chem. Int. Ed.* **2015**, *54*, 6506.
- (40) Knorn, M.; Rawner, T.; Czerwieniec, R.; Reiser, O. *ACS Catal.* **2015**, *5*, 5186.
- (41) Rawner, T.; Knorn, M.; Lutsker, E.; Hossain, A.; Reiser, O. *J. Org. Chem.* **2016**.
- (42) Zhang, Y.; Petersen, J. L.; Milsmann, C. *J. Am. Chem. Soc.* **2016**.
- (43) Yin, H.; Carroll, P. J.; Manor, B. C.; Anna, J. M.; Schelter, E. J. *J. Am. Chem. Soc.* **2016**, *138*, 5984.
- (44) Herrmann, J.-M. *Top. Catal.* **2005**, *34*, 49.
- (45) Lang, X.; Chen, X.; Zhao, J. *Chem. Soc. Rev.* **2014**, *43*, 473.
- (46) Colmenares, J. C.; Luque, R. *Chem. Soc. Rev.* **2014**, *43*, 765.
- (47) Palmisano, G.; Garcia-Lopez, E.; Marci, G.; Loddo, V.; Yurdakal, S.; Augugliaro, V.; Palmisano, L. *Chem. Commun.* **2010**, *46*, 7074.
- (48) Pelaez, M.; Nolan, N. T.; Pillai, S. C.; Seery, M. K.; Falaras, P.; Kontos, A. G.; Dunlop, P. S. M.; Hamilton, J. W. J.; Byrne, J. A.; O'Shea, K.; Entezari, M. H.; Dionysiou, D. D. *Appl. Catal. B* **2012**, *125*, 331.
- (49) Daghrir, R.; Drogui, P.; Robert, D. *Ind. Eng. Chem. Res.* **2013**, *52*, 3581.
- (50) Higashimoto, S.; Kitao, N.; Yoshida, N.; Sakura, T.; Azuma, M.; Ohue, H.; Sakata, Y. *J. Catal.* **2009**, *266*, 279.
- (51) Lang, X.; Ma, W.; Zhao, Y.; Chen, C.; Ji, H.; Zhao, J. *Chem. Eur. J.* **2012**, *18*, 2624.
- (52) Ohno, T.; Nakabeya, K.; Matsumura, M. *J. Catal.* **1998**, *176*, 76.
- (53) Wang, P.; Huang, B.; Dai, Y.; Whangbo, M.-H. *Phys. Chem. Chem. Phys.* **2012**, *14*, 9813.
- (54) Kumar, S. G.; Devi, L. G. *J. Phys. Chem. A* **2011**, *115*, 13211.
- (55) Zhao, J.; Zheng, Z.; Bottle, S.; Chou, A.; Sarina, S.; Zhu, H. *Chem. Commun.* **2013**, *49*, 2676.
- (56) Gonzalez-Bejar, M.; Peters, K.; Hallett-Tapley, G. L.; Grenier, M.; Scaiano, J. C. *Chem. Commun.* **2013**, *49*, 1732.
- (57) Sandbrink, L.; Klindtworth, E.; Islam, H.-U.; Beale, A. M.; Palkovits, R. *ACS Catal.* **2016**, *6*, 677.
- (58) Burstall, F. H. *J. Chem. Soc.* **1936**, 173.
- (59) Creutz, C.; Sutin, N. *Proc. Natl. Acad. Sci.* **1975**, *72*, 2858.
- (60) Takeda, H.; Ishitani, O. *Coord. Chem. Rev.* **2010**, *254*, 346.
- (61) Lalevée, J.; Blanchard, N.; Tehfe, M.-A.; Morlet-Savary, F.; Fouassier, J. P. *Macromolecules* **2010**, *43*, 10191.
- (62) Prier, C. K.; Rankic, D. A.; MacMillan, D. W. C. *Chem. Rev.* **2013**, *113*, 5322.
- (63) Tucker, J. W.; Stephenson, C. R. J. *J. Org. Chem.* **2012**, *77*, 1617.
- (64) McNally, A.; Prier, C. K.; MacMillan, D. W. C. *Science* **2011**, *334*, 1114.
- (65) Pirnot, M. T.; Rankic, D. A.; Martin, D. B. C.; MacMillan, D. W. C. *Science* **2013**, *339*, 1593.
- (66) Xuan, J.; Zhang, Z.-G.; Xiao, W.-J. *Angew. Chem. Int. Ed.* **2015**, *54*, 15632.
- (67) Jin, Y.; Fu, H. *Asian J. Org. Chem.* **2017**, *6*, 368.

- (68) Zhou, Q.-Q.; Guo, W.; Ding, W.; Wu, X.; Chen, X.; Lu, L.-Q.; Xiao, W.-J. *Angew. Chem. Int. Ed.* **2015**, *54*, 11196.
- (69) Le Vaillant, F.; Courant, T.; Waser, J. *Angew. Chem. Int. Ed.* **2015**, 11200.
- (70) Lackner, G. L.; Quasdorf, K. W.; Overman, L. E. *J. Am. Chem. Soc.* **2013**, *135*, 15342.
- (71) Tellis, J. C.; Primer, D. N.; Molander, G. A. *Science* **2014**, *345*, 433.
- (72) Ischay, M. A.; Ament, M. S.; Yoon, T. P. *Chem. Sci.* **2012**, *3*, 2807.
- (73) Lu, Z.; Shen, M.; Yoon, T. P. *J. Am. Chem. Soc.* **2011**, *133*, 1162.
- (74) Lin, S.; Ischay, M. A.; Fry, C. G.; Yoon, T. P. *J. Am. Chem. Soc.* **2011**, *133*, 19350.
- (75) Rueda-Becerril, M.; Mahé, O.; Drouin, M.; Majewski, M. B.; West, J. G.; Wolf, M. O.; Sammis, G. M.; Paquin, J.-F. *J. Am. Chem. Soc.* **2014**, *136*, 2637.
- (76) Hernandez-Perez, A. C.; Collins, S. K. *Acc. Chem. Res.* **2016**, *49*, 1557.
- (77) Gualandi, A.; Marchini, M.; Mengozzi, L.; Natali, M.; Lucarini, M.; Ceroni, P.; Cozzi, P. G. *ACS Catal.* **2015**, *5*, 5927.
- (78) Sun, C.-L.; Shi, Z.-J. *Chem. Rev.* **2014**, *114*, 9219.
- (79) Hoffmann, N. *J. Photochem. Photobiol. C Photochem. Rev.* **2008**, *9*, 43.
- (80) Pitre, S. P.; McTiernan, C. D.; Scaiano, J. C. *ACS Omega* **2016**, *1*, 66.
- (81) Pandey, G.; Karthikeyan, M.; Murugan, A. *J. Org. Chem.* **1998**, *63*, 2867.
- (82) Hintz, S.; Mattay, J.; van Eldik, R.; Fu, W.-F. *Eur. J. Org. Chem.* **1998**, 1998, 1583.
- (83) Rinderhagen, H.; Mattay, J. *Chem. Eur. J.* **2004**, *10*, 851.
- (84) Pandey, G.; Lakshmaiah, G.; Kumaraswamy, G. *J. Chem. Soc., Chem. Commun.* **1992**, 1313.
- (85) Albrecht, E.; Averdung, J.; Bischof, E. W.; Heidbreder, A.; Kirschberg, T.; Müller, F.; Mattay, J. *J. Photochem. Photobiol. A Chem.* **1994**, *82*, 219.
- (86) Albini, A.; Arnold, D. R. *Can. J. Chem.* **1978**, *56*, 2985.
- (87) Pandey, G.; Laha, R. *Angew. Chem.* **2015**, *127*, 15088.
- (88) Pandey, G.; Hajra, S.; Ghorai, M. K. *Tetrahedron Lett.* **1994**, *35*, 7837.
- (89) Dondi, D.; Protti, S.; Albini, A.; Carpio, S. M.; Fagnoni, M. *Green Chem.* **2009**, *11*, 1653.
- (90) Müller, C.; Bauer, A.; Maturi, M. M.; Cuquerella, M. C.; Miranda, M. A.; Bach, T. *J. Am. Chem. Soc.* **2011**, *133*, 16689.
- (91) Coote, S. C.; Bach, T. *J. Am. Chem. Soc.* **2013**, *135*, 14948.
- (92) Maturi, M. M.; Bach, T. *Angew. Chem. Int. Ed.* **2014**, *53*, 7661.
- (93) Neckers, D. C.; Valdes-Aguilera, O. M. In *Advances in Photochemistry*; John Wiley & Sons, Inc.: 2007, p 315.
- (94) Hari, D. P.; König, B. *Org. Lett.* **2011**, *13*, 3852.
- (95) Kee, C. W.; Chan, K. M.; Wong, M. W.; Tan, C.-H. *Asian J. Org. Chem.* **2014**, *3*, 536.
- (96) Srivastava, V. P.; Yadav, A. K.; Yadav, L. D. S. *Synlett* **2013**, *24*, 465.
- (97) Yadav, A. K.; Srivastava, V. P.; Yadav, L. D. S. *New J. Chem.* **2013**, *37*, 4119.
- (98) Yadav, A. K.; Srivastava, V. P.; Yadav, L. D. S. *RSC Adv.* **2014**, *4*, 4181.
- (99) Yang, X.-J.; Chen, B.; Zheng, L.-Q.; Wu, L.-Z.; Tung, C.-H. *Green Chem.* **2014**, *16*, 1082.
- (100) Yang, D.-T.; Meng, Q.-Y.; Zhong, J.-J.; Xiang, M.; Liu, Q.; Wu, L.-Z. *Eur. J. Org. Chem.* **2013**, *2013*, 7528.

- (101) Meyer, A. U.; Slanina, T.; Yao, C.-J.; König, B. *ACS Catal.* **2016**, *6*, 369.
- (102) Michal Majek, F. F. a. A. J. v. W. *Beilstein J. Org. Chem.* **2014**, *10*, 981.
- (103) Hari, D. P.; Schroll, P.; König, B. *J. Am. Chem. Soc.* **2012**, *134*, 2958.
- (104) Hari, D. P.; Hering, T.; König, B. *Org. Lett.* **2012**, *14*, 5334.
- (105) Xiao, T.; Dong, X.; Tang, Y.; Zhou, L. *Adv. Synth. Catal.* **2012**, *354*, 3195.
- (106) Yu, J.; Zhang, L.; Yan, G. *Adv. Synth. Catal.* **2012**, *354*, 2625.
- (107) Majek, M.; von Wangelin, A. J. *Chem. Commun.* **2013**, *49*, 5507.
- (108) Vila, C.; Lau, J.; Rueping, M. *Beilstein J. Org. Chem.* **2014**, *10*, 1233.
- (109) Teo, Y. C.; Pan, Y.; Tan, C. H. *ChemCatChem* **2013**, *5*, 235.
- (110) Griesbeck, A. G.; Hundertmark, T.; Steinwascher, J. *Tetrahedron Lett.* **1996**, *37*, 8367.
- (111) Yoshioka, E.; Kohtani, S.; Jichu, T.; Fukazawa, T.; Nagai, T.; Takemoto, Y.; Miyabe, H. *Synlett* **2015**, *26*, 265.
- (112) Marzo, L.; Ghosh, I.; Esteban, F.; König, B. *ACS Catal.* **2016**, 6780.
- (113) Shaikh, R. S.; Düsel, S. J. S.; König, B. *ACS Catal.* **2016**, *6*, 8410.
- (114) Ghosh, I.; König, B. *Angew. Chem. Int. Ed.* **2016**, *55*, 7676.
- (115) Miranda, M. A.; Garcia, H. *Chem. Rev.* **1994**, *94*, 1063.
- (116) Peglow, T.; Blechert, S.; Steckhan, E. *Chem. Commun.* **1999**, 433.
- (117) Riener, M.; Nicewicz, D. A. *Chem. Sci.* **2013**, *4*, 2625.
- (118) Wang, K.; Meng, L.-G.; Wang, L. *Org. Lett.* **2017**.
- (119) Kottisch, V.; Michaudel, Q.; Fors, B. P. *J. Am. Chem. Soc.* **2016**, *138*, 15535.
- (120) Perkowski, A. J.; You, W.; Nicewicz, D. A. *J. Am. Chem. Soc.* **2015**, *137*, 7580.
- (121) Fukuzumi, S.; Kotani, H.; Ohkubo, K.; Ogo, S.; Tkachenko, N. V.; Lemmetyinen, H. *J. Am. Chem. Soc.* **2004**, *126*, 1600.
- (122) Benniston, A. C.; Harriman, A.; Li, P.; Rostron, J. P.; van Ramesdonk, H. J.; Groeneveld, M. M.; Zhang, H.; Verhoeven, J. W. *J. Am. Chem. Soc.* **2005**, *127*, 16054.
- (123) Ohkubo, K.; Fujimoto, A.; Fukuzumi, S. *Chem. Commun.* **2011**, *47*, 8515.
- (124) Weber, M.; Weber, M.; Kleine-Boymann, M. In *Ullmann's Encyclopedia of Industrial Chemistry*; Wiley-VCH Verlag GmbH & Co. KGaA: 2000.
- (125) Ohkubo, K.; Kobayashi, T.; Fukuzumi, S. *Angew. Chem.* **2011**, *123*, 8811.
- (126) Kotani, H.; Ohkubo, K.; Fukuzumi, S. *J. Am. Chem. Soc.* **2004**, *126*, 15999.
- (127) Ohkubo, K.; Mizushima, K.; Iwata, R.; Souma, K.; Suzuki, N.; Fukuzumi, S. *Chem. Commun.* **2010**, *46*, 601.
- (128) Xu, H. J.; Xu, X. L.; Fu, Y.; Feng, Y. S. *Chin. Chem. Lett.* **2007**, *18*, 1471.
- (129) Ohkubo, K.; Mizushima, K.; Iwata, R.; Fukuzumi, S. *Chem. Sci.* **2011**, *2*, 715.
- (130) Romero, N. A.; Margrey, K. A.; Tay, N. E.; Nicewicz, D. A. *Science* **2015**, *349*, 1326.
- (131) Margrey, K. A.; Nicewicz, D. A. *Acc. Chem. Res.* **2016**, *49*, 1997.
- (132) Perkowski, A. J.; Nicewicz, D. A. *J. Am. Chem. Soc.* **2013**, *135*, 10334.
- (133) Wilger, D. J.; Gesmundo, N. J.; Nicewicz, D. A. *Chem. Sci.* **2013**, *4*, 3160.
- (134) Koike, T.; Akita, M. *Org. Biomol. Chem.* **2016**, *14*, 6886.
- (135) Chinzei, T.; Miyazawa, K.; Yasu, Y.; Koike, T.; Akita, M. *RSC Adv.* **2015**, *5*, 21297.
- (136) Wu, X.; Meng, C.; Yuan, X.; Jia, X.; Qian, X.; Ye, J. *Chem. Commun.* **2015**, *51*, 11864.

- (137) Zeng, T.-T.; Xuan, J.; Ding, W.; Wang, K.; Lu, L.-Q.; Xiao, W.-J. *Org. Lett.* **2015**, *17*, 4070.
- (138) Ghosh, S.; Kouamé, N. A.; Ramos, L.; Remita, S.; Dazzi, A.; Deniset-Besseau, A.; Beaunier, P.; Goubard, F.; Aubert, P.-H.; Remita, H. *Nat. Mater.* **2015**, *14*, 505.
- (139) Irigoyen-Campuzano, R.; González-Béjar, M.; Pino, E.; Proal-Nájera, J. B.; Pérez-Prieto, J. *Chem. Eur. J.* **2017**, *23*, 2867.
- (140) Zhang, L.; Huang, X.-H.; Hu, J.-S.; Song, J.; Kim, I. *Langmuir* **2017**, *33*, 1867.
- (141) Loudet, A.; Burgess, K. *Chem. Rev.* **2007**, *107*, 4891.
- (142) Li, W.; Zhang, W.; Dong, X.; Yan, L.; Qi, R.; Wang, W.; Xie, Z.; Jing, X. *J. Mater. Chem.* **2012**, *22*, 17445.
- (143) Liras, M.; Iglesias, M.; Sánchez, F. *Macromolecules* **2016**, *49*, 1666.
- (144) Jiang, J.-X.; Li, Y.; Wu, X.; Xiao, J.; Adams, D. J.; Cooper, A. I. *Macromolecules* **2013**, *46*, 8779.
- (145) Xu, J.; Luo, L.; Xiao, G.; Zhang, Z.; Lin, H.; Wang, X.; Long, J. *ACS Catal.* **2014**, *4*, 3302.
- (146) Su, C.; Tandiana, R.; Tian, B.; Sengupta, A.; Tang, W.; Su, J.; Loh, K. P. *ACS Catal.* **2016**, *6*, 3594.
- (147) Luo, J.; Zhang, X.; Zhang, J. *ACS Catal.* **2015**, *5*, 2250.
- (148) Zhang, M.; Rouch, W. D.; McCulla, R. D. *Eur. J. Org. Chem.* **2012**, *2012*, 6187.
- (149) Amaya, T.; Hata, D.; Moriuchi, T.; Hirao, T. *Chem. Eur. J.* **2015**, *21*, 16427.
- (150) Wang, X.; Maeda, K.; Thomas, A.; Takanabe, K.; Xin, G.; Carlsson, J. M.; Domen, K.; Antonietti, M. *Nat. Mater.* **2009**, *8*, 76.
- (151) Zhang, G.; Lan, Z.-A.; Wang, X. *Angew. Chem. Int. Ed.* **2016**, *55*, 15712.
- (152) Sprick, R. S.; Jiang, J.-X.; Bonillo, B.; Ren, S.; Ratvijitvech, T.; Guiglion, P.; Zwijnenburg, M. A.; Adams, D. J.; Cooper, A. I. *J. Am. Chem. Soc.* **2015**, *137*, 3265.
- (153) Sprick, R. S.; Bonillo, B.; Clowes, R.; Guiglion, P.; Brownbill, N. J.; Slater, B. J.; Blanc, F.; Zwijnenburg, M. A.; Adams, D. J.; Cooper, A. I. *Angew. Chem. Int. Ed.* **2016**, *55*, 1792.
- (154) Jung, J. W.; Jo, W. H. *Chem. Mater.* **2015**, *27*, 6038.
- (155) Gu, C.; Hu, W.; Yao, J.; Fu, H. *Chem. Mater.* **2013**, *25*, 2178.
- (156) Neto, B. A. D.; Carvalho, P. H. P. R.; Correa, J. R. *Acc. Chem. Res.* **2015**, *48*, 1560.
- (157) Wang, J.; Chepelianskii, A.; Gao, F.; Greenham, N. C. *Nat. Commun.* **2012**, *3*, 1191.
- (158) DaSilveira Neto, B. A.; Lopes, A. S. A.; Ebeling, G.; Gonçalves, R. S.; Costa, V. E. U.; Quina, F. H.; Dupont, J. *Tetrahedron* **2005**, *61*, 10975.
- (159) Mancilha, F. S.; DaSilveira Neto, B. A.; Lopes, A. S.; Moreira, P. F.; Quina, F. H.; Gonçalves, R. S.; Dupont, J. *Eur. J. Org. Chem.* **2006**, *2006*, 4924.
- (160) Arora, A.; Weaver, J. D. *Acc. Chem. Res.* **2016**, *49*, 2273.
- (161) Zhang, K.; Kopetzki, D.; Seeberger, P. H.; Antonietti, M.; Vilela, F. *Angew. Chem. Int. Ed.* **2013**, *52*, 1432.
- (162) Zhang, K.; Vobecka, Z.; Tauer, K.; Antonietti, M.; Vilela, F. *Chem Commun* **2013**, *49*, 11158.
- (163) Urakami, H.; Zhang, K.; Vilela, F. *Chem. Commun.* **2013**, *49*, 2353.
- (164) Shen, J.; Steinbach, R.; Tobin, J. M.; Mouro Nakata, M.; Bower, M.; McCoustra, M. R. S.; Bridle, H.; Arrighi, V.; Vilela, F. *Appl. Catal. B* **2016**, *193*, 226.

- (165) Ma, B. C.; Ghasimi, S.; Landfester, K.; Vilela, F.; Zhang, K. A. I. *J. Mater. Chem. A* **2015**, *3*, 16064.
- (166) Hou, H.-J.; Zhang, X.-H.; Huang, D.-K.; Ding, X.; Wang, S.-Y.; Yang, X.-L.; Li, S.-Q.; Xiang, Y.-G.; Chen, H. *Appl. Catal. B* **2017**, *203*, 563.
- (167) Yang, X.; Xiang, Y.; Qu, Y.; Ding, X.; Chen, H. *J. Catal.* **2017**, *345*, 319.
- (168) Su, F.; Mathew, S. C.; Möhlmann, L.; Antonietti, M.; Wang, X.; Blechert, S. *Angew. Chem. Int. Ed.* **2011**, *50*, 657.
- (169) Wang, Z. J.; Garth, K.; Ghasimi, S.; Landfester, K.; Zhang, K. A. I. *ChemSusChem* **2015**, *8*, 3459.
- (170) Wang, Z. J.; Ghasimi, S.; Landfester, K.; Zhang, K. A. I. *Adv. Mater.* **2015**, *27*, 6265.
- (171) Wang, Z. J.; Ghasimi, S.; Landfester, K.; Zhang, K. A. I. *Adv. Synth. Catal.* **2016**, *358*, 2576.
- (172) Nishino, M.; Hirano, K.; Satoh, T.; Miura, M. *J. Org. Chem.* **2011**, *76*, 6447.
- (173) Ju, X.; Li, D.; Li, W.; Yu, W.; Bian, F. *Adv. Synth. Catal.* **2012**, *354*, 3561.
- (174) Wang, Z. J.; Ghasimi, S.; Landfester, K.; Zhang, K. A. I. *Chem. Commun.* **2014**, *50*, 8177.
- (175) Wang, Z. J.; Landfester, K.; Zhang, K. A. I. *Polym. Chem.* **2014**, *5*, 3559.
- (176) Yang, C.; Ma, B. C.; Zhang, L.; Lin, S.; Ghasimi, S.; Landfester, K.; Zhang, K. A. I.; Wang, X. *Angew. Chem. Int. Ed.* **2016**, *55*, 9202.
- (177) Wang, S.; Yang, X.; Hou, H.; Ding, X.; Li, S.; Deng, F.; Xiang, Y.; Chen, H. *Catal. Sci. Tech.* **2017**, *7*, 418.
- (178) Huang, W.; Wang, Z. J.; Ma, B. C.; Ghasimi, S.; Gehrig, D.; Laquai, F.; Landfester, K.; Zhang, K. A. I. *J. Mater. Chem. A* **2016**, *4*, 7555.
- (179) Alonso, F.; Beletskaya, I. P.; Yus, M. *Chem. Rev.* **2002**, *102*, 4009.
- (180) Staveness, D.; Bosque, I.; Stephenson, C. R. J. *Acc. Chem. Res.* **2016**, *49*, 2295.
- (181) Qiu, G.; Li, Y.; Wu, J. *Org. Chem. Front.* **2016**, *3*, 1011.
- (182) Nguyen, J. D.; D'Amato, E. M.; Narayanam, J. M. R.; Stephenson, C. R. J. *Nat. Chem.* **2012**, *4*, 854.
- (183) Wang, Z. J.; Ghasimi, S.; Landfester, K.; Zhang, K. A. I. *J. Mater. Chem. A* **2014**, *2*, 18720.
- (184) Studer, A.; Curran, D. P. *Angew. Chem. Int. Ed.* **2016**, *55*, 58.
- (185) Yu, J.-T.; Pan, C. *Chem. Commun.* **2016**, *52*, 2220.
- (186) Liu, D.; Liu, C.; Lei, A. *Chem. Asian J.* **2015**, *10*, 2040.
- (187) Huang, W.; Ma, B. C.; Wang, D.; Wang, Z. J.; Li, R.; Wang, L.; Landfester, K.; Zhang, K. A. I. *J. Mater. Chem. A* **2017**, *5*, 3792.
- (188) Furst, L.; Matsuura, B. S.; Narayanam, J. M. R.; Tucker, J. W.; Stephenson, C. R. J. *Org. Lett.* **2010**, *12*, 3104.
- (189) Wang, L.; Huang, W.; Li, R.; Gehrig, D.; Blom, P. W. M.; Landfester, K.; Zhang, K. A. I. *Angew. Chem. Int. Ed.* **2016**, *55*, 9783.
- (190) Gao, X.; Wachs, I. E. *J. Phys. Chem. B* **2000**, *104*, 1261.
- (191) Viscarra Rossel, R. A.; McGlynn, R. N.; McBratney, A. B. *Geoderma* **2006**, *137*, 70.
- (192) Lakowicz, J. R. In *Principles of Fluorescence Spectroscopy*; Springer US: Boston, MA, 1999, p 1.

- (193) In *Electron Paramagnetic Resonance in Biochemistry and Medicine*; Springer US: Boston, MA, 2002, p 1.
- (194) Hussain, S. Z.; Maqbool, K. *Int. J. Curr. Sci.* **2014**, *13*, 116.
- (195) Xuan, J.; Xiao, W.-J. *Angew. Chem. Int. Ed.* **2012**, *51*, 6828.
- (196) Tucker, J. W.; Nguyen, J. D.; Narayanam, J. M. R.; Krabbe, S. W.; Stephenson, C. R. J. *Chem. Commun.* **2010**, *46*, 4985.
- (197) Kim, H.; Lee, C. *Angew. Chem. Int. Ed.* **2012**, *51*, 12303.
- (198) Larraufie, M.-H.; Pellet, R.; Fensterbank, L.; Goddard, J.-P.; Lacôte, E.; Malacria, M.; Ollivier, C. *Angew. Chem. Int. Ed.* **2011**, *50*, 4463.
- (199) Kohls, P.; Jadhav, D.; Pandey, G.; Reiser, O. *Org. Lett.* **2012**, *14*, 672.
- (200) Maity, S.; Zhu, M.; Shinabery, R. S.; Zheng, N. *Angew. Chem. Int. Ed.* **2012**, *51*, 222.
- (201) Condie, A. G.; González-Gómez, J. C.; Stephenson, C. R. J. *J. Am. Chem. Soc.* **2010**, *132*, 1464.
- (202) Neumann, M.; Fuldner, S.; König, B.; Zeitler, K. *Angew. Chem. Int. Ed. Engl.* **2011**, *50*, 951.
- (203) Majek, M.; Jacobi von Wangelin, A. *Angew. Chem. Int. Ed.* **2015**, *54*, 2270.
- (204) Chen, M.; Huang, Z.-T.; Zheng, Q.-Y. *Chem. Commun.* **2012**, *48*, 11686.
- (205) Wang, X.; Maeda, K.; Thomas, A.; Takanabe, K.; Xin, G.; Carlsson, J. M.; Domen, K.; Antonietti, M. *Nat. Mater.* **2009**, *8*, 76.
- (206) Reisner, E.; Powell, D. J.; Cavazza, C.; Fontecilla-Camps, J. C.; Armstrong, F. A. J. *Am. Chem. Soc.* **2009**, *131*, 18457.
- (207) Oh, S. H.; Malpani, Y. R.; Ha, N.; Jung, Y.-S.; Han, S. B. *Org. Lett.* **2014**, *16*, 1310.
- (208) Su, F.; Mathew, S. C.; Lipner, G.; Fu, X.; Antonietti, M.; Blechert, S.; Wang, X. J. *Am. Chem. Soc.* **2010**, *132*, 16299.
- (209) Nguyen, J. D.; Tucker, J. W.; Konieczynska, M. D.; Stephenson, C. R. J. *J. Am. Chem. Soc.* **2011**, *133*, 4160.
- (210) Nagib, D. A.; MacMillan, D. W. C. *Nature* **2011**, *480*, 224.
- (211) Cho, J.-Y.; Tse, M. K.; Holmes, D.; Maleczka, R. E.; Smith, M. R. *Science* **2002**, *295*, 305.
- (212) Ghosh, I.; Ghosh, T.; Bardagi, J. I.; König, B. *Science* **2014**, *346*, 725.
- (213) Wang, L.; Huang, W.; Li, R.; Gehrig, D.; Blom, P. W.; Landfester, K.; Zhang, K. A. *Angew. Chem. Int. Ed. Engl.* **2016**, *55*, 9783.
- (214) Fukuzumi, S.; Ohkubo, K. *Chem. Sci.* **2013**, *4*, 561.
- (215) Kang, N.; Park, J. H.; Ko, K. C.; Chun, J.; Kim, E.; Shin, H. W.; Lee, S. M.; Kim, H. J.; Ahn, T. K.; Lee, J. Y.; Son, S. U. *Angew. Chem. Int. Ed.* **2013**, *52*, 6228.
- (216) Ghasimi, S.; Prescher, S.; Wang, Z. J.; Landfester, K.; Yuan, J.; Zhang, K. A. I. *Angew. Chem. Int. Ed.* **2015**, *54*, 14549.
- (217) Li, R.; Wang, Z. J.; Wang, L.; Ma, B. C.; Ghasimi, S.; Lu, H.; Landfester, K.; Zhang, K. A. I. *ACS Catal.* **2016**, 1113.
- (218) Lowry, M. S.; Goldsmith, J. I.; Slinker, J. D.; Rohl, R.; Pascal, R. A.; Malliaras, G. G.; Bernhard, S. *Chem. Mater.* **2005**, *17*, 5712.
- (219) Cherevatskaya, M.; Neumann, M.; Fuldner, S.; Harlander, C.; Kümmel, S.; Dankesreiter, S.; Pfitzner, A.; Zeitler, K.; König, B. *Angew. Chem. Int. Ed.* **2012**, *51*, 4062.
- (220) Zhu, H.; Song, N.; Lv, H.; Hill, C. L.; Lian, T. *J. Am. Chem. Soc.* **2012**, *134*, 11701.
- (221) Tojo, S.; Toki, S.; Takamuku, S. *J. Org. Chem.* **1991**, *56*, 6240.

- (222) Gribble, G. W. *Chem. Soc. Rev.* **1999**, *28*, 335.
- (223) Dai, C.; Meschini, F.; Narayanam, J. M. R.; Stephenson, C. R. J. *J. Org. Chem.* **2012**, *77*, 4425.
- (224) Léonel, E.; Lejaye, M.; Oudeyer, S.; Paul Paugam, J.; Nédélec, J.-Y. *Tetrahedron Lett.* **2004**, *45*, 2635.
- (225) Dai, C.; Narayanam, J. M. R.; Stephenson, C. R. J. *Nat. Chem.* **2011**, *3*, 140.
- (226) De Luca, L.; Giacomelli, G.; Porcheddu, A. *Org. Lett.* **2002**, *4*, 553.
- (227) Léonel, E.; Paugam, J. P.; Nédélec, J. Y. *J. Org. Chem.* **1997**, *62*, 7061.
- (228) Shoute, L. C. T.; Neta, P. J. *Phys. Chem.* **1990**, *94*, 2447.
- (229) Miyaoura, N.; Suzuki, A. *Chem. Rev.* **1995**, *95*, 2457.
- (230) Sonogashira, K.; Tohda, Y.; Hagihara, N. *Tetrahedron Lett.* **1975**, *16*, 4467.
- (231) Heck, R. F.; Nolley, J. P. *J. Org. Chem.* **1972**, *37*, 2320.
- (232) Milstein, D.; Stille, J. K. *J. Am. Chem. Soc.* **1978**, *100*, 3636.
- (233) Guram, A. S.; Buchwald, S. L. *J. Am. Chem. Soc.* **1994**, *116*, 7901.
- (234) Paul, F.; Patt, J.; Hartwig, J. F. *J. Am. Chem. Soc.* **1994**, *116*, 5969.
- (235) Bose, A.; Mal, P. *Tetrahedron Lett.* **2014**, *55*, 2154.
- (236) Yadav, J. S.; Reddy, B. V. S.; Reddy, P. S. R.; Basak, A. K.; Narsaiah, A. V. *Adv. Synth. Catal.* **2004**, *346*, 77.
- (237) Mo, F.; Yan, J. M.; Qiu, D.; Li, F.; Zhang, Y.; Wang, J. *Angew. Chem. Int. Ed.* **2010**, *49*, 2028.
- (238) Podgoršek, A.; Zupan, M.; Iskra, J. *Angew. Chem. Int. Ed.* **2009**, *48*, 8424.
- (239) Yonehara, K.; Kamata, K.; Yamaguchi, K.; Mizuno, N. *Chem. Commun.* **2011**, *47*, 1692.
- (240) Fukuzumi, S.; Ohkubo, K. *Org. Biomol. Chem.* **2014**, *12*, 6059.
- (241) Moriya, T.; Yoneda, S.; Kawana, K.; Ikeda, R.; Konakahara, T.; Sakai, N. *Org. Lett.* **2012**, *14*, 4842.
- (242) Bedford, R. B.; Haddow, M. F.; Mitchell, C. J.; Webster, R. L. *Angew. Chem. Int. Ed.* **2011**, *50*, 5524.
- (243) Dubost, E.; Fossey, C.; Cailly, T.; Rault, S.; Fabis, F. *J. Org. Chem.* **2011**, *76*, 6414.
- (244) Yang, L.; Lu, Z.; Stahl, S. S. *Chem. Commun.* **2009**, 6460.
- (245) Wang, Y.; Li, L.; Ji, H.; Ma, W.; Chen, C.; Zhao, J. *Chem. Commun.* **2014**, *50*, 2344.
- (246) Brücher, O.; Hartung, J. *ACS Catal.* **2011**, *1*, 1448.
- (247) Palmisano, L.; Augugliaro, V.; Bellardita, M.; Di Paola, A.; García López, E.; Loddo, V.; Marci, G.; Palmisano, G.; Yurdakal, S. *ChemSusChem* **2011**, *4*, 1431.
- (248) Juris, A.; Balzani, V.; Barigelletti, F.; Campagna, S.; Belser, P.; von Zelewsky, A. *Coord. Chem. Rev.* **1988**, *84*, 85.
- (249) Xie, Z.; Wang, C.; deKrafft, K. E.; Lin, W. *J. Am. Chem. Soc.* **2011**, *133*, 2056.
- (250) Wang, C.; Xie, Z.; deKrafft, K. E.; Lin, W. *ACS Appl. Mater. Interfaces* **2012**, *4*, 2288.
- (251) Shalom, M.; Inal, S.; Fettkenhauer, C.; Neher, D.; Antonietti, M. *J. Am. Chem. Soc.* **2013**, *135*, 7118.
- (252) Kang, N.; Park, J. H.; Ko, K. C.; Chun, J.; Kim, E.; Shin, H.-W.; Lee, S. M.; Kim, H. J.; Ahn, T. K.; Lee, J. Y.; Son, S. U. *Angew. Chem. Int. Ed.* **2013**, *52*, 6228.

- (253) Dadashi-Silab, S.; Bildirir, H.; Dawson, R.; Thomas, A.; Yagci, Y. *Macromolecules* **2014**, *47*, 4607.
- (254) Li, B.; Gong, R.; Wang, W.; Huang, X.; Zhang, W.; Li, H.; Hu, C.; Tan, B. *Macromolecules* **2011**, *44*, 2410.
- (255) Shen, Y.; Liu, H.; Chen, Y. *J. Org. Chem.* **1990**, *55*, 3961.
- (256) Shin, W.; Jo, M. Y.; You, D. S.; Jeong, Y. S.; Yoon, D. Y.; Kang, J.-W.; Cho, J. H.; Lee, G. D.; Hong, S.-S.; Kim, J. H. *Synth. Met.* **2012**, *162*, 768.
- (257) Zhu, J.-H.; Chen, Q.; Sui, Z.-Y.; Pan, L.; Yu, J.; Han, B.-H. *J. Mater. Chem. A* **2014**, *2*, 16181.
- (258) Liu, J.; Liu, Y.; Liu, N.; Han, Y.; Zhang, X.; Huang, H.; Lifshitz, Y.; Lee, S.-T.; Zhong, J.; Kang, Z. *Science* **2015**, *347*, 970.
- (259) Narayanam, J. M. R.; Stephenson, C. R. J. *Chem. Soc. Rev.* **2011**, *40*, 102.
- (260) Zhang, J.; Zhang, G.; Chen, X.; Lin, S.; Möhlmann, L.; Dołęga, G.; Lipner, G.; Antonietti, M.; Blechert, S.; Wang, X. *Angew. Chem. Int. Ed.* **2012**, *51*, 3183.
- (261) Chen, Y.; Zhang, J.; Zhang, M.; Wang, X. *Chem. Sci.* **2013**, *4*, 3244.
- (262) Clennan, E. L.; Pace, A. *Tetrahedron* **2005**, *61*, 6665.
- (263) Su, C.; Acik, M.; Takai, K.; Lu, J.; Hao, S.-j.; Zheng, Y.; Wu, P.; Bao, Q.; Enoki, T.; Chabal, Y. J.; Ping Loh, K. *Nat. Commun.* **2012**, *3*, 1298.
- (264) Rao, P. S.; Hayon, E. *J. Phys. Chem.* **1975**, *79*, 397.
- (265) Namyslo, J. C.; Kaufmann, D. E. *Chem. Rev.* **2003**, *103*, 1485.
- (266) Xu, Y.; Conner, M. L.; Brown, M. K. *Angew. Chem. Int. Ed.* **2015**, *54*, 11918.
- (267) Sergeiko, A.; Poroikov, V. V.; Hanuš, L. O.; Dembitsky, V. M. *Open Med. Chem. J.* **2008**, *2*, 26.
- (268) Davis, R. A.; Carroll, A. R.; Duffy, S.; Avery, V. M.; Guymer, G. P.; Forster, P. I.; Quinn, R. J. *J. Nat. Prod.* **2007**, *70*, 1118.
- (269) Kleinbeck, F.; Toste, F. D. *J. Am. Chem. Soc.* **2009**, *131*, 9178.
- (270) Alberti, G.; Bernard, A. M.; Frongia, A.; Piras, P. P.; Secci, F.; Spiga, M. *Synlett* **2006**, *14*, 2241.
- (271) Boxer, M. B.; Yamamoto, H. *Org. Lett.* **2005**, *7*, 3127.
- (272) Duan, G.-J.; Ling, J.-B.; Wang, W.-P.; Luo, Y.-C.; Xu, P.-F. *Chem. Commun.* **2013**, *49*, 4625.
- (273) Sakai, K.; Kochi, T.; Kakiuchi, F. *Org. Lett.* **2013**, *15*, 1024.
- (274) Schultz, D. M.; Yoon, T. P. *Science* **2014**, *343*, 1239176.
- (275) Kärkäs, M. D.; Porco, J. A.; Stephenson, C. R. J. *Chem. Rev.* **2016**, *116*, 9683.
- (276) Poplata, S.; Tröster, A.; Zou, Y.-Q.; Bach, T. *Chem. Rev.* **2016**, *116*, 9748.
- (277) Du, J.; Yoon, T. P. *J. Am. Chem. Soc.* **2009**, *131*, 14604.
- (278) Du, J.; Skubi, K. L.; Schultz, D. M.; Yoon, T. P. *Science* **2014**, *344*, 392.
- (279) Neumann, M.; Földner, S.; König, B.; Zeitler, K. *Angew. Chem. Int. Ed.* **2011**, *50*, 951.
- (280) Studer, A.; Curran, D. P. *Nat. Chem.* **2014**, *6*, 765.
- (281) Yueh, W.; Bauld, N. L. *J. Phys. Org. Chem.* **1996**, *9*, 529.
- (282) Bauld, N. L.; Bellville, D. J.; Pabon, R.; Chelsky, R.; Green, G. *J. Am. Chem. Soc.* **1983**, *105*, 2378.
- (283) Schepp, N. P.; Johnston, L. J. *J. Am. Chem. Soc.* **1994**, *116*, 6895.
- (284) Hari, D. P.; König, B. *Angew. Chem. Int. Ed.* **2013**, *52*, 4734.
- (285) Phipps, R. J.; Gaunt, M. J. *Science* **2009**, *323*, 1593.

- (286) Deng, G.-B.; Wang, Z.-Q.; Xia, J.-D.; Qian, P.-C.; Song, R.-J.; Hu, M.; Gong, L.-B.; Li, J.-H. *Angew. Chem. Int. Ed.* **2013**, *52*, 1535.
- (287) Devery, J. J.; Nguyen, J. D.; Dai, C.; Stephenson, C. R. J. *ACS Catal.* **2016**, 5962.
- (288) Matsubara, R.; Shimada, T.; Kobori, Y.; Yabuta, T.; Osakai, T.; Hayashi, M. *Chem. Asian J.* **2016**, *11*, 2006.
- (289) Poelma, S. O.; Burnett, G. L.; Discekici, E. H.; Mattson, K. M.; Treat, N. J.; Luo, Y.; Hudson, Z. M.; Shankel, S. L.; Clark, P. G.; Kramer, J. W.; Hawker, C. J.; Read de Alaniz, J. *J. Org. Chem.* **2016**, *81*, 7155.
- (290) Discekici, E. H.; Treat, N. J.; Poelma, S. O.; Mattson, K. M.; Hudson, Z. M.; Luo, Y.; Hawker, C. J.; de Alaniz, J. R. *Chem. Commun.* **2015**, *51*, 11705.
- (291) Majek, M.; Faltermeier, U.; Dick, B.; Pérez-Ruiz, R.; Jacobi von Wangelin, A. *Chem. Eur. J.* **2015**, *21*, 15496.
- (292) Arceo, E.; Jurberg, I. D.; Álvarez-Fernández, A.; Melchiorre, P. *Nat. Chem.* **2013**, *5*, 750.
- (293) Woźniak, Ł.; Murphy, J. J.; Melchiorre, P. *J. Am. Chem. Soc.* **2015**, *137*, 5678.
- (294) Zeng, L.; Liu, T.; He, C.; Shi, D.; Zhang, F.; Duan, C. *J. Am. Chem. Soc.* **2016**, *138*, 3958.
- (295) Graml, A.; Ghosh, I.; König, B. *J. Org. Chem.* **2017**, *82*, 3552.
- (296) Uoyama, H.; Goushi, K.; Shizu, K.; Nomura, H.; Adachi, C. *Nature* **2012**, *492*, 234.
- (297) Cui, L.-S.; Nomura, H.; Geng, Y.; Kim, J. U.; Nakanotani, H.; Adachi, C. *Angew. Chem. Int. Ed.* **2017**, *56*, 1571.
- (298) Zhang, Q.; Kuwabara, H.; Potscavage, W. J.; Huang, S.; Hatae, Y.; Shibata, T.; Adachi, C. *J. Am. Chem. Soc.* **2014**, *136*, 18070.
- (299) Hirata, S.; Sakai, Y.; Masui, K.; Tanaka, H.; Lee, S. Y.; Nomura, H.; Nakamura, N.; Yasumatsu, M.; Nakanotani, H.; Zhang, Q.; Shizu, K.; Miyazaki, H.; Adachi, C. *Nat. Mater.* **2015**, *14*, 330.
- (300) Mishra, A.; Sahu, S.; Tripathi, S.; Krishnamoorthy, G. *Photochem. Photobiol. Sci.* **2014**, *13*, 1476.
- (301) Clarke, T. M.; Gordon, K. C.; Kwok, W. M.; Phillips, D. L.; Officer, D. L. *J. Phys. Chem. A* **2006**, *110*, 7696.
- (302) Park, I. S.; Lee, S. Y.; Adachi, C.; Yasuda, T. *Adv. Funct. Mater.* **2016**, *26*, 1813.
- (303) Lee, J.; Shizu, K.; Tanaka, H.; Nomura, H.; Yasuda, T.; Adachi, C. *J. Mater. Chem. C* **2013**, *1*, 4599.
- (304) Komatsu, R.; Sasabe, H.; Seino, Y.; Nakao, K.; Kido, J. *J. Mater. Chem. C* **2016**, *4*, 2274.
- (305) Lu, J.; Zheng, Y.; Zhang, J. *Phys. Chem. Chem. Phys.* **2015**, *17*, 20014.
- (306) Kalyanasundaram, K. *Coord. Chem. Rev.* **1982**, *46*, 159.
- (307) Hernández-Romero, Y.; Acevedo, L.; de Los Ángeles Sánchez, M.; Shier, W. T.; Abbas, H. K.; Mata, R. *J. Agric. Food Chem.* **2005**, *53*, 6276.
- (308) Zhang, X.; Xu, J.-K.; Wang, J.; Wang, N.-L.; Kurihara, H.; Kitanaka, S.; Yao, X.-S. *J. Nat. Prod.* **2007**, *70*, 24.
- (309) Li, Y.; Zhang, F.; Wu, Z.-H.; Zeng, K.-W.; Zhang, C.; Jin, H.-W.; Zhao, M.-B.; Jiang, Y.; Li, J.; Tu, P.-F. *Fitoterapia* **2015**, *102*, 120.
- (310) Guin, D.; Baruwati, B.; Manorama, S. V. *Org. Lett.* **2007**, *9*, 1419.

- (311) Kim, Y. J.; Kim, S. M.; Cho, E. J.; Hosono, H.; Yang, J. W.; Kim, S. W. *Chem. Sci.* **2015**, *6*, 3577.
- (312) Sato, K.; Inoue, Y.; Mori, T.; Sakaue, A.; Tarui, A.; Omote, M.; Kumadaki, I.; Ando, A. *Org. Lett.* **2014**, *16*, 3756.
- (313) Manley, D. W.; Walton, J. C. *Org. Lett.* **2014**, *16*, 5394.
- (314) Kumar, P.; Guntreddi, T.; Singh, R.; Singh, K. N. *Org. Chem. Front.* **2017**, *4*, 147.
- (315) ROLAND KUHN *Am. J. Psychiatry* **1958**, *115*, 459.
- (316) Tripathi, S.; Chan, M.-H.; Chen, C. *Bioorg. Med. Chem. Lett.* **2012**, *22*, 216.
- (317) Naidu, A. B.; Sekar, G. *Tetrahedron Lett.* **2008**, *49*, 3147.
- (318) Andrew, T. L.; Swager, T. M. *J. Org. Chem.* **2011**, *76*, 2976.

9 Scientific Contributions

Publications

Li, R.; Wang, Z. J.; Wang, L.; Ma, B. C.; Ghasimi, S.; Lu, H.; Landfester, K.; Zhang, K. A. I. *Photocatalytic selective bromination of electron-rich aromatic compounds using microporous organic polymers with visible light*, *ACS Catal.*, **2016**, 6, 1113-1121.

Highlight: Li, R.; Wang, Z. J.; Wang, L.; Ma, B. C.; Ghasimi, S.; Lu, H.; Landfester, K.; Zhang, K. A. I. *Photocatalyzed selective bromination of aromatic compounds*, *Synfacts*, **2016**, 12, 534-534.

Li, R.; Ma, B. C.; Huang, W.; Wang, L.; Wang, D.; Lu, H.; Landfester, K.; Zhang, K. A. I. *Photocatalytic regioselective and stereoselective [2 + 2] cycloaddition of styrene derivatives using a heterogeneous organic photocatalyst*, *ACS Catal.*, **2017**, 7, 3097-3101.

Wang, Z. J.*; Li, R.*; Landfester, K.; Zhang, K. A. I. *Porous conjugated polymer via metal-free synthesis for visible light-promoted oxidative hydroxylation of arylboronic acids*, *Polymer*, 2017, DOI: 10.1016/j.polymer.2017.04.052.

Li, R.; Gehrig, D.; Ramanan, C.; Blom, P. W. M.; Wagner, M.; Huang, W.; Wang, L.; Zhang, K. A. I. *A metal-free, dually redox-active organic photocatalyst for visible light-promoted Diels-Alder reaction and direct conversion of aliphatic alcohols to bromides* (submitted).

Li, R.; Bretschneider, S.; Huang, W.; Blom, P. W. M.; Landfester, K.; Zhang, K. A. I. *Design of twisted structure with thermally activated delayed fluorescence characteristic and its catalytic application for reduction of aryl and alkyl halides via consecutive visible light-induced charge transfer* (in preparation).

Yang, C.*; Li, R.*; Huang, W.; Zhang, K. A. I.; Wang, X. C. *Metal-free carbon nitride polymers coupled to flow photoreactors for scalable synthesis of cyclobutanes* (in preparation).

Wang, L.; Huang, W.; Li, R.; Gehrig, D.; Blom, P. W. M.; Landfester, K.; Zhang, K. A. I. *Structural design principle of small-molecule organic semiconductors for metal-free, visible-light-promoted photocatalysis*, *Angew. Chem. Int. Ed.*, **2016**, *55*, 9783-9787.

Huang, W.; Ma, B. C.; Wang, D.; Wang, Z. J.; Li, R.; Wang, L.; Landfester, K.; Zhang, K. A. I. *A fixed-bed photoreactor using conjugated nanoporous polymer-coated glass fibers for visible light-promoted continuous photoredox reactions*, *J. Mater. Chem. A*, **2017**, *5*, 3792-3797.

Huang, W.; Ma, B. C.; Lu, H.; Li, R.; Wang, L.; Landfester, K.; Zhang, K. A. I.; *Visible light-promoted selective oxidation of alcohols using a covalent triazine framework*, *ACS Catal.*, **2017**, *7*, 5438-5442.

Conference

Poster presentation: "Photocatalytic selective bromination of aromatic compounds using microporous organic polymers with visible light", Run Li, Katharina Landfester and Kai Zhang, at conference "Polymer Photocatalysts for Solar Fuels Synthesis", London, 13-14th April 2016, awarded with RSC, *Catalysis Science & Technology* poster prize.